Periodically driven photonic topological gapless systems

Lavi Kumar Upreti

Numéro de Thèse : **2020LYSEN017**

THÈSE de DOCTORAT DE L'UNIVERSITÉ DE LYON

opérée par

l'École Normale Supérieure de Lyon

Ecole Doctorale N°52

Physique et Astrophysique de Lyon

Discipline : Physique

Soutenue publiquement le 12/06/2020, par :

Lavi Kumar UPRETI

Periodically driven photonic topological gapless systems

Propriétés topologiques de systèmes photoniques non gappés modulés périodiquement

---

Devant le jury composé de :

Cayssol, Jérôme,	Professeur, Université Bordeaux	Rapporteur
Mortessagne, Fabrice,	Professeur, Université Côte d'Azur	Rapporteur
Carpentier, David,	Directeur de Recherche, ENS de Lyon	Examinateur
Meyer, Julia,	Professeure, Université Grenoble Alpes	Examinatrice
Delplace, Pierre	Chargé de recherche HDR, ENS de Lyon	Directeur de thèse

Abstract

Photonics has emerged a platform where electromagnetic waves (or photons) propagate inside a crystal (like Bloch waves) formed by the underlying discrete degrees of freedom, e.g., waveguide arrays. These waves cannot propagate if the incident frequency lies within the so-called photonic bandgap, then these waves are known as evanescent waves. Thus, the crystal behaves as a reflector to these waves. However, if there are modes for which there exist boundary waves that connect the bandgap, then these waves can exist at the boundary without leaking into the bulk. This is analogous to the chiral motion of electrons at the quantum Hall edges, with an extra ingredient of time-reversal symmetry breaking in photonic crystals via some gyromagnetic properties of the sample, or inherent time dependence of the system. In the latter case, when the system, specifically, driven periodically then the more exotic non-equilibrium phases can also be observed in these lattices.

In this work, we explore the topological properties in these periodically driven photonic lattices. For instance, how fundamental symmetries, e.g., particle-hole symmetry, can be implemented to engineer topology in 1D. We find a connection between crystalline symmetries and the fundamental symmetries, which facilitate such implementation. Moreover, a synthetic dimension can be introduced in these lattices that simulate higher dimensional physics. The difference between synthetic and spatial dimension becomes apparent when a specific crystalline symmetry, like inversion, is broken in these systems. This breaking changes a direct bandgap to an indirect one which manifests in the winding of bands in the quasienergy band spectrum. If it is broken in the synthetic dimension, it results in an interplay of two topological properties: one is the winding of the quasienergy bands, and the other one is the presence of chiral edge states in the finite geometry. This former property of winding manifests as Bloch oscillations of wavepackets, where we show that the stationary points in these oscillations are related to the winding number of the bands. This topological property can thus be probed directly in an experiment by the state-of-art technology. However, if this symmetry is broken in the spatial dimension, the winding of bands manifest as a quantized drift of mean position, which is still characterized by a winding number of the bands. Furthermore, we show that a different gapless regime can also be engineered while preserving the inversion symmetry. In this regime, the topology can be captured by enclosing the degeneracies in parameter space and calculating the Berry flux piercing through the enclosed surface. In this case, some of the degeneracies can host chiral edge states along with other protected ones at the same quasienergy.

Dedication

To my master Sir S. N. Goenkā,
my mum, dad, and sis.

"If wisdom arises in your mind, you become humble and modest, as a branch laden with fruit is sure to bow low."
— S. N. Goenkā

Acknowledgements

I spent 4 years at the Laboratoire de Physique, ENS de Lyon. I came in the fall of 2016. To admire autumn in France when trees are painting nature with beautiful colors. Obviously, things were not very easy in the beginning since I forgot to subscribe to the French classes. But things started to become better with time. First of all, I would like to thank in this journey to my parents and my sister for their constant support during my doctoral studies, despite not knowing what I am doing. However, their love has been crucial during these times.
I am deeply thankful to my advisor Pierre Delplace for nurturing me with the necessary knowledge. He never hesitated to repeat his points, many times knowing very well that half of the time I am lost on my own thoughts. He always made sure to make the point as simple as possible, however, profound it may be. This helped me in developing my communication and presentation skills. I not only learned physics from him but also English. Even though I disturbed him many times, moments before several deadlines, his unwavering patience, and easily approachable behavior have taught me these qualities. His very helping, caring and motivating nature has always kept me far from any troubles.
It was a great time to work on this project, so I would like to thank my collaborators and coauthors Mathieu Bellec, Alberto Amo, Clément Evain, Stephen Randoux, and Pierre Suret. In particular, I have learned a lot from Alberto Amo and Clément Evain.

I am also very thankful to David Carpentier for always there to help me in physics, or terms of moral support. His ability to explain every concept so pedagogically has always helped me in having nice perspectives about them. His moral support when I needed it the most has been a tremendous boost for me.
I cannot forget to thank the previous lab director Thierry Dauxois, who always made sure that I am comfortable in the lab.

I had a very nice time during these years also outside the lab. The credit goes to my friends who were always there for me, to help and understand me, every time putting their troubles down for me. They never made me feel that I am far from my country. They are undoubtedly an invaluable part of this thesis. The list starts chronologically, Camille Toullelan, Salvish Goomanee, Baptiste Pezelier, Clément Dutreix, Shweta Sharma, Nupur Khera, Santosh Kumar, Bineet Dash, Puskar Despande, Pragya Tripathi, Marco Marciani, Stavroula Lina, Dario Lucente, Marcelo Guzman Jara, Yeraldinne Carrasco Salas, Alex Fontana, Vincenzo, Ignacio Andrade, Christobal, Matthias Droth, Shefali Thakur, Sergio, Yannis, Mirella, Amit Sahu, Amith, Asta Heinesen, Sebastian Gallon, Jérôme Thibaut,

Raphael Menu, Thibaud Louvet, Barbara Pascal, Nam Hoang, Sunil, and Nicolas Perez. I am sorry if I missed any friends. I will definitely miss the Chilean parties till 5 AM; hiking adventure on the Grenoble's autoroute instead of mountains with Lina; Italian adventure with Marco, Marcelo, Dario, and Vincenzo; Indian festivals with French vines with Shefali, Amit; swimming lessons from Alex; Bordeaux fun with Marco, Lina, and Matthias; trying subway restaurant in Munich with Marco, and also with Marcelo in Rome; French classes with Dario, Lina, Yeraldinne, and Yannis; Trip to Saint-Étienne with Salvish; hiking in the Chamonix with Shweta, Nupur, and Santosh; Nice birthday cake form Lina and Yeraldinne; Winning in Fréjus trip even though Marcelo wanted otherwise; Wonderful physics discussions with Marco, Marcelo, and Dario. There are many more adventures that are possibly more than the pages of any chapter of my thesis.

Finally, I hope to enrich my knowledge that I receive from each of you.

Contents

Chapter 1

Introduction

1.1 Topological insulators and beyond

The most remarkable discovery of QHE (Klitzing et al. 1980) has opened the field of topological insulators. It showed the presence of a phase transition which cannot be explained by the versatile Landau theory of symmetry breaking (Landau 1937). Later, Thouless showed that one could obtain a similar 2D topological insulator by introducing an adiabatically varying potential $V(t)$ to a 1D system (Thouless 1983). The similarity between both comes from the fact that the same Chern number C distinguishes the topological phases. In the first case, C predicts the number of non-trivial chiral edge states, and its sign dictates their direction of motion (or chirality). In the Thouless case, it corresponds to the amount of charge pumped after a period T, where $V(t+T) = V(t)$, and sign (of C) corresponds to the direction of the charge pumped with respect to the direction of variation of the potential. It can be inferred from both the cases how a topological number (i.e., Chern number) manifests and can be probed experimentally by measuring an observable quantity, namely, the Hall conductance or the quantized number of pumped particles. This connection between the topological invariant and the presence of edge states is the most remarkable signature of topological systems, also known as *bulk edge correspondence* (Hatsugai 1993a,b; M. S. Rudner et al. 2013). In 2005, Kane and Mele predicted another example of topological insulator in the 2D fermionic system, but in the absence of magnetic field with strong spin-orbit couplings, known as the quantum spin Hall effect (Bernevig, Hughes, et al. 2006; Bernevig and Zhang 2006; Fu et al. 2007; Kane et al. 2005; J. E. Moore et al. 2007; Roy 2009), which was later confirmed experimentally (Hsieh et al. 2008; König et al. 2007; Roth et al. 2009). In contrast to the QHE, where the magnetic field breaks time-reversal symmetry, the quantum spin Hall effect restores it. Later, more other discoveries like 3D topological insulators showed the connection between the presence of topological insulators and symmetries. That posed a question: how many distinct topological insulators do exist in nature? Altland and Zirnbauer took a step in this direction in their seminal work (Altland et al. 1997; Kitaev 2009; Zirnbauer 1996), where they identified 10 symmetry classes responsible for giving non-trivial topological insulators depending on the dimension of the system. This classification contains SSH model (Su et al. 1980a) in 1D, QHE and quantum spin Hall effect in 2D(Bernevig, Hughes, et al. 2006; Bernevig and Zhang 2006; Kane et al. 2005; Klitzing et al. 1980; Thouless et al.

1982), and 3D topological insulators (M. Zahid Hasan et al. 2011; Joel E. Moore 2013), just to say few.

The search for distinct topological phases motivates us to look beyond the static regime. To go beyond the Thouless pump, where time varies adiabatically, one needs to consider general time dependence (e.g. diabatic). The next right candidate (or regime) became apparent to be periodically driven systems. Remarkably, there exist many domains to simulate the topological behavior in this regime. For example, in artificial systems, a periodic discrete-time quantum walks in 1D (Asbóth 2012; Kitagawa, M. S. Rudner, et al. 2010); in optical lattices, where atoms are trapped by lasers to simulate a solid-state system, it gives more flexibility and controllability[1], which facilitated the first experimental implementation of the Haldane model by circular modulation of each lattice position (Jotzu et al. 2014). The same setup of optical lattices allowed to theoretically propose to observe the fractional quantum Hall state of atoms by combining periodically time-varying quadrupolar potential ($V(t) = V_{qp} \sin \omega t$) and modulation of tunneling in time (by varying the laser intensity) (Sørensen et al. 2005). There are several other techniques to drive the system periodically, e.g. by injecting an electromagnetic wave to a quantum system. That in turn can induce topology to the system, which otherwise is absent. If this electromagnetic wave is circularly polarized, then it can gap the Dirac cone in graphene, it gives rise to photoinduced (changing the laser intensity with time) dc Hall current (Oka et al. 2009), this photoinducing can tune a conventional insulator into a quantum spin Hall system (Inoue et al. 2010). There are several other studies that have shown the richness of this regime, more specifically on irradiated graphene Ref (Calvo et al. 2011; Delplace, Á. Gómez-León, et al. 2013; Á. Gómez-León et al. 2014; Sie et al. 2015). In the case of quantum systems, it was predicted that by irradiating a semiconductor well can give rise to a non-equilibrium phase, known as "Floquet topological insulator" (Netanel H Lindner et al. 2011), which was later confirmed experimentally (Mahmood et al. 2016; McIver et al. 2020; Y. H. Wang et al. 2013). An early review article can be found in Ref (Cayssol et al. 2013).

Topological phases are not only restricted to solid-state systems but other systems. The reason being the topological properties are captured by topological invariant, e.g., Chern number emerges from single-particle formalism, and another vital element comes from the underlying wave nature, e.g., electron waves in quantum systems. These two ingredients together rendered to look for non-trivial phases beyond the quantum domain. It is ascertained in numerous classical systems. In particular in the photonics, Raghu and Haldane (Haldane et al. 2008; Raghu et al. 2008) theoretically proposed to implement the QHE in photonics. That was later observed in photonics in a 2D photonic crystal (Zheng Wang et al. 2009), quite recently, the Haldane model has experimentally been observed in coupled ring resonators (Mittal et al. 2019). In the case of periodically driven systems using photonics waveguide arrays, it leads to the observation of first of its kind "photonic Floquet topological insulator" (Rechtsman et al. 2013). The examples also emerged in other classical systems, e.g., in acoustic waves (Fleury et al. 2016), geophysical or astrophysical flows (Delplace, Marston, et al. 2017; Perrot et al. 2019), active matter (Shankar et al. 2017; Souslov, Das-

[1] As one can generate different lattice geometries by changing the angles, wavelengths and polarizations of laser beams

biswas, et al. 2019; Souslov, Zuiden, et al. 2017), just to say few. Surprisingly, as driving can induce novel topology, introducing a disorder to otherwise a clean system can also induce a non-trivial topology. For example, topological Anderson insulator was predicted in a static case (Groth et al. 2009; Guo et al. 2010; J. Li et al. 2009; C. Liu et al. 2017) and later also shown to be present in the periodically driven systems, known as Floquet Anderson insulator (Titum, Berg, et al. 2016; Titum, Netanel H. Lindner, et al. 2015). Despite the disorder, the topology manifests with the presence of enhanced transport at the edges, which was confirmed in the photonics experiment by the observation of photonic topological Anderson insulator (Stützer et al. 2018). In parallel, this promised to extend the domain of topology from regular crystalline structure to the amorphous solid, since topological edge states are protected against weak disorder. These symmetry protected edge states still exist up to some lattice density with random lattice points (Agarwala et al. 2017; Costa et al. 2019). Very recently, photonic topological edge states in the amorphous regime have been experimentally observed(P. Zhou et al. 2020).

Nevertheless, the topology is not restricted only to systems with gapped spectra, where all the above examples fall. It also extends to the gapless regime. This lead to the search to look for topological properties of waves inside the crystals beyond conventional topological insulators (M. Z. Hasan et al. 2010; Xiao et al. 2010). They can be semimetals and even metals (Armitage et al. 2018; Bahari et al. 2019; Burkov 2016; Kumar et al. 2019; S. Sun et al. 2020; Y. B. Yang et al. 2019; Ying et al. 2018, 2019; Z. Zhu, Winkler, et al. 2016). These topological gapless materials, unlike insulators, do not possess any well-defined gap, and in literature, all of these come under the same umbrella of topological metals (Armitage et al. 2018).

Topological gapless material classification according to various features (S. Li et al. 2020):

- Firstly, it can be based on the dimensionality of the band crossings near the Fermi energy, as shown in Fig. 1.1.
  - For example, for a 3D material, the band crossing can namely be nodal-point (0D) (Burkov et al. 2011; Koshino et al. 2016), nodal-line (1D) (Fang, Weng, et al. 2016; Koshino et al. 2016), and nodal-surface (2D) (Wu, Y. Liu, et al. 2018) topological metals.

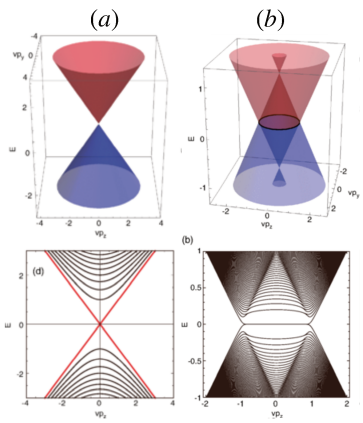

Figure 1.1: Classification on the basis of dimension of band crossing for (a) a nodal point and (b) Nodal line. From Koshino et al. 2016.

- Secondly, based on the degree of the degeneracy of the band crossings, as sketched in Fig.1.2.

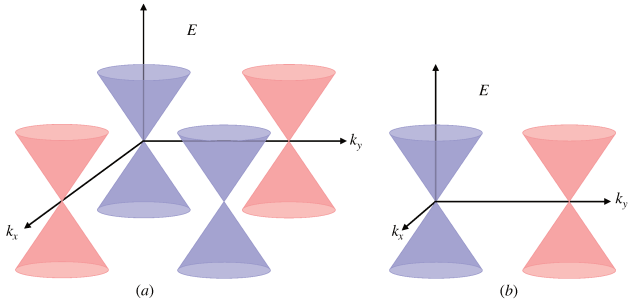

Figure 1.2: Classification on the basis of degree of band crossing for (a) a Dirac semimetal with four fold degeneracy and (b) a Weyl semimetal with two fold degeneracy

  - For instance, in 3D, breaking inversion and time-reversal symmetry leads to Weyl semimetals cited as two-fold degenerate nodal points topological metals (Murakami 2007; Murakami et al. 2007; Wan et al. 2011). In contrast, Dirac semimetals keep these symmetries intact and are referred to as topological metals with four fold degenerate nodal points (Zhijun Wang, Y. Sun, et al. 2012; Zhijun Wang, Weng, et al. 2013; Young et al. 2012).

- Thirdly, the nature of dispersion around the band touching, as sketched in Fig.1.3.

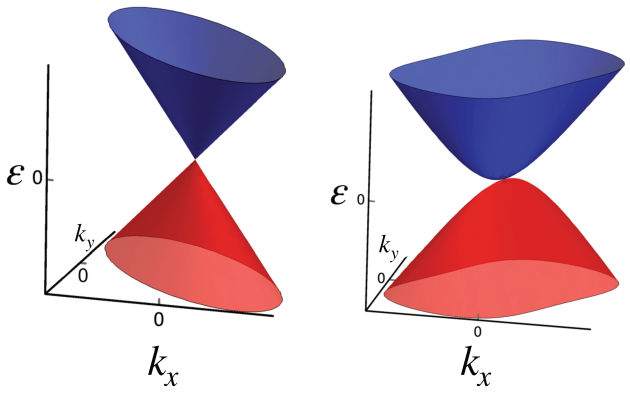

Figure 1.3: Classification on the basis of dispersion around the band crossing for (a) a linear and (b) a quadratic

  - For instance, the presence of a linear, quadratic or cubic dispersion as leading order terms in the Hamiltonian around nodal points or lines (Fang, Gilbert, et al. 2012; X.-P. Li et al. 2019; Wu, Yu, et al. 2019; B.-J. Yang et al. 2014; Yu et al. 2019; Z. Zhu, Y. Liu, et al. 2018)[2].

- Fourthly, still based on dispersion but also taking into account the sign of the slope of the band crossings, however, specific to linear band crossings (S. Li et al. 2020), as sketched in Fig. 1.4.

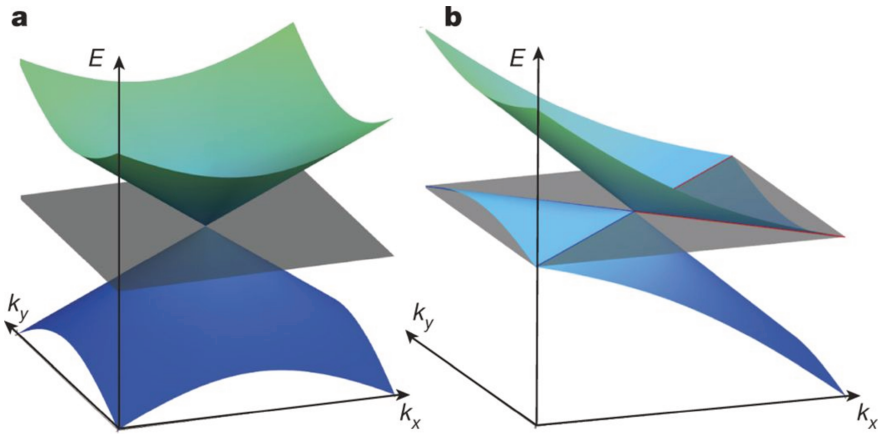

Figure 1.4: Weyl semimetal of (a) type I and (b) type II. From Ref(Soluyanov et al. 2015).

  - For example, Weyl semimetals of type-I contain a nodal point at the band crossing, while Weyl semimetals of type-II is tilted with respect to the energy (vertical) axis that have the same sign for the slopes of the two bands, as sketched in Fig. 1.4. However, both of them share the same topological properties, since both lacks any symmetries. The only difference is in their physical properties like conduction,

[2] A 3D crystal with only symmetry of n fold rotation symmetry about z axis, for $n = 2, 3, 4, 6$, on expanding around the band touching will give rise to a Hamiltonian whose leading order term is (quadratic) $\propto (ak_+^2 + bk_-^2)\sigma_+$, where $k/\sigma_\pm = \sigma_x \pm i\sigma_y$ (Fang, Gilbert, et al. 2012)

originating from the difference in their Fermi surface. For types-I, it is a Fermi point, and for types-II, there are Fermi pockets(Soluyanov et al. 2015).

- Lastly, based on the topology. When there is an indirect gap, they can be classified according to the global topology of their spectrally isolated bands over the Brillouin zone Fig. 3.7[3](Palumbo et al. 2015; Ying et al. 2018, 2019). When there are no gaps (direct or indirect), they can be characterized locally by the robustness of their nodal points or lines, that is somehow analogous to topological defects in reciprocal space.

  – For example, in Weyl semimetals, the degeneracy (or nodal point) is completely robust against any Hermitian disorder. These nodal points are monopoles of Berry curvature, and their robustness can be quantified by defining a Berry flux piercing through a closed surface in momentum space enclosing them (G. E. Volovik 2009). However, if there is a well-defined gap (direct or indirect) topology can be defined using standard tools, where the topology is captured by the full Hamiltonian[4].

[3]Since, by restoring inversion symmetry one can define a meaningful topological invariant—in other words, continuously deforming the bands without crossing the transition point.

[4]The full Hamiltonian refers that it is not approximated like in Weyl semimetal, where it is linearized around the band touching.

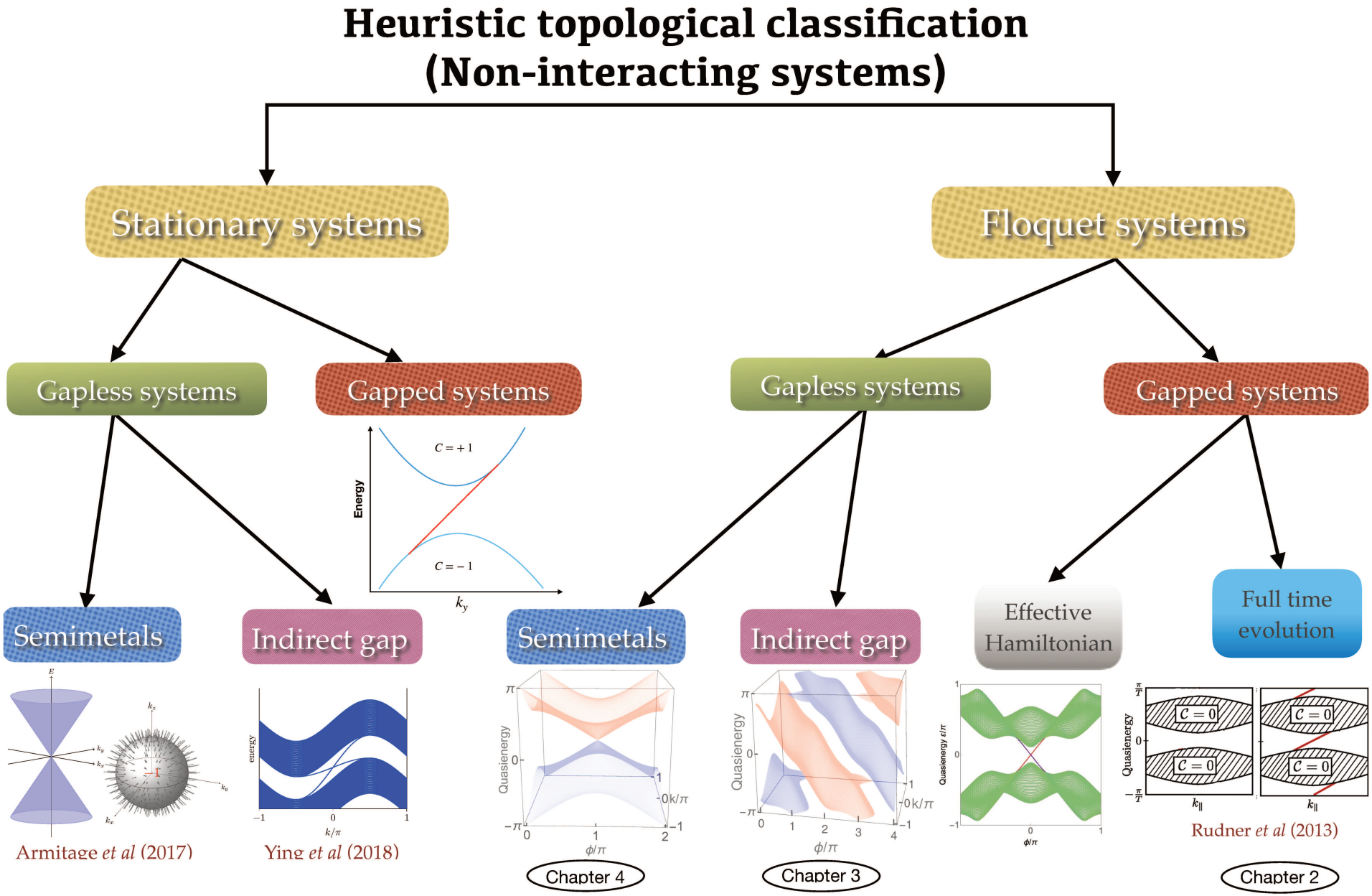

Figure 1.5: A heuristic classification of non-interacting topological system on the basis of time dependence and the nature of the spectrum, if it is gapless or gapped.

1.2 Outline

The Fig. 1.5 shows a heuristic topological classification. If we follow it then, firstly, the system can be classified based on Hamiltonian time dependence, if there is no time dependence we fall in stationary regime, whereas if the Hamiltonian is periodic under time $H(t+T) = H(t)$, then it falls in Floquet class. Then these classes can be further divided based on their spectrum, i.e., if the system posses any gaps, then it can host a topological edge state. In the case of the Floquet system, the gapped phase can be further subdivided into two, where topology in one case is quite similar to the static systems, and it is determined by the effective Hamiltonian. The other class has no analog in the static regime, and it is specific to the Floquet systems (M. S. Rudner et al. 2013). There is also a similar relation between symmetries and the dimension of the system in the Floquet system (Roy and Harper 2017), like AZ classification. I will present in the second chapter how these (abstract) symmetries (e.g. particle-hole) can be engineered in the photonic waveguide arrays, whose introduction shall follow in the next section. The spectrum here still possesses a well-defined gap.

Now, if the system is gapless, which means there are bulk states at each energy. Then for the stationary case, this can happen if the system initially has a well-defined gap, where the two bands are well separated in energy, then by breaking some symmetry(s), for instance, inversion symmetry, the spectrum can continuously deform into an indirect gap along with the edge states. If we define a Fermi level in the gap when there was a direct gap, then in the indirect case, the contribution at the Fermi level not only comes from the edge states but also the bands. Surprisingly, the situation in the Floquet system is very interesting, where both the quasimomenta axis and the (quasi-)energy axis are periodic. I shall present a situation in 2D in this regime of inversion symmetry breaking in chapter third, where the system under consideration will show the fully gapless spectrum and wind in BZ. It may fall in the fourth class of the gapless classification (of the previous section), where all the bands have the same sign for the group velocity of the bands but with no counterpart in the stationary regime. Moreover, this symmetry can be broken along a spatial dimension or some synthetic dimension, the bulk spectrum does not seem to differ, but the topological properties manifest differently. There are many platforms to realize this Floquet phenomenon like photonics, acoustics, or ultracold atoms, I primarily stick to the photonics. Unlike in the electronic systems where standard conductivity experiments can probe this indirect gap (Ying et al. 2018), I present in the same third chapter how in the photonics, these two different inversion symmetry breaking cases, namely spatial and synthetic can be implemented and how their manifestation can be probed.

Moreover, the gapless situation can also appear through the presence of robust degeneracies. In the stationary case, the well-known examples are the 3D Weyl semimetals, whose topologies are captured by their degeneracies in momentum space. I will present a similar gapless regime example in the 2D Floquet system, whose topology is captured similarly in chapter4. I present two systems, where one breaks inversion symmetry to show the gapless phase and another show gapless regime while preserving the inversion symmetry.

1.3 Photonics

The photonics (Joannopoulos J. D. et al. 2008) has emerged as an eminent platform to engineer and probe topological properties of waves. The topological properties like chiral edge states, were first predicted and also observed in condensed matter systems, which then spread to many domains, e.g., photonics (Haldane et al. 2008; Raghu et al. 2008), acoustics (Fleury et al. 2016), metamaterials (Krishnamoorthy et al. 2012), circuits (Lee, Imhof, et al. 2017), cold atoms (Cooper et al. 2019), and many more. We consider one such platform, namely photonics, where similar topological properties were seen, e.g., unidirectional propagation of light in photonic crystals (Rechtsman et al. 2013; Zheng Wang et al. 2009). Photonics is a vast field in itself where periodic arrangements of dielectric materials can form a lattice and guide the motion of photons, and these dielectrics are analogous to atoms in a lattice. These lattices can host topological edge states ranging from dielectric metamaterial (Khanikaev, Hossein Mousavi, et al. 2013), microwave cavities (Hu et al. 2015a), dielectric resonators (Bellec, Ulrich Kuhl, et al. 2013; U. Kuhl et al. 2010),coupled-ring optical resonators (CROW) (F. Gao et al. 2016; Hafezi et al. 2011), evanescently coupled waveguide arrays (Rechtsman et al. 2013; Szameit and Stefan Nolte 2010), circular fibers (Wimmer, Mohammed-Ali Miri, et al. 2015; Wimmer, Hannah M Price, et al. 2017), photonic quantum walk (Kitagawa, Matthew A Broome, et al. 2012), just to say few. The biggest plus point of the photonics is that it is classical, besides the photonic quantum walk. For this reason, phenomenon like nonhermiticity (Feng et al. 2017; El-Ganainy et al. 2018a; Zhao et al. 2018), where the parity and time-reversal symmetry is broken, can be engineered and it has been linked to novel applications like topological lasers (Bandres et al. 2018; Shao et al. 2020; Zeng et al. 2020).

I shall give a brief overview of the the three setups, namely evanescently coupled waveguide arrays, circular fibers, and photonic quantum walk, mainly because of their proximity to my projects. In these three setups, evanescently coupled waveguide arrays, and circular fibers form the underlying lattice where the electromagnetic waves propagate analogous to the electronic waves in a crystal. Similarly, in the photonic quantum walk, the photons propagate.

Specifically, we discuss the planar waveguide, where the boundary conditions give rise to the mode expansion, which in turn predicts the mode allowed for propagation. Keeping this as a background, we go to the next stage, where the array of such waveguides can be evanescently coupled through the modes. I will present two cases: (i) between the incoming and outgoing waves within the same waveguide, and (ii) between different but nearby waveguides. As we will see, this latter case would be analogous to the tight-binding model of electrons.

1.4 Waveguide: optical fiber

We start with the very basics of the planar waveguides. The most fundamental building block of any photonics waveguide network is a waveguide. It consists of a core, where mostly the light is confined, and it is surrounded by a cladding, as shown in Fig 1.6. More details of this section can be found in (Okamoto 2006) and (Amnon Yariv 1991).

If a light is injected at an incident angle θ to the normal to the boundary, using Snell's law for an angle of refraction ϕ, the critical condition for the total internal reflection is

$$\theta \leq \sin^{-1}\sqrt{n_1^2 - n_0^2} \equiv \theta_{\max}, \tag{1.1}$$

$$\theta_{\max} \approx \sqrt{n_1^2 - n_0^2}, \tag{1.2}$$

$$\phi_{\max} \approx \theta_{\max}/n_1. \tag{1.3}$$

Usually, the refractive index difference between core and cladding is of the order of 10^{-2} this allows us to write the equation(1.2) for the maximum acceptance angle of the waveguide. Thus, the maximum angle for the propagation of light inside the core is $\phi_{\max}$, given by equation(1.3).

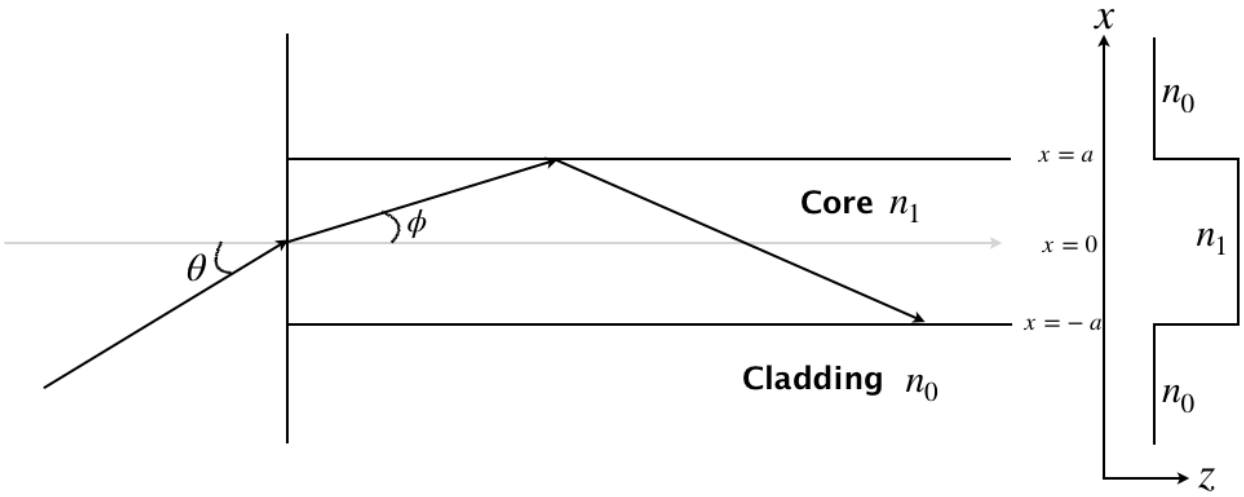

Figure 1.6: Basic geometry of an optical fiber with refractive index higher in the core (n_1) than in the cladding (n_0)

Even though the angle ϕ is chosen smaller than $\phi_{\max}$, the light rays with an arbitrary angle ϕ can not propagate inside the waveguide. Only some specific values of ϕ's are allowed, for instance $\phi \leq \phi_{\max}$, where each different values of angle ϕ corresponds to a specific (propagating) mode. These modes are analogous to the allowed energy levels in quantum mechanics, e.g., particle in a box. We will not go into much details on the modes as they can easily be found in the standard textbook.

There are different types of structures (or geometry) for waveguides, as shown in Fig 1.7, mostly depending on−
(1) the operating frequency bandwidth, for example, in the case of coaxial cable is below 3GHz,
(2) the amount of power to be transferred from one point in space to another, which in the coaxial cable is of the order of 1 kilowatt at 100 MHz (it decreases to 200 watt at 2GHz due to heating losses), and
(3) the amount of tolerable transmission losses. The coaxial cable has 3 decibels per 100 m at 100MHz, which increases to 10 decibels per 100 m at 1 GHz (which means more loss), for more details see Orfanidis 2016.

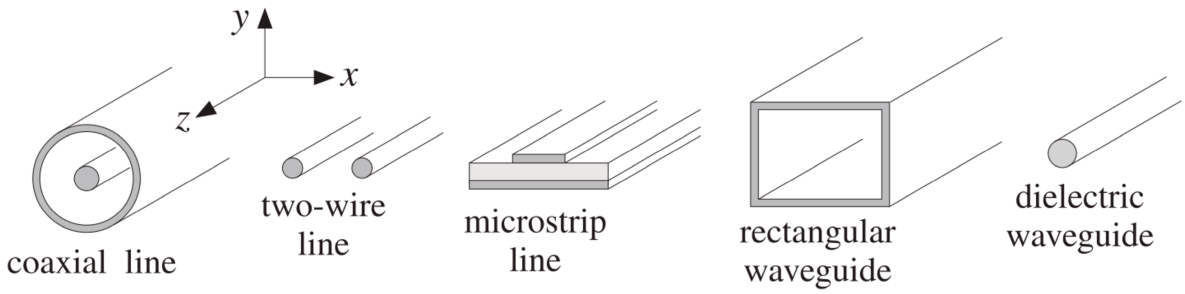

Figure 1.7: Optical waveguides of different geometries, from Orfanidis 2016

1.5 Propagation along a waveguide: Paraxial approximation

Another essential aspect besides the allowed mode of light propagation inside an optical fiber is the confinement of a light beam along the propagation axis. If the light beam is propagating along z direction (axis of the waveguide) such that the variations along the transverse plane (comprised of x and y) in comparison to z are very small, for example, in the case of a laser beam. Then this corresponds to a wavevector component along the z direction to be greater than those in the x and y directions, $k_0 \approx k_z \gg k_{x,y}$, this is referred to as the *paraxial approximation*.

Maxwell's wave equation governs the propagation of an electromagnetic wave in a source free, non-magnetic material with spatially dependent dielectric constant $\varepsilon(\mathbf{r})$:

$$\begin{aligned} \nabla\Big(\nabla\cdot\mathbf{E}(\mathbf{r},t)\Big) - \nabla^2\mathbf{E}(\mathbf{r},t) &= -\varepsilon(\mathbf{r})\frac{\partial^2}{\partial t^2}\mathbf{E}(\mathbf{r},t), \\ -\nabla\Big(\frac{\nabla\varepsilon(\mathbf{r})\cdot\mathbf{E}(\mathbf{r})}{\varepsilon(\mathbf{r})}\Big) - \nabla^2\mathbf{E}(\mathbf{r}) &= -\varepsilon(\mathbf{r})\Big(\frac{\omega}{c}\Big)^2\mathbf{E}(\mathbf{r}) \end{aligned} \tag{1.4}$$

where electric field $\mathbf{E}(\mathbf{r},t) = \mathbf{E}(\mathbf{r})\mathrm{e}^{i\omega t}$, ω is the frequency of light, and c is the speed of light in vacuum.
If the $\varepsilon(\mathbf{r}) = \varepsilon_0 + \delta\varepsilon(\mathbf{r})$ does not vary from its surrounding value $\varepsilon_0 = n_0^2$, we can neglect spatially varying term in eq.(1.4), that gives us

$$\nabla^2\mathbf{E}(\mathbf{r}) = \varepsilon(\mathbf{r})\Big(\frac{\omega}{c}\Big)^2\mathbf{E}(\mathbf{r}). \tag{1.5}$$

Let us apply the paraxial approximation to equation(1.5), where the electric field can be decomposed into two parts: one that is the axially slowly varying envelope term $\mathcal{E}(x,y,z)$ and another one that is the rapidly varying term $\mathrm{e}^{ik_0n_0z}$, where n_0 is the refractive index of the cladding (or surrounding):

$$E(x,y,z) = \mathcal{E}(x,y,z)\mathrm{e}^{ik_0n_0z}. \tag{1.6}$$

By substituting this eq(1.6) in eq(1.5), it gives us

$$\nabla^2 E - n_0^2 E = 0 \tag{1.7}$$

$$\nabla_T^2 \mathcal{E} + \frac{\partial^2 \mathcal{E}}{\partial z^2} + 2ik_0 n_0 \frac{\partial \mathcal{E}}{\partial z} + k_0^2 (n_1^2 - n_0^2)\mathcal{E} = 0. \tag{1.8}$$

The envelope term varies very slowly along z, i.e., $|\frac{\partial^2 \mathcal{E}}{\partial z^2}| \ll |\frac{\partial \mathcal{E}}{\partial z}|$, this simplifies the equation to

$$\nabla_T^2 \mathcal{E} + 2ik_0 n_0 \frac{\partial \mathcal{E}}{\partial z} + k_0^2 (n_1^2 - n_0^2)\mathcal{E} = 0 \tag{1.9}$$

where spatial transverse Laplacian is given by

$$\nabla_T^2 \equiv \frac{\partial^2}{\partial x^2} + \frac{\partial^2}{\partial y^2}.$$

Also, assuming the weakly guiding conditions[5], we can approximate $(n_1^2 - n_0^2) \cong 2n_0(n_1 - n_0)$[6].

$$ik_0 \frac{\partial \mathcal{E}}{\partial z} = -\left(\frac{1}{2n_0 k_0^2}\nabla_T^2 \mathcal{E} + (n_1 - n_0)\mathcal{E}\right), \tag{1.10}$$

$$i\lambda \frac{\partial}{\partial z}\mathcal{E}(x, y, z) = -\left(\frac{\lambda^2}{2n_0}\nabla_T^2 + \Delta n\right)\mathcal{E}(x, y, z) \tag{1.11}$$

where $\lambda = 1/k_0$ and $\Delta n = n_1 - n_0$ is the change in the refractive index from the bulk (n_0) to the propagating medium (n_1), this equation(1.11) is known as *paraxial Helmholtz equation*. It is very similar in form to the Schrödinger's equation,

$$i\hbar \frac{\partial}{\partial t}\Psi(x, y, z, t) = \left(-\frac{\hbar^2}{2m}\nabla^2 + V(x, y, z, t)\right)\Psi(x, y, z, t) \tag{1.12}$$

A correspondence between Schrödinger's equation and paraxial Helmholtz's equation can be made, where

Schrödinger's equation	**paraxial Helmholtz's equation**
time t	propagation axis z
mass m	bulk refractive index n_0
Planck's constant $\hbar$	reduced wavelength λ
Potential V	refractive index change Δn

Instead of wave packet evolution in time governed by Schrödinger's equation(1.12), we have a wave packet (electric field envelope) evolving along the propagation axis (z) (1.11). That facilitates monitoring the light propagation by direct observation in space, and as a result, preventing the problem of resolution of short time scales, which may arise in the case of electron. Another significant advantage, the experiments can be carried out at room

[5] weakly guiding refers to when the difference between the refractive indexes of the core(or film) and the cladding is very small.

[6] $(n_1^2 - n_0^2) = (n_1 + n_0)(n_1 - n_0) = 2n_0(n_1 - n_0)$, $n_1 \approx n_0$

temperature, unlike in solid-states, where thermal energy contribution is significant at room temperature and can thus be a downside. Besides, there is one dissimilarity between both equations, electrons are more localized at a lower potential since it minimizes their total energy. In contrast, there is a negative sign in front of Δn, meaning that an electromagnetic wave is more localized when the medium has a higher refractive index than the surrounding environment, this guides the motion of electromagnetic waves inside the waveguide.

1.6 Coupling between guided modes

In quantum mechanics, if the potential has spatial periodicity $V(r+a) = V(r)$, it provides an underlying lattice structure. Similarly, the correspondence between quantum mechanics and paraxial Helmholtz's equation also extends in this direction, where the waveguides spatial periodicity ($\Delta n(r+a) = \Delta n(r)$) is analogous to atoms in a conventional lattice. It is captured by coupled mode theory, where more detailed information can be found in books of Okamoto (Okamoto 2006) and Yariv (Amnon Yariv 1991). The present section is heavily drawn from these two books.

Until now, we assumed propagation of light in a single waveguide. However, if there is more than one waveguide adjacent to each other at a relatively close distance, then the co-propagating or contra-propagating light beams can interact and can give rise to two scenarios. One is desirable, as in the case of directional couplers, where this results in the coupling of modes, and the power is transferred from one waveguide to another. Another is undesirable, where it can result in a phenomenon of interference of modes called crosstalk. I stick to the positive aspect of it that is the coupling of modes. In this section, I present a brief sketch of this mutual interaction between two propagating modes, which falls under the formalism of coupled-mode theory (A. Yariv 1973).

Let us consider a case of two waveguides (as shown in Fig 1.8), where each waveguide supports its corresponding modes. If these two waveguides are far apart, then their modes do not couple and can continue unperturbed. However, if they are close, where the distance is such that the electromagnetic field distribution is significantly the same as in the former case, then the coupled waveguides propagation features can be understood by the perturbation method (Marcuse 1973). This is very analogous to the case of the hybridization of energy levels in solid-state due to the presence of more number of atoms in close vicinity.

The eigenmodes in each (optical) waveguide before the coupling of mode satisfy Maxwell's equations for the electric field $\tilde{\mathbf{E}}_l$ (where real field $\mathbf{E}_l = \mathrm{Re}[\tilde{\mathbf{E}}_l]$) and magnetic field $\tilde{\mathbf{H}}_l$ in the form

$$\begin{aligned} \nabla \times \tilde{\mathbf{E}}_l &= -i\omega\mu_0 \tilde{\mathbf{H}}_l \qquad (l = I, II) \\ \nabla \times \tilde{\mathbf{H}}_l &= i\omega\varepsilon_0 n_l^2 \tilde{\mathbf{E}}_l. \end{aligned} \tag{1.13}$$

To write electromagnetic fields of the coupled waveguide (see Fig 1.8) we assume that it can be written as the sum of eigenmodes of each waveguide-

$$\begin{aligned} \tilde{\mathbf{E}} &= A(z)\tilde{\mathbf{E}}_I + B(z)\tilde{\mathbf{E}}_{II}, \\ \tilde{\mathbf{H}} &= A(z)\tilde{\mathbf{H}}_I + B(z)\tilde{\mathbf{H}}_{II} \end{aligned} \tag{1.14}$$

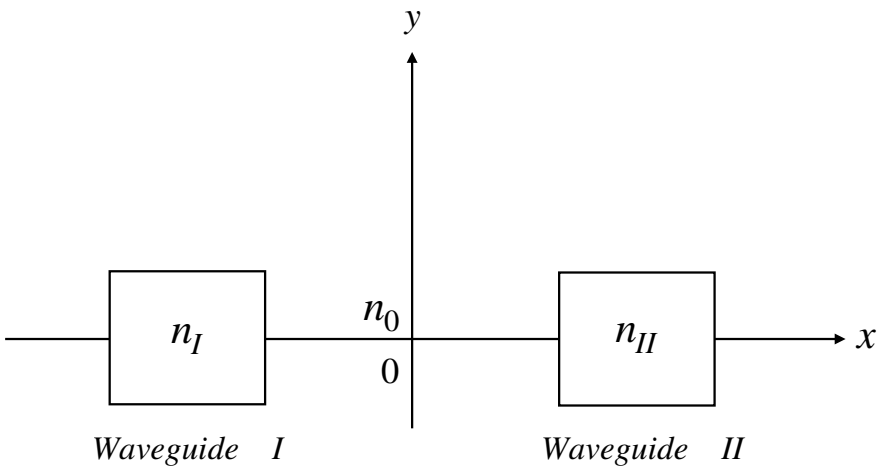

Figure 1.8: Directional coupling of two waveguides

In quantum mechanics, the above equation can be thought of as expressing a (perturbed) state vector in terms of eigenstates.

The full electromagnetic fields of coupled waveguide $\tilde{\mathbf{E}}$ and $\tilde{\mathbf{H}}$ satisfy similar to equation(1.13)

$$\begin{aligned} \nabla \times \tilde{\mathbf{E}} &= -i\omega\mu_0 \tilde{\mathbf{H}} \\ \nabla \times \tilde{\mathbf{H}} &= -i\omega\varepsilon_0 n^2 \tilde{\mathbf{H}} \end{aligned} \tag{1.15}$$

where n^2 gives the total refractive index distribution in the full coupled waveguide.

By substituting eq.(1.14) in eq.(1.15), we obtain following relation for the amplitudes[7],

$$(\hat{z} \times \tilde{\mathbf{E}}_I)\frac{\mathrm{d}A}{\mathrm{d}z} + (\hat{z} \times \tilde{\mathbf{E}}_{II})\frac{\mathrm{d}B}{\mathrm{d}z} = 0, \tag{1.16}$$

$$(\hat{z} \times \tilde{\mathbf{H}}_I)\frac{\mathrm{d}A}{\mathrm{d}z} + (\hat{z} \times \tilde{\mathbf{H}}_{II})\frac{\mathrm{d}B}{\mathrm{d}z} - i\omega\varepsilon_0(n^2 - n_I^2)\frac{\mathrm{d}B}{\mathrm{d}z}A\tilde{\mathbf{E}}_I - i\omega\varepsilon_0(n^2 - n_{II}^2)B\tilde{\mathbf{E}}_{II} = 0. \tag{1.17}$$

We can decompose the eigenmodes of each waveguide $\tilde{\mathbf{E}}_l$ and $\tilde{\mathbf{H}}_l$ in axial and transverse component as,

$$\begin{aligned} \tilde{\mathbf{E}}_l &= \vec{\mathcal{E}}_l \mathrm{e}^{i\beta_l z} \\ \tilde{\mathbf{H}}_l &= \vec{\mathcal{H}}_l \mathrm{e}^{i\beta_l z} \end{aligned} \tag{1.18}$$

By substituting above eq.(1.18) in eq.(1.16), we obtain the simplified coupled equation for the amplitudes variation along propagation axis as

$$\begin{aligned} \frac{\mathrm{d}A}{\mathrm{d}z} + c_{I,II}\frac{\mathrm{d}B}{\mathrm{d}z}\mathrm{e}^{+i(\beta_2-\beta_1)z} - i\chi_I A - i\kappa_{I,II}B\mathrm{e}^{+i(\beta_2-\beta_1)z} &= 0, \\ \frac{\mathrm{d}B}{\mathrm{d}z} + c_{II,I}\frac{\mathrm{d}A}{\mathrm{d}z}\mathrm{e}^{-i(\beta_2-\beta_1)z} - i\chi_{II}B - i\kappa_{II,I}A\mathrm{e}^{-i(\beta_2-\beta_1)z} &= 0 \end{aligned} \tag{1.19}$$

[7] where we are using the identity $\nabla \times (A\mathbf{E}) = \nabla A \times \mathbf{E} + A\nabla \times \mathbf{E} = \frac{\mathrm{d}A}{\mathrm{d}z}(\hat{z} \times \mathbf{E}_1) + A\nabla \times \mathbf{E}$

where coefficients are

$$\kappa_{l,m} = \frac{1}{N_l}\omega\varepsilon_0 \int_{-\infty}^{\infty} d\mathbf{r}(n^2 - n_m^2)\vec{\mathcal{E}}_l^* \cdot \vec{\mathcal{E}}_m, \tag{1.20}$$

$$c_{l,m} = \frac{1}{N_l} \int_{-\infty}^{\infty} d\mathbf{r}\Big(\vec{\mathcal{E}}_l^* \times \vec{\mathcal{H}}_m + \vec{\mathcal{E}}_m \times \vec{\mathcal{H}}_l^*\Big)_z, \quad (l,m) \in \{I, II\} \tag{1.21}$$

$$\chi_l = \frac{1}{N_l}\omega\varepsilon_0 \int_{-\infty}^{\infty} d\mathbf{r}(n^2 - n_l^2)\vec{\mathcal{E}}_l^* \cdot \vec{\mathcal{E}}_l \tag{1.22}$$

with normalization $N_l = \int_{-\infty}^{\infty} d\mathbf{r}\Big(\vec{\mathcal{E}}_l^* \times \vec{\mathcal{H}}_l + \vec{\mathcal{E}}_l \times \vec{\mathcal{H}}_l^*\Big)_z$ [8] where integration domain is $\mathbf{r} = \{x, y\}$. Here, κ_{lm} refers to mode coupling coefficient of the *directional coupling* analogous to tunnelling coefficient in tight binding formalism and it depends on the overlap of evanescent waves of l, m. Let us consider Fig. 1.9, where waveguide I exist for $z < 0$ and waveguide II exist for $z \geq 0$. When the light beam is incident on waveguide I, E_I then at $z = 0$ it excites the eigenmode of the waveguide II, E_{II}, this coupling or excitation efficiency is captured in $c_{l,m}$ also known as the *butt coupling* coefficient. χ_l denotes the amount of contribution coming to A from B, and vice versa[9], this can be seen as an analogue of an onsite potential term in quantum mechanics. In most of the cases, $c_{l,m}$ and χ_l are neglected as their contribution is far less than that of $\kappa_{l,m}$. However, they may be important for the full treatment of mode coupling effects.

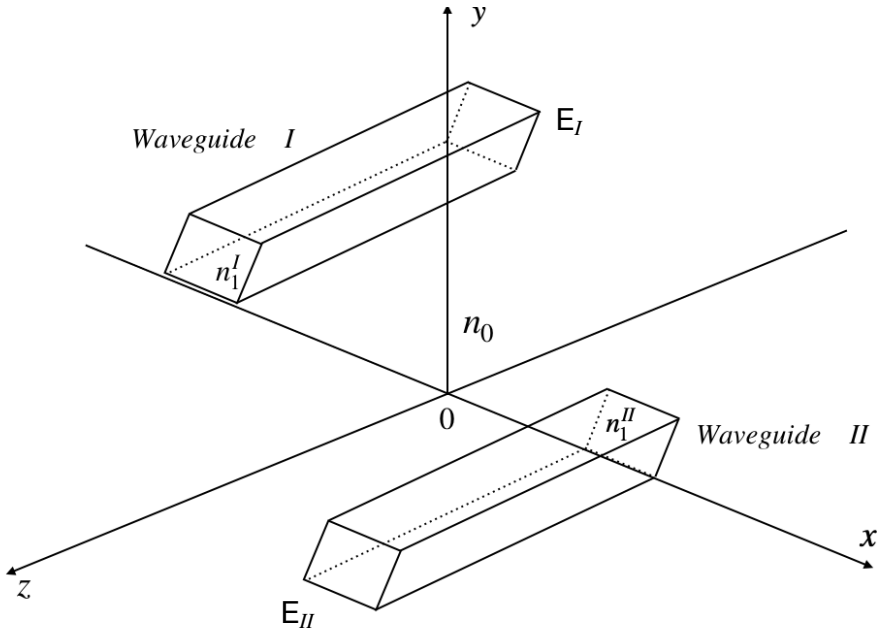

Figure 1.9: Butt coupling coefficient

We keep $c_{lm} = \chi_l = 0$, unless otherwise specified. This greatly simplifies the equation(1.19) which can easily be generalised to more than two waveguides as

[8] Here z^{th} component arise because when we substitute eq(1.14) in corresponding equation for electromagnetic fields eq(1.13). Then $\nabla \times (A(z)\vec{\mathcal{E}}) = A(z)\nabla \times \vec{\mathcal{E}} + \nabla A(z) \times \vec{\mathcal{E}} = A(z)\nabla \times \vec{\mathcal{E}} + \Big(\mathrm{d}A/\mathrm{d}z\Big)\mathbf{n}_z \times \vec{\mathcal{E}}$.

[9] Since, χ_I is only non-zero inside the core of waveguide II (where $n = n_{II}$), vice-versa.

$$\frac{\mathrm{d}A_m}{\mathrm{d}z} = i\kappa_{mm'}A_{m'}\mathrm{e}^{+i\beta_{mm'}z} \tag{1.23}$$

where A_m is the amplitude in the m^{th} waveguide with nearest neighbours m'. Just as a note there is an another way establishing the coupling of modes due to waveguide imperfections, a very brief sketch can be found in the appendix(5.1).

1.7 From coupled waveguide array to other photonics platforms

1.7.1 Experimental platform 1: Waveguide arrays

The two essential ingredients, namely, paraxial Helmholtz's equation and coupled-mode theory, enable us to explore the realm of solid-state phenomena governed by quantum mechanics in the classical domain of evanescently coupled optical waveguide array. These arrays were first proposed theoretically by Jones in 1965 (Jones 1965). Later, they were first engineered experimentally in 1973 on a GaAs substrate by Yariv's group (Somekh et al. 1973).

In the beginning, the idea was to map solid-state phenomena like Bloch oscillations to coupled waveguide networks, and later they seem to possess features only specific to these arrays. For example, due to underlying discrete structure[10], these coupled waveguide arrays display properties very different from the continuous and homogeneous media. When light undergoes diffraction in air (continuous medium) it has normal behaviour of spreading as shown in Fig 1.10(a), while in the discrete case of i.e., evanescently coupled waveguide arrays in Fig 1.10(c) light undergoes discrete diffraction as shown in Fig 1.10(b) (Eisenberg et al. 2000; T. Pertsch, Zentgraf, et al. 2002; Szameit, Dreisow, and Stefan Nolte 2012; Szameit and Stefan Nolte 2010).

Along with the analogies with quantum mechanics, in the 90s, Carl Zener (Zener et al. 1934)predicted an unintuitive phenomenon that when electrons in a lattice are in the presence of an electric field, they undergo oscillations, also known as *Bloch oscillations*. Intuitively, a charged particle should experience the Lorentz force that accelerates it instead of oscillating. In optical waveguides, this can be imposed by a transverse potential gradient whose role is played by a refractive index here. This potential gradient can be attained by linearly increasing the refractive index of the individual waveguides, which gives rise to optical Bloch oscillation, they were observed in 1D (Morandotti et al. 1999; T. Pertsch, Dannberg, et al. 1999), and in 2D (Trompeter et al. 2006). However, there is a clever way to implement this gradient, and it is by curving the waveguides as proposed in 1999 for 1D (Lenz et al. 1999) and observed in 1D erbium-doped curved waveguide arrays (Chiodo et al. 2006). The relation between curving and the transverse potential becomes evident by going into the frame of reference of curved coordinates of the waveguide, where there is an extra term in equation(1.11), acting as a transverse force responsible for *optical Bloch oscillations*.

[10]This causes the anisotropy in the medium and giving rise to anomalous refraction

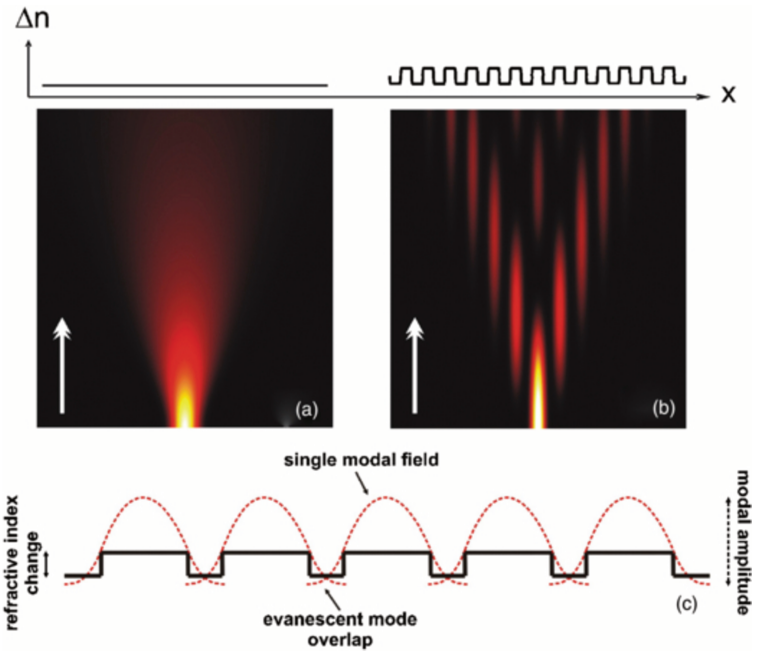

Figure 1.10: Diffraction of a light beam in a (a) continuous medium, (b) waveguide array with periodically varying refractive index along the transverse axis. Where array of waveguides is shown in (c). Fig. is from (Szameit and Stefan Nolte 2010)

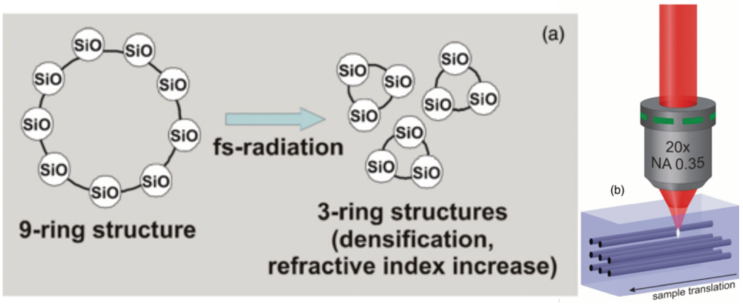

Figure 1.11: fs-laser writing of waveguide arrays in fused silica. (a) The intense fs-laser breaks the silica ring into small rings, which leads to densification or an increase in the refractive index in that region, and this is done by shining (b) a fs-laser along with a lens to focus on a particular region of interest. This supports a mode at wavelength $\lambda = 633$ nm, Fig. is from (Szameit and Stefan Nolte 2010)

Moreover, the experimental implementation of waveguide arrays mostly began with AlGaAs semiconductors (Morandotti et al. 1999; T. Pertsch, Dannberg, et al. 1999; Somekh et al. 1973). The major technical breakthrough came after the first femtosecond laser-written waveguides in the Nolte group (S. Nolte et al. 2003; Szameit, Dreisow, and Stefan Nolte 2012; Szameit and Stefan Nolte 2010). These waveguides are written in fused silica by injecting a femtosecond laser (fs-laser) pulses, as shown in Fig 1.11(b). This changes the local refractive index of the material and increasing the refractive index (see Fig 1.11(a)). Different refractive index can be engineered by controlling the writing speed of the fs-laser on the sample, as sketched in Fig. 1.12(b). This approach versatility has helped in developing

waveguide arrays (consisting of a bunch of waveguides inside the silica medium) in 2D and 3D (Szameit, Dreisow, and Stefan Nolte 2012; Szameit and Stefan Nolte 2010). In this array geometry, the distance between the waveguides l_w depends on the desired coupling κ[11] and the incident light wavelength λ, this is sketched in Fig. 1.12(a,c).

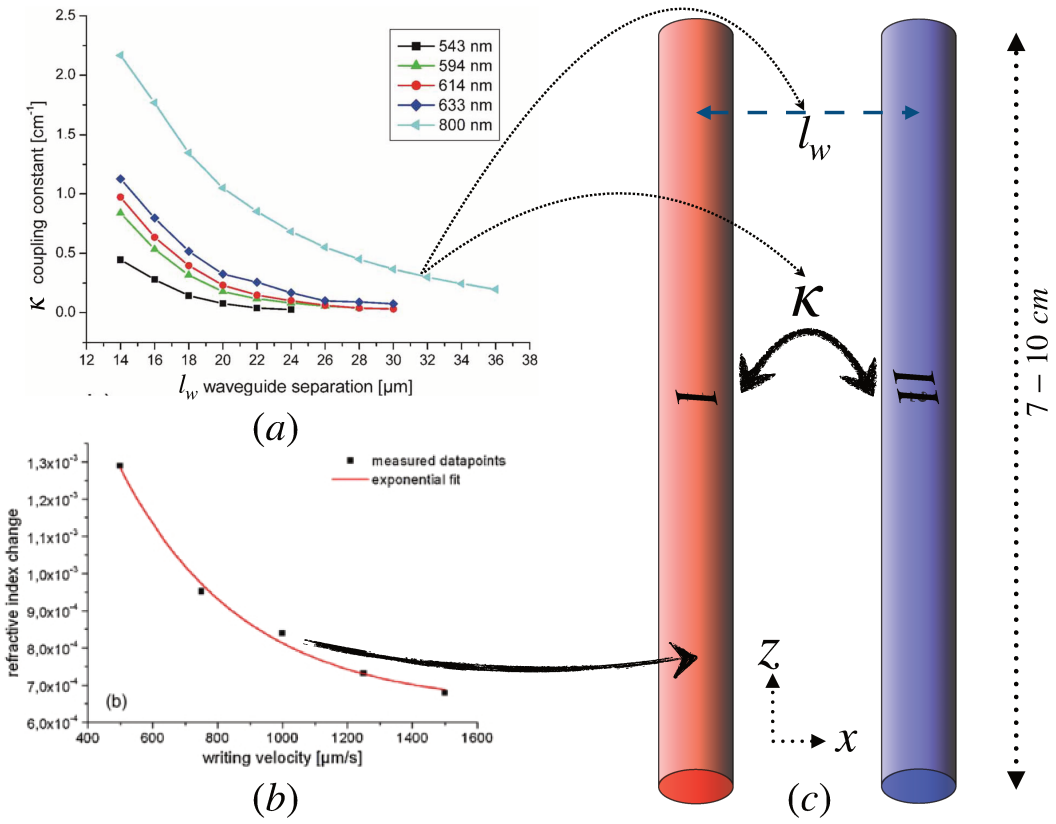

Figure 1.12: (a) Desired coupling between the two waveguides can depend on the waveguide separation length l_w and incident light wavelength λ, figure is from (Szameit, Dreisow, Thomas Pertsch, et al. 2007), by controlling (b) the writing speed of the laser on the silica (see Fig.1.11(b)) desired refractive index for the waveguide can be obtained, figure is from (Blömer et al. 2006). (c) A two waveguides setup stressed with number I for red and II for blue. The waveguides are monomodes, (i.e. allowing only single mode).

For example, for $\lambda = 800nm$, it corresponds to a transverse waveguide spacing in the range $14 - 30\mu m$. The propagation length of the sample is around $7 - 10$ cm, with a width of around 100 μm. Then the evolution of the light beam can be detected by the fluorescence spectroscopy technique.

Time dependent Hamiltonian realization

The resemblance of the waveguide propagation axis (or $z-$axis) with the time axis allows to engineer systems that are described by time-dependent Hamiltonian (see eq.(1.11)).

[11]Sometimes, if the waveguides are not straight but bent then the coupling also depends on the relative angle between them.

Let us consider a simple example of only two waveguides, as shown in red and blue color in Fig. 1.12, where the amplitude and the propagation vector in the first waveguide (in red) is A and β_I, and in the second waveguide (in blue) is B and β_{II}, respectively. For simplicity, we can consider the propagation wavenumber $\beta_I = \beta_{II}$[12]. The coupling between the two waveguides is $\kappa = \kappa_{I,II} = \kappa_{II,I}$ (see eq.(1.20)). Then the evolution of amplitudes along the propagation axis z can be described in this array by using coupled-mode theory equations (see eq.(1.23)) as,

$$-i \begin{pmatrix} \dot{A}(z) \\ \dot{B}(z) \end{pmatrix} = \begin{pmatrix} 0 & \kappa \\ \kappa & 0 \end{pmatrix} \begin{pmatrix} A(z) \\ B(z) \end{pmatrix} \tag{1.24}$$

where $\dot{A}(z) = \mathrm{d}A(z)/\mathrm{d}z$. The coupling matrix $\mathcal{K}$ form in $\dot{A}(z) = \mathcal{K}A(z)$ coincides with the form of tight-binding Hamiltonian, in the basis of waveguides and in units of $[L^{-1}]$ instead that of an energy.
Then the solution of these coupled equations can easily be found by differentiating one of the equation and substituting it from another, which gives

$$\begin{aligned} \frac{\mathrm{d}^2 A(z)}{\mathrm{d}z^2} &= -\kappa^2 A(z), \\ A(z) &= A_0 \cos \kappa z. \end{aligned} \tag{1.25}$$

The similar equation follows for the amplitude $B(z)$, where in eq.(1.25), we have chosen an initial condition. We incident a light beam only in the first waveguide (in red) of amplitude A_0, this translates to say that $A(z=0) = A_0$ and $B(z=0) = 0$. Then after a propagation length of $z = l_c = 2(p+1)\pi/2\kappa$, for some $p \in \mathbb{Z}$, all the light beam is transferred to the second waveguide (in blue), this is known as coupling length. It shows along with the eq.(1.25) that the light beam keeps oscillating from one waveguide to another. If the number of waveguides is increased in the array, this leads to a cascading process, where light beam from m^{th} waveguide is transferred to $(m-1)^{th}$ and $(m+1)^{th}$ after some propagation length, this results into a discrete diffraction Fig. 1.10(a).

Additionally, here the experimentally measurable quantities are output intensities, $I_A = |A(z)|^2, I_B = |B(z)|^2$, they in turn can determine the coupling constant between the waveguides

$$\kappa = \frac{1}{z} \arctan \sqrt{\frac{I_A}{I_B}} \tag{1.26}$$

[12]This means the identical modes are allowed in both the waveguides. In other words, two copies of same waveguide. By choosing a different geometry for waveguide I with respect to II can give $\beta_I \neq \beta_{II}$, we are not interested in those cases for the time being. Besides, the amplitudes can still be chosen different by initial condition.

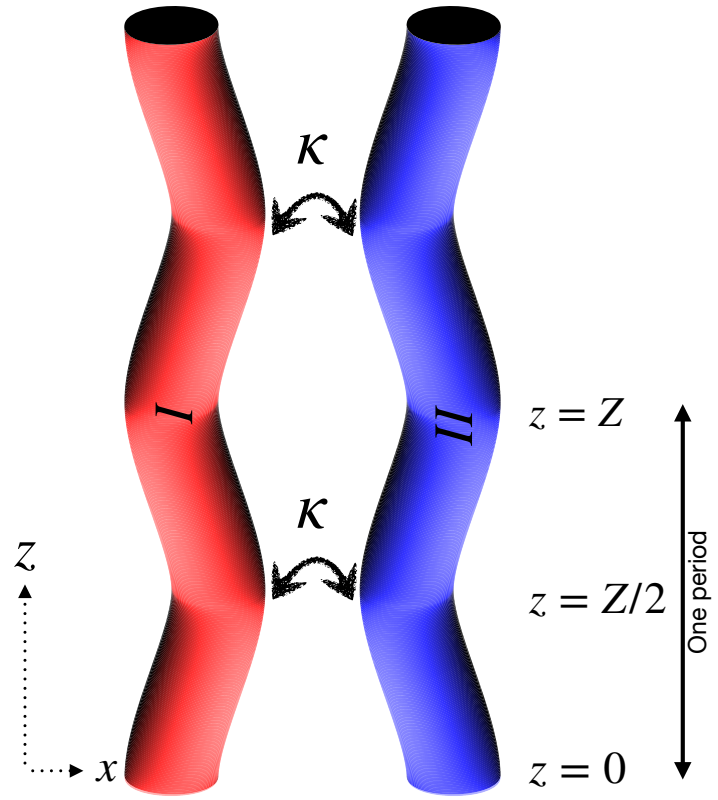

Figure 1.13: A waveguide array containing two waveguides with periodic modulation of period Z along z (time) axis.

In the last case, we consider a z-independent coupling between the waveguide, i.e., $\kappa(z) = \kappa$. However, if the $\kappa(z)$ depends on z then it mimics a time-dependent Hamiltonian system (see eq.(1.24)). For two waveguides, with z (or time) dependent coupling the evolution of amplitudes can be written as

$$-i\begin{pmatrix}\dot{A}(z)\\ \dot{B}(z)\end{pmatrix} = \begin{pmatrix}0 & \kappa(z)\\ \kappa(z) & 0\end{pmatrix}\begin{pmatrix}A(z)\\ B(z)\end{pmatrix} \tag{1.27}$$

Above eq.(1.27) can easily be generalized along four directions.

- First, if we consider a waveguide array where these two waveguides as a unitcell form a lattice along transverse axis (x), then the coupling matrix can be Bloch diagonalized. Then the coupling matrix $\mathcal{K}$ transforms into-

$$\mathcal{K} = \begin{pmatrix}0 & \kappa(z)\mathrm{e}^{ik_x a_x}\\ \kappa(z)\mathrm{e}^{-ik_x a_x} & 0\end{pmatrix}, \tag{1.28}$$

  where a_x is the lattice constant and k_x is the Bloch quasimomentum (or Fourier conjugate variable of x).

- Second, the size of this Bloch diagonalized coupling matrix encodes the information of the degree of freedom in the lattice. Hence this can be extended to any number of waveguides.

- Third, the periodicity of the waveguide array along the z (or time) axis, as sketched in Fig. 1.13, mimics the dynamics of periodically time dependent Hamiltonian (see eq.(1.11)), we discuss them in chapter(2). This is encoded in the couplings, where they are periodic in z with period Z, $\mathcal{K}(z+Z) = \mathcal{K}(z)$.

- Lastly, the dimension of the system can be extended from 1D to 2D, by exploiting also the y-axis and stacking the waveguides along that direction (see Fig. 1.12). Then the refractive index is periodic along both axes x and y, i.e., $\Delta n(x+a_x, y+a_y) = \Delta n(x,y)$. This redefines the above coupling matrix $\mathcal{K}$ eq.(1.28), with couplings κ_1 in x and κ_2 in y plane as

$$\mathcal{K} = \begin{pmatrix} 0 & \kappa_1(z)\mathrm{e}^{ik_x a_x} + \kappa_2(z)\mathrm{e}^{ik_y a_y} \\ \kappa_1(z)\mathrm{e}^{-ik_x a_x} + \kappa_2(z)\mathrm{e}^{-ik_y a_y} & 0 \end{pmatrix}. \tag{1.29}$$

This platform will be heavily discussed at the end of the chapter(2), where we will address the first three points in detail.

The governing equation for the evolution of light inside the waveguides has only two special dimensions (see eq(1.11)), this restricts us to go beyond 2D. However, relaxing the condition of monochromaticity can allow us to use temporal direction as another coordinate (x, y, t). This is reflected by adding the time-dependent term in eq(1.11), where this term additional term corresponds to the kinetic energy of slowly varying envelope term coming from t (Ozawa, Hannah M. Price, Amo, et al. 2019),

$$i\lambda\frac{\partial}{\partial z}\mathcal{E}(x,y,t;z) \;=\; -\left(\frac{\lambda^2}{2n_0}\nabla_T^2 + \Delta n + \frac{1}{2m_t}\frac{\partial^2}{\partial t^2}\right)\mathcal{E}(x,y,t;z) \tag{1.30}$$

where $m_t = -(d^2k(\omega)/d\omega^2)/n_0$ with $k(\omega) = n(\omega)\omega/c$ is proportional to the group velocity in a frequency dependent refractive index medium. Moreover, the dimension can also be extended by employing synthetic gauge fields (Ke et al. 2016; Zilberberg et al. 2018) or the different waveguide modes (Lustig et al. 2019) in the system, whose more detailed review and analysis will be presented in chapter(3).

1.7.2 Experimental platform 2:Optical mesh lattices

There is another equivalent platform in classical photonics to engineer a periodically time-dependent dynamics of a quantum Hamiltonian, where the time dependence of coupling parameters is encoded in terms of time-dependent scattering matrices. These time-dependent matrices are identical to the one that appears also at the coupling region between the waveguides in the waveguide arrays (see Fig. 1.13). This platform was developed in Ulf Peschel group in Jena (Regensburger, Bersch, Hinrichs, et al. 2011; Wimmer, Mohammed-Ali Miri, et al. 2015; Wimmer, Hannah M Price, et al. 2017; Wimmer, Regensburger, et al. 2013).

Let us describe this second platform, which consists in two spatially separated circular optical fibers, as shown in Fig. 1.14. They only differ in their length, where the loop v (on the left) of length $L + \Delta L$ is longer than the loop u (on the right) of length L by an amount ΔL. The two optical fibers are coupled by a standard coupler or known as a beam-splitter, shown with a black-gray box, in Fig. 1.14. It contains two inputs and two outputs, and it

decides the division of light intensity (or amplitude) going to each of the two outputs. For example, if it is a 50:50 beam splitter, then any input, it splits light amplitude into half for each of the output.

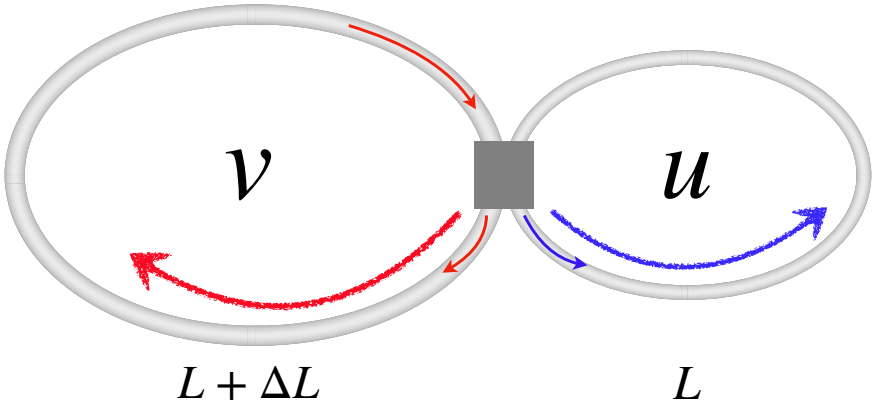

Figure 1.14: A pair of circular fibers (or waveguides) coupled through a coupler shown in black. The dimensions are $L \sim 5km$ and $\Delta L = 8m$.

The process starts by injecting a pulse of light, much shorter than the loops, of amplitude $\mathcal{A}$ in one of the optical fiber, say the loop v. Then the beam travels inside the large loop before it encounters a beam-splitter, which splits the light amplitude into two parts. Considering a 50:50 splitting for simplicity. This means a light amplitude splits into two halves, of amplitude $\mathcal{A}/2$ entering in each of the optical fibers. This is the only region where transverse coupling between the two fibers takes place.

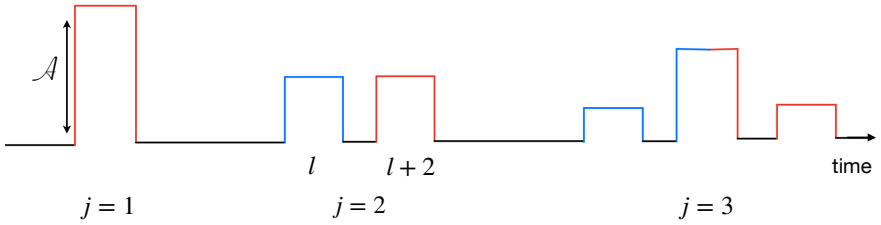

Figure 1.15: Recording of time multiplexing of pulses in one of the loops. The pulses color represent the respective loop they come from, where red correspond to loop v and blue to loop u.

Then owing to the length difference ΔL, the light beam lasts a shorter time T_u in the loop u than it does in loop v. In the longtime, this generates time-multiplexed pulses, where pulses in shorter loops advance by $\Delta L/c_{\text{fiber}}$, where c_{fiber} is the speed of light inside the fiber, in comparison to the longer one, where they are delayed by the same amount in comparison to the shorter one, as shown in Fig. 1.15. There are two time scales here, one is the shorter time $l = T_v - T_u = \Delta L/c_{\text{fiber}}$ and the other one is the longer time $j = T_v + T_u$. The shorter time differentiates between the two loops, where it decides the temporal position l depending on the pulse origination if it comes from shorter (l) or longer ($l + 2$) loop, while the longer time scale counts the total round trips j, i.e., one round through the longer (shorter) loop and one round through the shorter (longer) loop. In the long run, this effectively generates

an optical mesh lattice, where l is encoded in the transverse axis, and j in the propagation axis, as shown in Fig. 1.16. It can be seen after j rounds in this optical mesh lattice that the

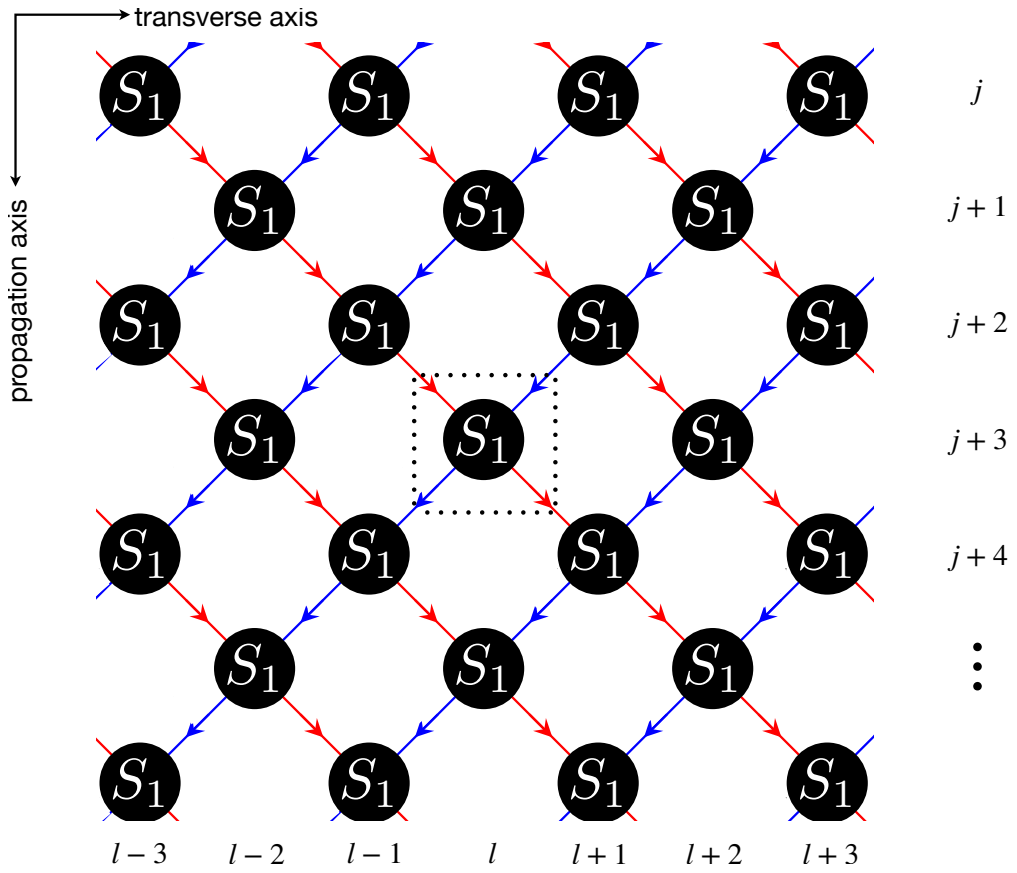

Figure 1.16: Optical mesh lattice generated by two time scales, where the shorter time scale is encoded along the transverse axis (x) and the longer time scale along the propagation axis (y).

pulse coming from loop u is advanced in time with respect to that of loop v. Thus it goes to the left (shown with a link in blue in Fig. 1.16) designated by the temporal position label l. However, the pulse coming from loop v is delayed. Hence it goes to the right (shown with a link in red in Fig. 1.16). The (scattering) node, where these two links meet the coupler (or the beam splitter), is displayed by S_1,

$$S_1 = \frac{1}{\sqrt{2}} \begin{pmatrix} 1 & i \\ i & 1 \end{pmatrix}. \tag{1.31}$$

Similarly to the waveguide case, the periodicity of the coupler (that stores the coupling information between the two fibers) along the propagation axis, determines the time periodicity of the lattice. In this simple case, where the scattering node is same along transverse and propagation axis, i.e., satisfies $S_1(j+2, l+2) = S_1(j, l)$, which defines a unitcell emphasized with dotted black square in Fig. 1.16, where $S_1(j = \text{time step}, l = \text{position})$.

In a more general case, the scattering node can change along both axes, while maintaining periodicity along each axes. Likewise before, this formalism can be extended.

- All the distinct nodes denoted by $S_{l,j}$ along the transverse axis, i.e., $S_{l',j}$ for $l \neq l'$, is $S_{l,j} \neq S_{l',j}$, this decide the degrees of freedom in the system (Mohammad-Ali Miri et al. 2012; Regensburger, Bersch, Hinrichs, et al. 2011; Regensburger, Bersch, Mohammad-Ali Miri, et al. 2012). For example, if there are n_l distinct nodes then there are total $2n_l$ links entering these nodes or $2n_l$ degrees of freedom (i.e. $S_{l+2n_l,j} = S_{l,j}$). This is similar to have $2n_l$ waveguides in the unitcell.

- Like in the waveguide arrays, the number of distinct nodes along the propagation axis corresponds to the number of time steps similar to a quantum walk or in case of waveguides array (see chapter(4)). For example, if there are n_j steps, where $n_j \in 2\mathbb{Z}$ then $S_{l,j+2n_j} = S_{l,j}$). The evenness of n_j comes from the underlying evenness of the number of circular fibers. In the waveguide arrays, this corresponds to a case where the number of waveguides are even, and with half of the intracell couplings and another half intercell.

- The dimension of the system can interestingly be increased by introducing a synthetic gauge field(Mohammad-Ali Miri et al. 2012; Regensburger, Bersch, Hinrichs, et al. 2011; Regensburger, Bersch, Mohammad-Ali Miri, et al. 2012; Wimmer, Mohammed-Ali Miri, et al. 2015; Wimmer, Hannah M Price, et al. 2017). This can be achieved by introducing a phase modulator in one of the circular fibers.

This platform will be discussed heavily along with the above points through the scattering network (see Fig. 1.16) in the chapter(3) and (4).

1.7.3 Quantum walk setup: Experimental platform 3

Till now, we mostly discussed the realization of quantum Hamiltonians in classical systems. However, there are a lot of platforms in the quantum regime For instance, in optical mesh lattices of single photons (M. A. Broome et al. 2010; Kitagawa, Matthew A Broome, et al. 2012; Schreiber, Cassemiro, Poto ček, Gábris, Jex, et al. 2011; Schreiber, Cassemiro, Poto ček, Gábris, Mosley, et al. 2010) or entangled photons(Crespi et al. 2013; Sansoni et al. 2012), ion traps (Schmitz et al. 2009), and photonic waveguides array with single-photons (Bromberg et al. 2009; Perets et al. 2008) or correlated photons (Matthews et al. 2013; Peruzzo et al. 2010). We focus our attention very briefly on an optical mesh lattice incident with a single photon or more comfortably known as a photonic quantum walk, as shown in Fig. 1.17.

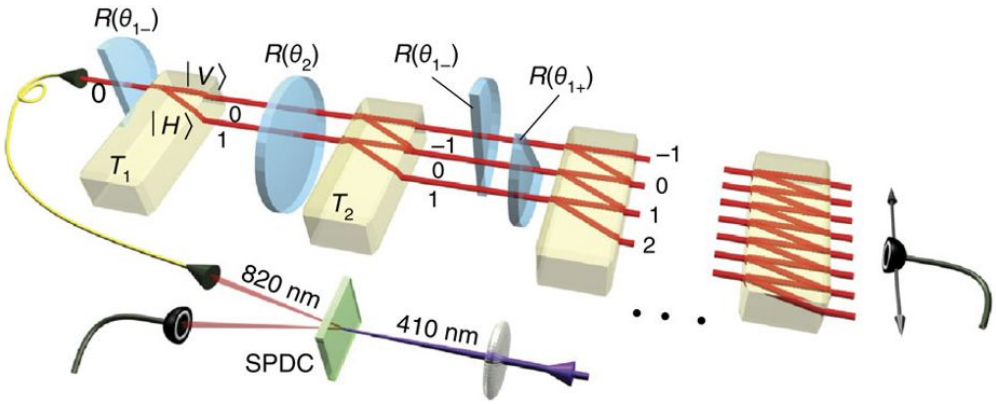

Figure 1.17: Experimental setup of a photonic quantum walk. Here, the degrees of freedom are the two polarization states of photons, namely horizontal $|H\rangle$ and vertical $|V\rangle$. This polarization in a single photon is encoded through SPDC. The photon undergoes a polarization-dependent rotations $R(\theta_{j=1,2})$, and translations $T_{j=1,2}$. Image is taken from Kitagawa, Matthew A Broome, et al. 2012.

A photon generates a quantum walk in a 1D lattice (see Fig. 1.17) (Kitagawa, Matthew A Broome, et al. 2012). This is achieved by a polarized photon with horizontal $|H\rangle$ and vertical $|V\rangle$ polarization states, which undergoes unitary transformations during discrete time steps evolutions. In the first step, there is a polarization-dependent rotation $R(\theta_1)$ of the single photon-induced via a suitable wave plate. Then there is a polarization-dependent translation T_1 (using a calcite beam displacer) where $|H\rangle$ is moved by one lattice to the right. Subsequently, there is a second rotation $R(\theta_2)$, and at last another translation T_2 of $|V\rangle$ to the left. These four steps constitute one complete step of this quantum walk, which is periodically reproduced. Here, the degree of freedom is decided by the two polarization states of the photons. The information of the coupling similar to before is encoded in the parameters $\theta_{j=1,2}$. Moreover, the big advantage of this setup is that it can be more useful to study features more dominant in the quantum regime, e.g., quantum entanglement or quantum correlations. The properties

These three platforms are summarized below:

Table 1.1: Comparison between the platforms

	Waveguides array or Optical mesh lattice	**Photonic quantum walk**
Ingredients	Classical electromagnetic wave	Photons
Entanglement	Amplifiers do not preserve quantum coherence	In presence of more than one photon (Crespi et al. 2013; Matthews et al. 2013; Peruzzo et al. 2010; Sansoni et al. 2012).
Non-Hermitian physics	This could be induced via losses and gain with the help of refractive index (Feng et al. 2017; El-Ganainy et al. 2018b; Zhao et al. 2018)	This is not possible, since the underlying quantum mechanics is Hermitian.
Detection	Fluorescence spectroscopy measurement (Mayers et al. 2005; Oki et al. 2002) or Intensity measurement using photodiode (Mohammad-Ali Miri et al. 2012; Regensburger, Bersch, Hinrichs, et al. 2011; Regensburger, Bersch, Mohammad-Ali Miri, et al. 2012; Wimmer, Mohammed-Ali Miri, et al. 2015; Wimmer, Hannah M Price, et al. 2017)	Probability distribution is imaged with a single- photon avalanche detector (Kitagawa, Matthew A Broome, et al. 2012) or photon correlations are detected using conditional measurement (Crespi et al. 2013; Peruzzo et al. 2010; Rohde et al. 2011; Sansoni et al. 2012).

1.8 Topology as a tool for physicists

Here I give a heuristic introduction to topological tools required to capture the topological properties in the gapless regime.

Topology is a branch of mathematics that is concerned with the properties of objects which are invariant under continuous deformations, such as stretching or bending. As an example, a hollow cylinder, a smooth solid sphere, or a rough surface potato are the same. That means topology is insensitive to the local details, and a potato can be continuously deformed into a solid smooth sphere, while it can not be deformed into a hollow cylinder, which has a hole at the center. All the objects which can be continuously deformed into each other are characterized by the same invariant that smoothens out the local details. This invariant, or topological invariant, for instance, can be the number of holes in an object, which is zero for the potato and 1 for the hollow cylinder. There is a well known formula from differential geometry, where this invariant can be defined mathematically for

a manifold M (in our example, it is a cylinder or a sphere) as –

$$\chi = \frac{1}{2\pi} \int_M K \mathrm{d}A \tag{1.32}$$

where K is the total curvature or Gaussian curvature, and $\mathrm{d}A$ is the element of area of the surface. This χ in above equation is in turn related to the number of holes (or genus) by the relation

$$\chi = 2 - 2g. \tag{1.33}$$

This can be seen, for example, for a sphere, which has $K = 1/R^2$, which means $\chi = 2$. So the number holes in a sphere is $g = 0$. Here, χ is known as Euler characteristic. Then all objects (or manifolds) that share the same genus can be continuously deformed into each other, and they form an equivalence class. A sketch of objects with different genus is shown in Fig. 1.18. The most remarkable thing about equation(1.32), which is also known as *Gauss-Bonnet* theorem, is that it connects a geometrical aspect (e.g., curvature, a local aspect) of a manifold to its topology (e.g., global aspects, like holes).

(a) $g = 0$ (b) $g = 1$ (c) $g = 2$

Figure 1.18: Manifolds with different genus (a) sphere, (b) doughnut and (c) double doughnut. Image is from Wikipedia/Genus˙(mathematics)

1.9 Homotopy

We can formalize our discussion of continuous deformation of objects to curves on a manifold. As we shall see, this gives rise to other kinds of topological invariants. This section is heavily drawn from the Nakahara (Nakahara 2003).

1.9.1 Continuous deformations of loops and maps

Let us consider two discs, as shown in Fig 1.19. One disc is a regular one, whereas the other one has one hole inside. The difference between these discs become apparent by drawing a loop (or a closed curve). In the second disc Y, any loops can be continuously shrunk to a

point. In contrast, any loop in X can not be continuously shrunk to a point. For example, loop $\gamma_{j=3,4,5}$ experience an obstruction in the middle of the disc, prohibiting them from being shrunk to a point. On shrinking the cylinder of the previous example, we obtain this disc.

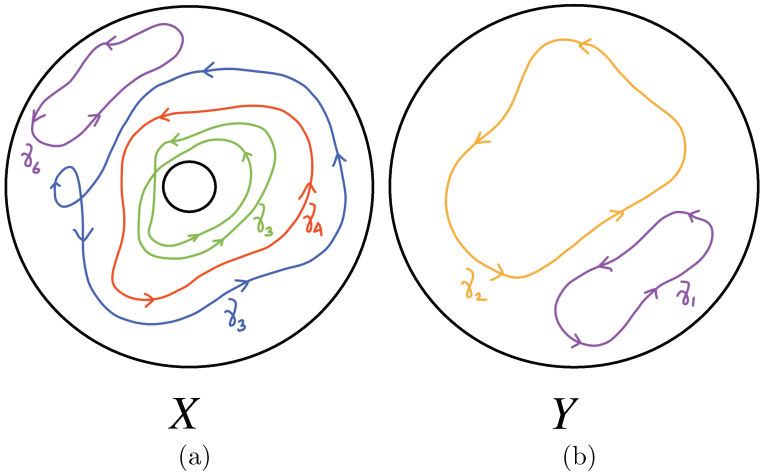

Figure 1.19: A disc (a) with a hole and (b) without a hole. Different loops are shown g_j.

However, some loops can be shrunk to a point in X, for example γ_6. We say a loop γ_j is *homotopic* to $\gamma_{j'}$, if γ_j can be obtained from $\gamma_{j'}$ by a continuous deformation. For example, any loop in Y is homotopic to a point, while this is not the case in X. Apparently, a "is homotopic to" b is an equivalence relation between a and b, denoted as $a \sim b$. The equivalence class of this equivalence relation is called the homotopy class (in which a and b falls together). In our example, there is only one homotopy class associated to Y. However, in X, each distinct loops that encircle the hole 'n' times fall in a different homotopy class. Moreover, the winding of loop has an orientation; if it winds clockwise $n < 0$, $n > 0$ if counter-clockwise, $n = 0$ if there is no winding around the hole. This homotopy class is characterized by $n \in \mathbb{Z}$.

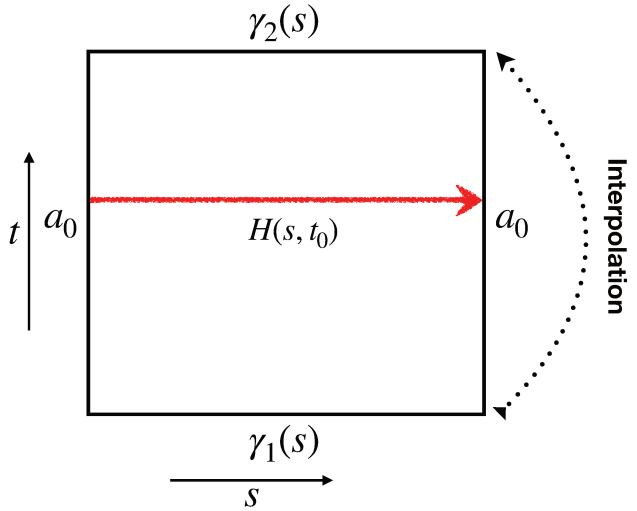

Figure 1.20: The interpolating map H from loop γ_1 to γ_2

Let us put this in a more elegant way. Let us consider a continuous map γ: [0,1] $\to X$ is defined as a path if the initial point $\gamma(0) = x_0$ and final point $\gamma(1) = x_1$, where $x_j \in X$. Similarly, if $\gamma(0) = \gamma(1) = x_0$ then it defines a loop at x_0.

If there are two loops γ_1, γ_2: [0,1] $\to X$ at say x_0. They are said to be homotopic, if there exists a continuous map $H : [0,1] \times [0,1] \to X$ such that

$$H(s,0) = \gamma_1(s), \quad H(s,1) = \gamma_2(s) \quad \forall s \in [0,1] \tag{1.34}$$

$$H(0,t) = H(1,t) = x_0 \quad \forall t \in [0,1] \tag{1.35}$$

The interpolating map H is called homotopy between γ_1 and γ_2, as shown pictorially in Fig. 1.20.

The idea of homotopy of loops can be extended to arbitrary maps. Let f, g: $X \to Y$ be a continuous map. If there also exists a continuous map $H : [0,1] \times X \to Y$ such that

$$H(x,0) = f(x), \quad H(x,1) = g(x) \quad \forall x \in X \tag{1.36}$$

then f is said to be homotopic to g the map H is called a homotopy between f and g.

In addition to continuous deformation of loops or maps, but underlying spaces X, and Y can also be continuously expanded. If we consider X to be a disc with a hole, on expanding its boundaries gives $X \equiv \mathbb{R}\ \{0\}$ this is a circle $\sim S^1$. Correspondingly, different windings on S^1 fall in different homotopy classes. It turns out, the set of homotopy classes is endowed with a group structure. Here the set of homotopy classes of loops in X is known as fundamental group or Poincaré group, denoted by $\pi_1(X) \equiv \pi_1(S^1) = \mathbb{Z}$. Just to show how calculating the higher homotopy group becomes very complicated as the dimensions of the underlying space increase S^n is shown in Fig. 1.21.

1.9.2 Winding number

There is a more intuitive way to calculate the winding of loops on a circle S^1. That can be seen by parametrizing the circle by an angle φ, as sketched in Fig. 1.22. Let us consider a continuous map $g(\varphi) : S^1 \to U(1)$, where $g(\varphi) = e^{i\alpha(\varphi)}$. This means, we can associate a complex phase to every point on the circle with above defined relation. The map does not need to be one-to-one; in fact, it can be two-to-one or many-to-one, as we see. Let us consider the case $\alpha(\varphi) = 2\varphi$, as shown in Fig. 1.23. Then, $\varphi = 0$ implies $g(\varphi = 0) = 1 \in U(1)$ (shown with green arrow) $\varphi = \pi/2$ implies $g(\varphi) = -1$ (shown with red arrow),
$\varphi = \pi$ implies $g(\varphi = 0) = 1$ (shown with green arrow) $\varphi = 3\pi/2$ implies $g(\varphi) = -1$ (shown with red arrow) .

This tells us how much time $U(1)$ wraps around S^1 (as φ), this is known as winding number.
However, there is a clever way and an elegant way to extract the winding number of an arbitrary map with $g(\varphi) = e^{i\alpha(\varphi)}$, where $\alpha(\varphi) = n\varphi$:

$$\nu = \frac{1}{2\pi i}\int_0^{2\pi} \mathrm{d}\varphi g^{-1}(\varphi)\partial_\varphi g(\varphi), \tag{1.37}$$

$$= \frac{1}{2\pi i}\int_0^{2\pi} \mathrm{d}\varphi e^{-i\alpha(\varphi)} i\partial_\varphi \alpha(\varphi) e^{i\alpha(\varphi)}, \tag{1.38}$$

$$= n. \tag{1.39}$$

	S^0	S^1	S^2	S^3	S^4	S^5	S^6	S^7	S^8
π_1	0	$\mathbb{Z}$	0	0	0	0	0	0	0
π_2	0	0	$\mathbb{Z}$	0	0	0	0	0	0
π_3	0	0	$\mathbb{Z}$	$\mathbb{Z}$	0	0	0	0	0
π_4	0	0	$\mathbb{Z}_2$	$\mathbb{Z}_2$	$\mathbb{Z}$	0	0	0	0
π_5	0	0	$\mathbb{Z}_2$	$\mathbb{Z}_2$	$\mathbb{Z}_2$	$\mathbb{Z}$	0	0	0
π_6	0	0	$\mathbb{Z}_{12}$	$\mathbb{Z}_{12}$	$\mathbb{Z}_2$	$\mathbb{Z}_2$	$\mathbb{Z}$	0	0
π_7	0	0	$\mathbb{Z}_2$	$\mathbb{Z}_2$	$\mathbb{Z}\times\mathbb{Z}_{12}$	$\mathbb{Z}_2$	$\mathbb{Z}_2$	$\mathbb{Z}$	0
π_8	0	0	$\mathbb{Z}_2$	$\mathbb{Z}_2$	$\mathbb{Z}_2^2$	$\mathbb{Z}_{24}$	$\mathbb{Z}_2$	$\mathbb{Z}_2$	$\mathbb{Z}$
π_9	0	0	$\mathbb{Z}_3$	$\mathbb{Z}_3$	$\mathbb{Z}_2^2$	$\mathbb{Z}_2$	$\mathbb{Z}_{24}$	$\mathbb{Z}_2$	$\mathbb{Z}_2$
π_{10}	0	0	$\mathbb{Z}_{15}$	$\mathbb{Z}_{15}$	$\mathbb{Z}_{24}\times\mathbb{Z}_3$	$\mathbb{Z}_2$	0	$\mathbb{Z}_{24}$	$\mathbb{Z}_2$
π_{11}	0	0	$\mathbb{Z}_2$	$\mathbb{Z}_2$	$\mathbb{Z}_{15}$	$\mathbb{Z}_2$	$\mathbb{Z}$	0	$\mathbb{Z}_{24}$
π_{12}	0	0	$\mathbb{Z}_2^2$	$\mathbb{Z}_2^2$	$\mathbb{Z}_2$	$\mathbb{Z}_{30}$	$\mathbb{Z}_2$	0	0
π_{13}	0	0	$\mathbb{Z}_{12}\times\mathbb{Z}_2$	$\mathbb{Z}_{12}\times\mathbb{Z}_2$	$\mathbb{Z}_2^3$	$\mathbb{Z}_2$	$\mathbb{Z}_{60}$	$\mathbb{Z}_2$	0

Figure 1.21: The higher homotopy groups π_n for n dimensional spheres denoted as S^n. The 0 entries show trivial group, where the loops or higher dimensional enclosing surfaces can be shrunk to a point. The non-zero entries show the non-trivial part either infinite cyclic $\mathbb{Z}$ or finitely cyclic $\mathbb{Z}_m$, for $m \neq \{0, 1\}$. Taken from Ref(Program 2013).

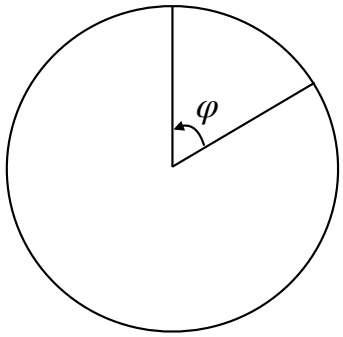

Figure 1.22: The interpolating map H from loop γ_1 to γ_2

Then all homotopic classes for different n are characterized by a homotopic invariant ν (or winding number). This invariant does not change under smoothly deforming $g(\varphi)$.

1.9.3 Degree of a map

The winding number can be generalized to higher dimensions. There is an equivalent but more handy way to define winding for the same continuous map $g : X \to S^1$. This can be done by considering the same disc X with a hole at the centre, however extending the boundaries to infinity ($\simeq \mathbb{R}^2 \{0\} \simeq S^1$) (see Fig. 1.19a). A semi-infinite line originating from the hole (or singularity) is drawn going towards infinity, as sketched with a dotted line in Fig. 1.24. Then the number of intersections of a loop with this line taking into account also

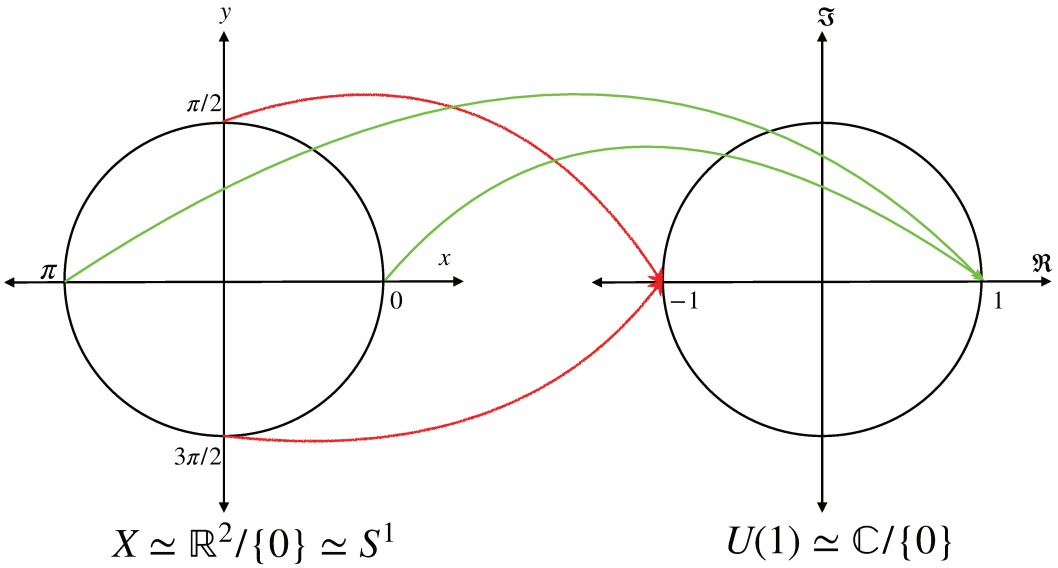

Figure 1.23: The map $S^1 \to U(1)$ for $\alpha(\varphi) = 2\varphi$.

the orientation of the loop gives exactly the winding number ν. The later (orientation) is shown with the sign + for the loops intersecting the dotted line from the top (or are oriented counter-clockwise) or − for the loops intersecting the dotted line from the bottom (or are oriented clockwise) in Fig. 1.19a. It turn out, this sign for an arbitrarily oriented loop can be

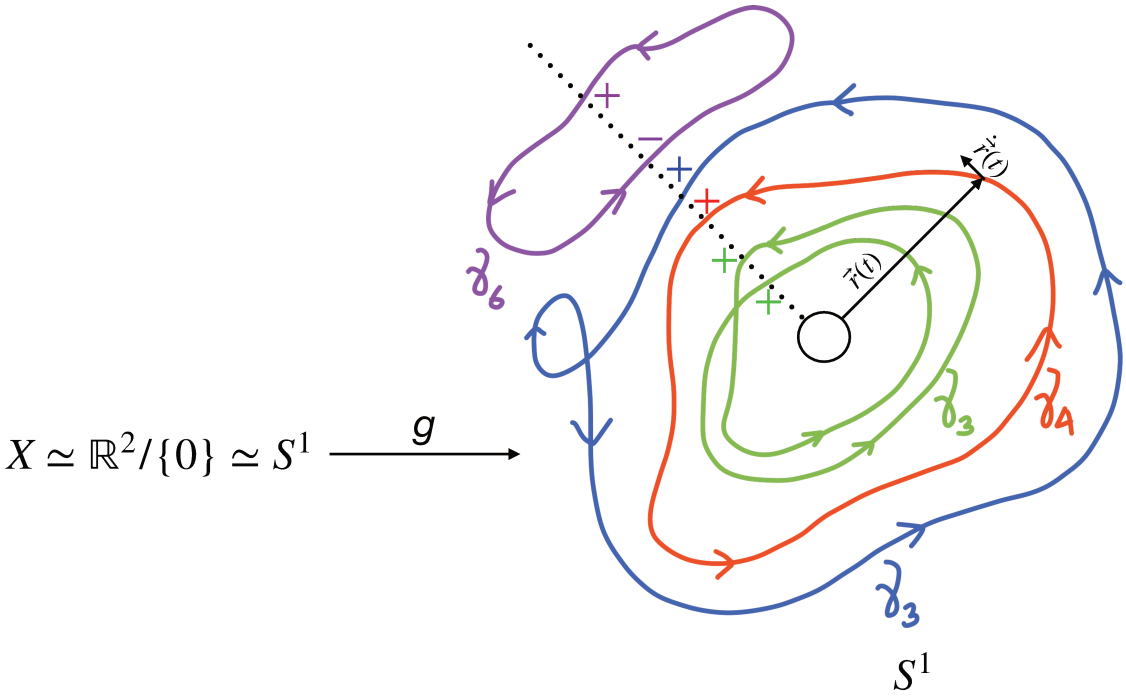

Figure 1.24: Counting of intersections of loops with the semi-infinite dotted line. The orientation of the loop (either cutting from the top or from the bottom the line) decides the sign.

extracted by parametrizing the loop with a vector $\vec{r}(t)$ whose origin is the same singularity. Then it is sign of the vector product of $\vec{r}(t)$ with the tangent vector $\dot{\vec{r}}(t)$ and the normal vector $\hat{n}_z$ at the dotted line (inclined at an angle φ_0). In addition, the intersection with a given loop g takes place for some images $g(t_j^{(0)}) = \varphi_0$. This in return gives us the pre-images $t_j^{(0)} \approx g^{-1}(\phi_0)$. This gives winding (or degree) of g as

$$\begin{aligned} \nu(g) &= \deg(g) = \sum_{t_j^{(0)} \approx g^{-1}(\phi_0)} \operatorname{sgn}\left[\vec{r}(t) \times \dot{\vec{r}}(t)|_{\varphi_0} \cdot \hat{n}_z\right], \\ &= \sum_{t_j^{(0)} \approx g^{-1}(\varphi_0)} \operatorname{sgn}\left[\frac{\mathrm{d}\phi}{\mathrm{d}t}|_{\varphi_0}\right]. \end{aligned} \tag{1.40}$$

There are two reasons to formulate the winding number in this way. First, there no integral evaluation, and secondly, the generalization to higher dimensions is quite simple. It can be seen for a general case, the degree (or winding number) of a map $g : X \to Y$ between two orientable surfaces with same dimensions is

$$\nu(g) = \sum_{x_j^{(0)} \approx g^{-1}(y_0)} \operatorname{sgn}\left[\det\left(\frac{\partial y^\alpha}{\partial x^\beta}\right)\Big|_{y_0}\right]. \tag{1.41}$$

where $x \in X$ and $y \in Y$, and the factor inside the determinant is the Jacobian matrix corresponding to the transfer of coordinates from x to y. This definition in terms of degree does not depend on the choice of image y_0. It is a homotopy invariant generalizing the winding number to higher dimensional manifolds from a map g: $S^1 \to S^1$.

1.10 Berry curvature and Chern number

The topological invariant has also pervaded in the physical systems, e.g., the quantum Hall effect (QHE) in 1980 by the von Klitzing group (Klitzing et al. 1980). This effect arises when a strong magnetic field is applied to a 2D electron gas, which leads to the vanishing longitudinal conductivity, whereas the transverse conductivity is still non-zero. That can be explained from a semiclassical picture of electrons experiencing the Lorentz force due to the magnetic field B. Then this force makes the electrons to exhibit close cyclotron orbits with cyclotron frequency $\omega_c = eB/m_e$, where e is the electronic charge and m_e is the mass of electron. As can be seen from a sketch in Fig. 1.25, these orbits experience an obstruction in making close circles at the boundaries, where they instead propagate. It becomes the source of conductivity in this 2D sample, where the bulk of the sample is insulating, which means there is no net motion of electrons. Remarkably, this (transverse) conductivity is very precisely quantized, given by

$$\sigma_H = n\frac{e^2}{h}. \tag{1.42}$$

where h is the Planck's constant and n is an integer, σ_H is also known as quantum Hall conductivity. Not long after the QHE discovery, Thouless, Kohmoto, Nightingale, and Nijs

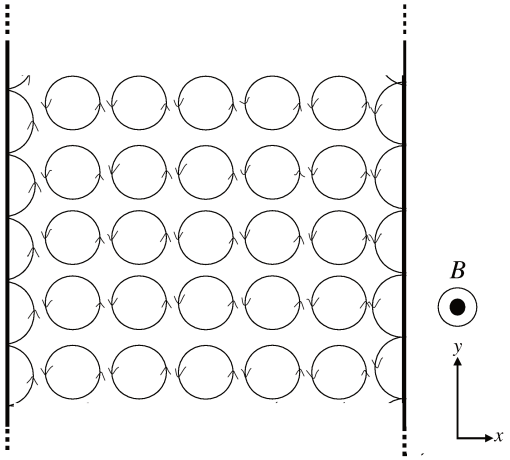

Figure 1.25: In the semiclassical picture, electrons are making cyclotron orbits under the influence of the Lorentz force. The electrons at the boundaries are unable to make a circular round, instead are skipping orbits.

in their seminal work (Kohmoto 1985; Thouless et al. 1982) showed the topological origin of this quantum Hall conductivity,

$$\sigma_H = \frac{e^2}{h} \sum_j C_j \tag{1.43}$$

where the sum runs over all filled states or bands, and C_j is called TKNN invariant or (first) Chern number. It can be expressed as an integral of a local quantity known as Berry curvature over the Brillouin zone (BZ)

$$C_j = \frac{1}{2\pi} \int_{BZ} \mathrm{d}k_x \mathrm{d}k_y \Omega_j(k_x, k_y) \tag{1.44}$$

This equation is similar to the Gauss-Bonnet theorem (in eq.(1.32)), where the integral was over the local quantity Gaussian curvature, here it is over the Berry curvature. We saw that the Euler characteristic χ gave the relation with the number of holes. Likewise, we can be curious about what does C relates to (or counts)?
Beyond the semiclassical picture, these skipping orbits are related to the edge states propagating at the boundaries in the quantum picture. The Chern number counts the number of such edge states, as sketched in Fig. 1.26. As can be seen from this figure, when the edge states leave a band. The corresponding band loses one state, and this is captured by this Chern number as $C = -1$, and the other band has $C = +1$, since it has gained one state. Even though there is a bulk gap, the edge states are conducting, if the Fermi energy lies in the gap, where the Chern number of the bands captures this physical property. These insulators are known as *Chern insulators*, a subclass of a big family of *topological insulators*.

We can more formally define what a Berry curvature is, how it is expressed in terms of more fundamental quantities like the eigenstates of the system.

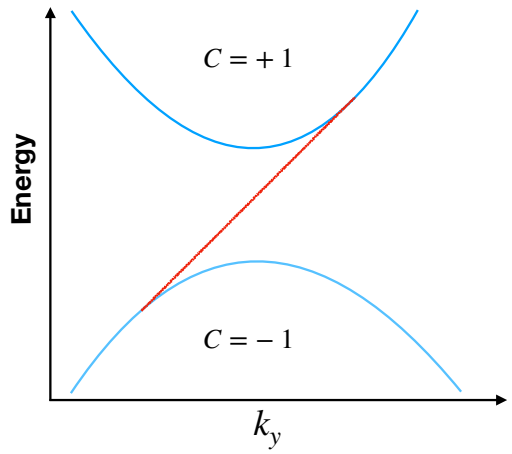

Figure 1.26: The edge state bridges the bulk gap. It leaves the lower band and merges to the upper band when varying k_y. This is referred to as a spectral flow. This lower band as lost one state, where this is captured by $C = -1$, while the upper band has $C = +1$ since it has gained one state.

1.10.1 Topology of eigenstates

Let us consider a Hamiltonian H that is parametrized by a set of parameters, denoted by $\mathbf{G} = (G_1, G_2, ...)$, we are concerned with the adiabatic evolution of the system as $\mathbf{G}$ moves slow enough along a closed path C in parameter space such that we can define an eigenvalue equation

$$H(\mathbf{G})|\psi_j\rangle = E_j(\mathbf{G})|\psi_j\rangle \tag{1.45}$$

If the system is prepared in one of the eigenstates and the system adiabatically evolves by changing $\mathbf{G}$, then due to the adiabatic theorem, the system remains in the same eigenspace. However, after one full evolution when the parameter G returns to its initial value, the eigenstate acquires a phase with respect to the initial value (Xiao et al. 2010). This phase contains the dynamical phase and geometric phase. This geometric phase γ_j can be expressed as

$$\gamma_j = \int_C \mathrm{d}\mathbf{G} \cdot \mathcal{A}_j(\mathbf{G}), \tag{1.46}$$

where $\mathcal{A}_j$ is

$$\mathcal{A}_j(\mathbf{G}) = i\langle\psi_j(\mathbf{G})|\frac{\partial}{\partial \mathbf{G}}|\psi_j(\mathbf{G})\rangle \tag{1.47}$$

This vector $\mathcal{A}(\mathbf{G})$ is known as the *Berry connection* and the geometric phase γ is known as the *Berry phase* (Berry 1984). Now, we can define the *Berry curvature* as,

$$\Omega_j(\mathbf{G}) = \nabla \wedge \mathcal{A} \tag{1.48}$$

where $\wedge$ becomes a vector product if the parameter space is 3D. Unlike Berry connection, which is gauge dependent quantity (i.e., under $\psi_j \to e^{i\alpha(\mathbf{G})}$, $\mathcal{A}$ has gauge dependent term, see eq.(1.47)), Berry curvature is a gauge invariant and a physical observable. Furthermore, it can be used to calculate the Chern number defined in the quantum Hall effect in eq.(3.15).

The Chern number may appear in topological band theory in mainly two contexts, one in the gapped band structure, which is the case of QHE and other in gapless one. This topological invariant also appear in the gapless systems like Weyl semimetals, where it has different interpretation than the number of edge states in QHE.

In order to capture the topology in gapless systems the above defined Berry curvature $\Omega_j(\mathbf{G})$ besides in differential form can also be expressed in terms of eigenstates, which can be derived by taking the derivative with respect to $\mathbf{G}$ of the eigenvalue equation(1.45) and using completeness of eigenstates[13] gives,

$$\Omega_j(\mathbf{G}) = i \sum_{m \neq n} \sum_{j,k} \frac{\langle \psi_j | \partial_{G_m} H | \psi_k \rangle \langle \psi_k | \partial_{G_n} H | \psi_j \rangle}{(E_j - E_k)^2} \mathrm{d}G_m \wedge \mathrm{d}G_n \tag{1.49}$$

where $\partial_{G_n} = \dfrac{\partial}{\partial G_n}$. Expressing Berry curvature in the above form tells us that $\sum_j \Omega_j(\mathbf{G}) = 0$, using the anti-symmetry property of wedge product. Another important observation comes from the denominator, which vanishes at degeneracy points i.e., when $E_j(\mathbf{G}_0) = E_k(\mathbf{G}_0)$. Thus, these degeneracies are either source or sink of Berry curvature, and it is singular at these points, which are called *Berry monopoles*. If these monopoles are enclosed by a surface (in parameter space or BZ), then the surface is pierced by a flux. The origin of the flux is connected to the fact that these monopoles carry charges, as sketched in Fig. 1.27. It turns out; this charge is an integer-valued topological number that can be quantified in terms of first Chern number $\mathcal{C}$

$$\mathcal{C}_j = \frac{1}{2\pi} \int_{S^2} \Omega_j. \tag{1.50}$$

The sign of $\mathcal{C}_j$ decides in turn the sign of the topological charge, in this regard Ω_j is also called *Berry flux* that pierce the surface enclosing the degeneracy (see Fig. 1.27). This is the same charge that also appears in the topological classification of Weyl nodes, where $\mathbf{G} = G_{i=1..3}$ is replaced by the Bloch vectors $\mathbf{k} = \{k_x, k_y, k_z\}$. It turns out that this Chern number $\mathcal{C}$ is related to the degree of Hamiltonian, where degree is defined in eq.(1.41). The degree of Hamiltonian can be defined by considering a 2 Hamiltonian, which can always be decomposed in terms of Pauli matrix $\boldsymbol{\sigma}$ as

$$H(\mathbf{G}) = \mathbf{h}(\mathbf{G}) \cdot \boldsymbol{\sigma} \tag{1.51}$$

where we have neglected any global shift i.e. $h_0(\mathbf{G}) = 0$, which can be removed by redefining the origin for the energy. Then eigenenergies is expressed as

$$E_\pm = \pm ||\mathbf{h}(\mathbf{G})||. \tag{1.52}$$

At a degeneracy point, we have $\mathbf{G}_0$, $E_\pm(\mathbf{G}_0) = 0 = ||\mathbf{h}(\mathbf{G}_0)||$. This creates an obstruction in defining the normalized eigenvectors $\hat{\mathbf{h}} \equiv \mathbf{h}(\mathbf{G})/||\mathbf{h}(\mathbf{G})||$ at these points. However, they are well defined, if we remove this degeneracy(s) point. These normalized eigenvectors defines a

[13] i.e. $\sum_j |\psi_j\rangle\langle\psi_j| =$ Identity.

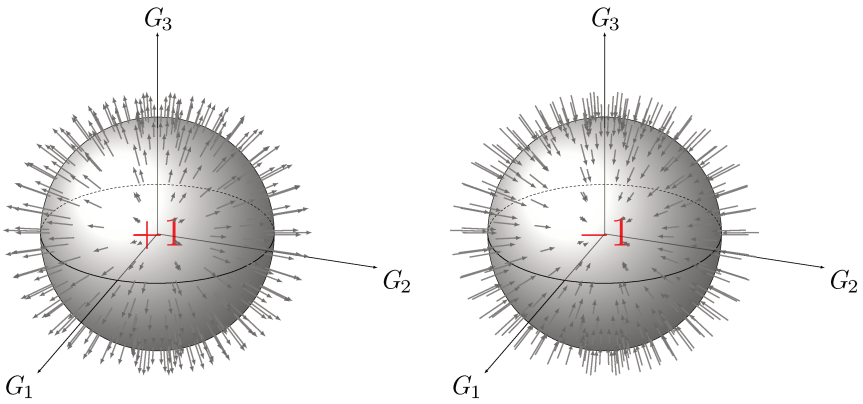

(a) (b)

Figure 1.27: The topological charge associated with degeneracy situated at the origin, for (a) a positive charge the (Berry) flux goes outwards from the origin, and for (b) a negative charge, it comes inwardly.

map from parameter space to the unit sphere $\hat{h} : \mathbf{G}\backslash\{\mathbf{G}_0\} \to S^2$. For this case, the degree of this map can be expressed in terms of the above defined Chern number eq.(1.50) as following,

$$\mathcal{C}_{\pm} = \mp \deg \hat{h}. \tag{1.53}$$

This expression shows the connection between the topological charge enclosed in the parameter space with the degree of Hamiltonian map that determines the homotopy invariant connected to the wrapping number over the sphere (S^2). This makes it convenient to calculate the Chern number by wrapping around the degeneracy (see Fig. 1.24). Thus, instead of calculating the integral in eq.(1.50), we can compute the pre-images as

$$\mathcal{C} = \sum_{\mathbf{G}_0 = h^{-1}(t_0)} sgn \det \begin{pmatrix} \partial_{G_1} h_x & \partial_{G_1} h_y & \partial_{G_1} h_z \\ \partial_{G_2} h_x & \partial_{G_2} h_y & \partial_{G_2} h_z \\ \partial_{G_3} h_x & \partial_{G_3} h_y & \partial_{G_3} h_z \end{pmatrix} |_{t_0 = \mathbf{h}(\mathbf{G}_0)} \tag{1.54}$$

where t_0 is any regular point so that the determinant is not singular, $\mathbf{G}_0$ are previously defined degeneracies in the parameter space (such that $E_+(\mathbf{G}_0) = E_-(\mathbf{G}_0)$). We removed the little hat from the $\mathbf{h}$, because the magnitude $||\mathbf{h}||$ does not affect the sign of the charge.

A quick example to see the ease of this formula is defining the topological charge for the Weyl nodes. By linearizing the Hamiltonian near the Weyl points gives $\mathbf{h} = \pm\mathbf{k}$. Then the topological charge of the Weyl nodes is $\mathcal{C} = \pm 1$. We shall come back to this formula in our last chapter, where we will encounter similar degeneracies.

Chapter 2

Floquet formalism: implementation in waveguide arrays

2.1 Introduction

In the current chapter, I discuss how periodic driving a system can induce novel topological phenomena, without any counterpart in the static regime. This driving translates to say that Hamiltonian has a time translational symmetry, $H(t+T) = H(t)$, where T is the period of a drive. This time dependence forbids to define a precise ground state of the system unlike in static or equilibrium[1]. Despite this, such time-dependent systems phenomena can give rise to many novel phenomena. For example, the presence of non-trivial edge states even though the band topological invariants vanish (M. S. Rudner et al. 2013).

2.2 Periodically driven systems

To look for a general solution for a particular class of ordinary differential equations was one of the significantly focused domains of interest during the 16^{th}-17^{th} century or even till now. As the description of a natural phenomenon, like the beating of a drum or the oscillation of a pendulum, involves such equations. A particular class of such equations was when the coefficients are periodic under either space, time, or both. Then Floquet theorem given by Gaston Floquet in 1883 (Floquet 1883), later by George Hill (Hill 1886), gives the canonical form of the solutions. Again discovered by Lyapunov (Lyapunov 1896) and by Felix Bloch in 1928(Bloch 1929), in the context of periodic quantum Hamiltonian in space, giving rise to band theory.

In physics, we stick to the terminology "Floquet theory" when the system has time periodicity and "Bloch theory" for space periodicity. I keep this convention.

The case of time-periodic Hamiltonians, which I am mostly interested in, was first studied

[1] As the (quasi) energy spectrum lies on a circle, so it is ambiguous to define low energy states or bands

by Shirley (Shirley 1965), Keldysh (Keldysh et al. 1965), Zel'dovich (Zel'Dovich 1967) and later a full framework was developed by Sambe (Sambe 1973). Then it was extended from one mode to the case of multiple modes (T.-S. Ho et al. 1983), and a detailed review can be found in Ref(Chu et al. 2004). A comprehensive survey of a periodically driven two-level system can be found in Ref (Dion et al. 1976). For more pedagogical view one can refer to notes by P. Hänggi (Hänggi 1998) or to the thesis of Michael Fruchart (Fruchart 2016) or Álvaro Gómez León (León 2014).

2.2.1 Floquet formalism

Let us consider a closed quantum system, described by a Hamiltonian H, which is non-interacting and periodically driven with period T, such that $H(t+T) = H(t)$. This driving can be achieved, for example, by emitting an electromagnetic wave on a quantum system (Netanel H Lindner et al. 2011; Y. H. Wang et al. 2013) or by periodically shaking the optical lattices (Jotzu et al. 2014; Lignier et al. 2007; Parker et al. 2013; Struck, Ölschläger, et al. 2012; Struck, Weinberg, et al. 2013) or by employing the periodicity along the propagation axis in optically coupled waveguides network (Ozawa, Hannah M. Price, Amo, et al. 2019; Szameit and Stefan Nolte 2010).

The system is initially prepared in a state $|\Psi(\vec{r}, t_0)\rangle$ evolves according to the evolution operator $U(t, t_0)$ to a state $|\Psi(\vec{r}, t)\rangle = U(\vec{r}; t, t_0)|\Psi(\vec{r}, t_0)\rangle$, at later time t. $|\Psi(\vec{r}, t_0)\rangle$ satisfies Schrödinger equation,

$$i\frac{\partial|\Psi(\vec{r},t)\rangle}{\partial t} = H(\vec{r},t)|\Psi(\vec{r},t)\rangle, \tag{2.1}$$

where the Hamiltonian generates the evolution ($\hbar = 1$),

$$U(\vec{r}; t, t_0) = \mathcal{T}\exp\Big[-i\int_{t_0}^{t} \mathrm{d}t'\, H(\vec{r}, t')\Big] \tag{2.2}$$

$$U(\vec{r}; t, t_0) = \lim_{\Delta t\to 0} \exp\Big[-i(N+1)\,\Delta t\, H(t)\Big]\cdots\exp\Big[-i2\Delta t\, H(t_0+\Delta t)\Big]\exp\Big[-i\Delta t\, H(t_0)\Big]. \tag{2.3}$$

where $N = (t - t_0)/\Delta t$.
A stationary Hamiltonian is also periodically driven with $T = 0$, however, corresponding evolution operator is "trivial"[2].
However, a non-trivial and interesting physics emerges when Hamiltonian is driven periodically with period T (or with single driving frequency $\omega = 2\pi/T$, where $T \neq 0$) i.e. $H(t+T) = H(t)$. Likewise, the evolution of the states is still described by equation (2.2).

Here, the evolution operator satisfies a multiplication rule,

[2]In the sense that the system has well defined eigenstates. So, if the system is prepared in one of the eigenstates, it will remain in it forever. The time evolution will only give a definite dynamical phase to the eigenstates depending on the initial and final times.

$$U(t_f, t_i) = U(t_f, t_{intermediate})U(t_{intermediate}, t_i) \tag{2.4}$$

which means that the time evolution from the initial time t_i to the final one t_f can written as a product from initial to some arbitrary intermediate time t and then from there to the final time. As shown pictorially in Fig. 2.1.

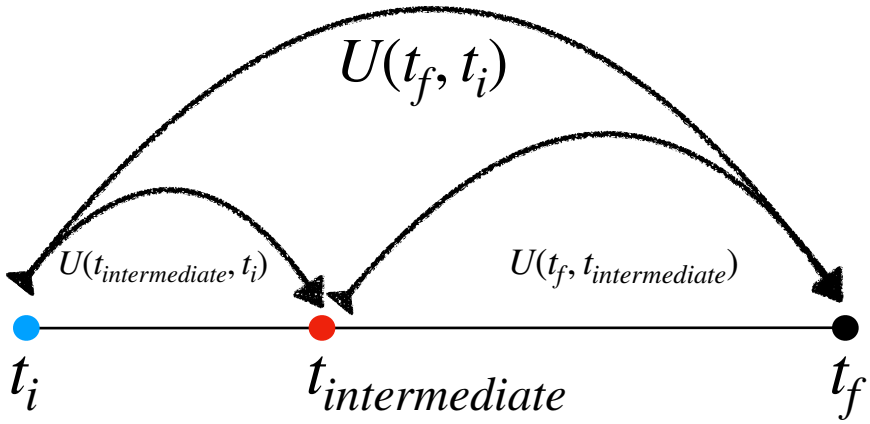

Figure 2.1: Multiplication rule for time evolution operator

We follow the decomposition of eq(2.1), with $H(t) = H_0 + V(t)$, $V(t+T) = V(t)$ (position dependence is dropped, for the sake of clarity) , where we assume that H_0 has a complete set of eigenstates ϕ_n with eigenvalues E_n.
According to Floquet theory there exists a solution to eq(2.1),

$$|\Psi_j(t)\rangle = \mathrm{e}^{-i\varepsilon_j t}|\Phi_j(t)\rangle, \tag{2.5}$$

$$|\Psi_j(t+T)\rangle = \mathrm{e}^{-i\varepsilon_j T}|\Psi_j(t)\rangle \tag{2.6}$$

where $|\Phi_j(t+T)\rangle = |\Phi_j(t)\rangle$, at $t = T$, $|\Phi_j(T)\rangle$ is referred to as a *Floquet state*, and ε_j is a real valued number known as the *quasienergy*, which is only define uniquely up to multiples of $\omega = 2\pi/T$. It is the total phase acquired by the state when the system has evolved by one period, it can be seen from equation (2.6). The Floquet theorem can be seen as a time analog of Bloch theorem, where quasimomentum is analogous to quasienergy. However, both do not play the same roles.

By substituting eq(2.5) in eq(2.1), it gives

$$\left[\varepsilon_j + i\frac{\partial}{\partial t}\right]|\Phi_j(t)\rangle = H(t)|\Phi_j(t)\rangle \tag{2.7}$$

$$\mathcal{H}(t)|\Phi_j(t)\rangle = \varepsilon_j|\Phi_j(t)\rangle \tag{2.8}$$

where $\mathcal{H}(t) \equiv H(t) - i\dfrac{\partial}{\partial t}$ is a Hermitian operator satisfying above eigenvalue equation. Problem boils down to solve equation (2.8).

In terms of numerical computation, we can separate Floquet formalism into two cases. In the first case, if Hamiltonian has continuous-time dependence, where we use the Sambe

Hamiltonian approach. In another case, Hamiltonians have a discrete-time dependence. For example, in quantum walks, we make use of the scattering network framework to describe the dynamics of the system.

Continuous-time dependence

When the Hamiltonian depends on time in a continous fashion, e.g. $H(t) = H_0 \cos \omega t$. Then it gives rise to an integral equation (2.8). This can be seen by a Fourier decomposition of $|\Phi(t+T)\rangle$, since $|\Phi(t+T)\rangle = |\Phi(t)\rangle$,

$$|\Phi(t)\rangle = \int_{-\infty}^{\infty} \mathrm{d}\omega \, \mathrm{e}^{i\omega t} |\Phi(\omega)\rangle \tag{2.9}$$

for the case of monochromatic frequency $\omega = 2\pi/T$, in which one is mostly interested in, the above expression can further be rewritten in some time independent basis $|\alpha\rangle$[3],

$$|\Phi(t)\rangle = \sum_{\alpha} \Phi_\alpha(t)|\alpha\rangle, \qquad \Phi_\alpha(t) = \sum_{m=-\infty}^{\infty} \phi_\alpha^{(m)} \mathrm{e}^{im\omega t} \tag{2.10}$$

Substituting above equation in eq(2.7), we get a stationary Schrödinger like equation for Fourier amplitudes as

$$\tilde{H}_{\alpha\beta}^{(m-n)} \phi_\beta^{(m)} \quad = \quad (\varepsilon - n\omega)\phi_\alpha^{(n)}, \tag{2.11}$$

where $\tilde{H}_{\alpha\beta}^{(m-n)} = \sum_{\beta,m} \frac{1}{T} \int^T \mathrm{d}t \mathrm{e}^{i(m-n)\omega t} \langle\alpha|H(t)|\beta\rangle$ is the Fourier transform of $H(t)$ and is known as Floquet Hamiltonian.
In above equation, $\langle\alpha|$ lives in some Hilbert space $\mathcal{R}$, satisfying

$$\langle\alpha|\beta\rangle = \delta_{\alpha\beta}, \tag{2.12}$$

similarly, the temporal part $\mathrm{e}^{in\omega t}$ lives in Hilbert space $\mathcal{T}$,

$$\frac{1}{T} \int^T \mathrm{d}t \, \mathrm{e}^{i(p-m)\omega t} = \delta_{m,p}, \tag{2.13}$$

They form a complete set of basis,

$$\sum_{\alpha} \Phi_\alpha^*(t)\Phi_\alpha(t') = \delta(t-t') \tag{2.14}$$

Essentially, the Hermitian operator $\mathcal{H}$ in eq(2.8) lives in a Hilbert space composed of $\mathcal{R} \otimes \mathcal{T}$. This space is sometimes referred to as *Sambe space* (Sambe 1973), in literature. The states form a complete set in the $\mathcal{R} \otimes \mathcal{T}$.

[3]For a N level system, $|\alpha\rangle$ will correspond to $|\alpha\rangle = 1, 2, \cdots, N$

In the R.H.S of the eq(2.11), the first term can be interpreted as an onsite energy term and the second term as the number of photons absorbed or emitted by the system. This term ($n\omega$ in eq(2.8)) can be interpreted as an effective electric field in an analogy with the Wannier-Stark ladder on a Floquet lattice generated by commensurate or incommensurate frequency drives (Chu et al. 2004; Martin et al. 2017). For example, if we subject a physical system to two incommensurate drives ω_1, and ω_2, then its dynamics can be represented on a two-dimensional Floquet lattice, where the hopping energies along one axis j of the lattice corresponds to either absorb (along $+j$) or emit (along $-j$) a photon of frequency ω_j.

Now, what remains to be solved is the L.H.S of the eq(2.11), which is an infinite-dimensional matrix. We consider some particular cases to calculate the quasienergy spectrum and Floquet states.

Considering a harmonic drive of period $T = 2\pi/\omega$, then $H(t) = H_0 + \delta e^{i\omega t} + \delta^\dagger e^{-i\omega t}$, where the Floquet Hamiltonian has a tridiagonal form,

$$\mathcal{H} = \begin{array}{c} \begin{array}{ccccccc} n & \cdots & +1 & & 0 & -1 & \cdots \end{array} \\ \begin{pmatrix} \ddots & & & & & & \\ & H_0+\omega & \delta & & & & \\ & \delta^\dagger & H_0 & \delta & & & \\ & & \delta^\dagger & H_0-\omega & & & \\ & & & & \ddots & & \end{pmatrix} \begin{array}{c} m \\ \vdots \\ +1 \\ 0 \\ -1 \\ \vdots \end{array} \end{array} \tag{2.15}$$

The diagonal term in the above Floquet Hamiltonian is frequency-dependent, in the sense that they are copies of H_0 just shifted by the multiples of the driving frequency, where the dimension of H_0 encodes the degree of freedom in the system, like the number of orbitals in a unitcell. This redundancy of multiple copies of H_0 reflects from the wavefunction(2.5) by substituting(2.10) and considering it in the present case by a shift of $k\omega$ of the quasienergy, it gives

$$|\Psi_j(t)\rangle \quad = \quad e^{-i(\varepsilon_j + k\omega)t} \sum_{\tilde{m}=-\infty}^{\infty} \phi_\alpha^{(\tilde{m})} e^{ik\omega t} e^{i\tilde{m}\omega t} \tag{2.16}$$

where shifting the Fourier mode cancels the shift contribution in quasienergy. Moreover, off-diagonal terms connects (or hybridize) the different "copies": as mentioned before, either the system gains one photon ($e^{i\omega t}$) from the drive or loses on photon ($e^{-i\omega t}$) to the drive. For arbitrary drive, i.e., $H(t) = H_0 + \delta e^{ip\omega t} + \delta^\dagger e^{-ip\omega t}$ where $p \in \mathbb{Z}$, there is a hybridization of bands separated by an energy gap $p\omega$ (Rudner n.d.).

Interestingly, in this situation, the Floquet matrix eq(2.15) can be thought of as a tight-binding Hamiltonian on some lattice. The hoppings are being mediated by δ's with the Wannier-Stark like onsite potential (Glück et al. 2002; A. Gómez-León et al. 2013; Martin et al. 2017), as shown in Fig 2.2. It reminds us of the presence of an electric field in a lattice that gives rise to a Bloch oscillation of an electron in a band, with bandwidth or kinetic

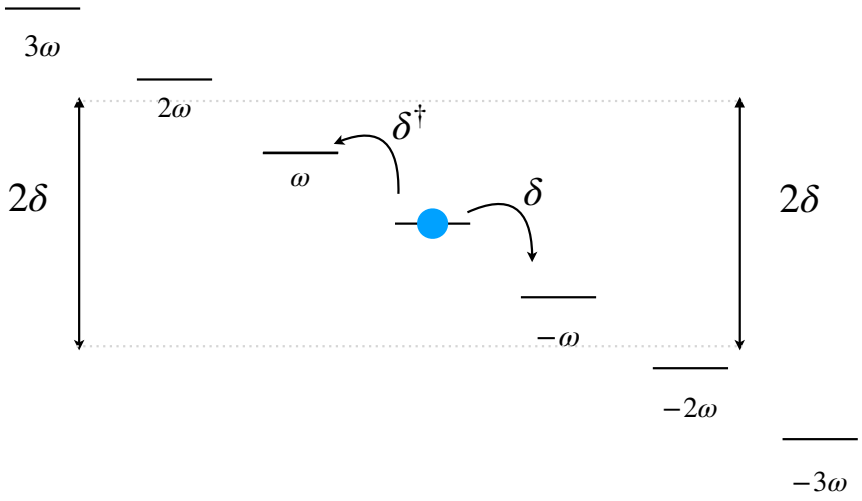

Figure 2.2: Tight binding model with Floquet Hamiltonian

energy of 2δ. It means electron can take or give at a maximum energy of 2δ. It allows us to define a (kinetic) energy window of 2δ (see Fig 2.2), beyond which the wavefunction starts to decay. This justifies in truncating an infinite-dimensional Floquet matrix to a finite one.

2.2.2 Stepwise Hamiltonian: discrete time dynamics

Now we digress our discussion from the continuous case to the stepwise Hamiltonians or stepwise evolutions, where the stepwise sequence is periodic in time. From equation(2.2), for $t = T$ and $t_0 = 0$, we get

$$U(T,0) = \mathcal{T} \exp\Big[-i\int_0^T \mathrm{d}t' H(t')\Big] \equiv \mathrm{e}^{-iH^{eff}T} \tag{2.17}$$

where full time evolution operator or $U(T,0)$ is known as Floquet evolution operator or *Floquet operator*,

$$U(T,0)|\Psi_j(T)\rangle = \mathrm{e}^{i\varepsilon_j T}|\Psi_j(T)\rangle. \tag{2.18}$$

Similarly, we can define the effective Hamiltonian H_{eff} as,

$$H^{eff} = \frac{i}{T}\log U(T,0), \tag{2.19}$$

$$H^{eff} = \frac{i}{T}\sum_j \log\left[\mathrm{e}^{i\varepsilon_j T}\right]|\Psi_j(T)\rangle\langle\Psi_j(T)|. \tag{2.20}$$

this can be seen as a restatement of the previous definition of quasienergy, where they are the eigenstates of the effective Hamiltonian. Unlike the Floquet Hamiltonian eq(2.8), the effective Hamiltonian is time-independent (Kitagawa, Berg, et al. 2010; M. S. Rudner et al. 2013).

There are two-time scales in Floquet theory with respect to the driving period T, namely long and short. The Floquet theory allows us to separate these two-time scales. The long

time dynamics come from the effective Hamiltonian, where it generates the bulk time evolution when examined stroboscopically at integer multiples of the driving period T, which is identical to the Floquet operator $U(T)$. This can be seen from the multiplication rule eq(2.4)

$$U(nT) = U^n(T). \tag{2.21}$$

This can written in more generally as

$$U(t + nT) = U(t)U^n(T). \tag{2.22}$$

The short time scale is generated by evolution operator itself at intermediate times between initial t_i one full period $t_i + T$(2.2). Floquet theory allows us to write the evolution operator with the two contributions as,

$$U(t) = V(t)\mathrm{e}^{-iH^{eff}t} \tag{2.23}$$

where, $V(t + T) = V(t)$ is known as periodized evolution operator that contains the short time scales. The above equation is very analogous to equation(2.5), however, in the operator form. In the next chapter, I shall show how the stepwise Hamiltonian (or discrete evolution) can easily be formulated in the scattering matrix framework.

2.2.3 Topological properties arising in Floquet systems

In the current subsection, I present a very brief description of the topology in the Floquet domain and the symmetries that are responsible for non-trivial topology. The topology in this domain differs from the static regime. In the static case, we look for the maps from the Brillouin Zone (BZ) to the Hamiltonian matrices (of dimension m, for m bands), which defines a closed loop in the space of $m \times m$ Hamiltonian matrices. This loop can be characterized in terms of homotopy, where all such loops that can be smoothly deformed into each other define an equivalence or homotopy class, which can thus be characterized by an invariant. However, in a periodically driven case, we look for maps from the Brillouin Zone times T (time) to space of Unitary matrices (of dimension m, for m bands), $BZ \times T \longrightarrow U(m)$. In the Floquet case, the number of bands is the same as the number of gaps, unlike static case. It gives rise to a regime not to be reproducible in the static case.

The topology in the Floquet regime can be divided into two classes (Nakagawa et al. 2020). In one of the class, the topology is characterized by the effective Hamiltonian or equivalently by the Floquet operator, involving the topology of gapped quasienergy spectra, e.g., Floquet Chern insulators (Budich et al. 2017; A. Gómez-León et al. 2013; Jiang et al. 2011; Kitagawa, Berg, et al. 2010; Kitagawa, Matthew A Broome, et al. 2012; Kitagawa, Oka, et al. 2011; Kundu et al. 2014; Netanel H Lindner et al. 2011; Oka et al. 2009; X.-Q. Sun et al. 2018). Another class is where the full dynamics of evolution operator characterize the topology during one period. This could give rise to the anomalous Floquet topological insulators (Delplace, Fruchart, et al. 2017; Fruchart 2016; Morimoto et al. 2017; Nathan et al. 2015; Roy and Harper 2017; M. S. Rudner et al. 2013; Yao, Yan, et al. 2017). This later one has no static part; even if the effective Hamiltonian is topologically trivial, the topology of the time evolution operator during one period can still be nontrivial.

Topology and symmetries

We assume that the Floquet operator $U(T)$ has translational symmetry, however, this constraint can also be relaxed for calculating topological invariants (Fulga et al. 2016; Titum, Berg, et al. 2016). Recently, a formal bulk edge correspondence has been made in the absence of translational symmetry (Graf et al. 2018).

In eq(2.23), we can rewrite effective Hamiltonian with a branch cut as,

$$V_\varepsilon(t) = U(t)\mathrm{e}^{-iH_\varepsilon^{eff}t} \tag{2.24}$$

where the branch cut dependence comes from $H_\varepsilon^{eff} = \frac{i}{T}\log_\varepsilon U(T)$.

Topology in static or periodically driven systems depends on the dimension of the system and on the symmetries that constrain the quasienergy spectrum and states. Here, the symmetries are particle-hole or charge conjugation $\mathcal{C}$, time-reversal Θ and chiral symmetry Γ.

The particle-hole symmetry acts on the evolution operator, the effective Hamiltonian and the periodized evolution operator, respectively, here $\mathcal{C}$ is anti-unitary

$$\mathcal{C}U(k,t)\mathcal{C}^{-1} = U(-k,t), \tag{2.25}$$
$$\mathcal{C}H_\varepsilon^{eff}(k)\mathcal{C}^{-1} = -H_{-\varepsilon}^{eff}(k) + \frac{2\pi}{T}\mathbb{1} \tag{2.26}$$
$$\mathcal{C}V_\varepsilon^{eff}(k,t)\mathcal{C}^{-1} = V_{-\varepsilon}^{eff}(-k,t)\mathrm{e}^{-i2\pi t/T}. \tag{2.27}$$

Similarly, for the anti-unitary time-reversal operator Θ, it follows

$$\Theta U(k,t)\Theta^{-1} = U(-k,-t), \tag{2.28}$$
$$\Theta H_\varepsilon^{eff}(k)\Theta^{-1} = H_\varepsilon^{eff}(-k) \tag{2.29}$$
$$\Theta V_\varepsilon^{eff}(k,t)\Theta^{-1} = V_\varepsilon^{eff}(-k,-t). \tag{2.30}$$

Lastly, the unitary operator of chiral symmetry satisfies

$$\Gamma U(k,t)\Gamma^{-1} = U(k,-t), \tag{2.31}$$
$$\Gamma H_\varepsilon^{eff}(k)\Gamma^{-1} = H_\varepsilon^{eff}(k) + \frac{2\pi}{T}\mathbb{1} \tag{2.32}$$
$$\Gamma V_\varepsilon^{eff}(k,t)\Gamma^{-1} = V_{-\varepsilon}^{eff}(k,-t)\mathrm{e}^{i2\pi t/T} \tag{2.33}$$

My main interest lies in photonics, which serves as an underlying platform to engineer these symmetries. I'll show you my result of how different symmetries can be engineered in an evanescently coupled waveguide network in 1D, and that can be generalized to higher dimensions.

2.3 Engineering symmetries in evanescently coupled optical waveguide array

Photonics provides a versatile platform to experimentally realize phenomena of quantum (solid-state) systems, where the photons (quantum) or electromagnetic waves (classical)

mimics the analogous properties of electrons, like the robust unidirectional motion of light and non-diffracting light propagation, which has promising applications (Bellec, Michel, et al. 2017; Zheng Wang et al. 2009).

In this section, we are interested in engineering topology in 1D waveguide arrays by exploiting the connection between lattice (crystalline) symmetry of waveguides, e.g., inversion symmetry, with the symmetries responsible for non-trivial topology e.g., particle-hole.

Crystalline symmetries play a vital role in constraining the energy spectrum and also on the topology. This symmetry is shared by Hamiltonian along with its spectrum. For example, graphene has rotational symmetry C_3 that it is shared by the position of Dirac points in BZ. If this symmetry is broken, for instance, by allowing anisotropic hoppings, then it is also broken in the BZ. Moreover, the Dirac points for some choice of anisotropic hoppings can even fuse together, and annihilate (Goerbig et al. 2008; Hasegawa et al. 2006; Montambaux et al. 2009a; Pereira et al. 2009; Wunsch et al. 2008; S.-L. Zhu et al. 2007).

Here, I shall show how some of these crystalline symmetries in photonics waveguide arrays are connected to fundamental symmetries like chiral symmetry, time-reversal symmetry, and particle-hole symmetry in 1D. To these crystalline symmetries another essential ingredient can be added it is the underlying bipartite structure of the lattice. These two together play a vital role in determining the significance of these fundamental symmetries. For example, what does it mean to have a particle-hole symmetry in a photonic waveguide array? As there are no particles or holes, but only electromagnetic waves propagating in a waveguide array lattice. Besides these three fundamental symmetries, there exists another symmetry responsible for giving rise to the non-trivial topology in 1D since non-trivial topology can not appear in the absence of any symmetry, in 1D.

In the present section, I shall show this connection for 1D waveguide arrays. Engineering, some of these symmetries like particle-hole and chiral, can give rise to a non-trivial topology in 1D. Moreover, to make things concrete, I shall also show how relaxing the constraints put forth by these symmetries can also lift them.

2.4 Symmetries in photonic waveguide array

In our case, we consider evanescently coupled optical waveguide arrays in 1D, where the refractive index is periodically modulated only along one of the direction, let us say x-axis. As we have seen at the end of chapter(1) that if the Hamiltonian is stationary, the coupling κ between the waveguides do not change along the propagation axis (z-axis), as shown in Fig. 2.3a. Likewise, in the case of driven Hamiltonian, couplings do change along the propagation axis. But we are interested in periodically driven systems, i.e., when the couplings are also periodic along the propagation axis, as shown in Fig. 2.3b. Here, the couplings $\kappa_{j=1,2}$ repeat after a period Z of the lattice.

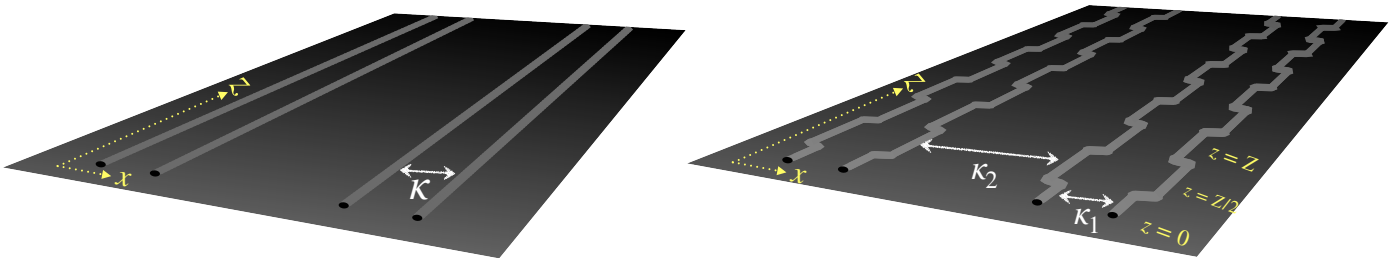

(a) (b)

Figure 2.3: 1D waveguide array when the couplings are (a) constant along z, an analogue of static Hamiltonian, (b) periodic along z, a analogue of periodically driven systems

In photonics, the relevant symmetries that may give rise to non-trivial topology are the time-reversal symmetry (TRS), which here referred to as z-reversal symmetry (z-RS)[4], chiral symmetry(CS) and particle-hole symmetry (PHS), where recall these symmetries at the level of time-dependent Bloch Hamiltonian $H(k,z)$,

$$\Gamma_z H(z)\Gamma_z^{-1} = -H(-z) \tag{2.34}$$
$$\theta_z H(k,z)\theta_z^{-1} = H^*(-k,-z) \tag{2.35}$$
$$\mathcal{C}H(k,z)\mathcal{C}^{-1} = -H^*(-k,z). \tag{2.36}$$
$$\tag{2.37}$$

Besides, we discuss two other symmetries of crystalline nature, which are not precisely additional symmetries but are of equal importance in waveguide array, namely bipartite symmetry (BPS) and z-reflection symmetry (z-Ref).

2.4.1 Lattice symmetries

Bipartite symmetry

A lattice is said to be BPS when the degrees of freedom (spin, orbitals, sublattices, or any combination of them) can be grouped into two uncoupled families. Let us say that these two families are A, and B then BPS can pictorially be shown as in Fig. (2.4) (Asbóth et al. 2016). The well-known examples are that of the two sublattices in SSH model (Su et al. 1980b) or two families in the Lieb lattice (Weeks et al. 2010a),

If P_A and P_B are orthogonal projectors corresponding to the two families, then BPS means that we can write H as,

$$H = P_A H P_B + P_B H P_A,$$
$$P_A H P_A = P_B H P_B = 0. \tag{2.38}$$

This guarantees the non-zero elements to be present only in the off-diagonal sector in the Hamiltonian if written in a A and B basis. It can be seen more clearly in writing the

[4]as Maxwell's equations are already TRS

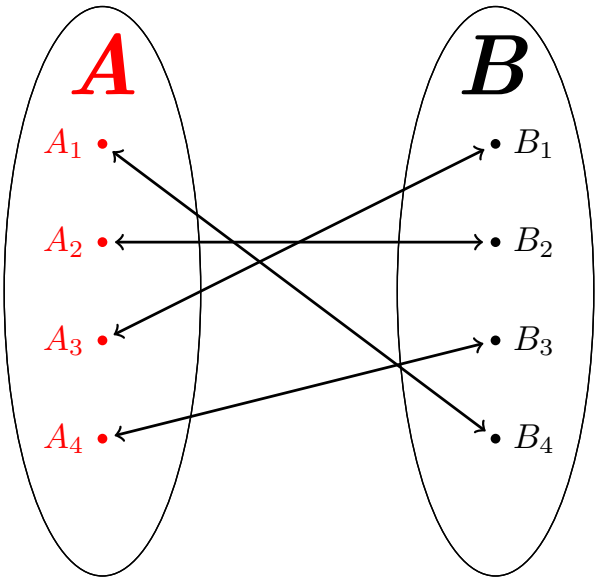

Figure 2.4: Bipartite structure of a lattice, where there is no coupling within the family only between the families

Hamiltonian in this sublattice basis (A and B), where there are n elements of A and m elements of B in a unitcell then

$$H = \begin{pmatrix} 0 & A_{n\times n} \\ B_{m\times m} & 0 \end{pmatrix}, \tag{2.39}$$

$$B_p H B_p^{-1} = -H \tag{2.40}$$

where B_p is BPS operator can be written as

$$B_p = \begin{pmatrix} \mathbb{1}_{n\times n} & 0 \\ 0 & -\mathbb{1}_{m\times m} \end{pmatrix}. \tag{2.41}$$

z-Reflection symmetry

The z-Ref is unitary symmetry denoted by $\mathcal{R}_z$, it holds as long as there exists a symmetry axis $z_0 : z \to -z$ of the lattice. This can be seen for the waveguide Fig. 2.3b by considering its unitcell, which fulfils above condition at $z = z_0 = Z/2$, as shown in Fig. 2.5.

$$\mathcal{R}_z H(z) \mathcal{R}_z^{-1} = H(-z) \tag{2.42}$$

If there exists a symmetric axis z_0 which is not origin, then this can be rewritten as,

$$\mathcal{R}_z H(z) \mathcal{R}_z^{-1} = H(z_0 - z) \tag{2.43}$$

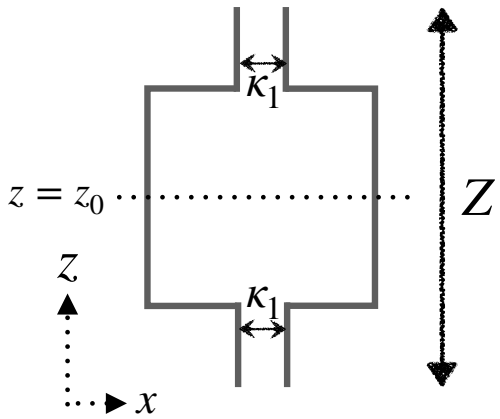

Figure 2.5: z-Ref space unitcell

2.4.2 Fundamental symmetries in photonics

Chiral symmetry

CS is a unitary operator Γ that anti-commutes with the stationary Hamiltonian H

$$\Gamma H \Gamma \equiv -H. \tag{2.44}$$

Such that $\Gamma = \Gamma^\dagger = \Gamma^{-1}$ and thus $\Gamma^2 = \mathbb{1}$[5].

The similar condition is also satisfied by the BPS operator B_p (see eq(2.40)), if the Hamiltonian is written in proper basis, i.e. A and B. Using the definition from eq(2.38), we can write

$$\Gamma = P_A - P_B \tag{2.45}$$

where the precise form for the Γ comes from eq.(2.41). This is an equivalent and sufficient definition of CS (Asbóth et al. 2016).
Let us take an example of Lieb lattice (Weeks et al. 2010a), as shown in Fig. 2.6. There is only hopping between the nearest neighbours, shown with thick black arrow. It has BPS, where two families are $A = \{a, c\}$ and $B = \{b\}$ (see Fig. 2.4). Then the Hamiltonian written in the proper basis $\{a, c, b\}$ comes out to be

$$H = \begin{pmatrix} 0 & 0 & \alpha \\ 0 & 0 & \beta \\ \alpha & \beta & 0 \end{pmatrix}. \tag{2.46}$$

Then the CS or BPS operator satisfying eq.(2.44),(2.40) in the same basis is

$$\Gamma = B_p = \begin{pmatrix} \mathbb{1}_{2\times 2} & 0 \\ 0 & -\mathbb{1}_{1\times 1} \end{pmatrix}. \tag{2.47}$$

[5]In general, any gauge dependence can be removed by redefinition. If $\Gamma^2 = e^{i\phi}$, then the $\Gamma \to e^{-i\phi/2}\Gamma$

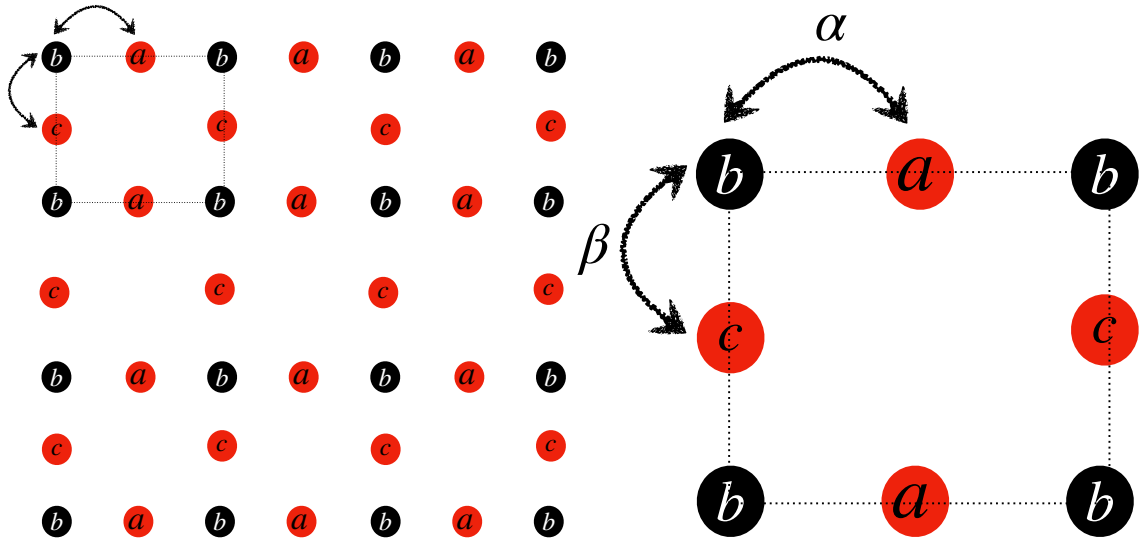

Figure 2.6: (a) Lieb lattice containing three types of atoms denoted by a, b and c, where hoppings are only among nearest neighbours, namely α, β, unitcell is emphasized by dotted square in (b)

Recently, in the same static regime, it was shown that to explain the full topology of chiral symmetric systems, e.g., the unitcell choice dependent topological zero modes in the SSH model(Asbóth et al. 2016) requires not only the description of bulk Hamiltonian but also the underlying real-space lattice (Guzmán et al. 2020). Since the 1D topological invariant Zak phase is a unitcell dependent quantity in SSH (i.e., not a gauge-invariant) and it is only meaningful to take its difference between the two phases, namely topological and trivial (or between the two unitcell choices).

The definition of CS changes in time-dependent case to

$$\Gamma_z H(z)\Gamma_z^{-1} = -H(-z) \tag{2.48}$$

where Γ_z is a chiral symmetry operator in time-dependent case.
Unlike in static cases, CS is non-local in time now. If we have translational symmetry in the system along with the periodic driven Hamiltonian then,

$$\Gamma_z H(k,z)\Gamma_z^{-1} = -H(k, Z-z), \tag{2.49}$$

which can be rewritten in terms of evolution operator as,

$$\Gamma_z U(k,z)\Gamma_z^{-1} \;\; = \;\; U(k,-z). \tag{2.50}$$

From eq(2.49), we see that there are unique points for which CS is local in time, for instance, when $z_0 = 0$ or $Z/2$.

At these points, CS can be defined locally, and these point(s) serves as a chiral symmetric point[6]. About these points, evolution is time-symmetric, e.g., $\Gamma_z U(k,0)\Gamma_z^{-1} = U(k,0)$.

[6]Not necessarily these points, but also by redefining origin *in some cases*, e.g., $H = H_0 + V\sin(\omega z)$, then $z_0 \to z_0 + \pi/2$

CS for the Floquet systems requires two essential ingredients. One is reminiscent of the static case, i.e., BPS, another one is z-Ref in the lattice. We can then decompose CS as the product of BPS and z-Ref.

$$B_p \mathcal{R}_z H(k,z) \mathcal{R}_z^{-1} B_p^{-1} = -H(k, z_0 - Z). \tag{2.51}$$

where $z_0 = Z$ for Chiral operator Γ_z.
Interestingly, CS can still hold if both of these symmetries are simultaneously broken. This shall motivate us to look for precise condition for CS to hold, e.g. on the structure of Hamiltonian. Since, in stationary case, the CS or BPS Hamiltonian is off-diagonal (see eq.(2.39)). Let us consider a Hamiltonian $H(z)$, which breaks both of the symmetries, namely z-Ref and BPS,

$$H(z) = \begin{pmatrix} V\sin(z) & J_1\cos(z) + J_2 e^{ik} \\ J_1\cos(z) + J_2 e^{-ik} & V\sin(z) \end{pmatrix}. \tag{2.52}$$

$H(z)$ breaks both BPS by the onsite potential and z-Ref (eq(2.42)) for the above choice of couplings, and the onsite potential, while still preserving the CS (where σ_x is the CS operator).

We can ask a general question, what are the constraints does CS put on H (we omit k label in H, since CS does not depend on it). These constraints are present irrespective of the case if both z-Ref and BPS are present, or both are absent together. To determine that, let us assume a periodically time-dependent Hamiltonian $H(z)$ with a period Z ($H(z+Z) = H(z)$) and with N (sublattice) degrees of freedom. This $H(z)$ has a CS operator Γ_z, then taking determinant on the eq.(2.49) gives,

$$\begin{aligned} \det(\Gamma_z)\det(H(z)) &= (-1)^N \det(H(Z-z))\det(\Gamma_z), \\ \det(H(z)) &= (-1)^N \det(H(Z-z)). \end{aligned}$$

This equation simplifies for two chiral symmetric point, namely $z_0 = 0, Z/2$ as

$$\det(H(Z/2)) = (-1)^N \det(H(Z/2)) \quad , \tag{2.53}$$

$$\det(H(0)) = (-1)^N \det(H(0)). \tag{2.54}$$

It shows that determinant puts a constraint on Hamiltonian for odd values of N, where it should vanish at $z = 0$ and $z = Z/2$.

Similarly, if we take the trace of eq(2.49), it yields

$$\mathrm{tr}(H(z)) = -\mathrm{tr}(H(Z-z)), \tag{2.55}$$

where,

$$\mathrm{tr}\, H(z) = \begin{cases} 0, & z = z_0 \\ \neq 0, & z \neq z_0 \end{cases}$$

For $z_0 = 0, Z/2$, irrespective of the value of N, the $\mathrm{tr}\, H(z)$ vanishes identically. This can mean, for instance, for the two atoms in a unitcell that either the onsite potential is zero

identically for each of them, or it is opposite. These two situations are actually our two cases where either both z-Ref and BPS are present or absent.
The above chiral constraints on Hamiltonian can be thought more general than to check if the two respective symmetries are present or not since they do not depend on those symmetries. It contradicts the point mentioned in the ref(Bellec, Michel, et al. 2017), where the authors said, as long as there exists a symmetry axis $z \to -z$ of the lattice with respect to some origin, the Floquet operator holds a chiral symmetry. Here, we have shown that reflection symmetry alone is not sufficient to induce CS, while z-Ref and BPS are. It can be summarised as,

- z-Ref and BPS $\Rightarrow$ CS
- CS $\not\Rightarrow$ z-Ref and BPS

z-Reversal symmetry

The z-RS is an anti-unitary operator denoted by Θ_z, which commutes with the (time-dependent) Bloch Hamiltonian $H(k,z)$. Here, we have $\Theta_z^2 = +1$. To look for a system with $\Theta_z^2 = -1$ would be interesting, as, for 2D, it gives rise to a remarkable quantum spin hall effect. However in photonics to achieve fermionic TRS is not apparent due to the underlying bosonic nature of photons, while using photon's polarization as a pseudospin can be achieved, and it was shown experimentally in stationary (Albert et al. 2015; Hafezi et al. 2011) and also in Floquet case using waveguide array (Maczewsky et al. 2018).
If $\Theta_z = \theta_z \mathcal{K}$, where $\mathcal{K}$ is conjugation, then in unitary form

$$\theta_z H(k,z)\theta_z^\dagger = H^*(-k,-z) \tag{2.56}$$

It is important to note that for photonics waveguide array, all the couplings are real, and only the complex dependence is in the Bloch phase[7] (Szameit and Stefan Nolte 2010). We can call this photonic Bloch Hamiltonian as H_p, it satisfies

$$H_p^*(-k) = H_p(k) \tag{2.57}$$

So, this yields for H_p and photonic evolution operator U_p a symmetry condition same as the z-Ref (see (2.42))

$$\theta_z H_p(k,z)\theta_z^\dagger = H_p(k, Z-z) \tag{2.58}$$
$$\theta_z U_p(k,z)\theta_z^\dagger = U_p^*(-k,-z). \tag{2.59}$$

We can infer from CS case that here also exists a z_0 point, about which evolution is symmetric. eq.(2.58) is precisely the z-Ref equation(2.42). In the photonic version of Hamiltonian, the z-RS acts as unitary instead of anti-unitary, due to the underlying real nature of real space Hamiltonian (i.e. $H(x)$), this shows the close connection of z-RS in photonics with z-Ref symmetry, which we exploit in next section.

[7] In general, complex couplings can appear in an effective Hamiltonian form. Besides, at most, there can be extra phases, coming from synthetic gauge fields (Wimmer, Hannah M Price, et al. 2017), they can be considered at the same level as Bloch quasimomentum k. Thus, this k can be though of as a generalized quasimomenta.

Particle-hole symmetry

Particle-Hole Symmetry, $C = \mathcal{C}\mathcal{K}$, refers to an anti-unitary operator which anti-commutes with Hamiltonian, we have $C^2 = +1$. At the level of z-dependent and Bloch Hamiltonian and photonic Bloch Hamiltonian, it satisfies

$$\begin{aligned} \mathcal{C}H(k,z)\mathcal{C}^{-1} &= -H^*(-k,z), \\ \mathcal{C}H_p(k,z)\mathcal{C}^{-1} &= -H_p(k,z) \end{aligned} \tag{2.60}$$

In general, $\mathcal{C}$ can depend on the origin, say k_0, let us represent the Hamiltonian with this dependence as H_p^s. For instance, 1D SSH model with three atoms in a unitcell with non-zero couplings between each of the atoms,

$$\begin{aligned} \mathcal{C}H(k+k_0,z)\mathcal{C}^{-1} &= -H^*(-k+k_0,z), \\ \mathcal{C}H_p^s(k+k_0,z)\mathcal{C}^{-1} &= -H_p^{s*}(-k+k_0,z) \end{aligned} \tag{2.61}$$

Let us call the origin dependent PHS to be the *shifted*-PHS (or s-PHS).
Similarly, here, PHS acts as a unitary symmetry on photonic Hamiltonian (H_p). Importantly eq(2.60) is identical to the eq(2.44), meaning that if there is a BPS, then we can define the PHS operator from eq.(2.41). Surprisingly, this does not hold for s-PHS, which only exists when there is no bipartite symmetry. In other words, PHS and s-PHS are mutually exclusive and s-PHS is always non-bipartite but not vice-versa.
Constraints on PHS from eq(2.60) for photonic Hamiltonians at any value of z are

$$\begin{aligned} \det(\mathcal{C})\det(H_p) &= (-1)^N \det(H_p)\det(\mathcal{C}), \\ \det(H_p) &= (-1)^N \det(H_p) \end{aligned} \tag{2.62}$$

It shows that determinant puts a constraint on Hamiltonian for odd values of N similar to Γ_z, however, irrespective of the value of z since time is irrelevant for BPS to hold.

However, the trace is identically zero.

$$\begin{aligned} \mathrm{tr}(\mathcal{C}H_p\mathcal{C}^{-1}) &= -\mathrm{tr}(H_p), \\ \mathrm{tr}(H_p) &= 0 \end{aligned} \tag{2.63}$$

Trace can only be zero if there is no onsite term in the H_p. Yet, for any value of N, it is possible to choose onsite terms such that there sum vanishes. Nevertheless, this condition alone is not sufficient; one needs to take into account the determinant condition as well. We have not considered the case for H_p^s since the form of the Hamiltonian is not the same on either side of the eq.(2.61). All the different symmetries acting on time-dependent Hamiltonians, evolution operators, and photonic Hamiltonians, along with the constraint they put on the spectrum, are tabulated in Tab(2.1). We can ask if there is more than one symmetry in the system then what kind of symmetries are compatible with each other. For instance, s-PHS and PHS can not be present together. Fig. 2.7 shows the compatibility between different types of symmetries.

Symmetries	***H(k,z)***	***U(k,z)***	H_p***(k,z)***	***Constraint on eigenvalues***
BPS	$-H(k,z)$	$U^{-1}(k,z)$	$-H_p(k,z)$	$\{\mathcal{E}(k)$, -$\mathcal{E}(k)\}$
z-Ref	$H(k,-z)$	$U^{-1}(k,-z)$	$H_p(k,-z)$	No constraints
CS	$-H(k,-z)$	$U(k,-z)$	$-H_p(k,-z)$	$\{\mathcal{E}(k)$, -$\mathcal{E}(k)\}$
z-RS	$H^*(-k,-z)$	$U^*(-k,-z)$	$H_p(k,-z)$	$\{\mathcal{E}(k)$, $\mathcal{E}(-k)\}$
PHS	$-H^*(-k,z)$	$U^*(-k,z)$	$-H_p(k,z)$	$\{\mathcal{E}(k)$, - $\mathcal{E}(-k)\}$
s-PHS	$-H^*(-k+k_0,z)$	$U^*(-k+k_0,Z)$	$-H_p(k-k_0,z)$	$\{\mathcal{E}(k+k_0)$, - $\mathcal{E}(-k+k_0)\}$

Table 2.1: Different symmetries are acting on time-dependent Hamiltonian, evolution operator, and photonic Hamiltonian with their constraints on eigenvalues.

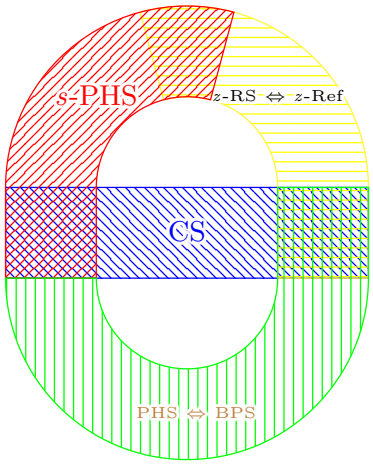

Figure 2.7: Symmetries compatibility relation in Photonic lattices

2.4.3 Engineering symmetries in photonic waveguide arrays and boundary modes

In this section, we consider examples in 1D waveguide (WG) array from each region of the graph shown in Fig. 2.7, with symmetry operations shown in Table(2.1). To investigate which symmetries can give rise to non-trivial edge states in 1D finite waveguide array.

Chiral Symmetry

In 1D photonic WG array Fig. 2.8, there are two cases with CS for a periodically driven Hamiltonian, namely if both are present BPS and z-Ref or are absent.
To engineer a waveguide array with CS, either we can implement both the lattice symmetries, namely BPS and z-Ref, or, the product of symmetries PHS and z-RS (i.e., PHS and TRS), as shown for 2WGs network with a period Z in Fig. 2.8a. For this case photonic Hamiltonian for two steps (0), looks like

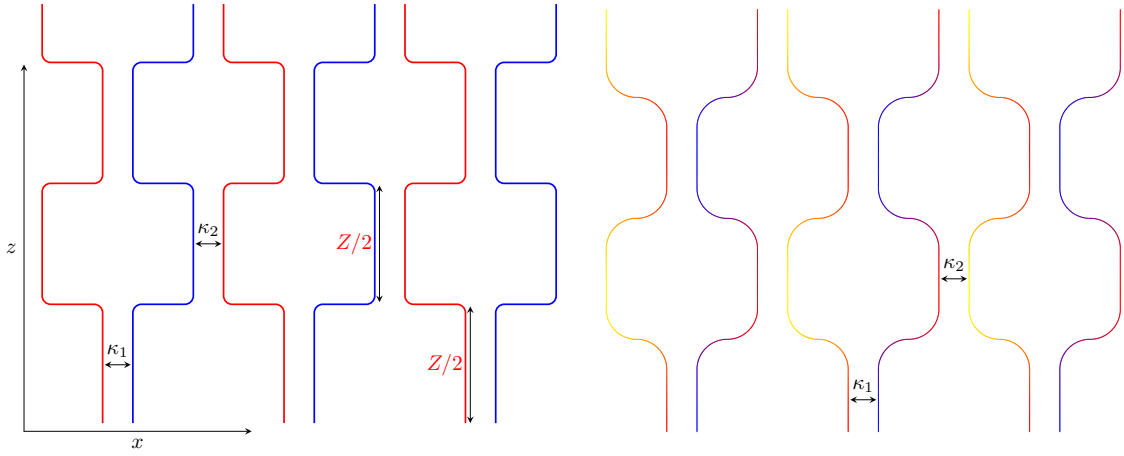

(a) (b)

Figure 2.8: 1D waveguide arrays with 2 WG in a unitcell with a period Z (a) with zero-onsite potential is BPS and z-Ref (b) with non-zero time varying potential shown as a varying color along $z-$axis breaks BPS and z-Ref

$$H_p^{(1)}(k) = \begin{pmatrix} 0 & \kappa_1 \\ \kappa_1 & 0 \end{pmatrix} \quad 0 \le z < Z/2 \tag{2.64}$$

$$H_p^{(2)}(k) = \begin{pmatrix} 0 & \kappa_2 e^{ik} \\ \kappa_2 e^{-ik} & 0 \end{pmatrix} \quad Z/2 \le z < Z \tag{2.65}$$

Differently, breaking both BPS and z-Ref also achieves this condition, while respecting the constraints on the Hamiltonian eq(2.54),(2.55). BPS breaks in the presence of an onsite potential term V(z) since it allows coupling within the same family, which otherwise is forbidden. Besides, modifying this onsite potential V(z) in such a way that it breaks reflection condition $V(z+z_0) = V(-z+z_0)$, this also breaks the z-Ref symmetry, as shown in Fig. 2.8b. In waveguide arrays this potential can be attained by periodically modulating the refractive index along z-axis, e.g. $n_0 \sin(z)$ (Ke et al. 2016). Likewise, the photonic Hamiltonian

$$H(z) = \begin{pmatrix} V\sin(z) & \kappa_1 h[Z/2-z] + \kappa_2 h[z-Z/2]\mathrm{e}^{ik} \\ \kappa_1 h[Z/2-z] + \kappa_2 h[z-Z/2]\mathrm{e}^{-ik} & V\sin(z) \end{pmatrix} \tag{2.66}$$

where $h[Z/2-z]$ is a Heaviside step function, $h[x] = 0, x < 0$ or $= 1, x \ge 0$.

In 1D Floquet system with CS, we can expect non-trivial topology, which manifest with the presence of boundary modes in a finite system (Asbóth et al. 2014; Bellec, Michel, et al. 2017; Fruchart 2016; Roy and Harper 2017), for the Hamiltonian in eq(2.64). We consider a finite geometry with 20 unitcells along the x-axis in Fig. 2.8a. For the numerical convenience this geometry is coupled at both the boundaries with another finite network but with a different choice of couplings parameters $\kappa_{j=1,2}$, forming a cylindrical geometry[8], as

[8]This choice of geometry allows us to get rid of additional edge states.

shown in Fig. 2.9a. By choosing the coupling parameters in one region $\kappa_1 < \kappa_2$ (shown in red in Fig. 2.9a) and in another $(\kappa_1' =)\kappa_1 > \kappa_2 = (\kappa_2')$ (shown in blue). Then the edge states appear at the interface between these two regions, where the energy gap closes, namely at quasienergy 0 and π. The results are shown in Fig. 2.9b. In the presence of BPS and z-Ref, on changing the interface coupling parameter, τ, the states at the interface remain robust. However, breaking the CS with the onsite potential enforces the edge states to couple to the bands, as shown in Fig. 2.9c.

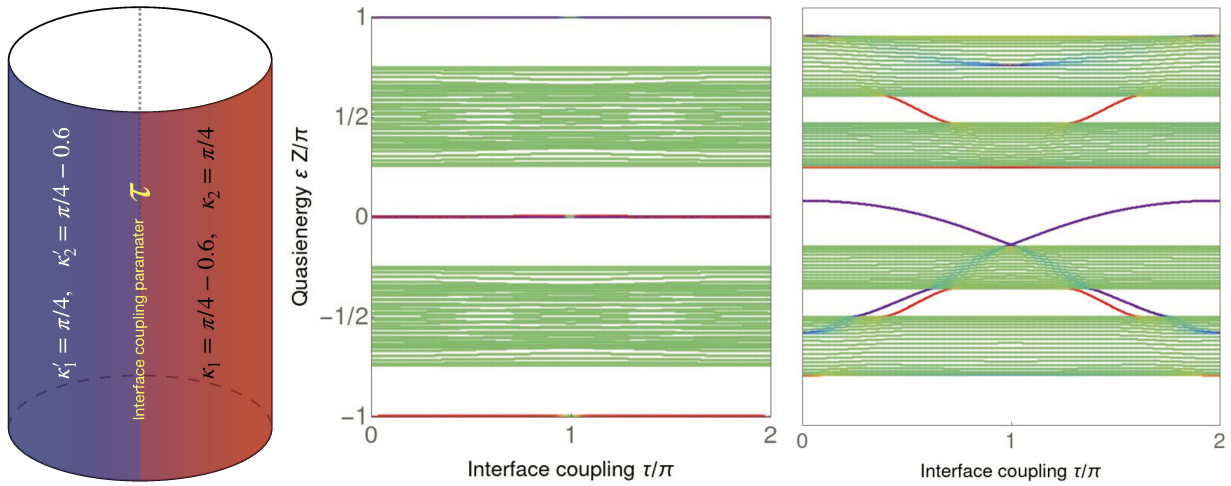

(a) (b) (c)

Figure 2.9: Presence of edge states at quasienergy 0 and π (a) for cylindrical geometry, (b) when the interface parameter τ is changed, the states remain robust in presence of BPS and z-Ref, and (c) they are coupled to the bands when CS is broken with BPS and z-Ref.

Particle-hole symmetry

In a 1D photonic waveguide array, PHS can be realized by implementing a bipartite structure. Previously, the 2WGs network was satisfying BPS (see Fig. 2.8a for Hamiltonian eq.(2.64)). Nevertheless, let us take examples beyond 2WG but with BPS. For instance, the 3WGs array, shown in Fig. 2.10a. It contains couplings between the waveguide as

$$H(z) = \begin{cases} 1^{\text{st}}\text{(in green) and } 2^{\text{nd}}\text{(in red) denoted by} \rightarrow \theta_{12} & 0 \leq z < Z/3 \\ 2^{\text{nd}}\text{and } 3^{\text{rd}}\text{(in black)} \rightarrow \theta_{23} & Z/3 \leq z < 2Z/3 \\ 2^{\text{nd}}\text{(in green) and } 1^{\text{st}}\text{(in green)} \rightarrow \theta_{21} & 2Z/3 \leq z < Z \end{cases}$$

where first two are within the unitcells and last one is outside the unitcell and when the third waveguide is out of the plane it is dashed black. However, there is no coupling between 3^{rd} and 1^{st} to maintain BPS. This model can be thought of a 1D version of Lieb lattice (Weeks et al. 2010b).

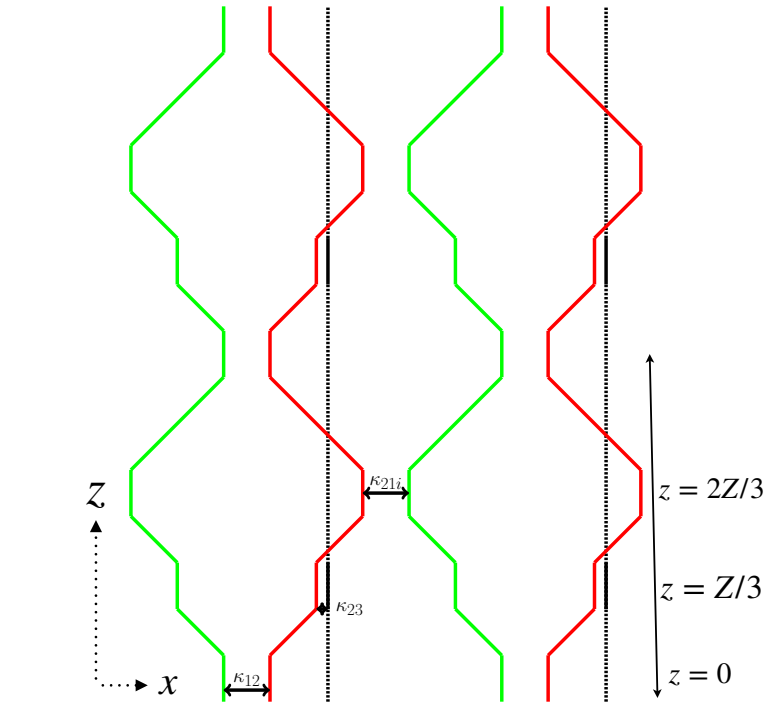

(a)

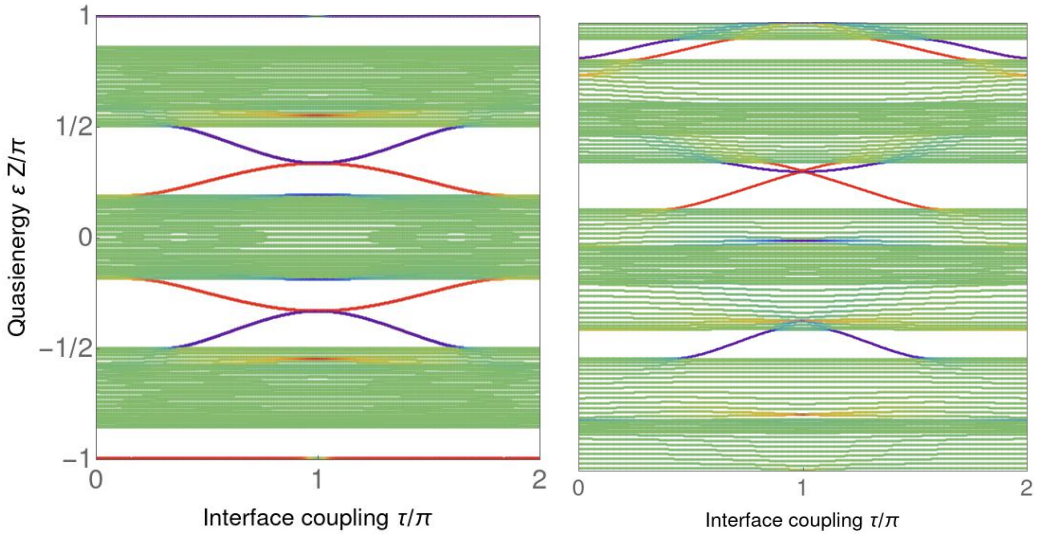

(b) (c)

Figure 2.10: (a) 3 WGs PHS network with bipartite structure, considering its finite version (a) edge states are robust at $\varepsilon = \pi$ under a change in interface coupling parameter, whereas (b) breaking of bipartiteness destroys the topological states.

Similarly, in 1D with particle-hole symmetry, we can expect non-trivial topology. It is confirmed by considering the same geometry, where non-trivial states appear at the interface, as shown in Fig. 2.10b. Moreover, the number of bands being odd, the only place where non-trivial states appear are necessarily at quasienergy π since there is a band at quasienergy 0, thus forbidding any gap. Consequently, PHS does not protect other edge states at any

quasienergy. This comes from the fact that other quasienergies are not respected under PHS, $\varepsilon(k) \to -\varepsilon(k)$, only 0 and π are invariant under this.

Breaking PHS would require to break the constraints derived in eq(2.62)-(2.63). One way to do so is to repeat what we did for CS, i.e., to introduce some constant onsite potential. This indeed destroys the edge states at $\varepsilon = \pi$, as confirmed in Fig. 2.10c, where we introduce the constant onsite potential on each of the WGs at only initial time $0 \leq z < Z/3$. Moreover, there is another way to break PHS would be to break BPS by introducing specific couplings in the model, e.g., restoring the coupling between the 3^{rd} and 1^{st} waveguide.

shifted **Particle-hole symmetry**

This symmetry is only present when PHS is absent. To do so, we introduce a coupling between the 3^{rd} and the 1^{st} waveguide, which respects the constraint and, at the same time, beaks BPS or PHS. This can be achieved as shown in Fig. 2.11, with the couplings between the waveguides

$$H(z) = \begin{cases} 1^{\text{st}}(\text{in black}) \text{ and } 2^{\text{nd}}(\text{in blue}) \to \theta_{12} & 0 \leq z < Z/3 \\ 2^{\text{nd}}\text{and } 3^{\text{rd}}(\text{in green }) \to \theta_{23} & Z/3 \leq z < 2Z/3 \\ 3^{\text{rd}} \text{ and } 1^{\text{st}} \to \theta_{31} & 2Z/3 \leq z < Z \end{cases}$$

This choice breaks all the symmetries CS, PHS and z-RS, as per our interpretation from last section with the lattice symmetries.

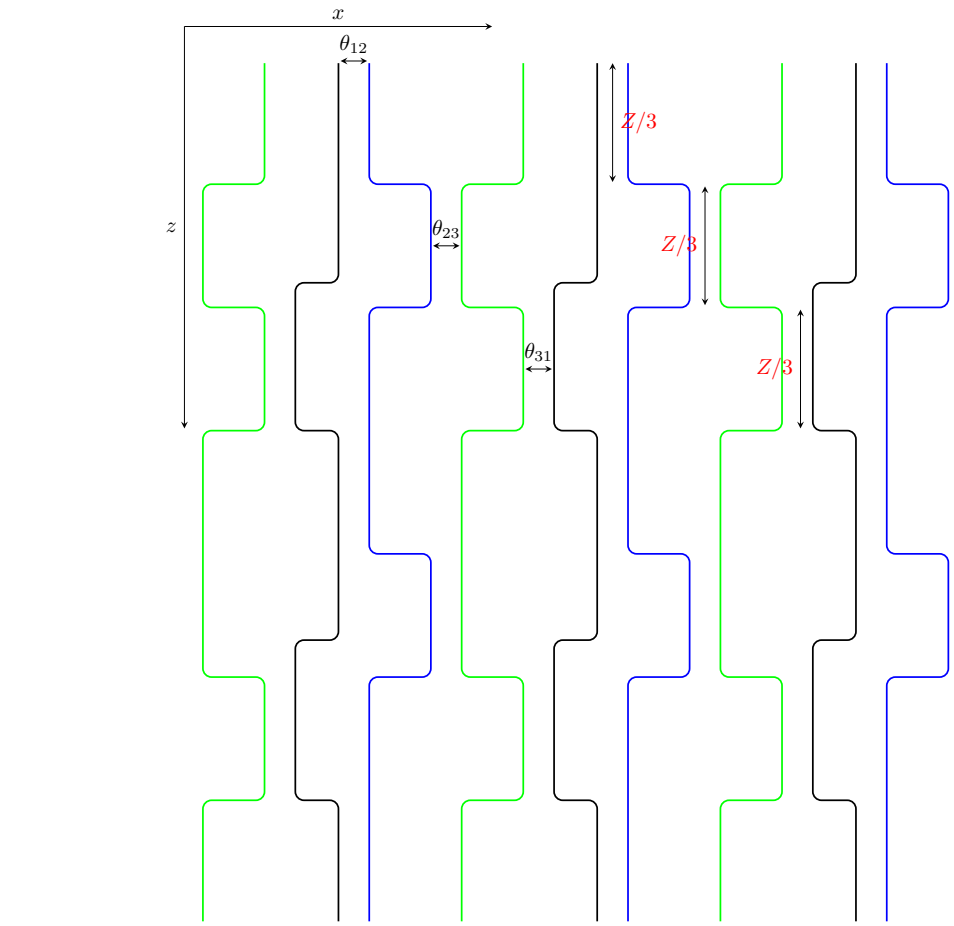

(a)

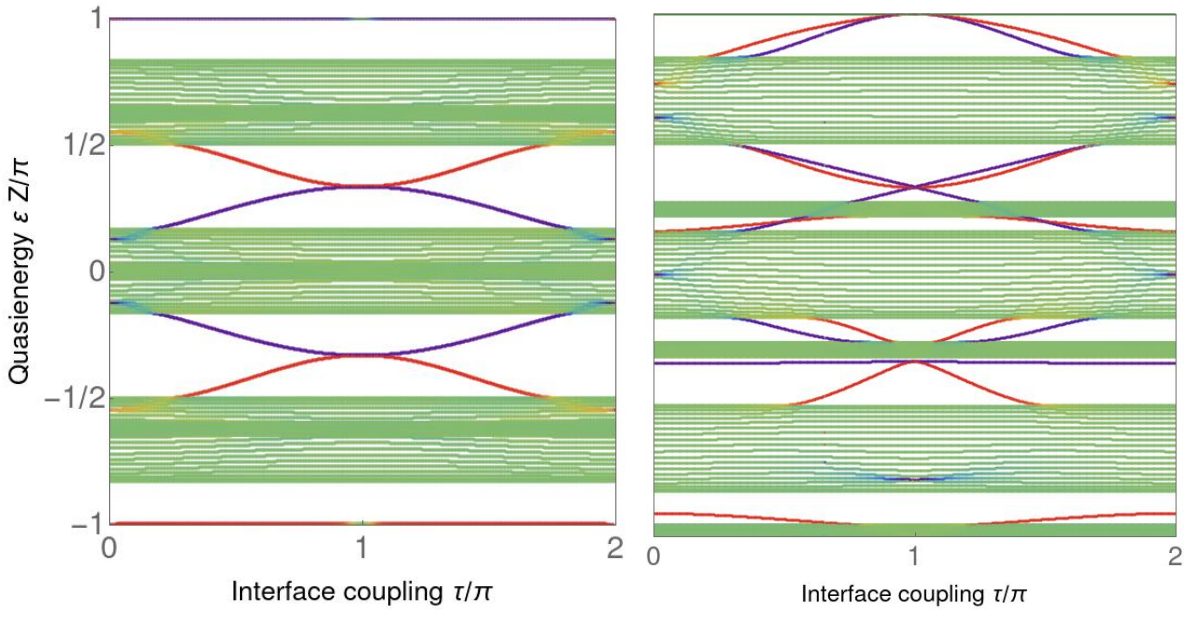

(b) (c)

Figure 2.11: (a) 3 WGs s-PHS network, with edge state spectrum (b) appearance of edge states in presence of s-PHS (b) breaking of s-PHS

However, in 1D without such symmetries, we do not expect any non-trivial topology to appear (Roy and Harper 2017). Surprisingly, the robust edge states are present (2.10b) at quasienergy π, like before. The existence of these topological edge states in 1D tells us that there is indeed some symmetry responsible for their protection. This symmetry is what we call shifted particle-hole symmetry. There are two reasons to use this terminology. First, when the spectrum is shifted by $k \to k + k_0$, it has the particle-hole symmetric spectrum $\{\varepsilon(k), -\varepsilon(-k)\}$. Second, there exists an antiunitary operator that anti-commutes with the Hamiltonian.

Likewise, using these two reasons of its connection with PHS, we can follow the same strategy to introduce a constant onsite potential on each of the waveguides at initial time $0 \leq z < Z/3$ breaks s-PHS, and this leads to the disappearance of π state, as expected in 1D in the absence of any of these symmetries.

z-reversal symmetry

If the waveguide array respects z-Ref symmetry, then it also respects z-reversal symmetry. To consider a network with only this symmetry would be to go again beyond 2WGs, as it already has CS and PHS. So, the next possibility is to look for three waveguides in a unitcell, as shown in Fig. 2.12a, where there is a coupling between the waveguides

$$H(z) = \begin{cases} 1^{\text{st}}(\text{red}) \text{ and } 2^{\text{nd}}(\text{green}) \to \theta_{12} \;\; \text{also } 2^{nd} \text{ and } 3^{rd}(\text{blue}) \to \theta_{23} & 0 \leq z < Z/2 \\ 3^{\text{rd}} \text{ and } 1^{\text{st}} \to \theta_{31} & Z/2 \leq z < Z \end{cases}$$

the last coupling is outside the unitcell.

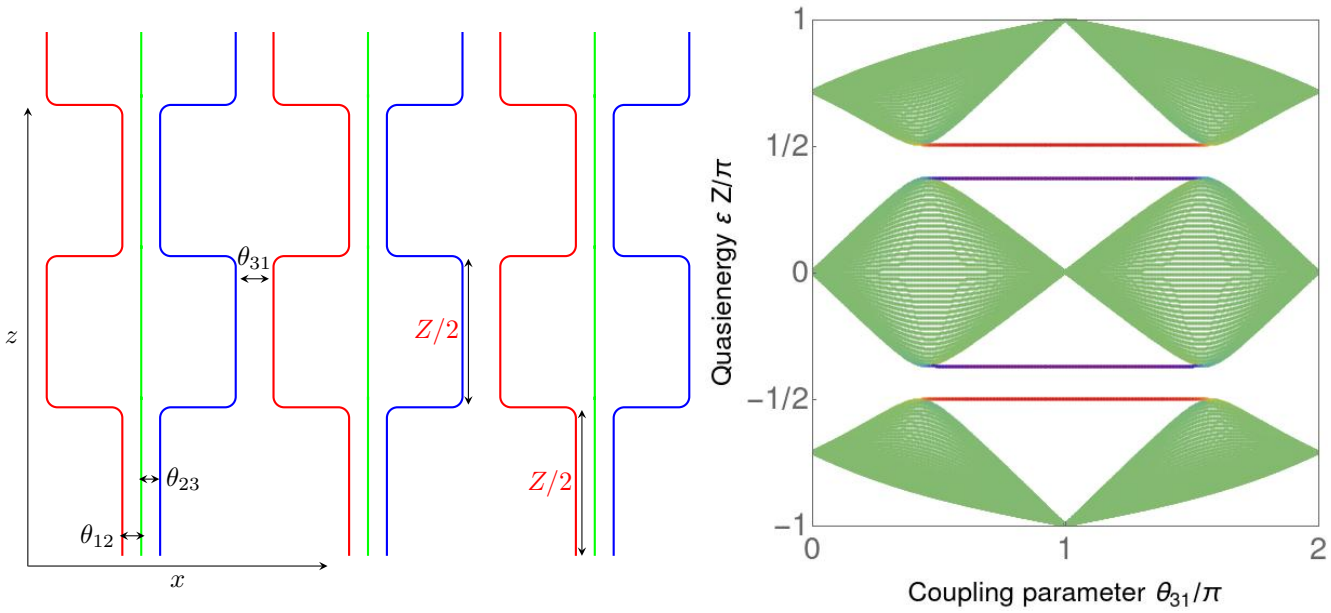

(a) (b)

Figure 2.12: (a) 3 WGs with z-RS network, with edge state spectrum (b) absence of edge states

Far from surprising, there is no nontrivial topology solely coming from z-RS in 1D. Considering a finite geometry confirms this assertion, where we consider a network with 40 unitcells but sharing the boundaries with vacuum, unlike previously[9]. In this case, we fix the values of coupling parameter θ_{12} and θ_{23} and varying the θ_{31} parameter. We see that for any choice of coupling parameters, the system only posses trivial edge states that only depends on how the network terminates, as shown in the fig 2.12a.

Inversion symmetry

For the sake of completion, we discuss ***inversion symmetry***, which is not responsible for any non-trivial topology. However, it is unusual in the presence of another symmetry, e.g. time-reversal symmetry, which can give rise to the non-trivial topology in 2D, as it simplifies the calculation of topological invariant (Fu et al. 2007). However, we consider it in its parent form that is without any other symmetry. Then at the level of Hamiltonian $H(x,z)$ or Bloch Hamiltonian, $H(k,z)$, it follows

$$\begin{aligned} \mathcal{P}H(x,z)\mathcal{P}^{-1} &= H(-x,z), \qquad \text{or} \\ \mathcal{P}H(k,z)\mathcal{P}^{-1} &= H(-k,z) \end{aligned} \tag{2.67}$$

where $\mathcal{P}$ is an inversion symmetry operator. This symmetry can be implemented in a 2WGs network where we have two different successive intra coupling separated in time and followed by an intercoupling, as shown in fig 2.13. The respective couplings are between the

[9]Due to absence of two different topological regime, namely trivial and topological, we cannot use previous geometry.

waveguides are

$$H(z) = \begin{cases} 1^{\text{st}}(\text{in black}) \text{ and } 2^{\text{nd}}(\text{in blue}) \rightarrow \theta_{12} & 0 \leq z < Z/3 \\ 1^{\text{nd}}\text{and } 2^{\text{rd}}(\text{in green}) \rightarrow \theta_{121} & Z/3 \leq z < 2Z/3 \\ 2^{\text{rd}} \text{ and } 1^{\text{st}} \rightarrow \theta_{21} & 2Z/3 \leq z < Z \end{cases}$$

where the only the last coupling connects two unitcell.

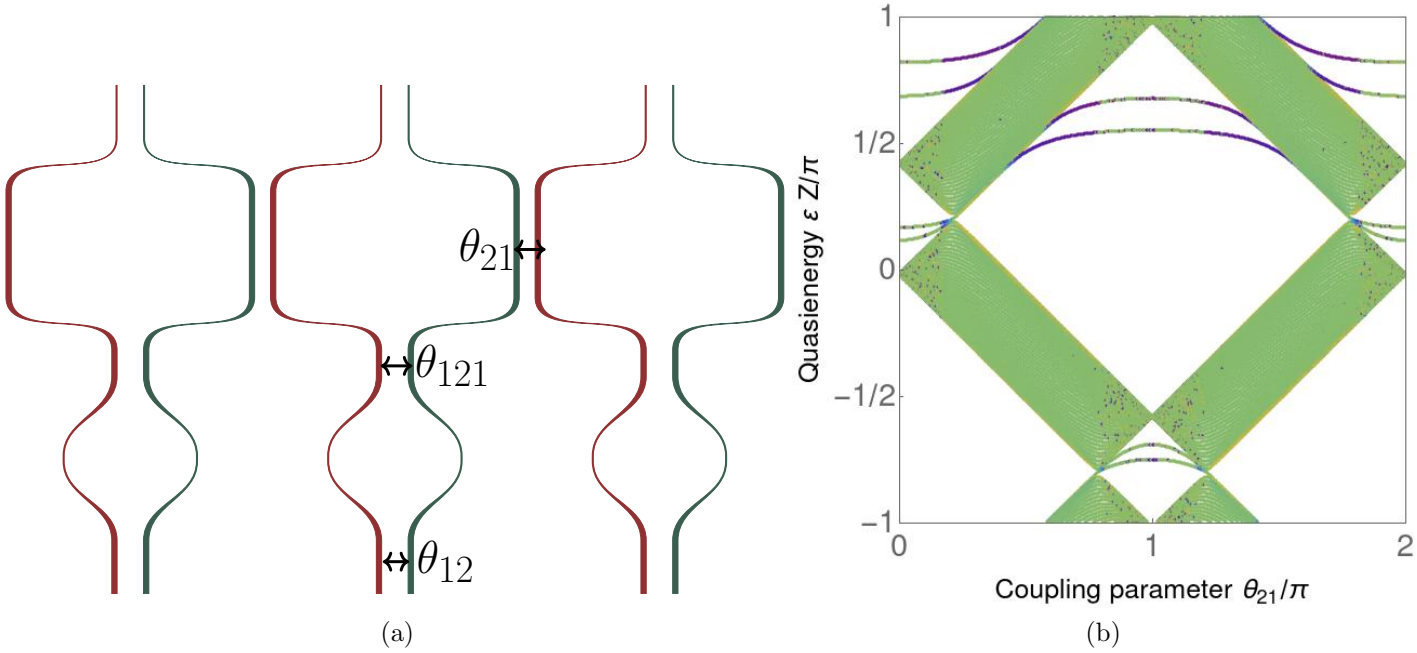

(a) (b)

Figure 2.13: (a) 2Wg with Inversion Symmetry network, with edge state spectrum (b) absence of edge states

The choice of two successive different intra couplings breaks z-RS. However, the network is still bipartite, so to break PHS, we added constant but same onsite potential on both the waveguides. On considering a similar finite geometry of 40 unitcells with boundaries with the vacuum. As expected by fixing the values of coupling parameter θ_{12} and θ_{121} and varying the θ_{21} parameter, the edge state spectrum only has trivial edge states.

2.5 Summary of chapter 3

We saw a connection between the symmetries responsible for non-trivial topology and the lattice symmetries. Moreover, we also saw how engineering particular symmetries induces topology to the 1D photonic waveguide array, e.g., CS, PHS, s-PHS, but z-RS alone can not. We discussed how PHS is responsible for bipartiteness or BPS in the photonic system. How CS can be viewed in two ways, the first composition of BS and z-symmetric lattice, second, without BS and z-symmetric, which is achieved by an odd function of z at onsite term. z-RS can be thought as a consequence of the presence of a symmetry axis $z \rightarrow -z$ of the lattice

with respect to some origin, i.e., z-Ref. Only non-trivial topology comes when there are two other symmetries along with z-RS, colored region Fig. (2.7). At last, we saw the consequences of inversion symmetry in 1D to be trivial on topology, similar to z-RS. In future, we can think of how complex couplings can be introduced, where our some of the interpretations will break. Moreover, how symmetries fermionic symmetries can be implemented $C^2 = -1$ or $\Theta^2 = -1$. The later symmetry has recently been implemented in the waveguide setup in the Szamiet's group (Maczewsky et al. 2018). To the best of my knowledge, $C^2 = -1$ is still missing.

Chapter 3

Beyond Floquet insulators 1: Winding regime

3.1 Introduction

After the discovery of the quantum Hall effect in 1980, the most perplexing question was how can electrons delocalize at the phase transition between quantum Hall plateaus in 2D in the presence of a disordered potential since this was not in compliance with the Anderson theory of localization (Anderson 1958). Later, this mystery was resolved in the semi-classical picture where electrons of some fixed energy or at an equipotential can percolate through the disorder. The external strong magnetic field directs the direction of the electron wavepackets inside each equipotential—thus allowing electrons to delocalize instead of undergoing strong localization. Chalker, Coddington, and Ho (Chalker et al. 1988; C.-M. Ho et al. 1996) proposed the first solution in this direction, where they proposed an oriented scattering network model for electron wave propagation on a random network, as sketched in Fig. 3.1. In this scattering matrix network, the orientation refers to a specific direction of flow. For instance, here, this preferential direction is a consequence of breaking time-reversal symmetry due to the external magnetic field. Also, it can be a directed flow of electrons in a lattice in the presence of an electric field, where electrons only follow the direction of electric field.

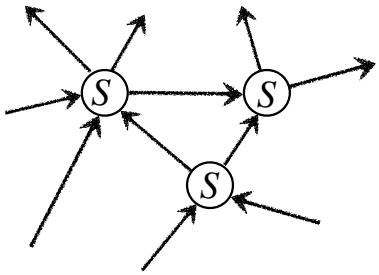

Figure 3.1: Sketch of a scattering network, where at each scattering node S the number of incoming arrows are the same as the number of outgoing ones. Thus, preserving unitarity of S.

In 2013, G. Q. Liang, Y. D. Chong, and M. Pasek (Liang et al. 2013; Pasek et al. 2014)

proposed a similar scattering model to study the propagation of light inside the coupled-resonator optical waveguides (CROW) model. In this model, the unitary scattering matrix represents the coupling between resonators, which stores the local information of transmission and reflection between the resonators, thus allowing this formalism to address problems beyond the Hamiltonian formalism or tight-binding models. A similar framework was also used in the array of acoustic networks (Khanikaev, Fleury, et al. 2015), showing the versatility of the network and experimental feasibility. The system considered in this framework thought of as an oriented scattering network. The arrows or links connecting the scattering matrices have specific orientation for the flows that are from incoming states to outgoing ones.

Interestingly, every continuously time-dependent Hamiltonian can be decomposed into discrete-time Hamiltonians eq(2.3). These, in turn, can be replaced by successive time-ordered scattering matrices—thus allowing to formulate this problem in terms of similar formalism where this order is maintained. However, we restrict ourselves to the periodically driven system, where such scattering matrices ordering repeats after one period. For instance, this appears in the quantum domain, where photons perform periodic discrete-time quantum walks (Kitagawa, Matthew A Broome, et al. 2012). The Floquet operator here after one period T can be decomposed for N total walks into time-ordered stepwise scattering events ($U_F(T) = S_N \cdots S_1$, $S_j = \mathrm{e}^{iH_jT/N}$). This situation can also appear in the classical domain, where light propagates inside the waveguides networks, the amplitudes of scattering matrices encode the couplings between the waveguides. Even though in these cases there is no explicit time, but can still host topological edge modes(Delplace 2019; Delplace, Fruchart, et al. 2017; Kitagawa, Oka, et al. 2011; Kitagawa, M. S. Rudner, et al. 2010; Clément Tauber et al. 2015).

Beyond theory, discrete-time dynamics have been implemented in different experimental platforms, ranging from the quantum regime in photonic quantum walks (Kitagawa, Matthew A Broome, et al. 2012) to the classical regime in the circular fibers (Regensburger, Bersch, Hinrichs, et al. 2011), waveguide arrays (Rechtsman et al. 2013) and electromagnetic metamaterials (Khanikaev, Hossein Mousavi, et al. 2013) and in microwaves in coaxial cables (Hu et al. 2015a), to cite a few.

This chapter is organized as follows. After giving a brief introduction to the oriented scattering network model, I shall propose four different models in 2D, namely I, II, III, and IV that differ by their symmetries. These symmetries dictate the topological properties in each model, where all of these models are only realizable in the Floquet regime.

3.2 Scattering network models

As we saw in chapter (1.7) that different photonic setups can serve as platforms to observe phenomena predicted in solid-state systems. On the contrary, there are specific topological properties that are not realizable in the solid-state systems, like topological properties of non-Hermitian physics, but these scattering network models allow us to explore them. Interestingly, all different photonic platforms in of sec(1.3) can be formulated in one common framework, of the scattering network model, where scattering amplitudes encode the information of coupling among the elements of the network, e.g., among the waveguides in waveguide arrays. The scattering network model, where scattering amplitudes encode

the information of coupling among the elements of the network, e.g., among the waveguides in waveguide arrays. To introduce our scattering network model, let us consider a one-dimensional spatial lattice of periodic discrete-time evolutions represented by oriented scattering networks, as sketched in Fig. 3.2. In this network, an initial state of a system is described by the superposition over amplitudes of incoming arrows (or oriented links). The number of these incoming arrows encodes the *degrees of freedom* in the system, e.g., the different polarization states (horizontal or vertical) of the photon in photonic quantum walk(Kitagawa, Matthew A Broome, et al. 2012) or the number of waveguides in a unitcell in a lattice. two oriented links, one going to the right (shown in red) with amplitude $\beta_{\text{time}}^{\text{position}}$ and another to the left (shown in blue) $\alpha_{\text{time}}^{\text{position}}$. Then the state evolves in discrete time from top to bottom followed by a unitary scattering process at each time step j denoted by scattering matrix S_j. From here, the respective amplitudes are scattered towards the next links depending on their orientation of left (blue arrow) or right (red arrow).

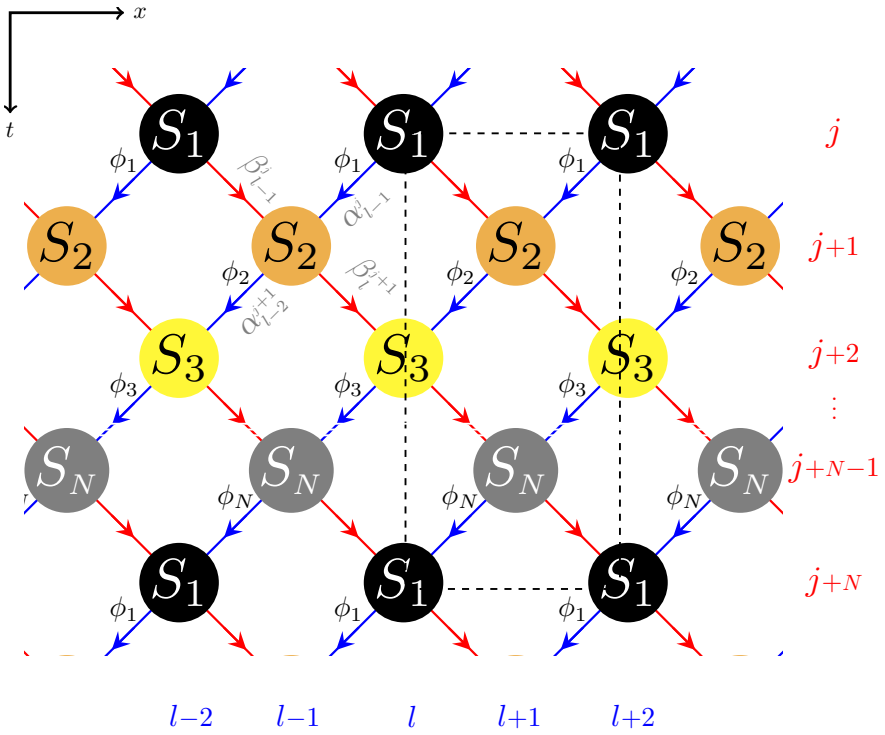

Figure 3.2: Two-dimensional oriented scattering lattice where the y axis plays the role of time and x axis of position. A time period consists of N successive steps represented by N 2×2 scattering matrices S_j. A phase ϕ_j is added for the states scattered out of the node j and propagating leftwards (shown with blue arrows). A dashed black rectangle emphasizes the unit cell of this lattice.

In addition to these scattering processes, we introduce a *phase shift* ϕ_j carried by the states along each link (Wimmer, Mohammed-Ali Miri, et al. 2015; Wimmer, Hannah M Price, et al. 2017; Wimmer, Regensburger, et al. 2013), see Fig. 3.2. We only consider a non-zero phase shift ϕ_j for the leftward going states (as depicted in Fig. 3.2). The critical point is that we allow the value of this phase to vary with time j.

Then, the evolution of incoming amplitudes from time step j to $j+1$ connected through

the scattering matrix S_j can be projected into a pair of equations of the form

$$\begin{aligned}\alpha_l^{j+1} &= (\cos\theta_j \alpha_{l+1}^j + i\sin\theta_j \beta_{l+1}^j)\mathrm{e}^{i\phi_j} \\ \beta_l^{j+1} &= (i\sin\theta_j \alpha_{l-1}^j + \cos\theta_j \beta_{l-1}^j)\,.\end{aligned} \tag{3.1}$$

Assuming the particular form for the scattering nodes (or matrix) as

$$S_j = \begin{pmatrix} \cos\theta_j & i\sin\theta_j \\ i\sin\theta_j & \cos\theta_j \end{pmatrix}. \tag{3.2}$$

In general case, we can associate a phase to each of the oriented links as ϕ_j^{left} and ϕ_j^{right}. Then employing a gauge transformation of

$$\tilde{\alpha}_l^j \to \mathrm{e}^{-i\frac{n^2}{2}\phi}\mathrm{e}^{-i\frac{j}{2}\phi}\alpha_l^j, \tag{3.3}$$

we can transfer the phase from both the links to only one of the links, e.g. to the left link (shown in blue in Fig. 3.2). Similarly, the phase ϕ could also vary along position l (Regensburger, Bersch, Mohammad-Ali Miri, et al. 2012), which again using proper gauge transformation,

$$\tilde{\alpha}_l^j \to \mathrm{e}^{i\frac{jn}{2}\phi}\mathrm{e}^{-i\frac{j^2}{4}\phi}\mathrm{e}^{i\frac{j}{4}\phi}\alpha_l^j, \tag{3.4}$$

can lead to only time dependence (Regensburger, Bersch, Mohammad-Ali Miri, et al. 2012).

One period of evolution corresponds to the time-ordered product of N such scattering events $(S_N \cdots S_1)$ acting on the initial state, as emphasized by a unitcell with dashed black in Fig. 3.2. Here, this time ordered product of the scattering matrices after one period is the *Floquet operator*. The scattering matrices retain the time periodicity as $S_{j+N} = S_j$. This network can thus model a 1D Floquet quantum walk. The topological properties concerning such Floquet operators of these scattering networks have been studied recently in 2D (Delplace 2019; Hu et al. 2015b; Liang et al. 2013; Pasek et al. 2014) and also in 3D (H. Wang et al. 2016).

Assuming the discrete translational invariance along x axis, a Bloch-Floquet operator U_F reads as

$$U_F(k_x, \{\phi_j\}) = B_{\mathrm{mod}(N,2)}(k_x) S_N D(\phi_N) .... B_1(k_x) S_1 D(\phi_1), \tag{3.5}$$

$$B_1(k_x) = \begin{pmatrix} 1 & 0 \\ 0 & \mathrm{e}^{-ik_x} \end{pmatrix}, \quad B_0(k_x) = \begin{pmatrix} \mathrm{e}^{ik_x} & 0 \\ 0 & 1 \end{pmatrix}, \quad D(\phi_j) = \begin{pmatrix} \mathrm{e}^{i\phi_j} & 0 \\ 0 & 1 \end{pmatrix} \tag{3.6}$$

Here, we assume a pattern for the phase shifts of the form $\phi_j = Q_j\phi$ that preserves the periodicity of the network, where Q_j is some rational number that will be specified later. This ϕ gives us a second-time scale with respect to one drive period N in the network. Hence, it may look like that the network is not any more periodic in time. However, we consider the case where variation in ϕ is so small in comparison to the Floquet period N, that, the long time stroboscopic dynamics can be described by the adiabatically modulated Floquet operator when continuously varying the phase parameter $\phi \in [0, 2\pi]$. Then, the Floquet operator $U_F(k_x, \phi, \{\theta_j\})$ depends on the quasimomentum along the x direction, k_x, the "synthetic quasimomentum" ϕ and the set of parameters $\{\theta_j\}$, where j runs from 1 to N.

The former k_x and ϕ lie at the same footings, thus they constitute a 2D synthetic Brillouin Zone (BZ), whereas θ_j (i.e., coupling parameters) predicts the topological regime. Note that the Floquet operator depends periodically on its parameters. Moreover, by considering some of the coupling parameters as other synthetic dimensions could provide an interesting framework to investigate topology in higher dimensions (e.g., >2).

The synthetic dimension ϕ in the context of photonics comes from two reasons. First, either by the phase shift of the light beam due to some extra path length that is being our case, implemented in circular fibers (Regensburger, Bersch, Hinrichs, et al. 2011; Wimmer, Mohammed-Ali Miri, et al. 2015; Wimmer, Hannah M Price, et al. 2017; Wimmer, Regensburger, et al. 2013), and resonator network model (Hafezi et al. 2011). Secondly, by considering different modes of the resonator (Ozawa, Hannah M. Price, Goldman, et al. 2016)or, the waveguide (Lustig et al. 2019) as a synthetic dimension. Furthermore, it can also come through quasiperiodicity, where 1D quasicrystal can possess properties of 2D periodic crystal (Kraus, Lahini, et al. 2012; Kraus, Ringel, et al. 2013; Kraus and Zilberberg 2012; Verbin, Zilberberg, Kraus, et al. 2013; Verbin, Zilberberg, Lahini, et al. 2015). This case will be similar to our, where mapping to a 2D crystal involves one of the dimension to behave as an adiabatic parameter. Thus, tuning this parameter in the topological regime can make the system behave like a topological pump (Thouless 1983), which has been observed in the photonics domain (Kraus, Lahini, et al. 2012; Kraus, Ringel, et al. 2013; Kraus and Zilberberg 2012; Tangpanitanon et al. 2016; Zilberberg et al. 2018) and in cold atoms (M. Lohse et al. 2016; Michael Lohse et al. 2018; Nakajima et al. 2016).

Model I: Wimmer, Hannah M Price, et al. 2017.

Let us consider the above scattering network (Fig. 3.2) in the simple case where $N = 2$ steps with $\phi_1 = +\phi, \phi_2 = -\phi$. In addition to that, it gives two parameters to tune with, namely $\{\theta_1, \theta_2\}$. Note that the net phase inside the unitcell is zero. Now, by diagonalizing the Floquet operator eq(3.5), we get two quasienergy bands $\varepsilon_\pm(k_x, \phi)$. As shown in Fig. 3.3a, the quasienergy spectrum ε is fully gapless for the critical value of parameters $\theta_{j=1,2} = \pi/4$.

This network generalizes previous models whose topological properties have been investigated experimentally in photonics setups. For instance, when $N = 2$ and in the absence of a phase shift ($\phi = 0$), the model describes 1D photonic quantum walk (Kitagawa, Matthew A Broome, et al. 2012) and 1D laser-written photonic waveguide arrays in silica (Bellec, Michel, et al. 2017), in which boundary modes have been observed. For non-vanishing ϕ but still $N = 2$, with $\phi_1 = +\phi, \phi_2 = -\phi$ together with the fixed coupling parameters $\theta_{j=1,2} = \pi/4$, it describes pair of coupled optical fiber loops in which the Berry curvature was measured using wavepacket dynamics (Wimmer, Hannah M Price, et al. 2017). We take a step ahead of (Wimmer, Hannah M Price, et al. 2017), where we allow the couplings to change from (a critical) value $\theta_{j=1,2} = \pi/4$ to arbitrary values, this gaps the spectrum at $\varepsilon = 0, \pi$, as shown in Fig. 3.3b.

In this model, the symmetry(s) prevailing can be determined by the Floquet operator [eq(3.5)].

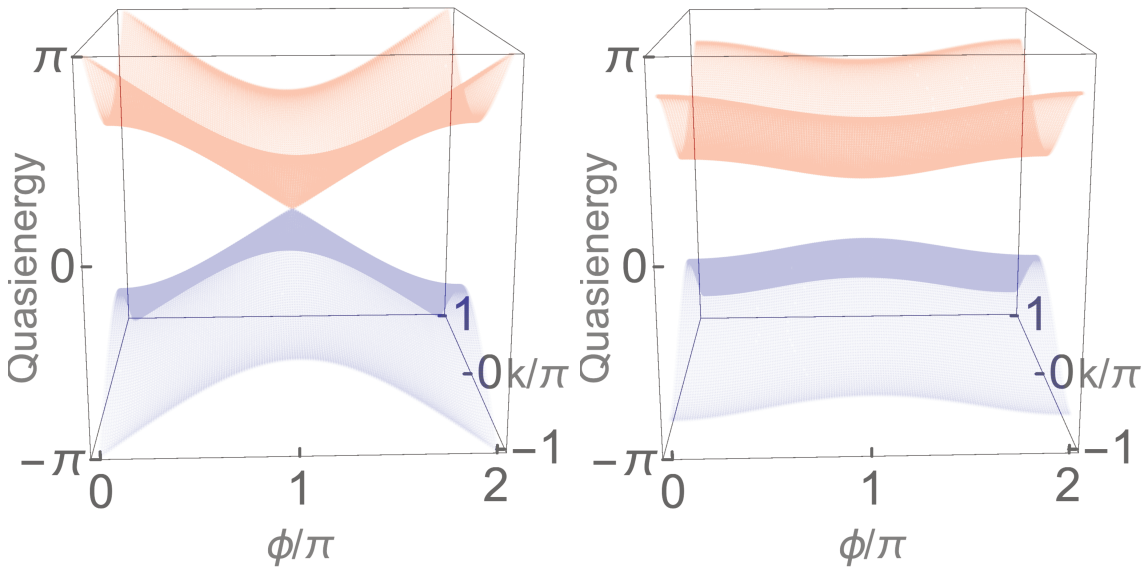

(a) $\theta_{j=1,2} = \pi/4$ (b) $\theta_1 \neq \theta_2$

Figure 3.3: Bulk bands for $\phi \equiv \phi_1 = -\phi_2$ (a) touching for $\theta_{j=1,2} = \pi/4$ at quasienergy $\varepsilon = 0$ and π (b) gap opening for $\theta_1 \neq \theta_2$ at $\varepsilon = 0$ and π

$$
\begin{aligned}
U_F(k_x,\phi) &= B_0(k_x)S_2D(-\phi)B_1(k_x)S_1D(+\phi), && (3.7)\\
&= B(k_x/2)S_2\tilde{D}^\dagger(\phi/2)B(k_x/2)S_1\tilde{D}(\phi/2), && (3.8)\\
B(k_x/2) &= \begin{pmatrix} e^{ik_x/2} & 0 \\ 0 & e^{-ik_x/2} \end{pmatrix}, \quad \tilde{D}(\phi/2) = \begin{pmatrix} e^{i\phi/2} & 0 \\ 0 & e^{-i\phi/2} \end{pmatrix}. && (3.9)
\end{aligned}
$$

The Floquet operator eq(3.8) is symmetric under inversion operator $\mathcal{P}$

$$
\begin{aligned}
\mathcal{P}U_F(k_x,\phi)\mathcal{P}^{-1} &= U_F(-k_x,-\phi) && (3.10)\\
\sigma_x U_F(k_x,\phi)\sigma_x &= B^\dagger(k_x/2)S_2\tilde{D}(\phi/2)B^\dagger(k_x/2)S_1\tilde{D}^\dagger(\phi/2),\\
&= U_F(-k_x,-\phi) && (3.11)
\end{aligned}
$$

where σ_x is the standard Pauli matrix.
It is also symmetric under particle hole operator $C = \mathcal{C}K$

$$
\begin{aligned}
\mathcal{C}U_F(k_x,\phi)\mathcal{C}^{-1} &= U_F^*(-k_x,-\phi) && (3.12)\\
\sigma_y U_F(k_x,\phi)\sigma_y &= B^\dagger(k_x/2)S_2^\dagger\tilde{D}(\phi/2)B^\dagger(k_x/2)S_1^\dagger\tilde{D}^\dagger(\phi/2),\\
&= U_F^*(-k_x,-\phi). && (3.13)
\end{aligned}
$$

where σ_y is the standard Pauli matrix.

It turns out that in the present case for each gapped phase, one can find specific values of the coupling parameters θ_1 and θ_2, such that the Floquet evolution operator satisfies another

symmetry, namely phase rotation (Delplace, Fruchart, et al. 2017), $\mathcal{L}U_F\mathcal{L}^{-1} = \mathrm{e}^{i\pi}U_F$ with

$$\mathcal{L} = \begin{pmatrix} 1 & 0 \\ 0 & \mathrm{e}^{i\pi} \end{pmatrix}. \tag{3.14}$$

It follows from this symmetry that the Chern number C_j

$$C_j = \frac{1}{2\pi}\int_{BZ} \mathrm{d}k_x \mathrm{d}\phi \left(\frac{\partial}{\partial\phi}\langle\psi_j|i\partial_{k_x}|\psi_j\rangle - \frac{\partial}{\partial k_x}\langle\psi_j|i\partial_\phi|\psi_j \right) \tag{3.15}$$

for each band necessarily vanishes (Delplace, Fruchart, et al. 2017), where ψ_j are quasi eigenstates, and therefore, the only two distinct topological regimes one can generate with $N = 2$ are either trivial or anomalous. This is confirmed in topological phase diagram for the above model, as a function of $\theta_{j=1,2}$ in Fig. 3.4.

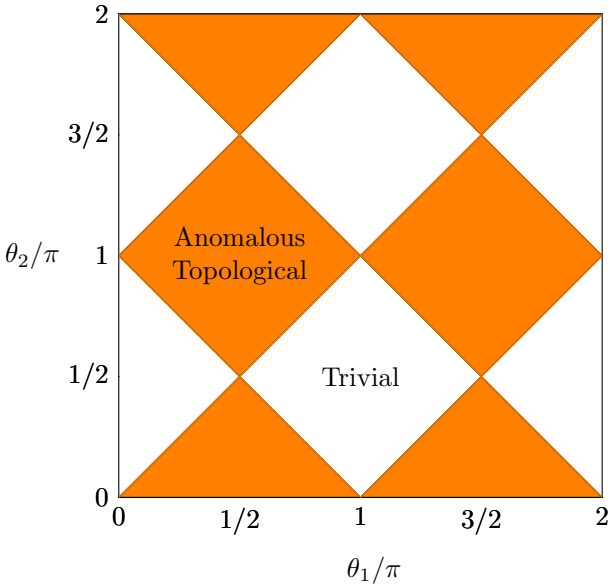

Figure 3.4: Topological phase diagram showing the presence of anomalous topological regime (color orange) and trivial regime (color white) as a function of coupling parameters. The boundaries between the two colors corresponds to the closing of the spectral gap of quasienergy at $\varepsilon = 0, \pi$.

In 2D with particle-hole symmetry, one expects to have a non-trivial topology. To investigate it, we determine the edge states spectrum, by considering a similar finite geometry along the x-direction, as discussed previously. It leads to two boundaries (one at the left and another at the right), to which we numerically couple another topological regime, making it periodic along x together with ϕ, therefore forming a torus like geometry, as sketched in Fig. 3.5a. If x runs from 0 to L, then $0 \leq x \leq L/2$ is chosen in one regime (i.e., one choice of coupling parameters) and another in $L/2 \leq x \leq L$, with $L = 100$ or 50 unitcells in each region. Then the edge states appear at these two interfaces at $x = 0$ and $L/2$, respectively. In general, the coupling parameters differ in each region, denoted by $\theta'_{j=1,2}$ in blue region, and $\theta_{j=1,2}$ in red region (see Fig. 3.5a). However, if both regions are chosen to be the same

(i.e., same coupling parameters $\theta'_{j=1,2} = \theta_{j=1,2}$), then there are no topological edge states, as confirmed in Fig. 3.5b. Then on tuning coupling parameters, they reach a critical point at $\theta_{j=1,2} = \pi/4$ in each region, leading to band touching at each of the quasienergies $\varepsilon = 0, \pi$. However, changing parameters in one of the regions to $\theta_1 = \pi/4, \theta_2 = \pi/4 - 0.6$ and another $\theta_1 = \pi/4 - 0.6, \theta_2 = \pi/4$ gives rise to topological chiral edge states in each of the quasienergy gap $\varepsilon = 0, \pi$, although the Chern number in each band vanishes. This regime is known as *Floquet topological anomalous insulator*.

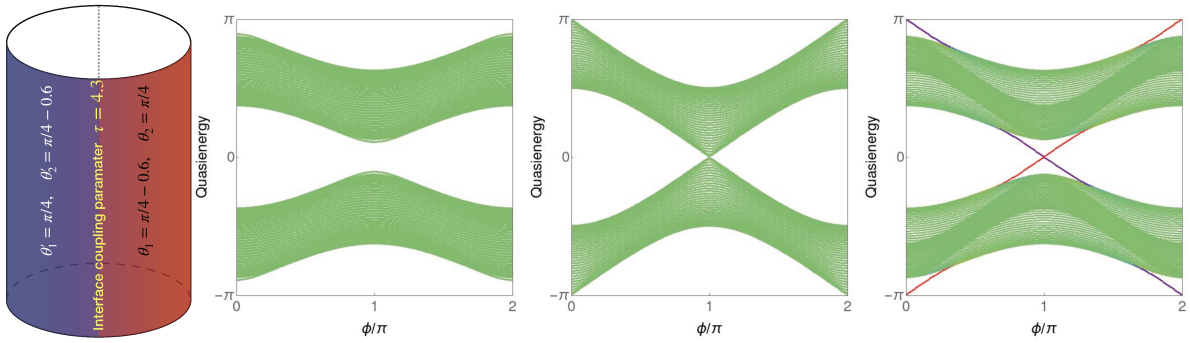

(a) (b) (c) (d)

Figure 3.5: Calculated bands for a cylinder geometry (a), when both the regimes ($\theta'_{j=1,2} = \theta_{j=1,2}$) (b) are $\theta_1 = \pi/4 - 0.6, \theta_2 = \pi/4$, which gives trivial insulating regime, (b) the bands touch at the critical point for $\theta'_{j=1,2} = \theta_{j=1,2} = \pi/4$ in each region and under go to (c) anomalous Floquet topological insulating regime when one is $\theta'_1 = \pi/4, \theta'_2 = \pi/4 - 0.6$ and another $\theta_1 = \pi/4 - 0.6, \theta_2 = \pi/4$.

There are only two regimes in this model, either trivial or anomalous. This is clearly confirmed in the edge state spectrum (see Fig 3.5) and more completely in the topological phase spectrum in Fig 3.4. However, allowing more steps (> 2) can give rise to other regimes, e.g., a Floquet Chern insulator, as shown in Fig. 3.6, where phase rotation symmetry is broken.

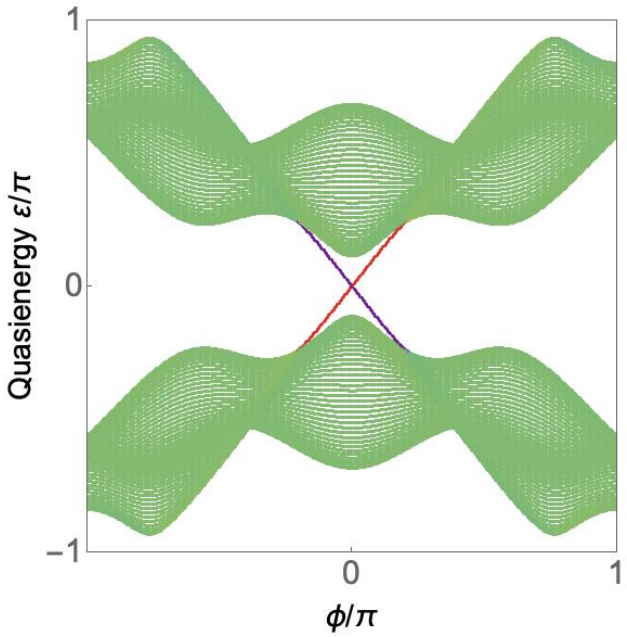

Figure 3.6: Floquet Chern insulator for $N = 4$ time steps, for $\phi_1 = +2\phi$, $\phi_2 = -\phi$, $\phi_1 = 0$, and $\phi_1 = +\phi$.

3.3 Beyond Floquet Topological *insulators*

One way to go beyond the usual topological insulators is to continuously deform the bands in such a way that it would tilt them, and the gap becomes incomplete while the bands still do not touch. It was proposed in the Lieb lattice model (Palumbo et al. 2015), in the superconductors (Ying et al. 2018, 2019) and Floquet system(L. Zhou et al. 2016). In that case, gaps can still host chiral edge states that, in this case, would coexist with bulk states at the same energy but with different quasimomenta. This gives rise to a *topological metal*.

More recently, it was proposed that threading a net flux Φ through a superconductor in a cylindrical geometry can break inversion symmetry and lead to such a "metallic regime" (Ying et al. 2018), as sketched in Fig 3.7b. A similar idea was proposed in periodically driven cold atoms by breaking inversion symmetry with onsite potential, which leads to topological phase transition taking place between gapless regimes (L. Zhou et al. 2016). Besides, it was seen that even in the quantum spin Hall effect, there is a contribution of bulk conductance to the helical edge states, hence prohibiting exact quantized edge conductance (Knez et al. 2011). It was shown to be connected to the metallic behavior of bulk states along with the edge states (C.-Z. Chen et al. 2019).

Now, we extend the above idea to the scattering matrix network. Previously, we considered the case of net phase in the unitcell to be zero, $\phi_1 + \phi_2 = 0$. This condition helps us to keep intact the inversion symmetry in the model I (see eq(3.10)). We distinguish two ways to break inversion symmetry in this scattering framework. In one case, we break it by keeping a net non zero phase inside the unitcell, namely model II. In other words, we break inversion symmetry along the synthetic dimension by allowing higher asymmetric hoppings in this dimension in time. In another case, we break inversion symmetry along the real or

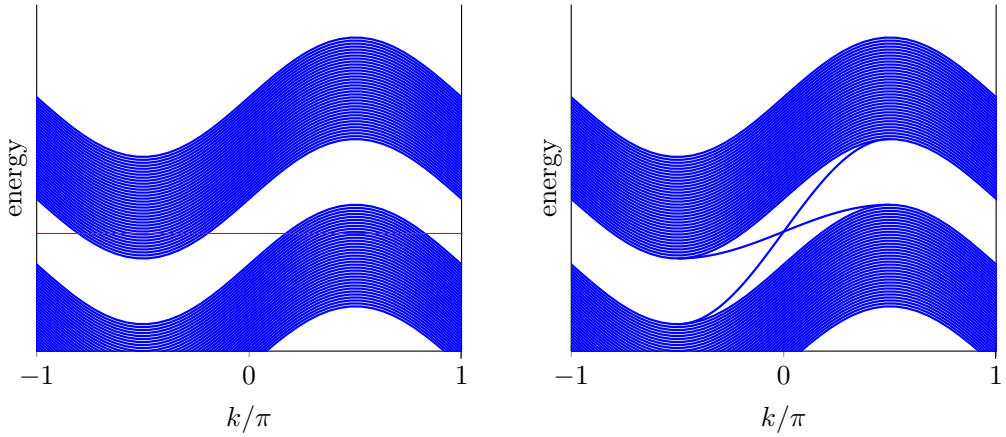

(a) $\Phi = 3.0$ (b) $\Phi = 1.5$

Figure 3.7: Topological transition on changing the flux Φ through the unitcell (a) trivial metal and (b) topological metal, from Ref(Ying et al. 2018)

spatial dimension (i.e., x), namely model III. These two different ways of breaking inversion symmetry give rise to two different types of topological metallic regimes with specific physical manifestations. In one case, it gives rise to Bloch oscillations of wavepackets, and in the other case, it gives rise to a transverse quantized drift of wavepacket motion. This clearly distinguishes inversion symmetry breaking in synthetic and real dimensions. At the end we club these two aspects in a single model, namely model IV, to explore complex wavepackets motion.

3.3.1 Model II: Inversion symmetry breaking in synthetic dimension and Bloch oscillations

Let us introduce our first model of breaking inversion symmetry in the synthetic dimension by allowing a net phase in the unitcell.

We consider only two steps $N = 2$ but with $\phi_1 = +\phi$ and $\phi_2 = -2\phi$, as sketched in Fig 3.8. This existence of a net phase in the unit cell, (i.e. $\phi_1 + \phi_2 \neq 0$, with ϕ_1 and ϕ_2 proportional to ϕ) breaks this symmetry. This can be shown from eq(3.8), where now

$$U_F(k_x, \phi) = \mathrm{e}^{i(\phi_1+\phi_2)/2} B(k_x/2)\, S_2\, \tilde{D}(\phi_2/2)\, B(k_x/2)\, S_1\, \tilde{D}(\phi_1/2) \tag{3.16}$$

Next we notice that $\sigma_x B(k_x/2)\sigma_x = B(-k_x/2)$ and $\sigma_x \tilde{D}(\phi_j/2)\sigma_x = \tilde{D}(-\phi_j/2)$ where we recall that ϕ_j is proportional to ϕ. Therefore, the net phase, in the phase factor in Eq. (3.16) prevents U_F to be inversion symmetric that is

$$\sigma_x U_F(k_x, \phi)\sigma_x \neq U_F(-k_x, -\phi)\ . \tag{3.17}$$

Remarkably, the consequence of this symmetry breaking can be seen on the quasienergy spectrum ε, where bands wind in ϕ axis, as illustrated in Fig. 3.3a. This net flux of $-\phi$ is

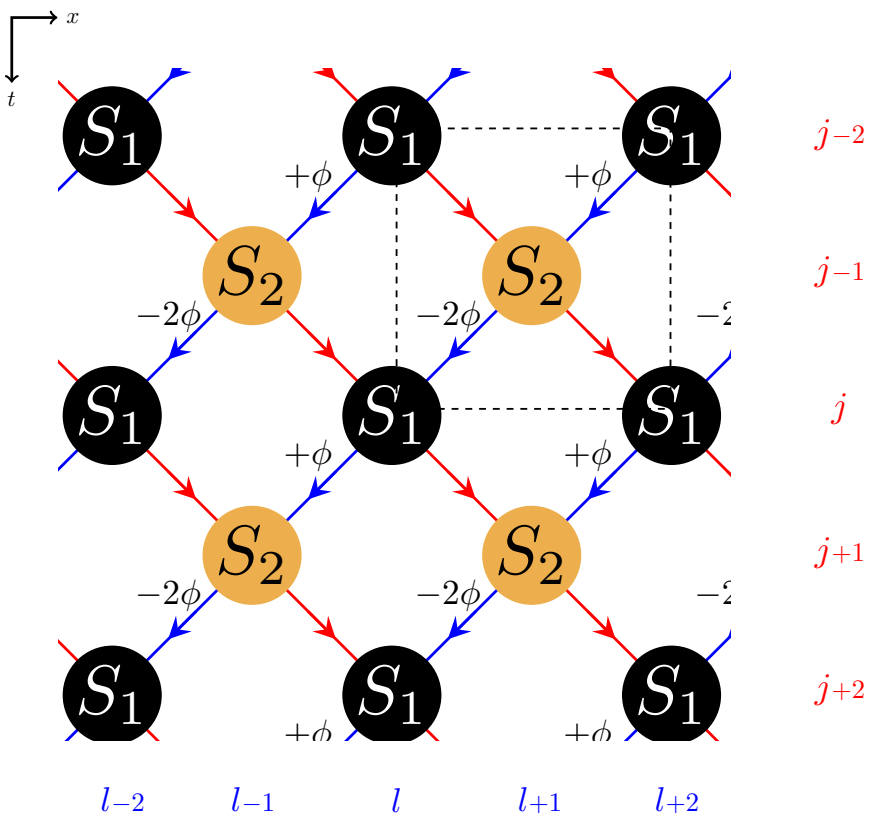

Figure 3.8: Two-dimensional oriented scattering lattice for $N = 2$ successive steps. A phase $\phi_1 = +\phi$ and $\phi_2 = -2\phi$ is added for the states scattered out the nodes S_1 and S_2. The unit cell of this lattice is emphasized by a dashed black rectangle.

reflected in the negative sign of the "group velocity" $\partial_\phi \varepsilon$ of either band for any values of ϕ (see Fig 3.9a).

A winding number, ν_ϕ can capture the winding of the bands along ϕ axis. For two steps periodic dynamics, so that the two distinct phase shifts are $\phi_1 = (m_1/n_1)\phi$ and $\phi_2 = (m_2/n_2)\phi$, where $m_i, n_i \in \mathbb{Z}$. As already discussed by Kitagawa, Berg, et al. 2010, the winding of the quasienergy bands along ϕ with condition $|m_1/n_1| \neq |m_2/n_2|$, defined as

$$\begin{aligned} \nu_\phi &\equiv \frac{1}{2\pi i}\int_0^{2\pi\gamma(\phi_1,\phi_2)} \mathrm{d}\phi \,\mathrm{tr}\left[U_F^{-1}\partial_\phi U_F\right] \\ &= \sum_p \frac{1}{2\pi}\int_0^{2\pi\gamma(\phi_1,\phi_2)} \mathrm{d}\phi \frac{\partial \varepsilon_p}{\partial \phi}, \end{aligned} \tag{3.18}$$

wherein the last equation(3.18), the sum runs over all the bands since the number of bands p is even, or more precisely, the number of links entering a scattering node, then the winding number is also an even integer. The $\gamma(\phi_1, \phi_2)$ as $T_\phi \equiv 2\pi\gamma(\phi_1, \phi_2)$ sets the period in the ϕ direction. It is equal to twice the least common multiple of $[(m_1/n_1 - m_2/n_2)^{-1}, (m_1/n_1 + m_2/n_2)^{-1}]$ (see Appendix(5.2)).

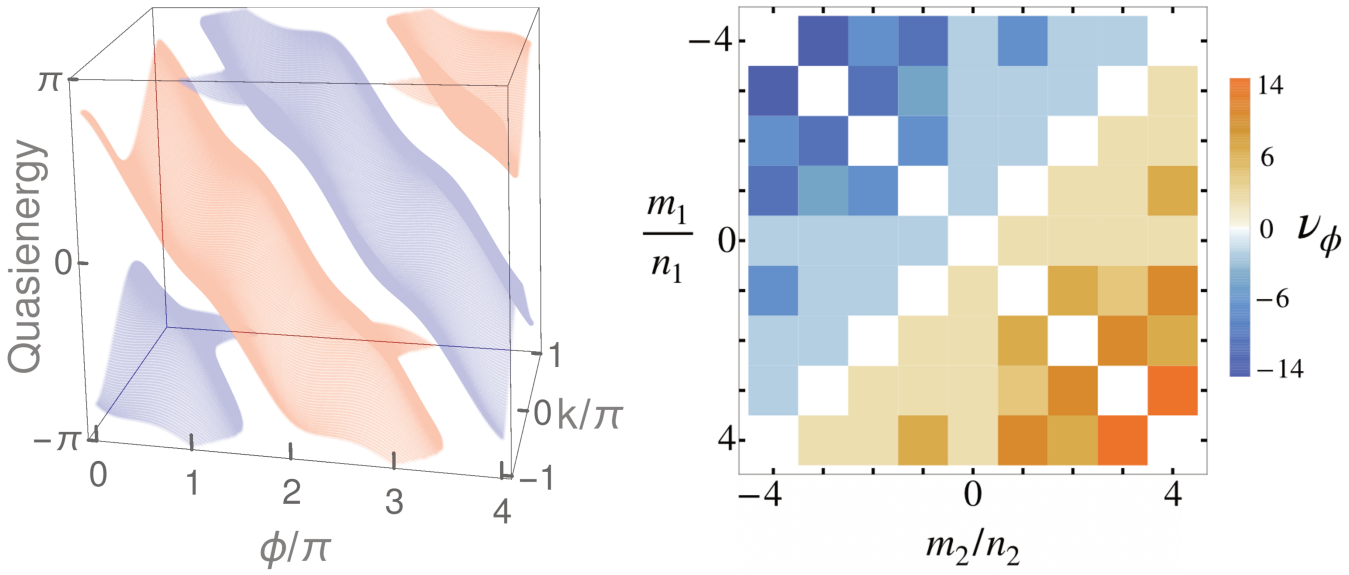

Figure 3.9: (a)Quasienergy spectrum with a winding $\nu_\phi = -2$ obtained for $\theta_1 = \pi/4$, $\theta_2 = \pi/4 - 0.6$, $\phi_1 = \phi$ and $\phi_2 = -2\phi$. (b) Values of ν_ϕ for integer values of m_i/n_i.

A direct calculation finally leads to the simple result

$$\nu_\phi = \frac{T_\phi}{2\pi}\left(\frac{m_1}{n_1} + \frac{m_2}{n_2}\right) \in 2\mathbb{Z} \tag{3.19}$$

which remarkably does not depend either on the quasimomentum k_x or on the scattering parameters $\{\theta_j\}$. A diagram is representing the different values for winding number ν_ϕ as a function of m_i/n_i, where $m_i/n_i \in \mathbb{Z}$, is shown in figure 3.9b.

3.4 Bloch oscillation induced by time-varying vector potential

The presence of a net ϕ in the unit cell is connected to the presence of a time varying potential, this extra phase redefines k_x (via Peierls substitution) in Floquet operator as $k \to \tilde{k}$, where $\tilde{k} = k \pm \phi$. Before going to section where we discuss the manifestation of the winding of bands, we can inspect what an extra ϕ or a time varying vector potential leads to, since in our case ϕ varies with time (Fig. 3.2). Let us demonstrate it by considering a 1D non-interacting lattice of single atom in a unitcell, denoted as a, as shown in Fig 3.10. There is a hopping energy J_1 between the unitcells, assumed to be real for simplicity. In addition, there is an electric field $\mathbf{E} = E_x\hat{x}$ acting on an electron of charge e. The origin of this electric field is a time dependent vector potential $\mathbf{A} = A_x\hat{x}$ as $\mathbf{E} = -\partial\mathbf{A}/\partial t$. Using Peierls substitution, this amounts to multiply J_1 by a phase $e^{ie\int_x^{x+1} dx' A(x',t)}$.

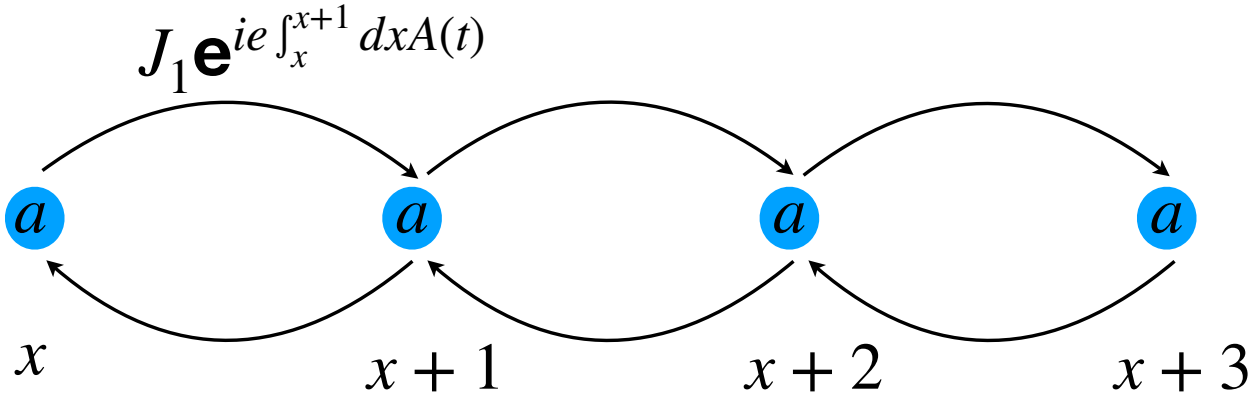

Figure 3.10: Lattice model realization of Bloch oscillation due to time dependent vector potential **A**.

The Hamiltonian H takes the form

$$H = -\sum_{x}^{N} J_1 e^{ie\int_x^{x+1} dx' A(x',t)} |x\rangle\langle x+1| + h.c. \tag{3.20}$$

Using the translational symmetry in the system, assuming lattice constant to be unity, and $A_x(t) = -E_x t$. The energy eigenvalues are

$$\mathcal{E}(k_x) = -2J_1 \cos(-eE_x t + k_x). \tag{3.21}$$

If we consider $eE_x t$ as a parameter, varying very slowly (via slow tuning of t), then eigenvalues in eq(3.21) are well defined. The corresponding group velocity v_g

$$\begin{aligned} v_g(k_x) &= \frac{\partial \mathcal{E}(k_x)}{\partial k_x}, \\ &= 2J_1 \sin(eE_x t + k_x) \end{aligned} \tag{3.22}$$

By integrating the above equation(3.22) in time, we get the centre of mass motion trajectory

$$\begin{aligned} X(k_x; t') &= \int_0^{t'} \mathrm{d}t \frac{\partial \mathcal{E}(k_x)}{\partial k_x}, \\ &= -\frac{2J_1}{eE_x}\{\cos(eE_x t' + k_x) - \cos(k_x)\} \end{aligned} \tag{3.23}$$

Defining $\chi(t) = eE_x t$ and for some fix value of $k_x = k_{x0}$, on tuning $\chi(t)$, the wavepacket undergoes oscillations eq(3.23) conserving the initial momentum k_{x0} (Krieger et al. 1986)

The gauge transformation in eq(3.4) shows the equivalence between the position-dependent phase and time-dependent phase, see eq(3.4). In other words, it a gauge transformation from the scalar potential (Φ) to the vector potential (**A**), this interpretation was missing in the Ref(Regensburger, Bersch, Mohammad-Ali Miri, et al. 2012).

Physical manifestation of the winding number ν_ϕ

We can already inspect the manifestation of the net phase, where a striking consequence of the winding of the bulk bands is seen in the unconventional dynamics of wavepackets in position space when adiabatically increasing the coordinate ϕ.

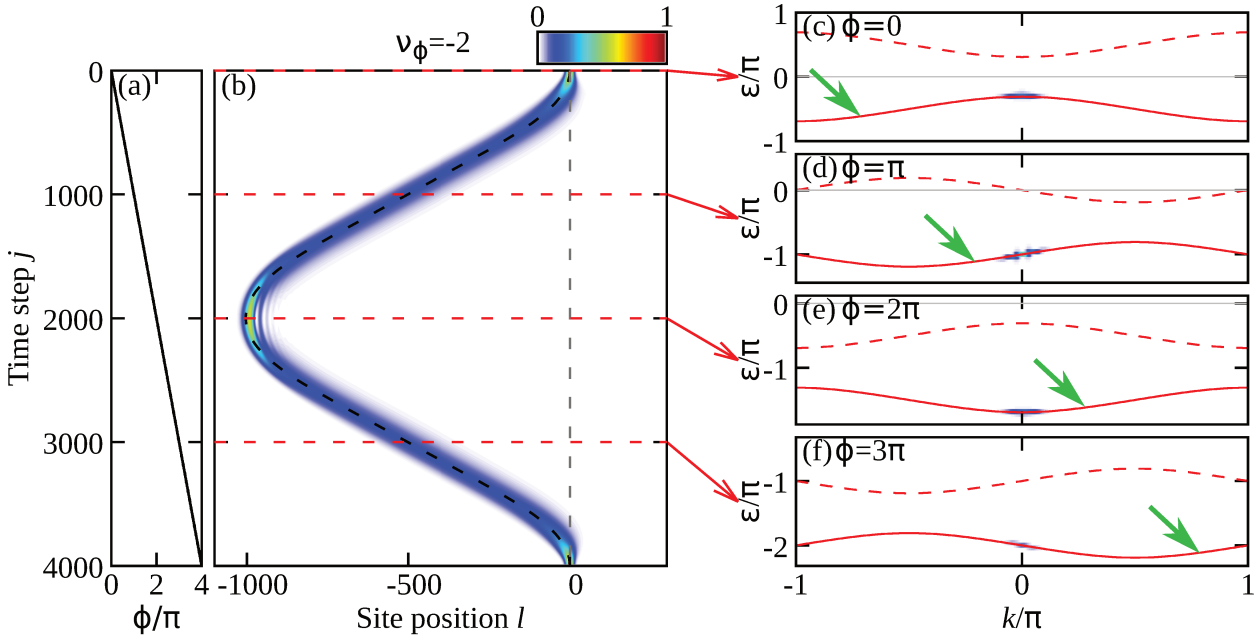

Figure 3.11: (a) Adiabatic increase of ϕ leads to (b) a standard Bloch oscillation ($\nu_\phi = -2$) of a wavepacket injected in the scattering network at time $j = 0$ and position $l = 0$. Colorscale: intensity ($|\alpha_l^j|^2+|\beta_l^j|^2$) of the wavepacket, injected with a Gaussian shape (with a rms width of 10 sites) in one band [the blue band shown in Fig. 3.9(a)]. Dashed black line on top of simulation represents analytical calculation of the centre of mass motion of a wavepacket from eq(3.23). (b) shows one period T_B of oscillation for the values of (m_1, m_2, n_1, n_2), θ_1, θ_2 as (1,-2,1,1), $\pi/4$, $\pi/4 - 0.5$. In (c)-(f), the norm of the 2D Fourier transform of the wavepacket (α part) after having evolved to the time step indicated by the horizontal lines in (b), and both the solid and the dashed red lines represent numerically calculated bands [from eq(5.34)]. The vertical scales differ in each panel, where the green arrows show the direction in which the bands wind when ϕ increases. The simulations are done by Clément Évain in PhLAM, Lille.

Figure 3.11(b) shows the m-time evolution of a Gaussian wavepacket injected at $m = 0$ in the blue band of Fig. 3.9(a) with $k = 0$, when ϕ is adiabatically increased from 0 to 4π: $\phi(m) = \phi_0 m$, with $\phi_0 = 2\pi/2000$ [see Fig. 3.11(a)]. Here, ϕ_0 is the rate of variation of ϕ with time (not to be confused with the one period of Floquet). The value $\phi_0 = 2\pi/2000$ means that after 2000 turns, the value ϕ has changed by a value 2π. Far from general fact, it is a matter of choice for experimentalist. To compute the spatio-temporal dynamics, we apply Eq. (3.1) to the initial wavepacket. The wavepacket periodically oscillates in space coordinate while keeping k constant. This can be readily seen in Fig. 3.11(c)-(f), where we show the two-dimensional Fourier transform of the wavepacket after having evolved to the time step indicated by the horizontal lines in Fig. 3.11(b). These panels provide an

understanding of the mechanism behind the oscillations: as ϕ is adiabatically increased, the band dispersions are displaced in a diagonal direction in quasienergy-k space [green arrows in Fig. 3.11(c)-(f)], a direct consequence of the winding of the bands. Therefore, a wavepacket with a given k is subject to group velocities that change sign when $\phi(m)$ increases, resulting in periodic oscillations in the spatial coordinate. Even though the simulations are done for $k = 0$, however, different choices of k_x will only result in a phase (or vertical) shift of the oscillations. A simple example demonstrates this after the end of this subsection.

An analytical calculation of the center of mass motion of the wavepacket centered at a given k_x can be deduced from the group velocity in parameter space (see Appendix(5.2))

$$X(k_x;t) = \int_0^t \mathrm{d}t \frac{\partial\varepsilon(k_x,\phi(\tau))}{\partial k_x} t, \tag{3.24}$$

$$X(k_x;t) = \int_0^{\phi(t)} \mathrm{d}\phi \frac{\partial\varepsilon(k_x,\phi(\tau))}{\partial k_x} \dot{\phi}(\tau)^{-1}, \tag{3.25}$$

where $\phi(\tau) = \phi_0\tau$ varies linearly, and the continuous time variable t extrapolates the discrete-time m, this semi-classical trajectory, shown in dashed black lines in Fig. 3.11(b), fits the simulation plot perfectly. Moreover, the period of Bloch oscillations T_B comes from the period of X, which in turn comes from quasienergy periodicity in ϕ, thus $T_B = T_\phi/\phi_0$. This directly relates the Bloch oscillations period to the quasienergy winding number via eq(3.19) as

$$T_B = \frac{2\pi}{\phi_0} \frac{\nu_\phi}{\left(\frac{m_1}{n_1} + \frac{m_2}{n_2}\right)} . \tag{3.26}$$

The physical origin of these oscillation comes from the fact that the modulation of the phase shifts ϕ along the propagation is analogous to a time-varying vector potential acting on a charged particle of unit charge in a lattice that induces a (fictitious) electric field E on it. One thus expects that a wavepacket corresponding to this charged particle is subjected to the resulting electric force to be displaced accordingly in the lattice, finally leading to Bloch oscillations with period $T_B = 2\pi/E$. We recognize in eq(3.26) the (fictitious) average electric field as $E = (E_1 + E_2)/2$, where $E_j = \frac{m_j}{n_j}\frac{\phi_0}{2}$ for time step j. Interestingly, the winding number ν_ϕ modifies this expression. Thus, higher winding numbers will not only change the oscillation period but will also yield more stationary points within the period. Remarkably, these number of stationary points $\mathcal{N}_S$ in a Bloch period is precisely

$$\mathcal{N}_S = |\nu_\phi| \tag{3.27}$$

which bestows a topological property of Bloch oscillations. Fig. 3.11 shows the standard Bloch oscillation with $\mathcal{N}_S = |\nu_\phi| = 2$, and the more exotic oscillations with $\mathcal{N}_S = |\nu_\phi| = 6, 8$ are shown in Fig. 3.12. The opposite sign for ν_ϕ will give rise to the trajectory in out of phase to their counterpart. The Fig. 3.13 shows an interplay of winding number, Bloch period, and the net phase in the unitcell $\Delta m/\Delta n = \left(\frac{m_1}{n_1} + \frac{m_2}{n_2}\right)$.

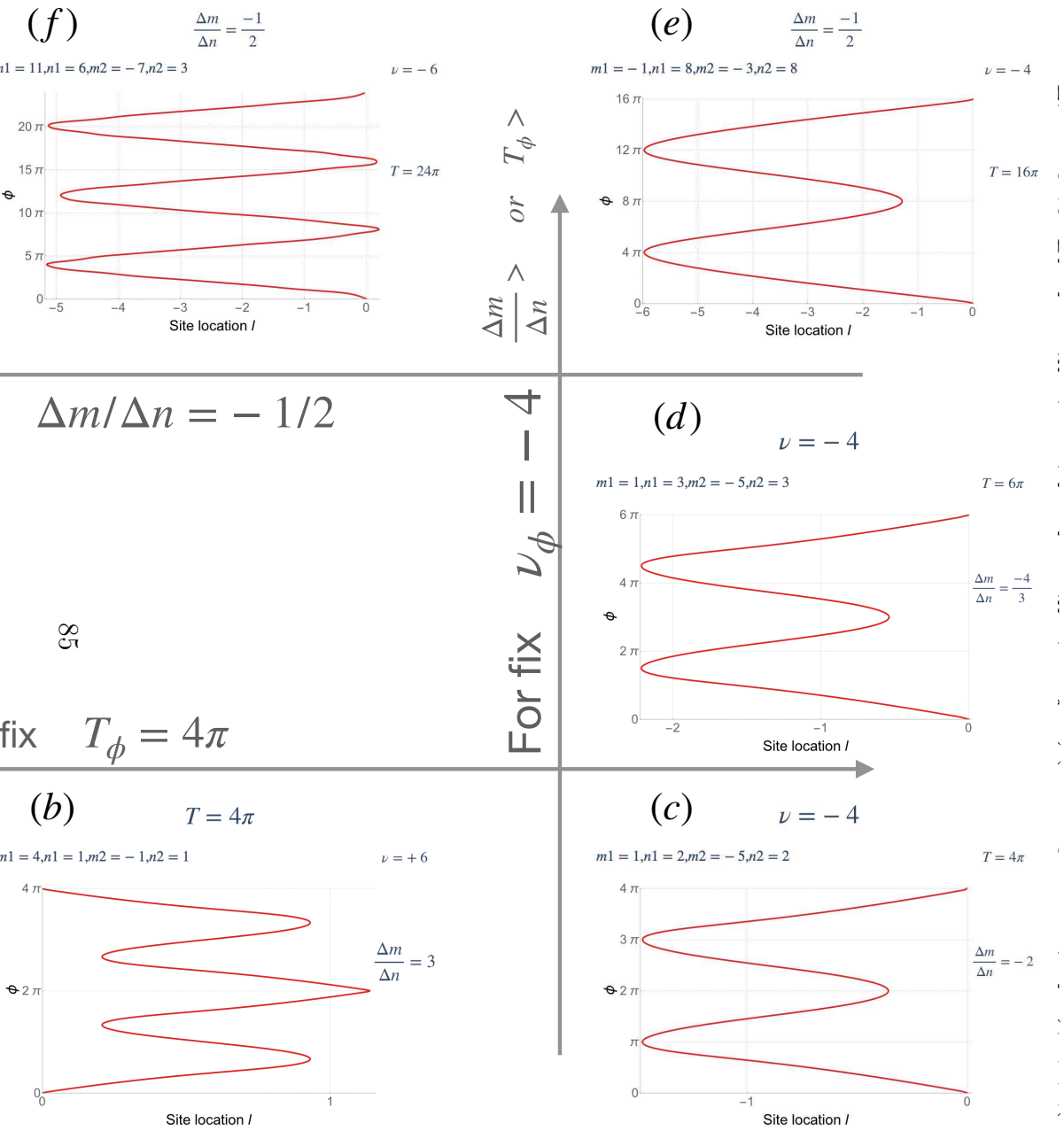

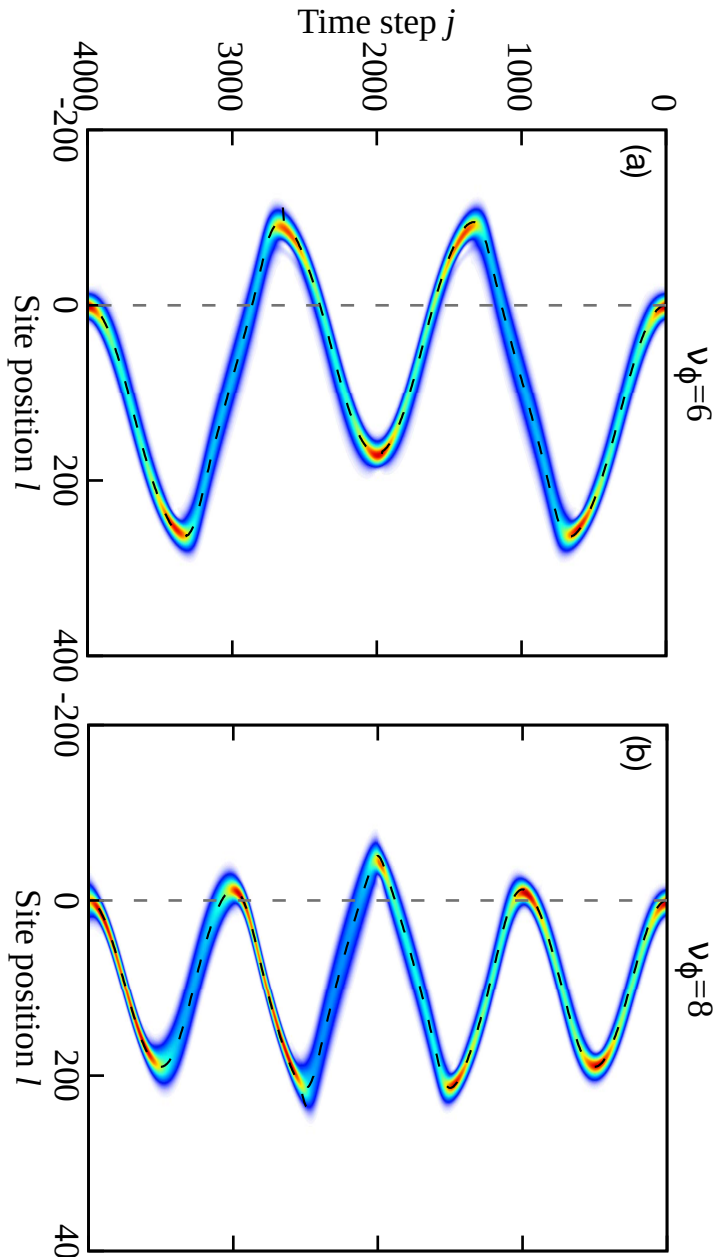

or T and the net non-zero phase shift in the unit cell $\Delta m/\Delta n$. By fixing the value of Δn also decreases the value of ν_ϕ. By fixing the value of (c)-(d) $\nu_\phi = 4$, on increasing the fixing (e)-(f) $\Delta m/\Delta n = -1/2$, increasing $|\nu_\phi|$ (or decreasing ν_ϕ) also increases the value

3.5 ν_ϕ can always be connected to Bloch oscillations

We can demonstrate the presence of winding and Bloch oscillations in a very intuitive model. Let us consider a 1D non-interacting and periodically driven lattice with period T, composed of two atoms in a unitcell, denoted by a and b, as shown in Fig 3.14. Here, one driving period T constitutes three steps. At first step, time $t = 0$, there are no hoppings but a non-zero potential V_a for atom a. A second step, $t = T/3$, there is only hopping J_1 within the unitcell. At the final step, $t = 2T/3$, there is only hopping J_2 between the unitcells, all hoppings are assumed to be real for simplicity.

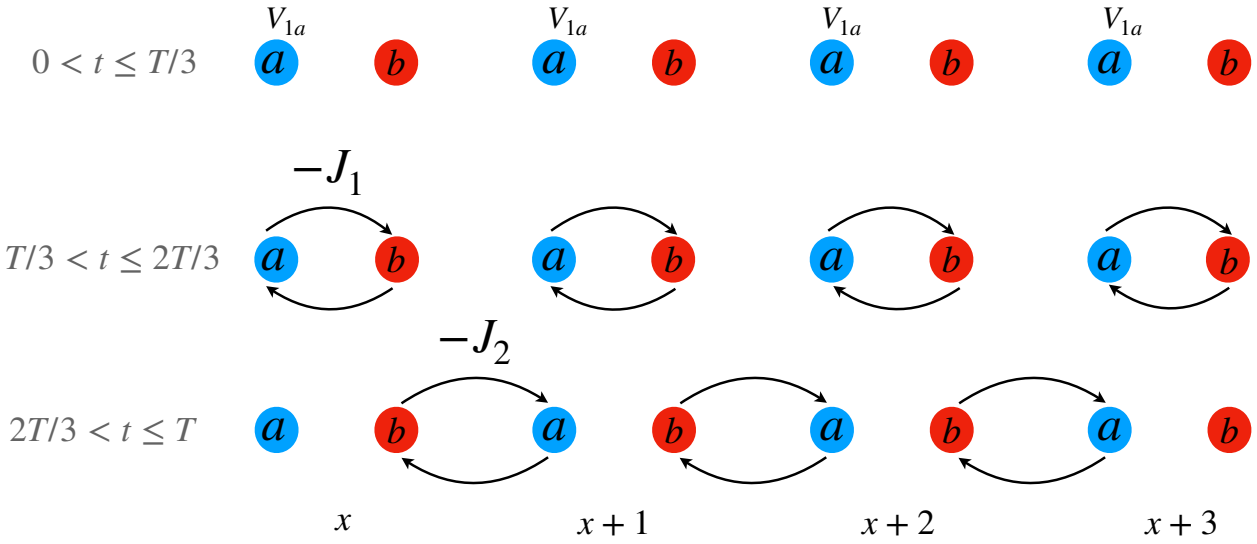

Figure 3.14: Lattice model realization of Floquet winding bands.

The stepwise Hamiltonian along with respective evolution operator under translational symmetry comes out to be

$$H_1 = \begin{pmatrix} V_a & 0 \\ 0 & 0 \end{pmatrix}, \quad U_1 = \mathrm{e}^{-iH_1T/3} = \begin{pmatrix} \mathrm{e}^{-i\phi_a} & 0 \\ 0 & 1 \end{pmatrix} \tag{3.28}$$

$$H_2 = \begin{pmatrix} 0 & J_1 \\ J_1 & 0 \end{pmatrix}, \quad U_2 = \mathrm{e}^{-iH_2T/3} = \begin{pmatrix} \cos\theta_1 & -i\sin\theta_1 \\ -i\sin\theta_1 & \cos\theta_1 \end{pmatrix} \tag{3.29}$$

$$H_3 = \begin{pmatrix} 0 & J_2\mathrm{e}^{ik_x} \\ J_2\mathrm{e}^{-ik_x} & 0 \end{pmatrix}, \; U_3 = \mathrm{e}^{-iH_3T/3} = \begin{pmatrix} \cos\theta_2 & -i\mathrm{e}^{ik_x}\sin\theta_2 \\ -i\mathrm{e}^{-ik_x}\sin\theta_2 & \cos\theta_2 \end{pmatrix}. \tag{3.30}$$

where $\theta_i = J_iT/3$ and $\phi_a = V_aT/3$. Note, that we have evaluated the evolution operator only at their respective or fix times, instead of evaluating them at stepwise time interval. For example, U_2 should have been written for time interval $T/3 \leq t < 2T/3$ as $\mathrm{e}^{-iH_2(t-T/3)}\mathrm{e}^{-iH_1T/3}$. We are interested in the Floquet operator, so we do not specify evolution operator in this stepwise evolution form.

Then the Floquet operator is $U_F = U_3U_2U_1$. This asymmetric net potential V_a in the unitcell breaks the inversion symmetry of the evolution operator. It is reflected in the winding of the

bulk quasienergy bands, as shown in Fig 3.15. Similarly, the consequence of these windings are the wavepacket oscillations, while the origin is the same the fictitious electric field. We demonstrate it,

$$U_F = \mathrm{e}^{-i\phi_a/2}\tilde{B}(k_x/2)S_2\tilde{B}(k_x/2)\tilde{D}(\phi_a/2)S_1, \tag{3.31}$$

$$= \mathrm{e}^{-i\phi_a/2}\tilde{B}(k_x/2)S_2\tilde{B}(\tilde{k}_x/2)S_1 \tag{3.32}$$

where $\tilde{B}$ and $\tilde{D}$ are defined in eq(3.9) In the last equation(3.32), $\tilde{k}_x/2 = (k_x + \phi_a)/2$ has been re-defined, which can be linked to the presence of a vector potential ($p_x \to p_x + qA_x$). Moreover, this equation separates into two parts– one is the "winding factor" $\mathrm{e}^{-i\phi_a/2}$, and the other is a sinusoidal periodic term $f(k_x, \phi_a)$, this is reminiscent of the non-winding version. This former part results into the winding of the quasienergy bands eq(3.19), which in the scattering case was $\mathrm{e}^{i(\phi_1+\phi_2)/2}$ for the non-zero winding condition ($\phi_a =)\phi_1 + \phi_2 \neq 0$.

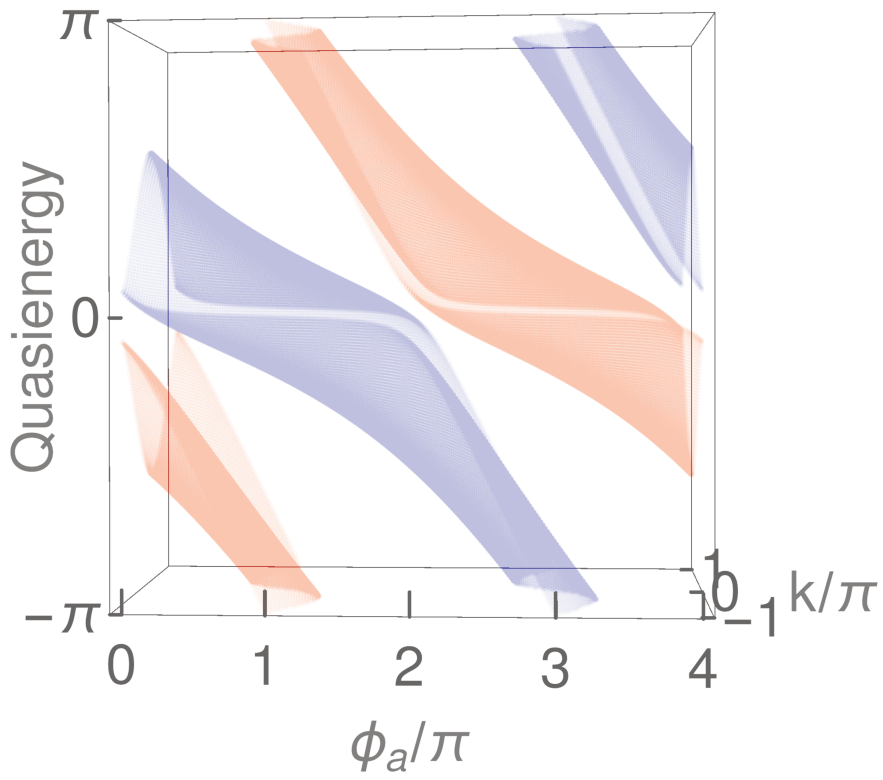

Figure 3.15: Quasienergy spectrum showing winding along ϕ_a.

There is another type of winding which does not give rise to any oscillations, and we call it winding regime of type 2. One way to engineer this regime is by restoring inversion symmetry in synthetic space while keeping non-zero onsite potential. For instance, in our previous example of winding in the Hamiltonian model, for the first time step, we introduce the same potential V_a for both atoms, see eq(3.28), it helps us in restoring inversion symmetry in the synthetic dimension (see eq(3.10)). Now, $U_1 = \mathrm{e}^{i\phi_a}\mathbb{1}_2$ ($\mathbb{1}_2$ is the identity matrix). This factor directly adds to the quasienergy[1], which gives rise to a winding along the ϕ_a axis.

[1] $U_F = \sum_j \mathrm{e}^{i(\varepsilon_j+\phi_a)}\mathcal{P}_j$, where $\mathcal{P}_j$ is a projector onto band j.

Thus, in the general situation, we can have two types of winding regime, as summarized in this table:

Properties	**Winding regime of type 1**	**Winding regime of type 2**
1. Inversion symmetry (responsible symmetry)	Breaking along synthetic axis with net potential in the unit-cell.	Preserving along synthetic axis with net potential in the unit-cell.
2. Consequences	Bloch oscillations for fixed quasimomentum.	Absence of oscillations.
3. Physical origin	Presence of a fictitious electric field **E**, generated by a time varying vector potential **A**.	Absence of fictitious electric field **E** or vector potential **A**.
4. Implementation (at the level of Hamiltonian)	At first time step, introducing asymmetric potential $V_a \neq V_b$ (see the model and eq(3.10))	At first time step, introducing symmetric potential $V_a = V_b$ (see the model and eq(3.10)).

3.6 Eigenspace anholonomy

Interestingly, if we look at closely the Floquet operator in eq(3.5), it is always periodic under $\phi_i + 2p\pi$, where $p \in \mathbb{Z}$

$$\begin{aligned} U_F(k_x, \phi_i + 2p\pi) &= B(k_x/2)S_2D(\phi_2 + 2p\pi)B(k_x/2)S_1D(\phi_1 + 2p\pi), \\ &= U_F(k_x, \phi_i). \end{aligned} \tag{3.33}$$

However, this is not the case for the quasienergies when they wind. For instance, when $\phi_1 = +\phi$ and $\phi_2 = -2\phi$, they are periodic after 4π, $\varepsilon(\phi + 4p\pi)$ (see Fig 3.9a and a derivation in Appendix(5.2)). On the other hand, let us consider the quasienergy spectrum over a period of U_F, as shown in Fig 3.16. To begin with, if initially the system is in eigenstate $|\Psi_{red}(k_{x0}, \phi)\rangle$ at some fix $k_x = k_{x0}$, then by changing ϕ, we follow the blue arrow going towards the blue-colored band, and it appears at the other (blue colored) band. In other words, we have parallel transported an eigenstate $|\Psi_{red}(k_{x0}, \phi + 2\pi)\rangle = |\Psi_{blue}(k_{x0}, \phi)\rangle$ to its orthogonal state. This has been referred to as *eigenspace anholonomy* or eigenspace holonomy (Cheon 1998; Miyamoto et al. 2007; Tanaka et al. 2007; L. Zhou et al. 2016). It is completely different from the Wilczek-Zee's phase holonomy (Wilczek et al. 1984), which is concerned with the change of an eigenvector in a degenerate and single eigenspace in which the eigenvector can rotate due to degeneracy. Moreover, holonomies also appear when a system is prepared in its eigenstate, assumed to be non-degenerate and discrete. Tuning a parameter of the Hamiltonian adiabatically, the system remains in the eigenstate due to the adiabatic theorem(Born et al. 1928). However, when the parameter returns to its initial value, after traversing a cyclic path adiabatically, the final and initial states differ by a phase. This phase difference contains two pieces of information: one about the dynamical phase and the other one of the geometric phase. This later phase is also referred to as phase holonomy or, more commonly, the Berry phase(Berry 1984), while in this case, the eigenstate remains the same (up to a phase) after one adiabatic period, but it the eigenstates changes in eigenspace holonomy.

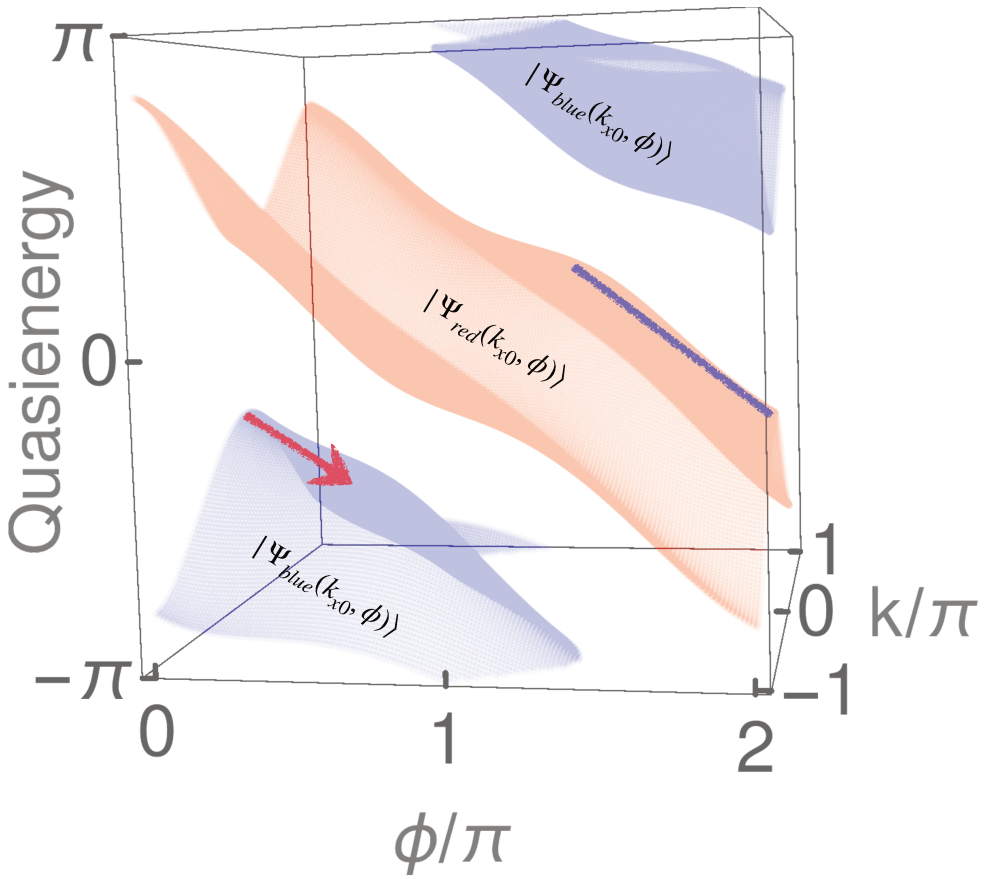

Figure 3.16: Quasienergy spectrum of Fig 3.9a over a period of 2π in ϕ of $2U_F$.

If we symmetrize (as we did in eq(3.8)) the Floquet operator expression eq(3.33), we get

$$\begin{aligned} U_F(k_x,\phi_i) &= e^{i(\phi_1+\phi_2)/2} B(k_x/2) S_2 \tilde{D}(\phi_2/2) B(k_x/2) S_1 \tilde{D}(\phi_1/2), \\ &= e^{i(\phi_1+\phi_2)/2} \tilde{U}_F(k_x,\phi_i). \end{aligned} \tag{3.34}$$

where $\tilde{D}(\phi_i/2)$ is defined in eq(3.9). Whenever, $(\phi_1+\phi_2)/2\phi$ is an integer this discrepancy of periodicity under ϕ does not arise. Both quasienergy and Floquet operator share the same periodicity of 2π this is the case in model I, where $\phi_1+\phi_2=0$. However, if this does not hold as in model II, then we can expect eigenspace holonomy as per the Floquet period consideration. On the contrary to all of this, we showed that the periodicity of quasienergy under ϕ could not be explained directly from the Floquet operator, instead, from (the analytical, if exists) the quasienergy expression, which was not considered in the past works, Miyamoto et al. 2007; Tanaka et al. 2007; L. Zhou et al. 2016.

Presence of chiral edge states Model II

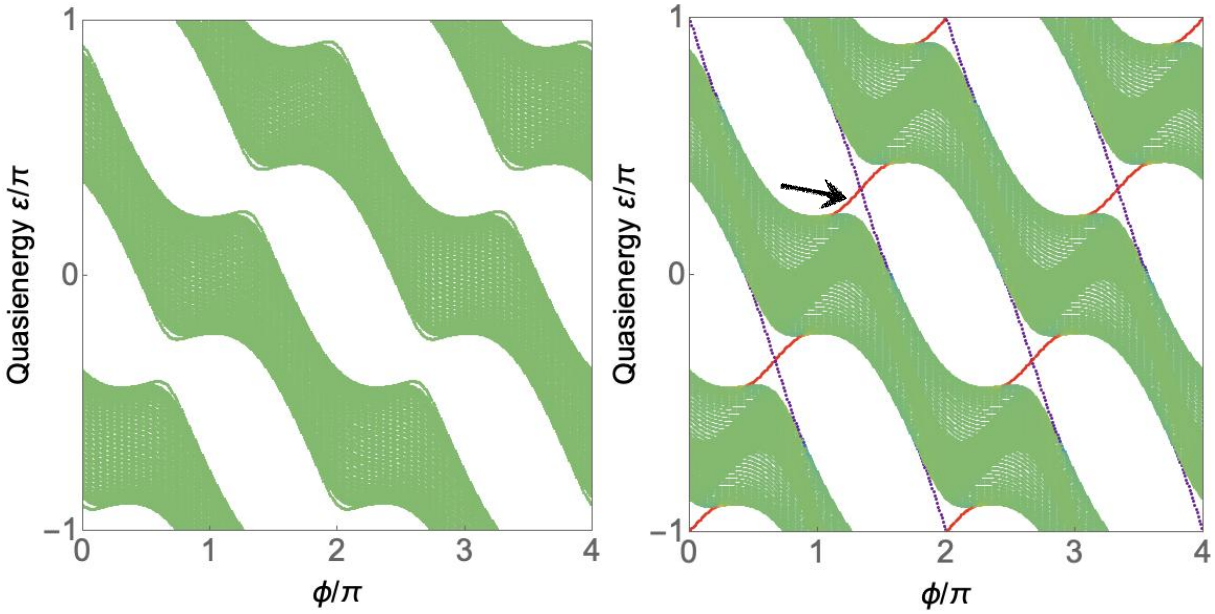

(a) (b)

Figure 3.17: Quasienergy in cylindrical geometry bands (a) when both the regimes are $\theta_1 = \pi/4 - 0.6, \theta_2 = \pi/4$, which gives trivial insulating regime and (b) anomalous Floquet topological insulating regime when one is $\theta_1 = \pi/4, \theta_2 = \pi/4 - 0.6$ and another $\theta_1 = \pi/4 - 0.6, \theta_2 = \pi/4$.

The Floquet winding regime combines two distinct topological properties– the winding of bulk bands, as we saw, and the existence of chiral edge states that we discuss now. Accordingly, a topological transition can be induced in this regime on top of these robust winding of bulk bands. This, in principle, could already be inferred from the discussion of the model I with inversion symmetry in the section(3.2), exhibiting the chiral edge states shown in Fig. 3.5. The only thing we have done so far is breaking inversion symmetry in the synthetic dimension, which does not affect the topology (Fu et al. 2007) while still preserving particle-hole symmetry. Thus model II shares the same topological phase diagram as that of model I (see Fig. 3.4).

To investigate the second topological property, we consider the edge states spectrum, in a similar finite cylindrical geometry, finite along x-direction while periodic ϕ. If both regions in this geometry are chosen in the same topological regimes by proper choice of coupling parameters (from the phase diagram in Fig. 3.4), then there are no edge states. It corresponds to the trivial regime shown in Fig. 3.5b. The Floquet anomalous topological regime, in contrast, exhibits chiral edge states in each indirect quasienergy gap. Indeed, even though the spectrum in this regime is fully gapless, in the sense that for any values of the quasienergy, there exists an allowed bulk state, the bulk quasienergy bands $\varepsilon(k_x, \phi)$ in the synthetic Brillouin zone are separated and do not touch. The chiral edge states remain topologically robust under the perturbation in the interface coupling parameters. Moreover,

the winding regime still keeps the phase rotation symmetry (Delplace, Fruchart, et al. 2017) of the insulating regime, implying that the Chern number vanishes identically for each band. It gives rise to only the two distinct insulating regimes aforementioned (see Fig.3.17).

The presence of chiral edge states in the winding regime manifests one remarkable feature. In this regime, all the states have a "synthetic group velocity" with the same sign except for the chiral edge states localized on one of the two edges, shown in red and marked by a black arrow in Fig. 3.17b. This peculiar property results from the interplay of two distinct topological properties, namely the winding of the bulk bands and the chirality of the edge states that have to be reversed for the two edges.

3.6.1 Model III: Inversion symmetry breaking in spatial dimension and Thouless pumping

A winding of the quasienergy bands along k_x can similarly be obtained by breaking inversion symmetry in the real spatial dimension. In a simple model with two time-steps, this can be achieved by connecting to the next nearest nodes of the network, as sketched in Fig. 3.18. The first time step matches with previous models, where scattering nodes S_1 at time j are connected to their nearest neighbor nodes S_2 at time $j+1$. However, it differs at the second (or final) time step, where right going arrows (in red) link to the next-nearest neighbor nodes but keeping the nearest-neighbors along left. This changes the evolution equations of motions for the scattering amplitudes at two steps, thus allowing us to write a more general equation for the two steps as

$$\begin{aligned} \alpha^{j+1}_{l+l_1} &= (\cos\theta_j \alpha^{j}_{l+l_2} + i\sin\theta_j \beta^{j}_{l+l_2}) \mathrm{e}^{i\phi_j} \\ \beta^{j+1}_{l+l_1} &= (i\sin\theta_j \alpha^{j}_{l+l_0} + \cos\theta_j \beta^{j}_{l+l_0}) \,, \end{aligned} \tag{3.35}$$

$$\begin{aligned} \alpha^{j+2}_{l+l_3} &= (\cos\theta_{j+1} \alpha^{j+1}_{l+l_1} + i\sin\theta_{j+1} \beta^{j+1}_{l+l_1}) \mathrm{e}^{i\phi_{j+1}} \\ \beta^{j+2}_{l+l_3} &= (i\sin\theta_{j+1} \alpha^{j+1}_{l+l_4} + \cos\theta_{j+1} \beta^{j+1}_{l+l_4}) \,. \end{aligned} \tag{3.36}$$

Here l_j are the links connecting the scattering nodes at time step $j+p-1$ to $j+p$, for some integer p. We can again define l_j in terms of r_j/s_j as,

$$\begin{aligned} \frac{r_1}{s_1} &= \frac{l_2 - l_3}{2}, \\ \frac{r_2}{s_2} &= \frac{(l_2 - l_3) + (l_0 - l_1)}{2}, \end{aligned} \tag{3.37}$$

Previously, there was only one compact evolution equation for the amplitudes for two-time steps (see eq.(3.1)). Due to the asymmetric nature of couplings at the two-time steps in model III, the evolution equations split at these time steps. The above relations in eq.(3.37) quantify these anisotropic couplings at the those time steps. For our present case, the link parameters are respectively as $l_0 = -2, l_1 = -1, l_2 = 0, l_3 = -2, l_4 = -5$. This gives $r_1/s_1 = 1$ and $r_2/s_2 = -2$. These following parameters r_j/s_j characterize the anisotropy in

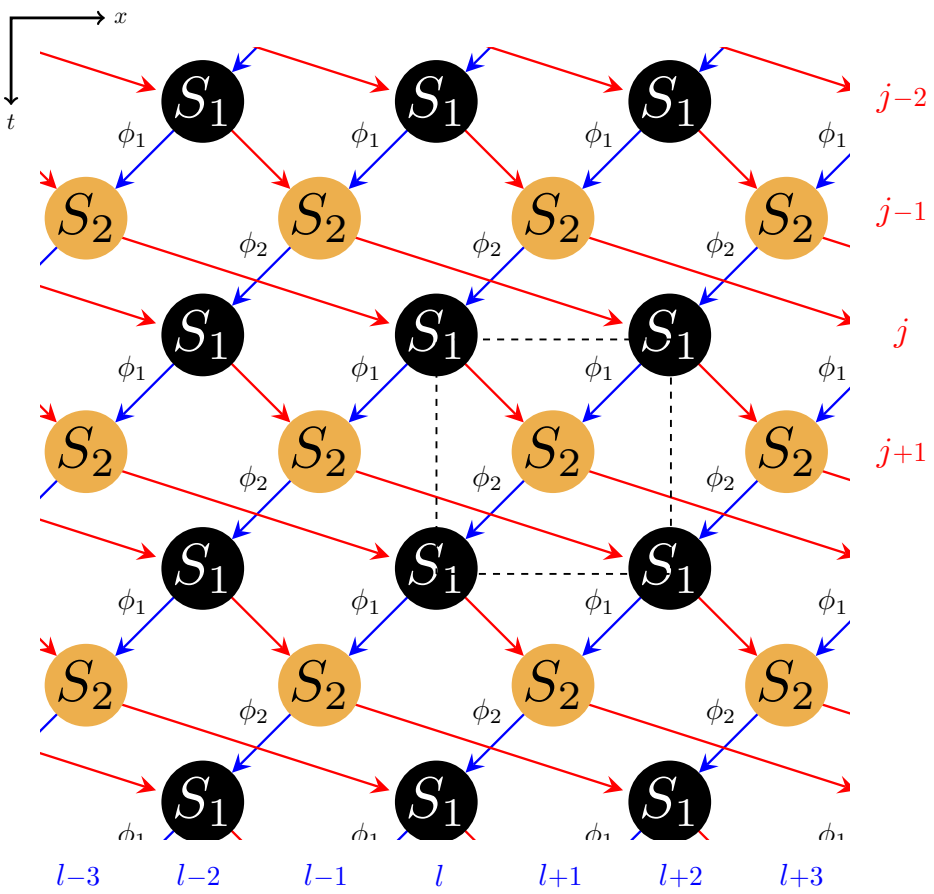

Figure 3.18: Two-steps scattering network implements the next nearest coupling in the second step. A dashed black rectangle emphasizes the unit cell of this lattice.

the coupling that connects the nodes at time j. These are equivalent to m_j/n_j parameters in the former case of a winding in ϕ. Thus, this anisotropy in the couplings breaks inversion symmetry in the spatial dimension, as can be seen from eq(3.10). This breaking reflects in the winding of the quasienergy bulk bands along k_x, as shown in Fig.3.19.

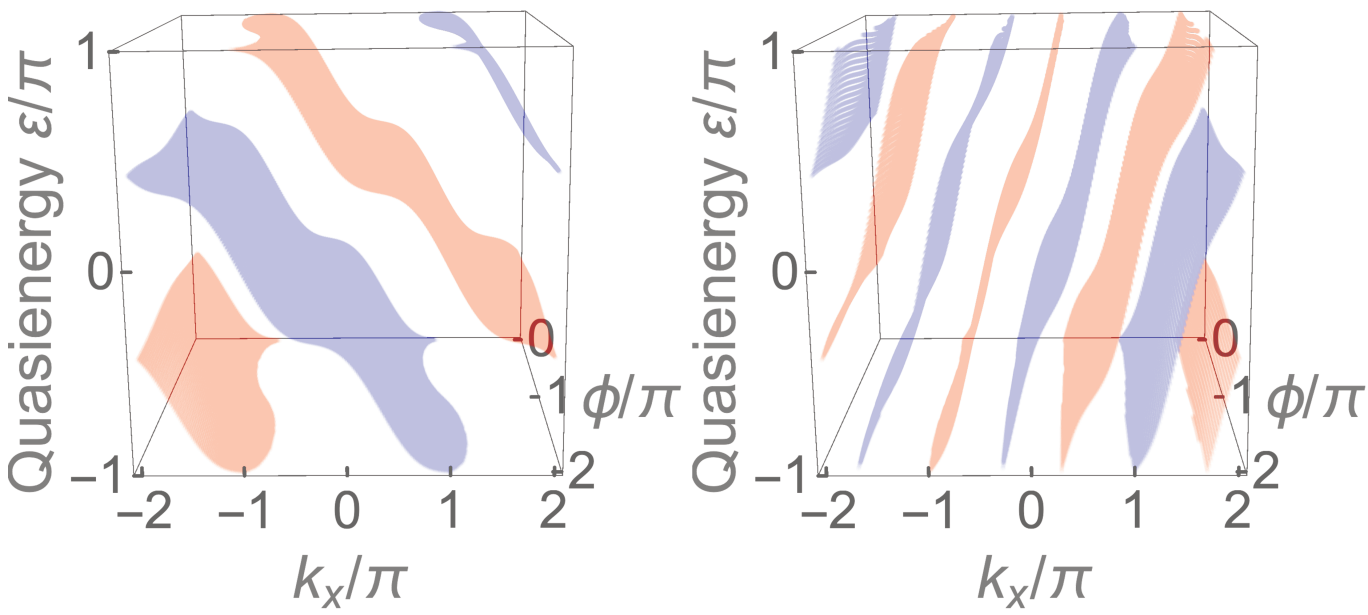

(a) $\nu_k = -2$ (b) $\nu_k = +6$

Figure 3.19: Floquet quasienergy bands winding along the quasimomentum axis k_x, an implication of inversion symmetry breaking in spatial dimension, for (a) $\nu_k = -2$ for $\phi_1 = +\phi$, $\phi_2 = -2\phi$, and (b) $\nu_k = +6$ for $\phi_1 = +4\phi$, $\phi_2 = -\phi$.

This winding of the bulk bands can be captured similarly by a winding number. The linking of nodes at two-time steps amounts to say $k_1 = (r_1/s_1)k_x$ and $k_2 = (r_2/s_2)k_x$, where $r_i, s_i \in \mathbb{Z}$ depend on the lattice geometry, and with $|r_1/s_1| \neq |r_2/s_2|$. The winding number of the quasienergy bands along k_x then reads

$$\nu_k \equiv \frac{1}{2\pi i}\int_0^{T_k} \mathrm{d}k_x \,\mathrm{tr}\left[U_F^{-1}\partial_{k_x}U_F\right] \in 2\mathbb{Z} \tag{3.38}$$

where $T_k \equiv 2\pi\gamma(k_1, k_2)$ sets the length of the Brillouin along k_x and it is equal to 2π times twice the least common multiple of $[(r_1/s_1 - r_2/s_2)^{-1}, (r_1/s_1 + r_2/s_2)^{-1}]$ (see Appendix(5.2)). A direct calculation leads to the expression

$$\nu_k = \frac{T_k}{2\pi}\left(\frac{r_1}{s_1} + \frac{r_2}{s_2}\right). \tag{3.39}$$

similar to that obtained for ν_ϕ (see eq.(3.19)). The bulk quasienergy bands in Fig. 3.19 carries different winding number given by above equation3.39, where Fig. 3.19a shows for winding number $\nu_k = -2$, and Fig. 3.19b for $\nu_k = +6$.

Physical manifestation of the winding number ν_k

Similarly to the case of the winding of the quasienergy in ϕ, the Floquet operator can be thought of as being made up of two factors (see eq(3.32)). The first one is the reminiscent

of non-winding ,we denote this by $f(k_x, \phi)$. Another factor is arising from the winding (or $r_1/s_1 + r_2/s_2 \neq 0$) part, of the form $e^{ig(k_1,k_2)}$, where $g(k_1, k_2) \equiv g(r_j/s_j)k_x$ (exact form can be found in Appendix(5.2)). This latter part is the one that directly adds to the quasienergy $\tilde{\varepsilon} = \varepsilon + g(r_j/s_j)k_x$. This gives the group velocity as

$$\frac{\partial \tilde{\varepsilon}}{\partial k_x} = \frac{\partial \varepsilon}{\partial k_x} + g(r_j/s_j) \tag{3.40}$$

A striking consequence is a quantized transverse drift of a wavepacket in position space (this comes from $g(r_j/s_j) \gg \partial\varepsilon/\partial k_x$). This quantized transverse drift $\langle x^{(n)} \rangle_{T_\phi}$ of the center of the mass of the wavepacket in the n^{th} band is directly related to the winding number ν_k (see eq(3.39)) (Kitagawa, Berg, et al. 2010).

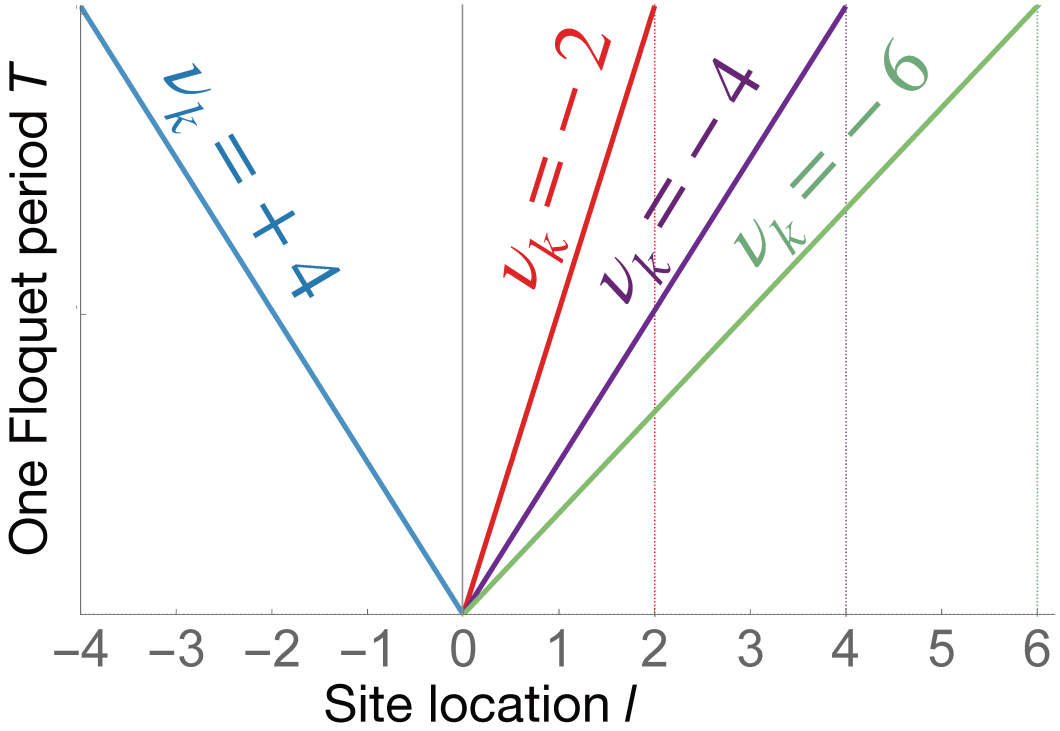

Figure 3.20: Quantized displacement of the mean particle position with associated winding numbers ν_k.

$$\langle x^{(n)} \rangle_{T_\phi} = \int_0^{mT} \mathrm{d}\tau \int \frac{\mathrm{d}k_x}{T_k} \langle \psi_n(k;\tau) | \dot{x} | \psi_n(k;\tau) \rangle \tag{3.41}$$

$$= m \int_0^{T} \mathrm{d}\tau \int \frac{\mathrm{d}k_x}{T_k} \langle \psi_n(k;0) | U_F^{-1} i[H(t,k), \hat{x}] U_F | \psi_n(k;0) \rangle \tag{3.42}$$

$$= -m \int \frac{\mathrm{d}k_x}{iT_k} \langle \psi_n(k;0) | U_F^{-1} \partial_k U_F | \psi_n(k;0) \rangle \tag{3.43}$$

$$= -\frac{2\pi}{T_k} m \nu_k^{(n)} \tag{3.44}$$

where we used the Heisenberg picture, $\dot{x} = \partial H/\partial k = i[H, \hat{x}]$, to get this final elegant answer. This expression connects the mean particle position in the n^{th} band to the winding number of n^{th} band, i.e.,$\nu_k^{(n)}$ times the stroboscopic time m.

Such a drift was introduced initially by Thouless but in a completely different context, where the pumped current quantization roots in the first Chern number of the instantaneous states of the adiabatically driven periodic Hamiltonian parametrized over the synthetic Brillouin zone span by (t, k_x). The big difference between the Thouless pump and our model III comes by considering the semi-classical motion equation of wavepackets (see eq.(3.23)). In the semi-classical equation of motion, the evolution equation of a wavepacket has two main contributions: first, the group velocity part, and second, the Berry curvature part, which is coming from adiabatic correction (from perturbation theory) (Xiao et al. 2010). This gives for our model

$$v^{(n)}_{\text{group velocity}} = \frac{\partial \varepsilon(k,\phi)}{\partial k} + \frac{\partial \phi}{\partial t}\Omega^{(n)}(k,\phi). \tag{3.45}$$

In our case, the first term characterizes the winding number ν_k (or ν_ϕ) in eq.(3.39), while the second term characterizes the Chern number for Thouless pump. Besides, our case is not adiabatic for the transverse drift case as it takes the Floquet time (mT) as an input, while the Thouless case is an adiabatic pump. Moreover, for the Thoules case, if we consider an example of two bands, then the value of the total Chern number should vanish. Hence, each band will have an opposite Chern number (or Berry curvature in above expression eq.(3.45)), which means both bands experience opposite transverse force. On the contrary, in our case, there is no such restriction since both bands share the same topological invariant.

Importantly, the winding in ϕ (by breaking inversion symmetry in synthetic dimension) can also be engineered at the level of a stepwise time-dependent Hamiltonian (**Gong2016**) (see Fig 3.14). In contrast, a quasienergy winding in k_x (by breaking spatial inversion symmetry) requires the presence of a momentum dependent potential (as can be seen from eq(3.28)), which is far from being trivial to engineer. Kitagawa *et al.* (Kitagawa, Berg, et al. 2010) proposed a 1D non-interacting spin-1/2 chain model on a lattice. In this model, there is a time-dependent lattice potential which only affects the spin of one kind, say spin up, and moves slowly to the right, such that after one full modulation, it shifts by exactly l times the lattice constant, where l is an integer. Then by adiabatically modulating this potential, it moves the spin-up particles from a unit cell at position x to another unit cell at $x + l$ to the right, whereas spin down remains unaffected. This reflects on the quasienergy band spectrum as the spin-up band winds l times while the spin-down band remains flat. However, this model is experimentally non-trivial to realize. Interestingly, as we saw this similar winding can be engineered in scattering network. Consequently, it is fully implementable experimentally.

Edge states in Model III

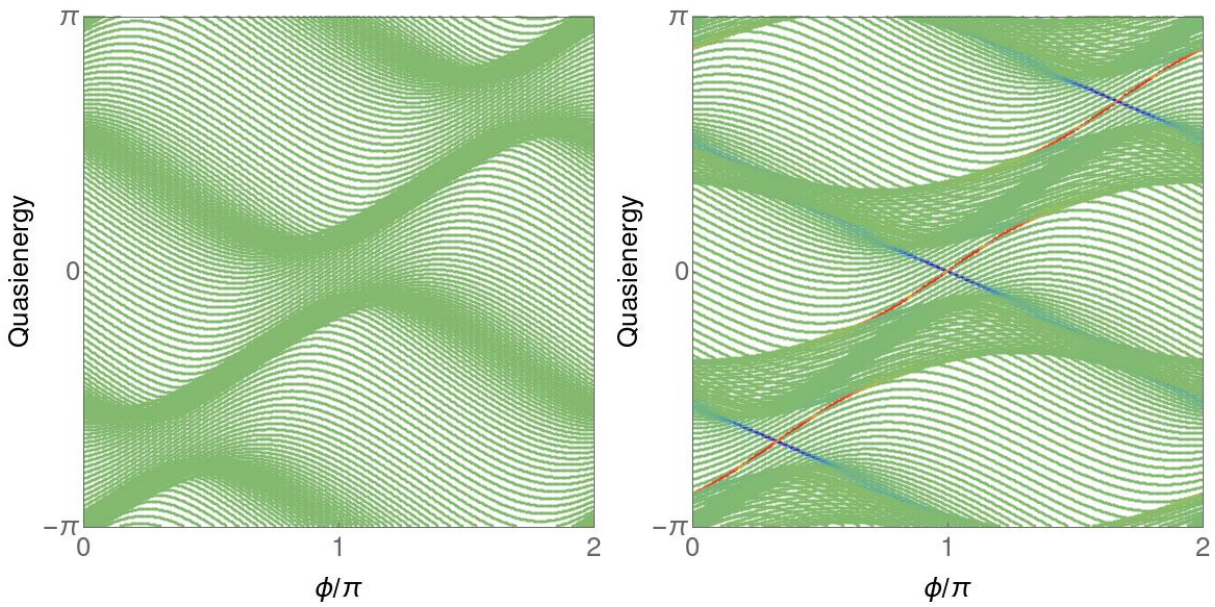

(a) (b)

Figure 3.21: Quasienergy spectra in cylindrical geometry for $\nu_k = -2$, (a) when both the regimes are $\theta_1 = \pi/4 - 0.6, \theta_2 = \pi/4$, which gives trivial insulating regime and (b) anomalous Floquet topological insulating regime when one is $\theta_1 = \pi/4, \theta_2 = \pi/4 - 0.6$ and another $\theta_1 = \pi/4 - 0.6, \theta_2 = \pi/4$.

We consider the quasienergy edge state spectrum for model III in a similar cylindrical geometry along the x axis. Likewise, phase rotation symmetry precludes only two regimes, depending on the choice of coupling parameters from the same phase diagram in Fig. 3.5b, namely the trivial and Floquet anomalous regimes, as shown in Fig. 3.21.

Interestingly, in this case, the bands wind along the k_x direction, while they are fully gapless in the ϕ direction, as reflected in the spectrum in Fig. 3.21. Moreover, unlike model II, the edge states are embedded within the bulk. So, any perturbation in the coupling parameters at the interface can result in the coupling of the edge states with the bulk bands. In the next chapter(4), we shall see another situation where similar properties of edge states being embedded in bulk arise but for entirely different reasons.

3.6.2 Model IV: inversion symmetry breaking along both synthetic and real dimension

In the general case, breaking inversion symmetry be achieved in either dimension, namely k_x and ϕ. This can be realized in the scattering network (see Fig. 3.18) yielding winding along k_x by adding $\phi_1 + \phi_2 \neq 0$. The combination of these two windings gives rise to an intricate quasienergy spectrum, showing such combined windings in Fig. 3.22.

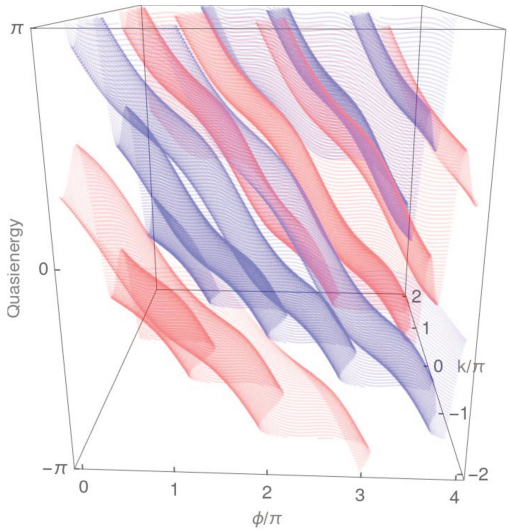

Figure 3.22: Floquet quasienergy bands winding along k_x and ϕ, an implication of inversion symmetry breaking in either dimensions for $\nu_k = \nu_\phi = -2$ with $\phi_1 = -2\phi$, $\phi_2 = +\phi$.

Straightforwardly, this winding manifests itself by giving rise to more complex motions of wavepackets centers, determined by the pair of topological indices (ν_ϕ, ν_k).

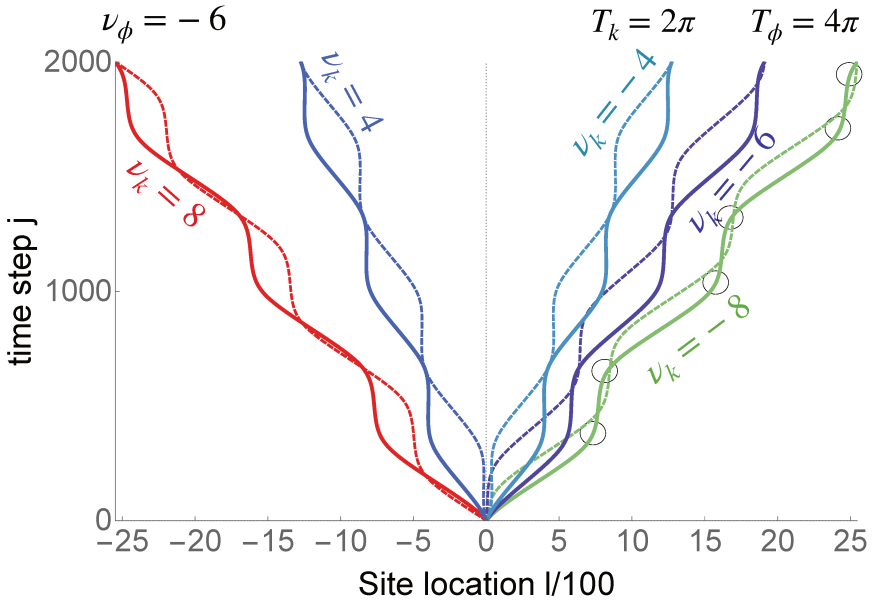

Figure 3.23: Trajectories in a two-steps model for bands with $\nu_\phi = -6$ for $\theta_1 = \pi/4$, $\theta_2 = \pi$, and different values of ν_k, ranging from $\nu_k = +8$ to $\nu_k = -8$, where the thick curves are for $k = 0$, and the dashed curves are for $k = 1$. Thus, changing k merely shifts the curve in vertical direction. Moreover, $|\nu_\phi| = 6$ can still be read even in this case of winding in both k and ϕ from the number of turning points, irrespective of the initial value of k, as shown with little circles for $\nu_k = -8$ (in green). Here, ϕ increases as $\phi(j) = \phi_0 j$, with $\phi_0 = 2\pi/2000$.

One such class of complex wavepacket motion for some fixed value of k_x, and fixed value of $\nu_\phi = +6$ (of Fig. 3.12(a) for $T_\phi = 4\pi$) but for different ν_k (with $T_k = 2\pi$) is sketched in

Fig. 3.23. In this figure, the number of turning points gives the value of ν_ϕ, they are marked with small circles for the last curve that has $\nu_k = -8$, the number tallies with their ν_k. Likewise, the slope of each curve is the manifestation of ν_k. All plots are for an initial value of $k_x = k_{x0}$ (see eq.(3.23)). However, changing the value of k_{x0} only shifts the wavepackets oscillations vertically, as shown with an inset at the left bottom in Fig. 3.23, and leaving the number of sub-oscillations unchanged.

Edge states in Model IV

We consider the quasienergy edge state spectrum for model IV. Similarly, considering the finite geometry leads to only two regimes depending on the choice of coupling parameters from the same phase diagram in Fig. 3.5b, the trivial and the Floquet anomalous regimes, as shown in Fig. 3.24.

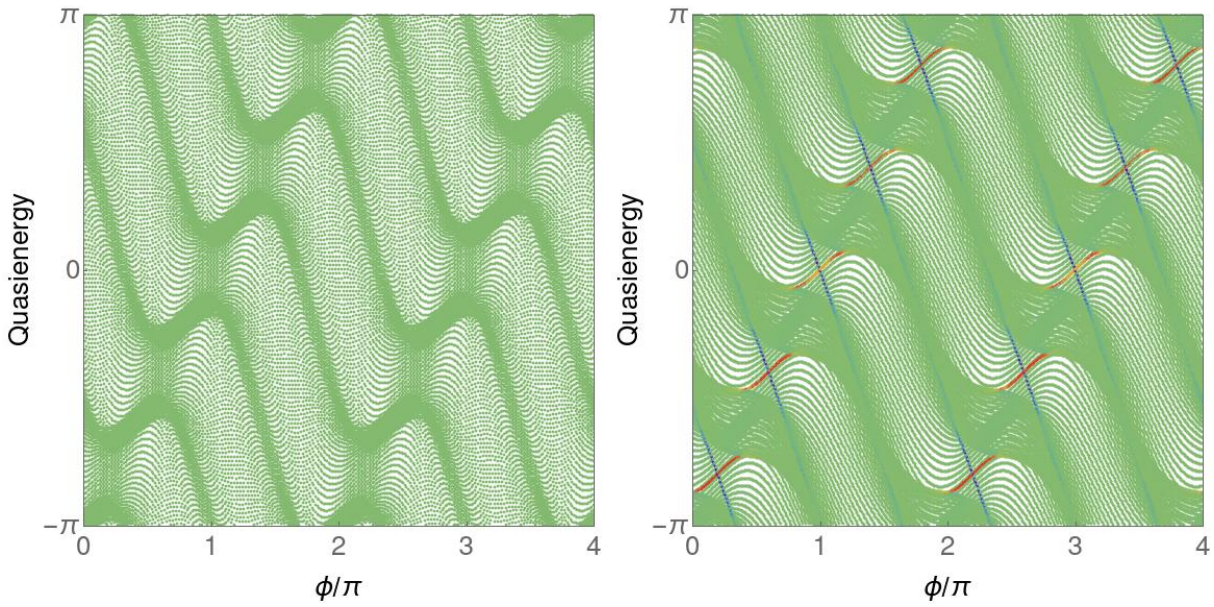

Figure 3.24: Quasienergy spectra in cylindrical geometry bands (a) when both the regimes are $\theta_1 = \pi/4 - 0.6, \theta_2 = \pi/4$, which gives trivial insulating regime and (b) anomalous Floquet topological insulating regime when one is $\theta_1 = \pi/4, \theta_2 = \pi/4 - 0.6$ and another $\theta_1 = \pi/4 - 0.6, \theta_2 = \pi/4$.

In this case, the bands wind along k_x and ϕ. Thus they are fully gapless in the ϕ direction, as reflected in the spectrum in Fig. 3.24. Still this does not prevent the existence of edge states, since the bulk bands do not touch, thus allowing the standard definitions of bulk topological invariants.

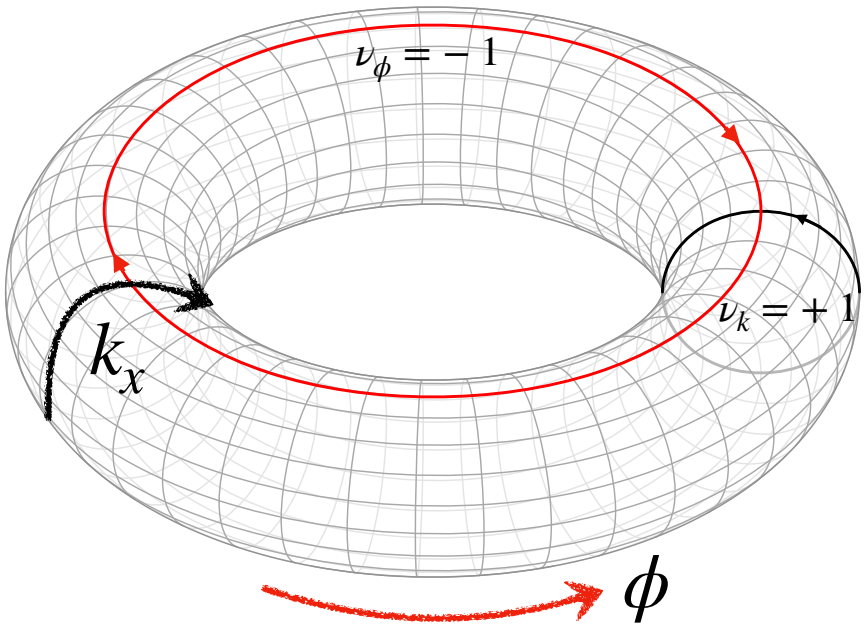

Figure 3.25: A general winding is made up of $\{\nu_\phi, \nu_k\}$ and they can be represented on a torus using the underlying manifold of BZ. Then the number of windings along the bigger circle represents ν_ϕ and smaller one ν_k, where the counter-clockwise direction can be chosen as a convention for positive values.

3.6.3 Summary of chapter 4: Main results

- In the oriented scattering network with two time-steps, lifting the condition of the same coupling parameters, i.e., $\theta_1 \neq \theta_2$, the two gaps emerged at 0 and pi, hosting chiral edge states in the topological regime. There are only two topological regimes in this model, namely the trivial and the anomalous Floquet regime due to phase rotation symmetry.

- Adding a net phase in the unitcell yields inversion symmetry breaking along the synthetic dimension, and this manifests as the winding of the quasienergy bulk bands. This net phase is connected to a non-zero time-dependent vector potential, which gives rise to a fictitious electric field. In turn, this electric field can lead to Bloch oscillations, where the number turning (or stationary) points are given by the winding number ν_ϕ of the bands. This topological property can thus be probed directly in a photonic experimental setup by the state-of-art technology.

- The winding of the bands in ϕ along with the chiral edge states brings a situation where one of the chiral edge states propagates opposite to the net synthetic group velocity of the bands and these two topological properties, winding, and the chiral edge states, only combines for the Floquet system.

- When inversion symmetry is broken along the spatial dimension, instead of net direction to the synthetic group velocity, there is a net direction to the actual group velocity.

It manifests as a transverse drift of the wavepacket, where the amount of drift is connected to another winding number ν_k. As a remarkable consequence, if we consider the finite geometry, then the edge states are embedded in the bulk quasienergy spectrum.

- Finally, these two results can be put in the same bowl, namely winding in both ϕ, and k, where each preserves its physical manifestation, transverse drift, and oscillations. Here, the BZ is a torus with two periodic axes k_x and ϕ, then these two winding numbers correspond to two different loops on the torus, as sketched in Fig. 3.25, where these two loops can not be continuously deformed into each other.

Chapter 4

Beyond Floquet insulators 2: Semi-metallic regime

4.1 Introduction

In this chapter, we present another gapless scenario in the 2D Floquet scattering network model. The most characteristic feature shown by this gapless model is the number of degeneracies can be selectively manipulated at the Fermi level (in our case, $\varepsilon = 0$ or at $\varepsilon = \pi$). It can be seen as a phase transition from D number of degeneracies to the $D - d$ degeneracies. Roughly speaking, this model mixes the Weyl and the usual topological insulator properties classification. At the same quasienergy ε, there are protected degeneracies (Weyl type) and also chiral edge states but at a different points in the BZ.

4.2 Semimetal Model 1: Gapless states in four-steps networks

To go beyond a model that only possesses two regimes, namely trivially gapped or Floquet anomalous insulators (chapter(3)) while keeping the inversion symmetry, one way would be to increase the number of steps along the transverse axis, and another way is by increasing the time steps in the Floquet period, as shown in Fig. 4.1. As a result, this leads to the first increment in the number of tuning (or coupling) parameters, thus ensuring that the phase rotation symmetry breaks (Delplace, Fruchart, et al. 2017). Hence more regimes can be expected, for example, the Floquet Chern insulator (see Fig. 3.6). Lastly, the number of bands touchings at the same quasienergy in the BZ also increases. Their stability depends on different (combination of) parameters than the pre-existing ones.[1]

We choose the second option of increasing the size of the unitcell along the time axis. Let us consider a period of $N = 4$ steps in one Floquet period, and fixing the distinct phase shifts inside a unit cell as $\phi_1 = +\phi, \phi_2 = -\phi, \phi_3 = +\phi$, and $\phi_4 = -\phi$. Note that the net

[1]For example, in two steps models, the stability of Dirac points requires $\theta_1 - \theta_2 = 0$. Hence, for more parameters (say N) ensure more such different combinations of these parameters, like $\sum_j^N \rho_j \theta_j = 0$, where $\rho_j = +/-$, to satisfy and thus ensuring their stabilities.

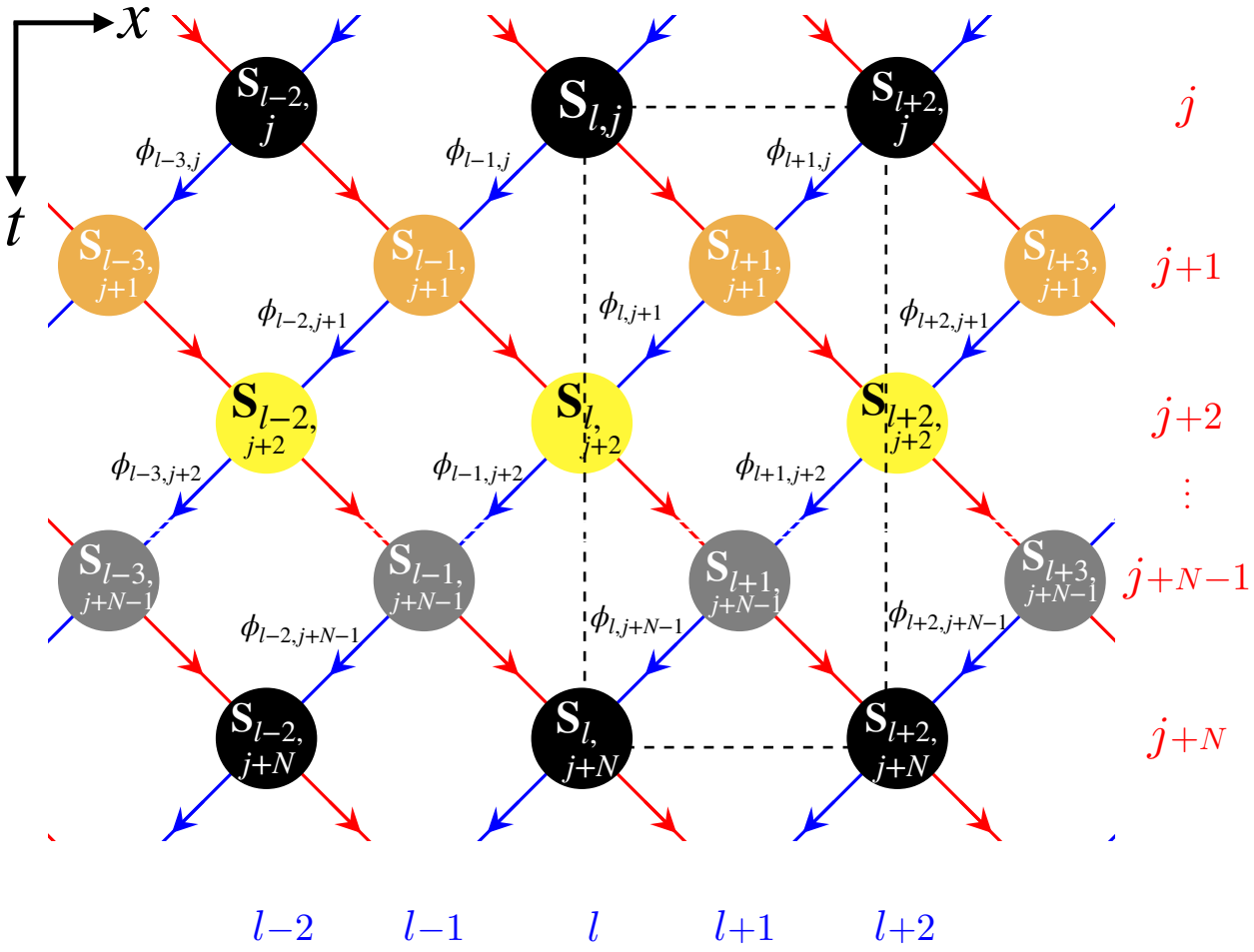

Figure 4.1: A general version of previously oriented scattering lattice. A time period consists of N successive steps. The scattering matrix, along with the phase $\phi_{l,j}$, not only depends on time j now but also on the position l. A black dashed rectangle emphasizes the unit cell of this lattice.

phase inside the unit cell is zero, which conserves inversion symmetry along the synthetic dimension ϕ, thus avoiding any winding of the quasienergy bands (chapter(3)). This model can be seen as just two copies of model I (see(3.2)) in one period. Thus conserving the inversion and particle-hole symmetry, like before.

Using the spatial periodicity along x, i.e. $\theta_{l,j} = \theta_j$ the Floquet-Bloch evolution operator can be written as the succession of translation-like $T_\pm$ operations and local scattering processes S_j as

$$U_F(\phi, k_x; \{\theta_j\}) = T_- S_4 T_+ S_3 T_- S_2 T_+ S_1 \tag{4.1}$$

where

$$T_{\pm} = \begin{pmatrix} e^{i(k_x \pm \phi)/2} & 0 \\ 0 & e^{-i(k_x \pm \phi)/2} \end{pmatrix} \tag{4.2}$$

$$S_j = \begin{pmatrix} \cos\theta_j & i\sin\theta_j \\ i\sin\theta_j & \cos\theta_j \end{pmatrix} . \tag{4.3}$$

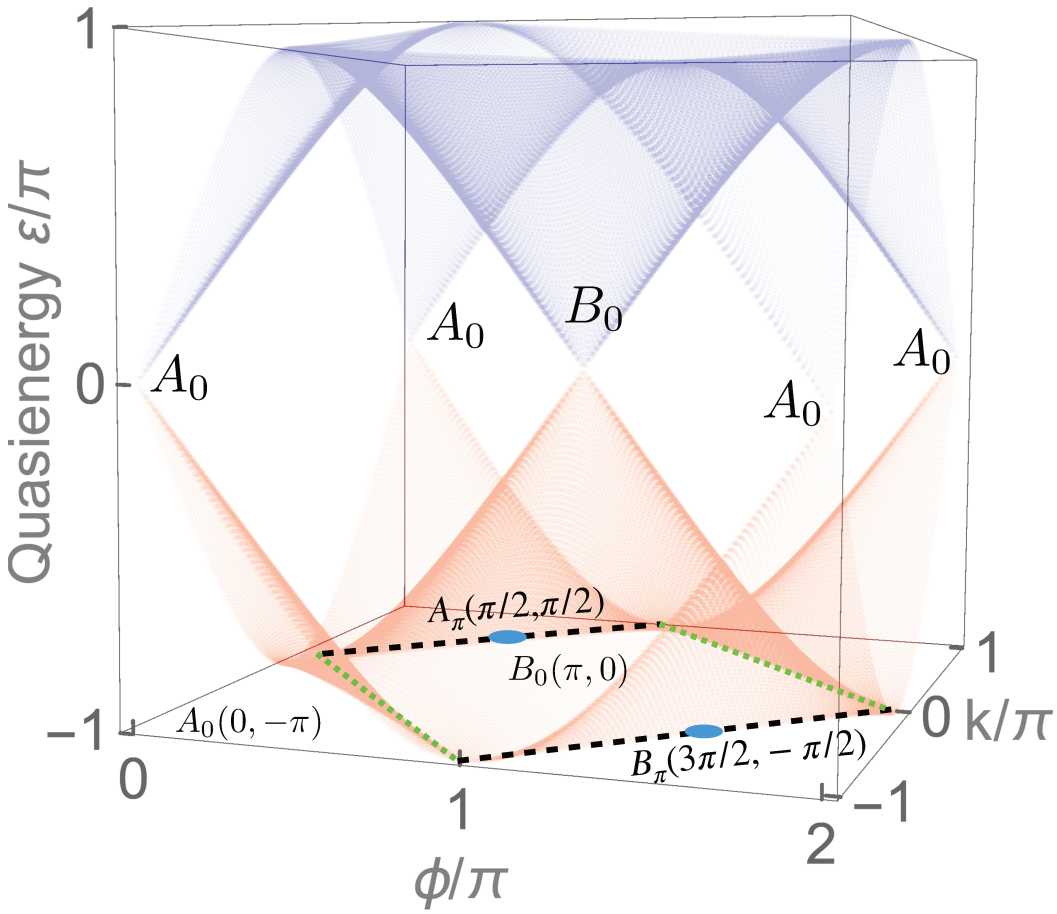

Figure 4.2: Quasienergy spectrum of the four-step Floquet operator for $\phi_1 = -\phi_2 = \phi_3 = -\phi_4 = \phi$ and $\theta_{j=1..4} = \pi/4$. Bands touch at different points at $\varepsilon = 0$ and along lines at $\varepsilon = \pi$.

As shown in figure 4.2, the corresponding quasienergy spectrum ε is fully gapless for the critical value of parameters $\{\theta_j = \pi/4\}$, as expected. But now, there exists two Dirac points A_0, B_0 at $\varepsilon = 0$, and the two bands also touch at $\varepsilon = \pi$ along four lines (instead of points) satisfying $k_x \pm \phi = 0$ and $k_x \pm \phi = 2\pi$ (dashed black and green lines in Fig 4.2). In total, we have two nodal points at $\varepsilon = 0$ and four nodal lines at $\varepsilon = \pi$. Thus, it fails to satisfy the first classification as a whole. However, depending on the quasienergy, we have only one class of semimetal characterized either by a nodal point or lines.

4.2.1 Selective manipulation of degeneracy in semimetal model 1

Once deviating from the critical point, it is then possible to lift some of these degeneracies, while leaving untouched the other ones. The conditions required to lift a specific nodal point or a nodal line are then inferred by expanding the Floquet operator U_F in coupling parameters around these degeneracies away from $\theta_j = \pi/4$.

At the two Dirac points sitting at $\varepsilon = 0$, namely A_0 and B_0, the Floquet operator must satisfy $U_F = \mathbb{1}_2$, where $\mathbb{1}_2$ is the identity matrix of size 2×2. Substituting their coordinates (ϕ, k_x) (see Fig. 4.2) respectively $(0, \pi)$ and $(\pi, 0)$ in equation(3.5) and then expanding in scattering parameters around the critical point $\{\theta_j = \pi/4 \to \pi/4 + \delta\theta_j\}$, yields the constrain

$$S(-\delta\theta_1 + \delta\theta_2 - \delta\theta_3 + \delta\theta_4) = \mathbb{1}_2 \quad \text{at } A_0 \text{ and } B_0 \tag{4.4}$$

(where $S(\theta_j) \equiv S_j$), which is only satisfied when $-\delta\theta_1 + \delta\theta_2 - \delta\theta_3 + \delta\theta_4 = 0$ holds. Conversely, a gap opens at A_0 and B_0 when this condition is not fulfilled. An interesting twist comes at $\varepsilon = \pi$, where now the Floquet operator must satisfy $U_F = -\mathbb{1}_2$. Expanding the Floquet operator in scattering parameters for the four degeneracy lines $k_x \pm \phi = 0$ and $k_x \pm \phi = 2\pi$, yields the condition

$$S(\delta\theta_1 + \delta\theta_2 + \delta\theta_3 + \delta\theta_4) = \mathbb{1}_2 \tag{4.5}$$

that clearly differs from the condition (4.4). Furthermore, there are two special points, namely A_π at $(\phi = \pi/2,\ k_x = \pi/2)$ and B_π at $(\phi = 3\pi/2,\ k_x = -\pi/2)$, shown with blue dots in Fig 4.2, where this expansion does not hold. There, one finds a third condition that reads

$$S(\delta\theta_1 - \delta\theta_2 - \delta\theta_3 + \delta\theta_4) = \mathbb{1}_2 \quad \text{at } A_\pi \text{ and } B_\pi\ . \tag{4.6}$$

To summarize, the different gap opening terms $\delta\theta_j$ follow from

$$\nu_1\delta\theta_1 + \nu_2\delta\theta_2 + \nu_3\delta\theta_3 + \nu_4\delta\theta_4 \neq 0 \tag{4.7}$$

with combinations of $\nu_j = \pm 1$, as summarized in Table 4.1.
Thus, doubling the "time period" of the network indeed brings new degeneracies, namely, $A_{0,\pi}$ and $B_{0,\pi}$. However, degeneracies at a fixed quasienergy, 0 or π, are (un)stable under the same perturbations $\delta\theta_j$. The only exception being at $\varepsilon = \pi$ where the degeneracy lines (in eq(4.5)) and degeneracy points (in eq(4.6)) do not share the same stability, and hence can be gapped separately.

4.3 Semimetal Model 2: Selective manipulation of degeneracies instabilities

In semimetal(SM) model 1, we have a symmetry of Floquet operator which is responsible for the appearance of the nodal line at the quasienergy $\varepsilon = \pi$ at critical point $\theta_{j=1..4} = \pi/4$.

Quasienergy	Degeneracy points	ν_1	ν_2	ν_3	ν_4
$\varepsilon = 0$	B_0	$-$	$+$	$-$	$+$
	A_0	$-$	$+$	$-$	$+$
$\varepsilon = \pi$	$k_x \pm \phi = 0, 2\pi$ (excluding A_π, B_π)	$+$	$+$	$+$	$+$
	A_π	$+$	$-$	$-$	$+$
	B_π	$+$	$-$	$-$	$+$

Table 4.1: Stability of the different band touchings (points or lines) under a perturbation $\nu_j \delta\theta_j$. Nodal points at $\varepsilon = 0$ or π have the same stability: they are gapped together, even though a point at a given ε can be gapped while the other pair remains stable.

That is an exchange symmetry of $k \leftrightarrow \phi$. Thus quasienergy spectrum is unaffected by this symmetry. It can be demonstrated by taking a cyclic permutation of Eq(4.1),

$$\begin{aligned} U_F(\phi, k_x; \theta_j = \pi/4) &= T_- S_4 T_+ S_3 T_- S_2 T_+ S_1, \\ &= T_+ S_1 T_- S_4 T_+ S_3 T_- S_2, \\ &= T_+ S_4 T_- S_3 T_+ S_2 T_- S_1 \end{aligned} \tag{4.8}$$

where we used the fact that at critical value $\theta_{j=1..4} = \pi/4$ all scattering matrices are identical (see eq.(4.3)) i.e.,

$$S_{j=1..4} = \frac{1}{\sqrt{2}} \begin{pmatrix} 1 & i \\ i & 1 \end{pmatrix} .$$

This property yields an exchange $k \leftrightarrow \phi$.
However, this exchange symmetry of quasimomenta can be broken by employing the different phase pattern than that of SM model 1.

We now propose the following phase shift pattern that decorates the four-step period : $\phi_1 = +2\phi, \phi_2 = -\phi, \phi_3 = 0$, and $\phi_4 = -\phi$. This choice clearly breaks the previous prevailing exchange symmetry, as can be seen from Eq(4.9). Also, this choice still preservers $\sum \phi_j = 0$ and thus prevents windings of the quasienergy bands (see chapter(3)). The new Floquet operator reads

$$\begin{aligned} U_F(\phi, k_x; \theta_j) &= B(k_x) S_4 D(-\phi) B(k_x) S_3 B(k_x) S_2 D(-\phi) B(k_x) S_1 D(+2\phi) \\ &= T(k_x + 2\phi) S_4 T(k_x - \phi) S_3 T(k_x) S_2 T(k_x - \phi) S_1 \end{aligned} \tag{4.9}$$

where the previously defined T in Eq.(4.2) has been used in the form of $T_\pm = T(k_x \pm \phi)$, and $D(\phi)$ and $B(k_x)$ are the same as in Eq.(3.9).

Similarly, the consequence of this breaking of exchange symmetry can be seen on the quasienergy spectrum calculated from the Bloch-Floquet operator (4.9), and depicted in Fig. 4.3 at the critical point $\{\theta_j = \pi/4\}$. This spectrum is still fully gapless, but now the two bands touch at $\varepsilon = 0$ and $\varepsilon = \pi$ only at points, either linearly in both directions (Dirac points A_0, C_0, A_π and C_π) or linearly in one direction and quadratically in the other one (known as semi-Dirac points, namely at B_0 and B_π) (S. Banerjee et al. 2009; Swapnonil Banerjee 2015; Huang et al. 2015; Mawrie et al. 2019; Montambaux et al. 2009b; Zhong et al. 2017).

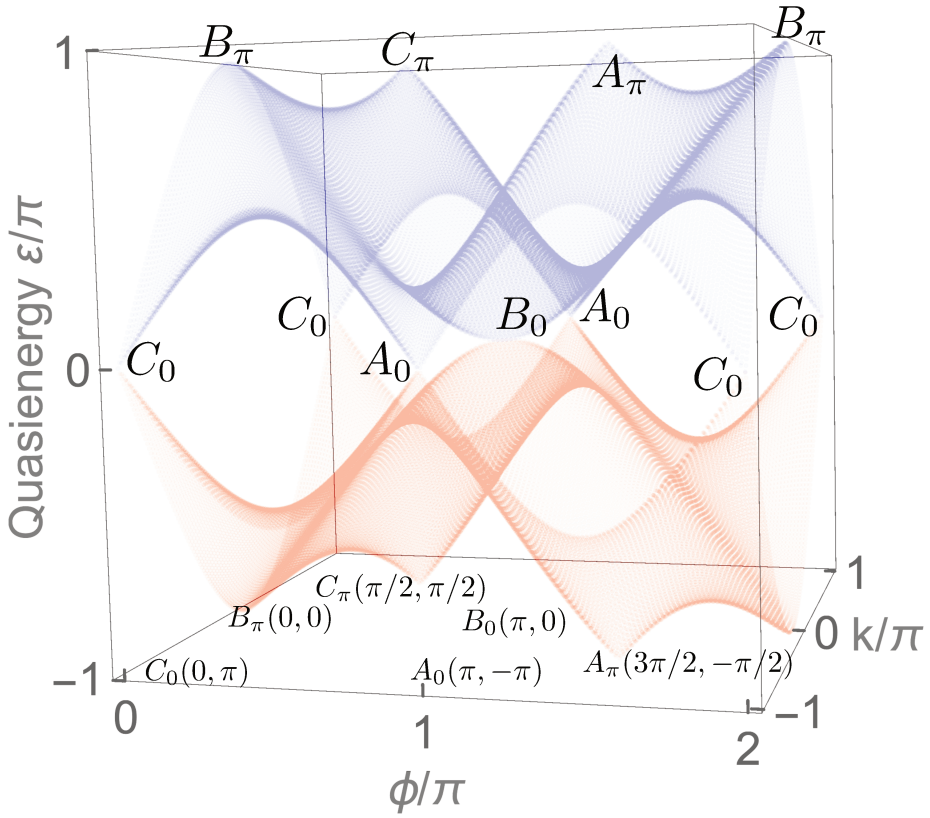

Figure 4.3: Quasienergy spectrum for the four-step Floquet operator with $\phi_1 = 2\phi, \phi_2 = -\phi, \phi_3 = 0$, and $\phi_4 = -\phi$ and $\theta_{j=1..4} = \pi/4$. It shows Dirac points at $A_{0/\pi}$, $C_{0/\pi}$ and semi-Dirac points at $B_{0/\pi}$

4.3.1 Selective manipulation of degeneracy in SM model 2

Following the same reasoning as in section(4.2.1), the stability of these six band touching points with respect to a perturbation in scattering parameters $\delta\theta_j$ can be calculated from the Floquet operator (4.9). By expanding it around each of the respective degeneracy points, one ends up with a new classification shown in Table 4.2. It reveals four distinct gap opening processes. In particular, C_0, A_π and C_π behave identically under any perturbation $\delta\theta_j$, but differently than the nodal points A_0, B_0, and B_π. In other words, these different degeneracy points are stable against distinct perturbations (or mass terms). It is thus now possible to lift a specific degeneracy at $\varepsilon = 0$ or $\varepsilon = \pi$ without opening a bulk gap. For the sake of simplicity, instead of considering the combination of all the $\delta\theta_j$'s, we fix $\delta\theta_1 = \delta\theta_2 = 0$, and focus only on the effect of $\delta\theta_3$ and $\delta\theta_4$. According to table(4.2), the stability of the degeneracies under the perturbations $\{\theta_3, \theta_4\} \to \{\pi/4 + \nu_3\delta\theta_3, \pi/4 + \nu_4\delta\theta_4\}$ can then be characterized by the sign of the product of $\nu_3\nu_4$ only, that leaves us two possibilities. Therefore, one needs to distinguish two distinct gap opening processes driven by two independent mass terms

$$m_\pm \equiv (\delta\theta_3 \pm \delta\theta_4)/2 \tag{4.10}$$

as summarized in Table 4.2 (in blue). These two mass terms will allow us to generate topological spectral flows of localized modes in a gapless (semimetallic) regime, where both the Chern numbers and the Floquet gap invariants (M. S. Rudner et al. 2013) of the evolution operator are ill-defined.

Quasienergy	Degeneracy points	ν_1	ν_2	ν_3	ν_4	mass term
$\varepsilon = 0$	A_0	$-$	$-$	$+$	$+$	m_+
	B_0	$+$	$-$	$-$	$+$	$-m_-$
	C_0	$+$	$-$	$+$	$-$	m_-
$\varepsilon = \pi$	A_π	$+$	$-$	$+$	$-$	m_-
	B_π	$+$	$+$	$+$	$+$	m_+
	C_π	$+$	$-$	$+$	$-$	m_-

Table 4.2: Stability of the different band touching points of figure 4.3, under a perturbation $\nu_j \delta\theta_j$. The mass terms $m_\pm$ encode this stability when considering $\nu_3\delta\theta_3$ and $\nu_4\delta\theta_4$ only.

4.4 Topological spectral flow through bulk modes

The tools developed in the section(1.9) are exploited to capture the topology of degeneracies in parameter space and calculating the topological charge. That is similar to the charge which characterizes the topology of Weyl nodes in momentum space, where the sign of the charge predicts if the (Berry) flux is piercing the enclosed surface outwardly or inwardly, for $+$ or $-$, as sketched in Fig. 4.4 (Armitage et al. 2018).

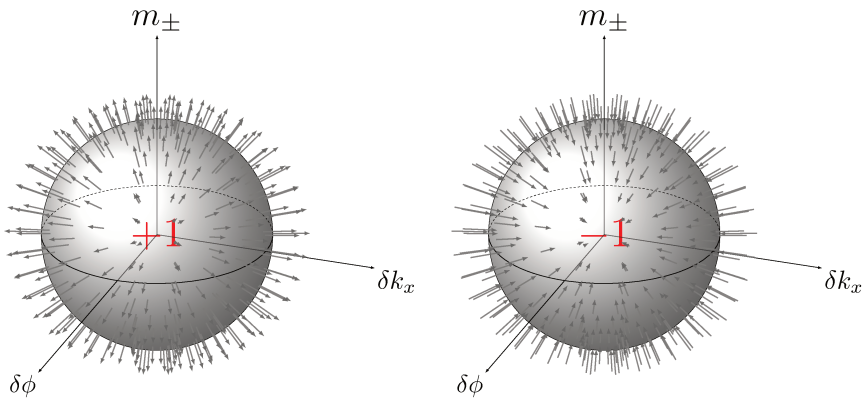

Figure 4.4: The topological charge associated with Weyl nodes, the node is situated at the origin, for (a) a positive charge the Berry flux goes outwards from the origin, and for (b) a negative charge, it comes inwardly.

4.4.1 Topological charge of degeneracy points

In the vicinity of each band touching point X, one can expand the (dimensionless) effective Hamiltonian defined via the Floquet operator as

$$U_F = \mathrm{e}^{-iH^X_{\text{eff}}} \tag{4.11}$$

at the lowest order terms in mass term m, phase shift $\delta\phi$ and quasimomentum δk_x. Such Hamiltonians have the generic form

$$H^X_{\text{eff}}(\delta\phi, \delta k_x, m) = \mathbf{h}^X \cdot \boldsymbol{\sigma} \tag{4.12}$$

where $\boldsymbol{\sigma}$ is the vector of Pauli matrices and $\mathbf{h}^X$ defines a family of continuous maps from $\mathbb{R}^3$ to $\mathbb{R}^3$. Therefore, $\mathbf{h}^X/|\mathbf{h}^X|$ defines continuous maps from parameter space $\mathbb{R}^3\backslash\{X\}$ to target space S^2 that are classified by the homotopy group $\pi_2(S^2) = \mathbb{Z}$. The elements of this group are integer numbers that tell how many times $\mathbf{h}^X/|\mathbf{h}^X|$ warps the sphere. They are given by the degree of $\mathbf{h}^X$ defined as

$$\deg(\mathbf{h}^X) = \sum_{p_i^{(0)}} \operatorname{sgn}\left[\det\left(\frac{\partial h_j^X}{\partial \lambda_i}\right)|_{h^{(0)}}\right] \tag{4.13}$$

where the pre-images $p_i^{(0)} = (\delta\phi_i^{(0)}, \delta k_{xi}^{(0)}, m_i^{(0)})$ satisfy $\mathbf{h}(p_i^{(0)}) = \mathbf{h}^{(0)}$, with $\mathbf{h}^{(0)}$ an arbitrary vector in $\mathbb{R}^3$, and where $\{\lambda_i\}$ stands for $\{\delta\phi, \delta k_x, m_\pm\}$.

For a two band Hamiltonian, this degree is directly related to the Chern number $\mathcal{C}_\pm$ of the continuous family of normalized eigenstates $\psi_\pm(\delta\phi, \delta k_x, m)$ of H^X_{eff} as

$$\mathcal{C}_\pm = \mp \deg \mathbf{h}^X \ . \tag{4.14}$$

Importantly, a nonvanishing value of $\mathcal{C}_n$ is known to guarantee the existence of a spectral flow towards bands n when the mass term ($m_\pm$ here) is varied in space and changes sign(Delplace, Marston, et al. 2017; Faure 2019; Marciani et al. 2019; Nakahara 2003; Perrot et al. 2019; G. E. Volovik 2009). As we saw in the introduction, this Chern number is different from the band Chern number C_j that is usually computed for the isolates bands of a gapped spectrum of the entire BZ. This Chern number C_j characterizes Chern insulators, and is ill-defined if the bands touch, like in our semmetallic phase. In contrast, $\mathcal{C}$ (eq(4.14)) characterizes nodal points in 3 paramter space, and thus suitable for our gapless model.
This spectral flow usually consists in a unidirectional mode, localized where the mass term vanishes, and whose (quasi-)energy bridges a spectral gap when a parameter (here ϕ) is tuned.

In the following, we compute this topological index (via the degree formula (4.13)) for different band touching points (Dirac and semi-Dirac) and check numerically that their value correctly predicts a spectral flow of localized modes, even in the absence of a gap.

4.4.2 Spectral flow induced by a spatial variation of m_+

According to Table 4.2, the degeneracy points A_0 and B_π are both lifted when $m_+ \neq 0$. One can thus assign them a topological charge (in the sense of section 4.4.1) by computing the

degree of their respective expanded effective Hamiltonian, with the parameter (base) space being $(\delta\phi, \delta k_x, m_+)$.

Let us detail the calculation for A_0 whose coordinates are $(\phi, k_x) = (\pi, \pi)$. At lowest order in each parameter, the effective Hamiltonian $H_{\text{eff}}^{A_0} = \mathbf{h}^{A_0} \cdot \boldsymbol{\sigma}$ yields

$$\mathbf{h}^{A_0}(\delta\phi, \delta k_x, m_+) = \begin{pmatrix} -2\, m_+ \\ \delta\phi + \delta k_x \\ \delta\phi \end{pmatrix} . \tag{4.15}$$

The spectrum of $H_{\text{eff}}^{A_0}$ simply consists in the two branches $\varepsilon_\pm = \pm|\mathbf{h}^{A_0}|$ that touch linearly when $m_+ = 0$, as expected (see Fig 4.5). Since $\mathbf{h}^{A_0}$ is linear with respect to each parameter,

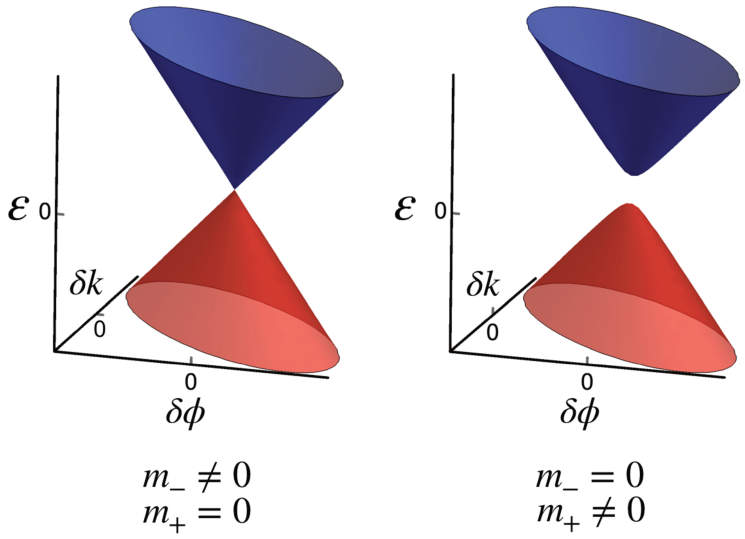

Figure 4.5: Dirac point A_0 at quasienergy $\varepsilon = 0$ located at $(\phi, k_x) = (\pi, \pi)$. This degeneracy point is robust against a perturbation m_- but a gap opens due to the introduction of m_+.

there is only one pre-image, so that the degree can be straightforwardly computed as

$$\begin{aligned} \deg(\mathbf{h}^{A_0}) &= \operatorname{sgn}\det \begin{pmatrix} \partial_{\delta\phi} h_x^{A_0} & \partial_{\delta\phi} h_y^{A_0} & \partial_{\delta\phi} h_z^{A_0} \\ \partial_{\delta k_x} h_x^{A_0} & \partial_{\delta k_x} h_y^{A_0} & \partial_{\delta k_x} h_z^{A_0} \\ \partial_{m_+} h_x^{A_0} & \partial_{m_+} h_y^{A_0} & \partial_{m_+} h_z^{A_0} \end{pmatrix} \\ &= \operatorname{sgn}\det \begin{pmatrix} 0 & 1 & 1 \\ 0 & 1 & 0 \\ -1 & 0 & 0 \end{pmatrix} \\ &= +1 \end{aligned} \tag{4.16}$$

Likewise, the topological charge for B_π is $\deg \mathbf{h}^{B_\pi} = +1$. Correspondingly, a spectral flow appears in the spectrum when considering now a spatial dependence of $m_+(x)$ that changes sign. This anisotropy is taken into account in the network model by considering a variation of $\delta\theta_{l,3} = \delta\theta_{l,4} = m_+(l)$ along x, thus breaking translation invariance. For numerical convenience, we consider periodic boundary conditions along x, so that the mass term $m_+(l)$ changes sign twice, as sketched in Fig. 4.6, giving rise to two opposite spectral flows (instead of one) visible in Fig. 4.7a. This is a typical situation where the chiral interface states

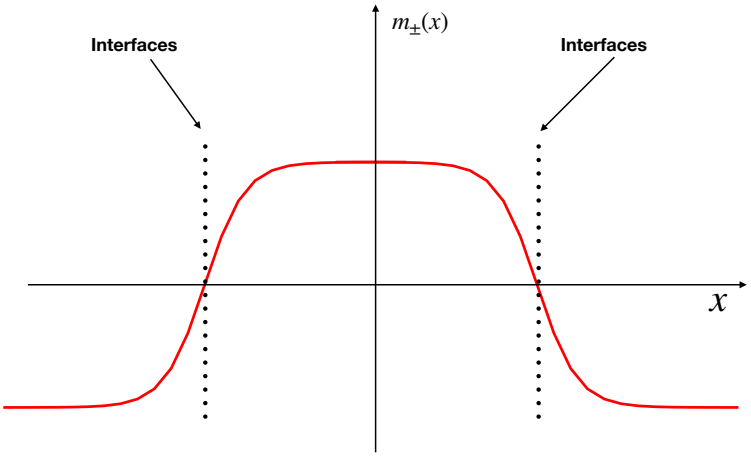

Figure 4.6: Spectral flow is observed when mass term changes sign, where it cuts twice the $x-$axis.

bridge a spectral gap. Note that the situation is, however, different from what is currently encountered in topological insulating phases, since the two bands actually touch at $\varepsilon = \pi$ at two other points of the Brillouin zone, A_π and C_π, that are stable against the perturbation in m_+. Therefore, these chiral states cannot be interpreted as the interface modes between two distinct topological (e.g., Chern) insulators, as they appear at the interface between two gapless semimetals. The situation is maybe even more unusual with A_0, since its ϕ coordinate matches that of semi-Dirac degeneracy B_0 (see Fig. 4.3) which remains stable under the perturbation in m_+, according to Table 4.2. It follows that the spectral flow coexists with bulk modes and does not bridge a gap, as shown in Fig. 4.7b. Notice that the direction of the spectral flow is the same for B_π and A_0, in agreement with the common value of their topological charge.

4.4.3 Spectral flow induced by a spatial variation of m_-

Similarly, a spatial variation of the mass term m_- leads to a topological spectral flow for B_0, C_0, A_π and C_π when ϕ is varied, provided m_- changes sign. Let us focus on B_0, which is a semi-Dirac point since their topological charge and their associated spectral flow is overlooked in the literature in comparison to Dirac points. An expansion of the effective Hamiltonian $H_{\text{eff}}^{B_0} = \mathbf{h}^{B_0} \cdot \boldsymbol{\sigma}$ in coupling parameters and quasimomenta gives

$$\mathbf{h}^{B_0}(\delta\phi, \delta k_x, m_-) = \begin{pmatrix} -2m_- - \frac{\delta k_x}{2}(\delta\phi + \delta k_x) \\ 2\delta\phi\, m_- \\ \delta\phi - \delta k_x \end{pmatrix} \tag{4.17}$$

The eigenvalues $\varepsilon_\pm = \pm|\mathbf{h}^{B_0}|$ yields a semi-Dirac behavior when $m_- = 0$, as announced (see Fig. 4.8). The introduction of m_- opens a gap, and allows us to define the topological charge

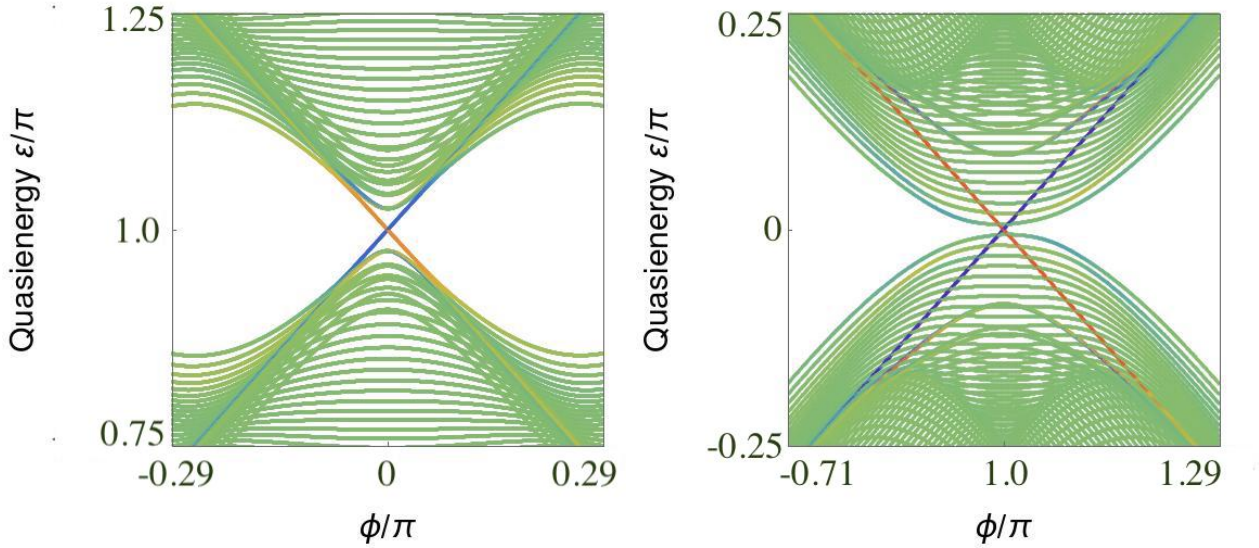

(a) Spectral flow associated to B_π

(b) Spectral flow associated to A_0, with stable B_0.

Figure 4.7: Existence of chiral edge modes where the mass term m_+ changes sign twice with x (periodic geometry). For degeneracy point (a) A_0 at quasienergy 0, which exists along with the gapless B_0 and another for (b) B_π at quasienergy π.

of this degeneracy point as

$$\begin{aligned}\deg(\mathbf{h}^{B_0}) &= \sum_{p_i^{(0)}} \operatorname{sgn}\det\begin{pmatrix} -\frac{\delta k_x}{2} & 2m_- & 1 \\ -\delta k_x - \frac{\delta\phi}{2} & 0 & -1 \\ -2 & 2\delta\phi & 0 \end{pmatrix} \\ &= \sum_{p_i^{(0)}} \operatorname{sgn}\left[4m_- - (3\delta k_x + \delta\phi)\delta\phi\right] \end{aligned} \tag{4.18}$$

One can evaluate the pre-images by fixing a direction for $\mathbf{h}^{B_0}$, say along z. This imposes the three following conditions

$$-4m_- = \delta k_x(\delta\phi + \delta k_x) \tag{4.19a}$$
$$\delta\phi\, m_- = 0 \tag{4.19b}$$
$$\delta\phi > \delta k_x \tag{4.19c}$$

Three pre-images $(\phi_i, k_{x,i}, m_i)$ are found to satisfy these conditions : $p_1^{(0)} = (-k_1, k_1, 0)$ with $k_1 > 0$, $p_2^{(0)} = (0, k_2, -k_2^2/4)$ with $k_2 < 0$ and $p_3^{(0)} = (\phi_3, 0, 0)$ with $\phi_3 > 0$. The pre-image $p_1^{(0)}$ yields a positive contribution to the sum (4.18) while both $p_2^{(0)}$ and $p_3^{(0)}$ contribute negatively, so that finally $\deg \mathbf{h}^{B_0} = -1$. A similar calculation leads to $\deg \mathbf{h}^{C_\pi} = +1$, $\deg \mathbf{h}^{A_\pi} = +1$ and $\deg \mathbf{h}^{C_0} = +1$.

Accordingly, a numerical calculation is performed in a periodic geometry where $m_-(l)$ changes sign twice when varying with the discrete position index l on the network (see Fig. 4.6). Spectral flows are found in agreement with the value of the topological charge.

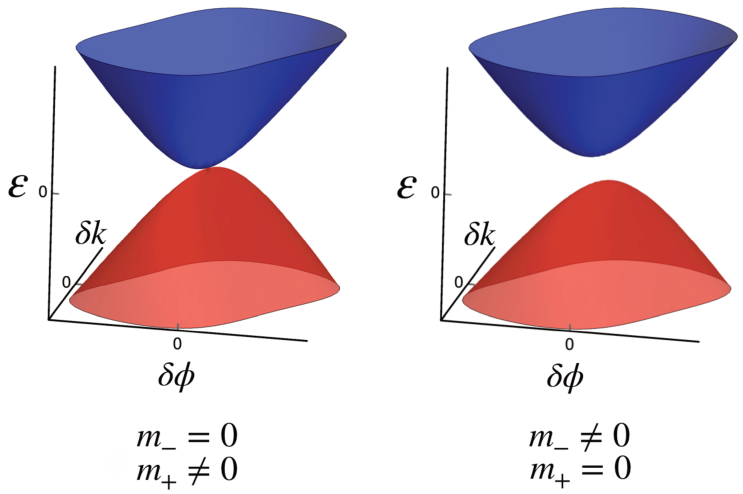

Figure 4.8: Semi-Dirac point B_0 at quasienergy $\varepsilon = 0$ located at $(\phi, k_x) = (\pi, 0)$. This degeneracy point is robust against a perturbation m_+ but a gap opens due to the introduction of m_-.

The cases of the semi-Dirac point C_π and B_0 are depicted in Fig. 4.9, where the spectral flow for B_0 is indeed the opposite to that of C_π. They both illustrate the same phenomenology, like that discussed in the previous section 4.7. In particular, there is a spectral flow around B_0 that coexists with bulk states since the Dirac nodal point A_0 that has the same ϕ coordinate is stable under a perturbation of m_- type.

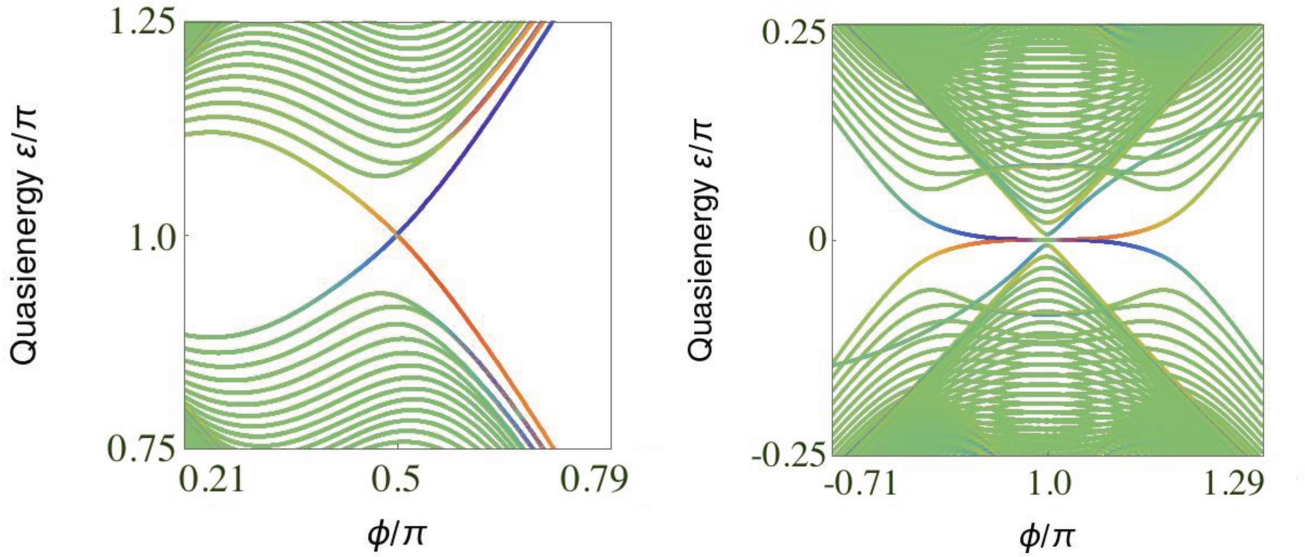

(a) C_π (b) B_0

Figure 4.9: Existence of a spectral flow of modes localized at the two interfaces of the cylindrical geometry (in blue and red), where the mass term m_- changes sign twice, in the vicinity of (a) C_π at quasienergy π, and (b) B_0 at quasienergy 0. In the second case, the spectral flow crosses the Dirac point A_0.

The existence of a spectral flow when a mass term is continuously varied and changes sign is traditionally understood as a mode emerging at the interface between two topologically nonequivalent systems. This description is, of course, meaningful provided that each system's topology is well defined in itself, when the mass term is fixed, like in topological insulators. However, it is not always the case. In particular, in continuous media, the Chern numbers C of the bands are only well defined when the projectors are regularized at infinity (Silveirinha 2015; Souslov, Dasbiswas, et al. 2019; C. Tauber et al. 2019, 2020; G. Volovik 1988). Here, we have provided another model in which the topological properties of the bulk bands are ill-defined but where chiral edge states with a well defined topological origin can however exist. In all these situation, the topological charge approach used here remains thus a powerful valid strategy (Delplace, Marston, et al. 2017; Marciani et al. 2019; Perrot et al. 2019).

4.5 Chiral edge states in gapless systems

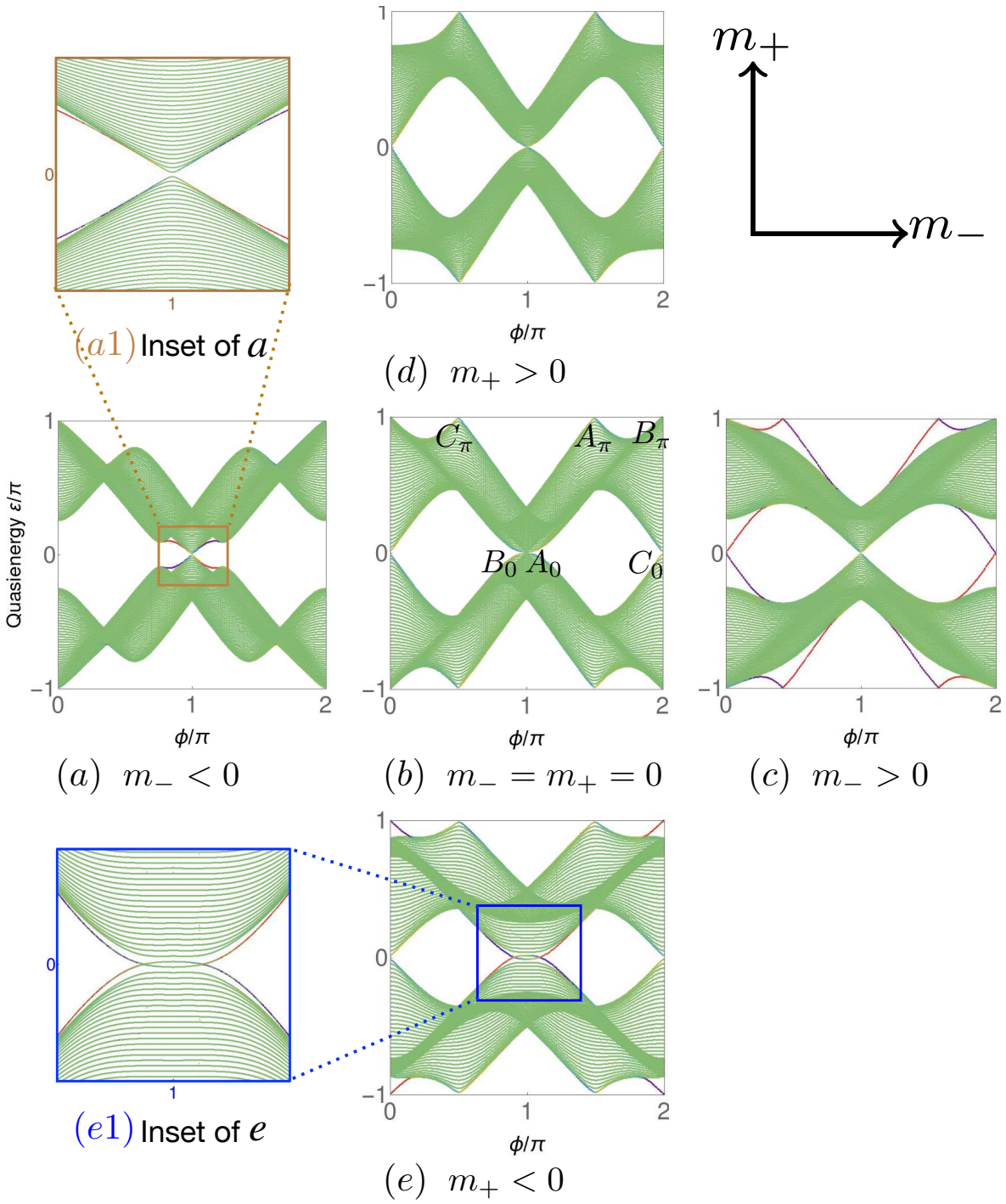

Figure 4.10: Quasienergy spectra of the four-step Floquet operator for $\phi_1 = -\phi_2 = \phi_3 = -\phi_4 = \phi$ in finite geometry as a function of either m_+ or m_-. Imposing a vanishing of either m_+ or m_- prevents a gap opening at 0 and π so that all the spectra are gapless. The two insets (a1) and (e1) show edge states at $\varepsilon = 0$ that merge to the bulk bands and disappear, unlike other chiral edge states for $m_\pm < 0$ that live in local gaps.

Since the topological spectral flow consists in confined modes at the frontier between two domains of $m_\pm$ with opposite signs, a natural question to ask is thus whether chiral states may exist at the boundary of a finite network with a fixed mass term $m_\pm$, that is specifically when the Chern number C of the bands (to be distinguished from the Chern numbers assigned to the degeneracy $\mathcal{C}$ (4.14)) cannot be defined. Quasienergy spectra computed in that geometry are shown in figure 4.10 for different values of uniform $m_\pm$, and different observations can be drawn. We find chiral edge states (with respect to ϕ) at A_π, C_π and C_0 when $m_- > 0$, and at B_π when $m_+ < 0$. Edge states are also found around A_0 for $m_+ < 0$ and B_0 for $m_- < 0$, where the gap remains close.

The first remark is that the sign of $m_\pm$ that gives rise to edge states does not seem obviously related to the topological charge computed above. Moreover, while these edge states look very similar to what can be found in gapped systems for A_π, C_π, C_0 and B_π, as they bridge a local gap, the situation is different for A_0 and B_0 that are affected by the bulk modes. The inset figures show that these edge states actually do not connect the two bands, but eventually couple to the bulk modes and disappear (figures 4.10 (a1) and (e1)). This is in sharp contrast with the continuous interfaces in $m_\pm$ that revealed a continuous spectral flow through the bulk modes (figures 4.7b and 4.9b).

4.6 Summary of Chapter 5 and perspectives

- In a 2D Floquet system, there exists a regime with a gapless spectrum that prohibits the definition of a Chern number for the bands and also the Floquet gap index. We saw that in this gapless spectrum, each nodal point (or line) had associated mass term. If at given quasienergy, there is more than one different mass term, then the mass term shared by the same nodal points (or line) can be lifted all together without affecting the other ones. For this, we provided a general recipe to calculate this mass term. Likewise, by considering a mass term as a continuous function of the position that changes sign, the system then host topological chiral spectral flows of interface states, which can be captured by topological charge. The sign of this charge predicts the direction of the spectral flow. These spectral flows can be interpreted as robust chiral states at the interface between gapless semimetallic phases.

- In the last part, we saw that by considering a finite geometry with open boundary conditions, all the nodal points which are not affected by the bulk modes in the sense of stability under different mass terms, show similar spectral flow to the continuous case, whereas the nodal points that are affected by the bulk modes are in sharp contrast to the continuous case. However, the direction of the spectral flow cannot be a priori known from the edge state spectrum, while in the continuous case, it was one to one with the sign of the topological charge.

- In our semimetal model 1 and 2 there is a priori no need for the system to be Floquet. So, it would be tempting to look for their counterparts in static regime.

- It would be interesting to extend the above model to 3D by introducing another synthetic dimension. It will allow us to look for Weyl semimetal like a phase in this simple

model. Recently, the Weyl semimetal type I has been observed in a double-gyroid 3D photonic crystal with inversion-breaking (Lu et al. 2015) and type II in the 3D laser-written waveguides (Noh et al. 2017). However, both the experimental setups require high-level manufacturing precision, whereas this can be observed in a far more simply in a photonic setup, e.g., circular fibers.

Chapter 5

Appendix

5.1 Demonstration of coupled mode theory: due to waveguide imperfections

If we perturb the waveguide,where the perturbation can come from waveguide imperfections, bending, or surface corrugations. This perturbation perturbs the modes and couples the energy between them (this is very much analogous to the presence of potential term in Schrödinger's equation(1.12), which connects the different states). This boils down to say, when a pure mode is excited in the in the waveguide, then some of its power can get transferred to other modes.

The perturbation to the modes will be described in terms of distributed polarization source, $\mathbf{P}_{pert}$, which accounts for the deviation of the dielectric polarization from the one in unperturbed mode.
Confined mode can be excited and propagate along the axis of the waveguide structure independently provided the dielectric constant $\boldsymbol{\varepsilon}(x,y) = \varepsilon_0 \boldsymbol{n}^2(x,y)$, remains independent of z. However, if there is a dielectric perturbation $\Delta\varepsilon(x,y,z)$ due to waveguide imperfections, bending, or the surface corrugations, result in to the coupling of propagating modes. Which means, if we have excited a pure mode at the beginning of the waveguide, then some of its power may be transferred to other modes. The details of the coupling depends on the dielectric perturbation, i.e. $\Delta\varepsilon(x,y,z)$.

$$\mathbf{D} = \varepsilon\mathbf{E} = \varepsilon_0\mathbf{E} + \mathbf{P} \tag{5.1}$$

(5.2)

Now, any perturbation can be written as, which

$$\tilde{\mathbf{D}} = \varepsilon\mathbf{E} + \mathbf{P}_{pert} \tag{5.3}$$

Then we can write the wave equation,

$$\nabla^2\mathbf{E} = \mu\varepsilon_0\frac{\partial^2\mathbf{E}}{\partial t^2} + \mu\frac{\partial^2\mathbf{P}}{\partial t^2} \tag{5.4}$$

So the total medium polarization,

$$\mathbf{P}(\mathbf{r},t) = \mathbf{P}_0(\mathbf{r},t) + \mathbf{P}_{pert}(\mathbf{r},t), \tag{5.5}$$

where, (5.6)

$$\mathbf{P}_0(\mathbf{r},t) = (\varepsilon(\mathbf{r}) - \varepsilon_0)\mathbf{E}(\mathbf{r},t) \tag{5.7}$$

is the polarization induced by the $\mathbf{E}(\mathbf{r},t)$ in the unperturbed waveguide (one with dielectric constant $\varepsilon(\mathbf{r})$)

$$\nabla^2 E_y - \mu\varepsilon(\mathbf{r})\frac{\partial^2 E_y}{\partial t^2} = \mu\frac{\partial^2 P_{pert}}{\partial t^2} \tag{5.8}$$

and similar expression for E_x and E_z, in general.
We will only consider the coupling between the guided modes not with the unguided (radiation) modes. The field in the perturbed waveguide can be written in terms of the eigenmodes expansion

$$E_y(x,z,t) = \frac{1}{2}\sum_m A_m(z)\mathcal{E}_y^{(m)}(x)e^{i(\omega t - \beta_m z)} + c.c \tag{5.9}$$

To say some words about the above equation, what precisely we have done is that we used unperturbed eigenmode expansion for solving the perturbation. This is very much similar to or analogous to time dependent perturbation theory in quantum mechanics[1]
Each m^{th} eigenmode satisfies[2]

$$\left(\frac{\partial^2}{\partial x^2} - \beta_m^2\right)\mathcal{E}_y^{(m)}(\mathbf{r}) + \omega^2\mu\varepsilon(\mathbf{r})\mathcal{E}_y^{(m)}(\mathbf{r}) = 0 \tag{5.10}$$

Our goal is to develop an expansion for the coupling between amplitudes of the individual modes of the waveguide.

- If there is no coupling(i.e. no perturbation) : we will get the independent some of the eigenmodes in (5.9).
- If there is a coupling: then modes will vary with position.

Let us derive equation for amplitude by substituting (5.9) in (5.8)

$$e^{i\omega t}\frac{1}{2}\sum_m \Bigg[\left(\frac{d^2A_m(z)}{dz^2} - 2i\beta_m\frac{dA_m(z)}{dz} + (\omega^2\mu\varepsilon(\mathbf{r}) - \beta_m^2)A_m\right)\mathcal{E}_y^{(m)}(x)e^{-i\beta_m z} + \frac{\partial^2\mathcal{E}_y^{(m)}}{\partial x^2}A_m e^{-i\beta_m z}\Bigg] + c.c = \mu\frac{\partial^2 P_{pert}}{\partial t^2} \tag{5.11}$$

For further simplification we will make use of the paraxial approximation discussed in section(1.5). We assume slow variation along the axis of propagation z,

$$\left|\frac{d^2A_m(z)}{dz^2}\right| \ll \beta_m\left|\frac{dA_m(z)}{dz}\right| \tag{5.12}$$

[1]There we have φ_n, as the solution for steady state Hamiltonian (H_0) and we write time dependent perturbation, $H_1(t)$, in terms of $\Psi(t) = \sum_n c_n(t)\varphi_n \cdots$. Where our $A_m(z)$ are analogous to $c_n(t)$.
[2]similar to the one in QM, $H_0\varphi_n = E_n\varphi_n$, when $H_1 \to 0$, and here when $P_{pert} \to 0$

Then the above equation is simplified to, also making use of (5.10)

$$\sum_m -i\beta_m \frac{dA_m(z)}{dz}\mathcal{E}_y^{(m)}(x)e^{i(\omega t-\beta_m z)} + c.c \;=\; \mu\frac{\partial^2 P_{pert}}{\partial t^2} \tag{5.13}$$

To simplify this further we make use of orthogonality relation of the modes,

$$\frac{dA_s^{(-)}(z)}{dz}e^{i(\omega t+\beta_m z)} - \frac{dA_s^{(+)}(z)}{dz}e^{i(\omega t-\beta_m z)} - c.c \;=\; -\frac{i}{2\omega}\frac{\partial^2}{\partial t^2}\int_{-\infty}^{\infty} dx P_{pert}\mathcal{E}_y^{(s)}(x), \tag{5.14}$$

it is important to recall that the m summation in (5.13), contains two terms $\pm|m|$ for each $|m|$ involving $\mathcal{E}_y^{(m)}(x)$. Where $(+)$ designates the propagation along $+z$ axis and $(-)$ designates the propagation along $-z$ axis.

We can see from (5.14), that amount of variation of s^{th} amplitude with respect to propagation axis is proportional to the degree of overlap of perturbed polarization(P_{pert}) with modal distribution field $\mathcal{E}_y^{(s)}(x)$.
Equation (5.14) will be the platform or primary equation for different mode interactions. Different situation will correspond to different driving term i.e. RHS of (5.14).

We consider the 2D oriented scattering network defined in the main text, and reproduced in figure 5.1 for the time period of $N = 2$ steps. We detail in this section the derivation of the evolution operator, its quasienergies and the center of mass trajectories showing Bloch oscillations.

5.1.1 Derivation of the Floquet evolution operator

The oriented network shown in figure 5.1 is constituted of two distinct successive scattering nodes S_1 and S_2. The incoming arrow from left (right) toward the S_1 node is denoted by a_1 (b_1). It denotes a time evolution from the time step $j-1$ to time step j. Similarly, the outgoing arrows are denoted by a_2, b_2. These four oriented paths and the two scattering nodes constitute the unit cell of the network, that is emphasized with a dashed square in figure 5.1. The dynamics is then given by the relations

$$\begin{pmatrix} a_2(j,l+1) \\ b_2(j,l-1) \end{pmatrix} = S_1 \begin{pmatrix} a_1(j-1,l) \\ b_1(j-1,l) \end{pmatrix} \tag{5.15}$$

and

$$\begin{pmatrix} a_1(j-1,l) \\ b_1(j-1,l) \end{pmatrix} = S_2 \begin{pmatrix} a_2(j-2,l+1) \\ b_2(j-2,l-1) \end{pmatrix}, \tag{5.16}$$

which can be grouped together as

$$\begin{pmatrix} a_1(j-1,l) \\ b_1(j-1,l) \\ a_2(j,l+1) \\ b_2(j,l-1) \end{pmatrix} = \begin{pmatrix} 0 & S_2 \\ S_1 & 0 \end{pmatrix} \begin{pmatrix} a_1(j-1,l) \\ b_1(j-1,l) \\ a_2(j-2,l+1) \\ b_2(j-2,l-1) \end{pmatrix}. \tag{5.17}$$

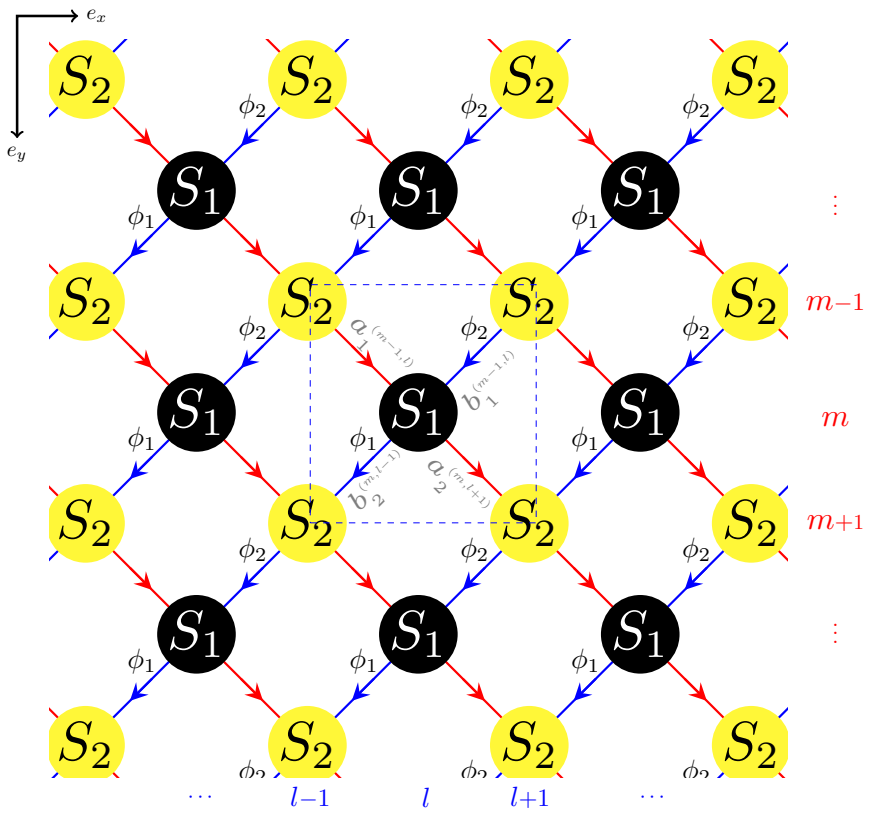

Figure 5.1: 2D oriented two-steps scattering network model with a preferential direction from top to bottom.

The current scattering matrix notations correspond to that of the main text (Eq.(2)), as follows $a_1(j-1,l) = \alpha_l^{j-1}$, $b_1(j-1,l) = \beta_l^{j-1}$, similarly, $a_2(j,l+1) = \alpha_{l+1}^{j}$, $b_2(j,l-1) = \beta_{l-1}^{j}$.

Using translation symmetry of the scattering network, we can Fourier decompose as

$$\begin{pmatrix} a_m(j,l) \\ b_m(j,l) \end{pmatrix} = \sum_{k_x,k_y} \mathrm{e}^{i\vec{k}.(l\hat{e}_x + j\hat{e}_y)/2} \begin{pmatrix} a_m(k_x,k_y) \\ b_m(k_x,k_y) \end{pmatrix}, \quad m = 1,2\ . \tag{5.18}$$

This gives,

$$\begin{pmatrix} a_1(k_x,k_y) \\ b_1(k_x,k_y) \\ a_2(k_x,k_y) \\ b_2(k_x,k_y) \end{pmatrix} = \begin{pmatrix} 0 & 0 & s_2^{11}\mathrm{e}^{ik_x/2}\mathrm{e}^{-ik_y/2} & s_2^{12}\mathrm{e}^{-ik_x/2}\mathrm{e}^{-ik_y/2} \\ 0 & 0 & s_2^{21}\mathrm{e}^{ik_x/2}\mathrm{e}^{-ik_y/2} & s_2^{22}\mathrm{e}^{-ik_x/2}\mathrm{e}^{-ik_y/2} \\ s_1^{11}\mathrm{e}^{ik_x/2}\mathrm{e}^{-ik_y/2} & s_1^{12}\mathrm{e}^{-ik_x/2}\mathrm{e}^{-ik_y/2} & 0 & 0 \\ s_1^{21}\mathrm{e}^{ik_x/2}\mathrm{e}^{-ik_y/2} & s_1^{22}\mathrm{e}^{-ik_x/2}\mathrm{e}^{-ik_y/2} & 0 & 0 \end{pmatrix} \begin{pmatrix} a_1(k_x,k_y) \\ b_1(k_x,k_y) \\ a_2(k_x,k_y) \\ b_2(k_x,k_y) \end{pmatrix} \tag{5.19}$$

$$\begin{pmatrix} \vec{a_1}(\vec{k}) \\ \vec{a_2}(\vec{k}) \end{pmatrix} = \begin{pmatrix} 0 & S_2(\vec{k}) \\ S_1(\vec{k}) & 0 \end{pmatrix} \begin{pmatrix} \vec{a_1}(\vec{k}) \\ \vec{a_2}(\vec{k}) \end{pmatrix} \tag{5.20}$$

where $\vec{a_1}(\vec{k}) = \{a_1(\vec{k}), b_1(\vec{k})\}$ and $s_j^{m_1 m_2}$ $(m_1, m_2 = 1,2)$, are the scattering coefficients of the

scattering matrix S_j. In the main text, we choose the specific form

$$S_j = \begin{pmatrix} \cos\theta_j & i\sin\theta_j \\ i\sin\theta_j & \cos\theta_j \end{pmatrix}. \tag{5.21}$$

although, the calculations are independent of this specific form. Squaring Eq.(5.20) allows one to define the Floquet operators starting for different time origins as

$$\begin{pmatrix} S_2(\vec{k})S_1(\vec{k}) & 0 \\ 0 & S_1(\vec{k})S_2(\vec{k}) \end{pmatrix} = \begin{pmatrix} U_F^{21}(\vec{k}) & 0 \\ 0 & U_F^{12}(\vec{k}) \end{pmatrix} \tag{5.22}$$

Substituting Eq.(5.21) gives more specifically

$$U_F^{21}(\vec{k}) = \begin{pmatrix} e^{-ik_y}(e^{ik_x}\cos\theta_1\cos\theta_2 - \sin\theta_1\sin\theta_2) & ie^{-ik_y}(\cos\theta_2\sin\theta_1 + e^{-ik_x}\cos\theta_1\sin\theta_2) \\ ie^{-ik_y}(\cos\theta_2\sin\theta_1 + e^{ik_x}\cos\theta_1\sin\theta_2) & e^{-ik_y}(e^{-ik_x}\cos\theta_1\cos\theta_2 - \sin\theta_1\sin\theta_2) \end{pmatrix} \tag{5.23}$$

$$U_F^{12}(\vec{k}) = \begin{pmatrix} e^{-ik_y}(e^{ik_x}\cos\theta_1\cos\theta_2 - \sin\theta_1\sin\theta_2) & ie^{-ik_y}(e^{-ik_x}\cos\theta_2\sin\theta_1 + \cos\theta_1\sin\theta_2) \\ ie^{-ik_y}(e^{ik_x}\cos\theta_2\sin\theta_1 + \cos\theta_1\sin\theta_2) & e^{-ik_y}(e^{-ik_x}\cos\theta_1\cos\theta_2 - \sin\theta_1\sin\theta_2) \end{pmatrix} \tag{5.24}$$

Then, we add a phase ϕ to the b_j amplitudes, that is to the blue arrows in Fig. (5.1), such that $b_1 \to b_1 e^{i\phi_2}$ and $b_2 \to b_2 e^{i\phi_1}$. Then in Eq.(5.19), s_2^{12} and s_2^{22} will be multiplied by $e^{i\phi_1}$, likewise, s_1^{12} and s_1^{22} are multiplied by $e^{i\phi_2}$. That gives

$$U_F^{21}(\vec{k},\phi) = e^{-ik_y}\begin{pmatrix} e^{ik_x}\cos\theta_1\cos\theta_2 - e^{i\phi_1}\sin\theta_1\sin\theta_2 & i(e^{i\phi_2}\cos\theta_2\sin\theta_1 + e^{-ik_x}\cos\theta_1\sin\theta_2) \\ i(e^{i\phi_1}\cos\theta_2\sin\theta_1 + e^{ik_x}\cos\theta_1\sin\theta_2) & e^{-ik_x}\cos\theta_1\cos\theta_2 - e^{i\phi_2}\sin\theta_1\sin\theta_2 \end{pmatrix} \tag{5.25}$$

$$U_F^{12}(\vec{k},\phi) = e^{-ik_y}\begin{pmatrix} e^{ik_x}\cos\theta_1\cos\theta_2 - e^{i\phi_2}\sin\theta_1\sin\theta_2 & i(e^{-ik_x}\cos\theta_2\sin\theta_1 + e^{i\phi_1}\cos\theta_1\sin\theta_2) \\ i(e^{ik_x}\cos\theta_2\sin\theta_1 + e^{i\phi_2}\cos\theta_1\sin\theta_2) & e^{-ik_x}\cos\theta_1\cos\theta_2 - e^{i\phi_1}\sin\theta_1\sin\theta_2 \end{pmatrix}. \tag{5.26}$$

These two evolution operators describe the same physical system, and either of them can be used to compute the quasienergy spectrum and the winding numbers. The common phase factor $\exp\{-ik_y\}$ in Eqs.(5.25)-(5.26) is reminiscent of the preferential orientation of the network from top to bottom. This is the only k_y dependence of the evolution operator on the network. In the main text, the Floquet operator refers to U_F^{21} where this phase factor is factorized out, that is

$$U_F(k_x,\phi) \equiv U_F^{21}(k,\phi)e^{ik_y} \tag{5.27}$$

and we set $k_x = k$ through out the paper. The eigenvalues of U_F are defined as $e^{-i\epsilon T} \equiv e^{i\varepsilon}$, where the dimensionless quasienergy ε is the quantity considered in the main text. Then the Floquet operator can usefully be factorized as

$$U_F = B_0(k)S_2D(\phi_2)B_1(k)S_1D(\phi_1), \tag{5.28}$$

where

$$B_1(k) = \begin{pmatrix} 1 & 0 \\ 0 & e^{-ik} \end{pmatrix}, \; B_0 = \begin{pmatrix} e^{ik} & 0 \\ 0 & 1 \end{pmatrix}, \; D_j = D(\phi_j) = \begin{pmatrix} 1 & 0 \\ 0 & e^{i\phi_j} \end{pmatrix}. \tag{5.29}$$

5.1.2 Derivation of the quasienergy bands

Let us derive now the quasienergy bands of the scattering model, that is, diagonalizing the Floquet operator. This can be carried out analytically either by a direct diagonalization of U_F or equivalently by decomposing the evolution as in Ref (Wimmer, Hannah M Price, et al. 2017). Let us detail the second strategy. Using the same terminology as in the main text, where right going arrows are denoted with α and left going with β, then the time evolution is described by

$$\begin{aligned} \alpha_l^{m+1} &= (\cos\theta_1 \alpha_{l+1}^m + i \sin\theta_1 \beta_{l+1}^m) \mathrm{e}^{i\phi_1}, \\ \beta_l^{m+1} &= \cos\theta_1 \beta_{l-1}^m + i \sin\theta_1 \alpha_{l-1}^m \end{aligned} \tag{5.30}$$

for the first step and

$$\begin{aligned} \alpha_{l-1}^{m+2} &= \left(\cos\theta_2 \alpha_l^{m+1} + i \sin\theta_2 \beta_l^m\right) \mathrm{e}^{i\phi_2}, \\ \beta_{l-1}^{m+2} &= \cos\theta_2 \beta_{l-2}^m + i \sin\theta_2 \alpha_{l-2}^m \end{aligned} \tag{5.31}$$

for the second (final) step. Using Floquet-Bloch ansatz,

$$\begin{pmatrix} \alpha_l^m \\ \beta_l^m \end{pmatrix} = \begin{pmatrix} A \\ B \end{pmatrix} \mathrm{e}^{i\varepsilon m/2} \mathrm{e}^{ikl/2} \tag{5.32}$$

and substituting Eq.(5.30) in (5.31) using Eq.(5.32) gives the determinant problem

$$\mathrm{e}^{2i\varepsilon} - \left[\cos\theta_1 \cos\theta_2 \left(\mathrm{e}^{ik} \mathrm{e}^{i(\phi_1+\phi_2)} + \mathrm{e}^{-ik}\right) - \sin\theta_1 \sin\theta_2 \left(\mathrm{e}^{i\phi_1} + \mathrm{e}^{i\phi_2}\right)\right] \mathrm{e}^{i\varepsilon} + \mathrm{e}^{i(\phi_1+\phi_2)} = 0 \,. \tag{5.33}$$

By rewriting the Eq.(5.33), we get the relation

$$\cos\left(\varepsilon - \frac{\phi_1+\phi_2}{2}\right) = \cos\theta_1 \cos\theta_2 \cos\left(k + \frac{\phi_1+\phi_2}{2}\right) - \sin\theta_1 \sin\theta_2 \cos\left(\frac{\phi_1-\phi_2}{2}\right),$$

that leads to

$$\varepsilon(k,\phi) = \pm \cos^{-1}\left[\cos\theta_1 \cos\theta_2 \cos\left(-k + \frac{\phi_1+\phi_2}{2}\right) - \sin\theta_1 \sin\theta_2 \cos\left(\frac{\phi_1-\phi_2}{2}\right)\right] + \left(\frac{\phi_1+\phi_2}{2}\right) \tag{5.34}$$

We can finally substitute the general form for the ϕ's to $\phi_j = (m_j/n_j)\phi$, to get the expression

$$\varepsilon(k,\phi) = \pm \cos^{-1}\left[\cos\theta_1 \cos\theta_2 \cos\left(-k + \left[\frac{m_1}{n_1} + \frac{m_2}{n_2}\right]\frac{\phi}{2}\right) - \sin\theta_1 \sin\theta_2 \cos\left(\left[\frac{m_1}{n_1} - \frac{m_2}{n_2}\right]\frac{\phi}{2}\right)\right] + \left[\frac{m_1}{n_1} + \frac{m_2}{n_2}\right]\frac{\phi}{2} \tag{5.35}$$

for the quasienergy bands.

5.1.3 Derivation of the group velocities

Let us introduce $\Delta^- \equiv \frac{m_1}{n_1} - \frac{m_2}{n_2}$ and $\Delta^+ \equiv \frac{m_1}{n_1} + \frac{m_2}{n_2}$. Then the "synthetic group velocity" is defined as

$$v_\phi(k,\phi) \equiv \frac{\partial\varepsilon(k,\phi)}{\partial\phi} \tag{5.36}$$

where we substitute the Eq. (5.35) of the quasienergy bands to get

$$v_\phi(k,\phi) = \frac{1}{2}\Delta^+ \mp \frac{1}{2}\frac{\Delta^- \sin\theta_1 \sin\theta_2 \sin\left(\frac{1}{2}\phi\Delta^-\right) - \Delta^+ \cos\theta_1 \cos\theta_2 \sin\left(k+\frac{1}{2}\phi\Delta^+\right)}{\sqrt{1-\left(\cos\theta_1\cos\theta_2\cos\left(k+\frac{1}{2}\phi\Delta^+\right) - \sin\theta_1\sin\theta_2\cos\left(\frac{1}{2}\phi\Delta^-\right)\right)^2}}. \quad (5.37)$$

Similarly, the transverse group velocity is

$$v_k(k,\phi) = \frac{\partial\varepsilon(k,\phi)}{\partial k} \quad (5.38)$$

$$v_k(k,\phi) = \pm\frac{\cos\theta_1\cos\theta_2\sin\left(k+\frac{1}{2}\phi\Delta^+\right)}{\sqrt{1-\left(\cos\theta_1\cos\theta_2\cos\left(k+\frac{1}{2}\phi\Delta^+\right) - \sin\theta_1\sin\theta_2\cos\left(\frac{1}{2}\phi\Delta^-\right)\right)^2}}. \quad (5.39)$$

For our case $(m_1 = 1, n_1 = 1, m_2 = -2, n_2 = 1)$, energy dispersion relation simplifies to

$$\varepsilon(k,\phi) = \pm\cos^{-1}\left[\cos\theta_1\cos\theta_2\cos\left(k-\frac{\phi}{2}\right) - \sin\theta_1\sin\theta_2\cos\left(\frac{3\phi}{2}\right)\right] + \frac{\phi}{2}. \quad (5.40)$$

Similarly, the expression for both the group and the synthetic group velocity is

$$v_{gk}(k,\phi) = \pm\frac{\cos\theta_1\cos\theta_2\sin\left(k-\frac{\phi}{2}\right)}{\sqrt{1-\left(\cos\theta_1\cos\theta_2\cos\left(k-\frac{\phi}{2}\right) - \sin\theta_1\sin\theta_2\cos\left(\frac{3\phi}{2}\right)\right)^2}}, \quad (5.41)$$

$$v_{g\phi}(k,\phi) = \frac{1}{2} \mp \frac{\frac{3}{2}\sin\theta_1\sin\theta_2\sin\left(\frac{3\phi}{2}\right) + \frac{1}{2}\cos\theta_1\cos\theta_2\sin\left(k-\frac{\phi}{2}\right)}{\sqrt{1-\left(\cos\theta_1\cos\theta_2\cos\left(k-\frac{\phi}{2}\right) - \sin\theta_1\sin\theta_2\cos\left(\frac{3\phi}{2}\right)\right)^2}}. \quad (5.42)$$

Mathematically, the numerator in the Eq.(5.38) for group velocity contains the term $\sin\left(k+\frac{1}{2}\phi\Delta^+\right)$, which can essentially change the sign on changing ϕ, for some fixed value of $k = k_0$. It only happens because Δ^+ is non-zero in case of winding in ϕ that gives rise to the wave-packet oscillations.

Along the same lines, we can calculate the motion of centre of mass from Eq. (5.41), for arbitrary k as,

$$X(t',k) = \int_0^{t'} \mathrm{d}\phi\, v_{gk}(\phi(t),k)\left(\frac{\partial\phi}{\partial t}\right)^{-1}, = \int_0^{t'} \mathrm{d}\phi\, v_{gk}(\phi(t),k) \quad (5.43)$$

where in the last equation, we used the case where ϕ varies linearly with the time with unit slope, and t' is the $y-$axis in Fig. 3.11.

5.2 Calculation of the winding number ν_ϕ

Let us compute the winding number ν_ϕ defined in the main text, for $N = 2$ time-steps, where the Floquet operator $U_F(k,\phi)$ given in Eq. (5.28) with $\phi_1 = (m_1/n_1)\phi$ and $\phi_2 = (m_2/n_2)\phi$. When

$|m_1/n_1| \neq |m_2/n_2|$, then

$$\begin{aligned}
\nu_\phi &= \frac{1}{2\pi i}\int_0^{T_\phi} \mathrm{d}\phi\, \mathrm{Tr}\left[U_F^{-1}\partial_\phi U_F\right] && (5.44)\\
&= \frac{1}{2\pi i}\int_0^{T_\phi} \mathrm{d}\phi\, \mathrm{Tr}\Big[D_1^\dagger S_1^\dagger B_1^\dagger(k) D_2^\dagger S_2^\dagger B_0^\dagger(k)\partial_\phi\{D_1 S_1 B_1(k) D_2 S_2 B_0(k)\}\Big] && (5.45)\\
&= \frac{1}{2\pi i}\int_0^{T_\phi} \mathrm{d}\phi\, \mathrm{Tr}\Big[D_2^\dagger\partial_\phi D_2 + D_1^\dagger\partial_\phi D_1\Big] && (5.46)
\end{aligned}$$

where the period of T_ϕ of the quasienergy in ϕ is inferred from the analytical expression (5.35). More precisely, it reads

$$T_\phi = 2\pi\ \mathrm{LCM}\left[\frac{2}{\frac{m_1}{n_1}-\frac{m_2}{n_2}}, \frac{2}{\frac{m_1}{n_1}+\frac{m_2}{n_2}}\right] \tag{5.47}$$

where LCM stands for least common multiple. Replacing the D_j's matrices by their expression, one gets

$$\begin{aligned}
\nu_\phi &= \frac{1}{2\pi i}\int_0^{2\pi\ \mathrm{LCM}\left[\frac{2}{\frac{m_1}{n_1}-\frac{m_2}{n_2}}, \frac{2}{\frac{m_1}{n_1}+\frac{m_2}{n_2}}\right]} \mathrm{d}\phi\, \mathrm{Tr}\left[i\frac{m_1}{n_1} + i\frac{m_2}{n_2}\right],\\
&= 2\ \mathrm{LCM}\left[\frac{1}{\frac{m_1}{n_1}-\frac{m_2}{n_2}}, \frac{1}{\frac{m_1}{n_1}+\frac{m_2}{n_2}}\right]\left(\frac{m_1}{n_1}+\frac{m_2}{n_2}\right),\\
&= 2\ \mathrm{LCM}\left[\frac{2n_1n_2}{m_1n_2-m_2n_1}, \frac{2n_1n_2}{m_1n_2+m_2n_1}\right]\left(\frac{m_1}{n_1}+\frac{m_2}{n_2}\right),\\
\nu_\phi &= \frac{T_\phi}{2\pi}\left(\frac{m_1}{n_1}+\frac{m_2}{n_2}\right). && (5.48)
\end{aligned}$$

5.3 Relation between winding number and the stationary points

Consider a situation where the quasienergy bands wind along ϕ, and let us count the number of stationary points $\frac{\mathrm{d}X_c}{\mathrm{d}t}$ in Eq.(5.43) over one Bloch period of oscillation. These points are determined by the vanishing of the group velocity v_k. Therefore, it suffices to find the number of roots in ϕ of Eq.(5.38), which are given by

$$\cos\theta_1\cos\theta_2\sin\left(\frac{1}{2}\phi\Delta^+\right) = 0 \tag{5.49}$$

This leads to

$$\begin{aligned}
\frac{1}{2}\phi\Delta^+ &= p\pi, \qquad p\in\mathbb{Z}\\
\phi &= 2p\pi\frac{1}{\Delta^+}. && (5.50)
\end{aligned}$$

which can be expressed in terms of the winding number given by Eq.(5.48) as

$$\phi = p\frac{T_\phi}{\nu_\phi}. \tag{5.51}$$

Hence, over one oscillation period, p takes values from the set $\{1, ..., |\nu_\phi|\}$, and thus the group velocity vanishes ν_ϕ times. Then, following the same lines, one can easily check that the second derivative also vanishes at these same points. There are therefore ν_ϕ turning points per period of Bloch oscillation.

5.4 Fictitious electric field in the network model

5.4.1 Gauge transformation from a uniform electric field to winding bands with an adiabatic increase of ϕ

As pointed out by M. Wimmer et al. in Ref. (Wimmer, Mohammed-Ali Miri, et al. 2015) in the case of a single step model ($N = 1$) with an adiabatic increase of the phase factor $\phi(j) = \gamma_0\, j$, the gauge transformation:

$$\begin{aligned} \alpha_l^{j+1} &= \tilde{\alpha}_l^{j+1} \mathrm{e}^{-\frac{il j\gamma_0}{2} + \frac{ij^2\gamma_0}{4} - \frac{ij\gamma_0}{4}} \\ \beta_l^{j+1} &= \tilde{\beta}_l^{j+1} \mathrm{e}^{-\frac{il j\gamma_0}{2} + \frac{ij^2\gamma_0}{4} - \frac{ij\gamma_0}{4}} \end{aligned} \tag{5.52}$$

results in a set of equations in which the phase factor does not depend anymore on the time step, but presents a uniform gradient of phase :

$$\begin{aligned} \tilde{\alpha}_l^{j+1} &= (\cos\theta_j \tilde{\alpha}_{l+1}^j + i \sin\theta_m \tilde{\beta}_{l+1}^j) \mathrm{e}^{\frac{i\gamma_0 l}{2}} \\ \tilde{\beta}_l^{j+1} &= (i \sin\theta_j \tilde{\alpha}_{l-1}^j + \cos\theta_m \tilde{\beta}_{l-1}^j) \mathrm{e}^{\frac{i\gamma_0 l}{2}} \ . \end{aligned} \tag{5.53}$$

This set of equations corresponds to a scattering network subject to a homogeneous spatial phase gradient $V = E \cdot l$, where $E = \gamma_0/2$ can be interpreted as a homogeneous electric field along the l direction. When considering an initial wavepacket, the time evolution results in standard Bloch oscillations with period $T = 2\pi/E = 4\pi/\gamma_0$.

The same gauge transformation can be applied to each of the two-steps of the model with $n = 2$ discussed in the main text subject to an adiabatic increase of $\phi(j) = +\gamma_0 j$ (Fig. 3 of the main text).

Recall that in the first step $\phi_1(j) = (m_1/n_1)\gamma_0 j$ and in the second step $\phi_2(j) = (m_2/n_2)\gamma_0 j$. The transformation (5.52) results in a set of the Bloch-like Eqs.(5.53) for each of the two Floquet steps, each set characterized by a constant electric field in space. In the first step, the electric field is $E_1 = (m_1/n_1)\gamma_0/2$, and in the second step is $E_2 = (m_2/n_2)\gamma_0/2$. Therefore, we get back the Bloch oscillation picture in this case with an electric field that alternates between E_1 and E_2 at each subsequent step. The period T_B of the oscillations can be computed from the average electric field $(E_1 + E_2)/2$ over a full Floquet cycle.

The above discussion can also be simply understood from basic classical electrodynamics arguments (Krieger et al. 1986; Zak 1988). Indeed, in its most general form, an electric field can be expressed as $\mathbf{E} = -\nabla V + \partial\mathbf{A}/\partial t$. The Eq.(5.52) is the gauge transformation that transforms a gradient of spatial potential V, to a time-varying vector potential A.

5.4.2 Fictitious uniform electric field from a fictitious vector potential

The above discussion can also seen from the Floquet operator Eq.(5.28) (also defined in eq.(3) in the main text) using the simplification as in Eq.(3.16),

$$U_F(k, \phi) = \mathrm{e}^{i(\phi_1+\phi_2)/2}\, B(k)\, S_2\, \tilde{D}(\phi_2)\, B(k)\, S_1\, \tilde{D}(\phi_1) \ , \tag{5.54}$$

where B and $\tilde{D}$ are defined in Eq.(**??**) and Eq.(**??**). Then U_F can be further simplified by combining two diagonal matrices $\tilde{D}$ and B together, to give $\tilde{C}$ as

$$U_F(k,\phi) = \mathrm{e}^{i(\phi_1+\phi_2)/2}\,\tilde{C}_1(\tilde{k}_1)\,S_2\,\tilde{C}_2(\tilde{k}_2)\,S_1, \tag{5.55}$$

$$\text{where} \quad \tilde{C}_j(\tilde{k}_j) = \begin{pmatrix} \mathrm{e}^{i\tilde{k}_j/2} & 0 \\ 0 & \mathrm{e}^{-i\tilde{k}_j/2} \end{pmatrix} \tag{5.56}$$

where $\tilde{k}_j = k - \phi_j$. This form of the Floquet operator can be thought as describing a 1D lattice that is periodically driven in the presence of a time-varying vector potential $A(t) = Et$. The period T of this driving consists of two-steps where the vector potential redefines the Bloch momentum via Peierls' substitution. In the first step, for some fictitious charge q, $\phi_1 = qA_1 = qE_1t$ that generates a fictitious electric field of magnitude E_1. Similarly, during the second step, $\phi_2 = qA_2 = qE_2t$. This electric field translates in our case as $\phi_1 = -2\phi = -2qE$ and $\phi_2 = +\phi = +qE$. Thus, it gives rise to a net electric field $E_1 + E_2 \neq 0$, which is responsible for the Bloch oscillations.

5.5 Extended network model for quasienergy winding in k

5.5.1 Derivation of the winding number ν_k

For an arbitrary winding number in k and ϕ, the Floquet operator reads

$$U_F(k,\phi) = B_0(k_2)\,S_2\,D(\phi_2)\,B_1(k_1)\,S_1\,D(\phi_1) \tag{5.57}$$

where, $k_j \equiv \left(\frac{r_j}{s_j}\right)k$ and $\phi_j \equiv \left(\frac{m_j}{n_j}\right)\phi$. This gives the quasienergies $\varepsilon_\pm(k,\phi)$

$$\varepsilon_\pm(k,\phi) = \pm\cos^{-1}\left[\cos\theta_1\cos\theta_2\cos\left(\delta^-\frac{k}{2}+\Delta^+\frac{\phi}{2}\right) - \sin\theta_1\sin\theta_2\cos\left(\delta^+\frac{k}{2}-\Delta^-\frac{\phi}{2}\right)\right] + \delta^+\frac{k}{2} + \Delta^+\frac{\phi}{2} \tag{5.58}$$

where, $\delta^+ \equiv \frac{r_1}{s_1}+\frac{r_2}{s_2}$ and $\delta^- \equiv \frac{r_1}{s_1}-\frac{r_2}{s_2}$. In the absence of a quasienergy winding along ϕ (or k), the corresponding δ^+ (Δ^+) terms vanish. The group velocity can then be derived exactly as

$$v_{g\pm}(\phi,k) = \frac{1}{2}\delta^+ \pm \frac{1}{2}\frac{\delta^+\sin\theta_1\sin\theta_2\sin\left(\delta^+\frac{k}{2}-\Delta^-\frac{\phi}{2}\right) - \delta^-\cos\theta_1\cos\theta_2\sin\left(\delta^-\frac{k}{2}+\Delta^+\frac{\phi}{2}\right)}{\sqrt{1-\left(\cos\theta_1\cos\theta_2\cos\left(\delta^-\frac{k}{2}+\Delta^+\frac{\phi}{2}\right) - \sin\theta_1\sin\theta_2\cos\left(\delta^+\frac{k}{2}-\Delta^-\frac{\phi}{2}\right)\right)^2}} \tag{5.59}$$

Next, the winding number in k can be computed similarly to ν_ϕ as

$$\begin{aligned}
\nu_k &\equiv \frac{1}{2\pi i}\int_0^{T_k} \mathrm{d}k\, \mathrm{Tr}\left[U_F^{-1}\partial_k U_F\right] \qquad (5.60)\\
&= \frac{1}{2\pi i}\int_0^{T_k} \mathrm{d}k\, \mathrm{Tr}\left[i\frac{r_1}{s_1}+i\frac{r_2}{s_2}\right],\\
&= 2\ \mathrm{LCM}\left[\frac{1}{\frac{r_1}{s_1}-\frac{r_2}{s_2}}, \frac{1}{\frac{r_1}{s_1}+\frac{r_2}{s_2}}\right]\left(\frac{r_1}{s_1}+\frac{r_2}{s_2}\right),\\
&= 2\ \mathrm{LCM}\left[\frac{2s_1s_2}{r_1s_2-r_2s_1}, \frac{2s_1s_2}{r_1s_2+r_2s_1}\right]\left(\frac{r_1}{s_1}+\frac{r_2}{s_2}\right),\\
\nu_k &= \frac{T_k}{2\pi}\left(\frac{r_1}{s_1}+\frac{r_2}{s_2}\right) \qquad (5.61)
\end{aligned}$$

where $T_k = 2\pi\ \mathrm{LCM}\left[\frac{2}{\frac{r_1}{s_1}-\frac{r_2}{s_2}}, \frac{2}{\frac{r_1}{s_1}+\frac{r_2}{s_2}}\right]$.

5.6 Relation between the winding number ν_k and the quantized drift Δx

Let us introduce the mean current over a Floquet period T as

$$J \equiv \int_0^T \frac{\mathrm{d}t}{T} j(t) \qquad (5.62)$$

that we express in terms of the instantaneous current $j(t)$

$$j(t) = \int_0^{T_k} \frac{\mathrm{d}k}{T_k} \langle\psi(k,t)|\frac{\mathrm{d}x(t)}{\mathrm{d}t}|\psi(k,t)\rangle, \qquad (5.63)$$

where $|\psi(k,t)\rangle$ is an arbitrary evolving Bloch state, i.e. $|\psi(k,t)\rangle = U(k;t,0)|\psi(k,0)\rangle$ with $U(k;t,0)$ the Block evolution operator from time $t=0$ to arbitrary time $t<T$. Rewriting $U(k;t,0) = U(k;t,T)U(k;T,t)$, and using the relation $i\frac{\partial U_F}{\partial k} = \int_0^T \mathrm{d}t\, U(k;T,t)\,\frac{\partial H(k,t)}{\partial k}\,U(k;t,0)$, where $H(k,t+T)=H(k,t)$ is the periodically driven Bloch Hamiltonian, the mean current can be written in terms of the Floquet operator only

$$J = -\frac{2\pi/T_k}{T}\int_0^{T_k}\frac{\mathrm{d}k}{2\pi i}\,\langle\psi(k,0)|\,U_F^{-1}\frac{\partial U_F}{\partial k}\,|\psi(k,0)\rangle \qquad (5.64)$$

Equivalently, one assigns a mean displacement $\Delta x = TJ$ to this current.

5.6.1 Adiabatic regime

Consider an instantaneous eigenstate $\varphi^{(n)}(k,t)$ of $H(k,t)$, such that $\psi(k,0)=\varphi^{(n)}(k,t=0)$. In the adiabatic limit, $\varphi^{(n)}(k,t)$ remains an eigenstate of $H(k,t)$ at each time. After a cycle $t:0\to T$, $\varphi^{(n)}(k,0)$ can only acquire a phase, which is by definition the quasienergy $\epsilon_n T$. It is thus an eigenstate of the Floquet operator, which therefore allows the spectral decomposition $U_F = \sum_n^N \exp(-i\epsilon_n T)|\varphi^{(n)}(k,0)\rangle\langle\varphi^{(n)}(k,0)|$, so that the mean current (5.64) simply becomes

$$J_{ad}^{(n)} = -\frac{2\pi/T_k}{T}\int_0^{T_k}\frac{\mathrm{d}k}{2\pi}\frac{\partial\varepsilon_n}{\partial k} \qquad (5.65)$$

where the dimensionless quasienergy $\varepsilon_n = -\epsilon_n T$ corresponds to that of the main text. The adiabatic pumped current is quantized in terms of the quasienergy winding numbers along the k direction, as found in Ref (Kitagawa, Berg, et al. 2010). As pioneered by Thouless (Thouless 1983), this quantization can be consistently rephrased in terms of the Chern numbers C_n of the adiabatically driven eigenstates $\varphi^{(n)}(k,t)$ that defined a $U(1)-$fiber bundle over the two-dimensional torus span by (k,t), assuming the instantaneous energy band $E_n(k,t)$ (the eigenvalue of $H(k,t)$) remains well separated from the other bands. One way to see the connection between the two topological points of view consists in identifying the quasienergy in terms of the dynamical phase and the geometrical Berry phase

$$\epsilon_n T = E_n T + i \int_0^T \mathrm{d}t \langle \varphi^{(n)}(k,t) | \partial_t | \varphi^{(n)}(k,t) \rangle \ . \tag{5.66}$$

Taking, the "winding" of this expression, that is applying $\int \mathrm{d}k \partial_k$ yields

$$-\int \frac{\mathrm{d}k}{2\pi} \partial_k \varepsilon_n = i \int \frac{\mathrm{d}k}{2\pi} \int_0^T \partial_k \mathrm{d}t \langle \varphi^{(n)}(k,t) | \partial_t | \varphi^{(n)}(k,t) \rangle \tag{5.67}$$

since the instantaneous energy band $E_n(k,t)$ cannot wind along k. Inserting the relation $\partial_k \langle \varphi | \partial_t \varphi \rangle = \langle \partial_k \varphi | \partial_t \varphi \rangle - \langle \partial_t \varphi | \partial_k \varphi \rangle + \partial_t \langle \varphi | \partial_k \varphi \rangle$, into the right-hand side of (5.67), the quasienergy winding reads

$$-\int \frac{\mathrm{d}k}{2\pi} \partial_k \varepsilon_n = \frac{1}{2\pi} \int_0^T \int \mathrm{d}k F^{(n)}_{k,t} + \int_0^T \partial_t Z^{(n)}(t) \tag{5.68}$$

where $F^{(n)}_{k,t}$ is the Berry curvature and $Z^{(n)}(t)$ is the time-dependent Zak phase of the instantaneous state $\varphi^{(n)}$, i.e. $Z^{(n)}(t) \equiv i \int \mathrm{d}k \langle \varphi^{(n)}(k,t) | \partial_k \varphi^{(n)}(k,t) \rangle$. After an adiabatic cycle, one has $Z^{(n)}(T) = Z^{(n)}(0)$, which leads to the relation between the winding number $\nu_k^{(n)}$ of the quasienergy band n in the k direction and the Chern number C_n of the adiabatically periodically driven Bloch eigenstate $\varphi^{(n)}(k,t)$

$$-\int \frac{\mathrm{d}k}{2\pi} \partial_k \varepsilon_n = C_n \ . \tag{5.69}$$

When the α lowest bands are filled, the adiabatic pumped current reads

$$\bar{J}_\alpha = \sum_{n=1}^{\alpha} J^{(n)}_{ad} = \frac{2\pi/T_k}{T} \sum_{n=1}^{\alpha} C_n \tag{5.70}$$

in agreement with the famous Thouless result on adiabatic pumping. Clearly, if all the bands are filled, then $\bar{J}_N = \nu_k = 0$ owing to the vanishing sum of the Chern numbers over all the bands.

5.6.2 Non-adiabatic regime

We now consider the case where the instantaneous eigenstates $\varphi^{(n)}(k,t)$ do not remain eigenstates during the evolution, so that the total mean current $\bar{J}_N$ reads

$$\bar{J}_N = \sum_{n=1}^{N} \int_0^T \frac{\mathrm{d}t}{T} \int_0^{T_k} \frac{\mathrm{d}k}{T_k} \langle \varphi^{(n)}(k,t) | \frac{\mathrm{d}x(t)}{\mathrm{d}t} | \varphi^{(n)}(k,t) \rangle \tag{5.71}$$

$$= -\frac{2\pi/T_k}{T} \int_0^{T_k} \frac{\mathrm{d}k}{2\pi i} \mathrm{tr} \left[U_F^{-1} \frac{\partial U_F}{\partial k} \right] \tag{5.72}$$

$$= -\frac{2\pi/T_k}{T} \nu_k \tag{5.73}$$

with $\nu_k \in \mathbb{Z}$ is the winding number of the map $k \in S^1 \to U_F \in U(N)$, and whose another expression is given by Eq.(9) of the main text. Moreover, since $\mathrm{tr}\, U_F^{-1} \frac{\partial U_F}{\partial k} = \frac{\partial}{\partial k} \ln \det U_F$, this winding number reads

$$\nu_k = \sum_{n=1}^{N} \int_0^{T_k} \frac{\mathrm{d}k}{2\pi} \frac{\partial(-\epsilon_n T)}{\partial k} = \sum_{n=1}^{N} \int_0^{T_k} \frac{\mathrm{d}k}{2\pi} \frac{\partial \varepsilon_n}{\partial k} \tag{5.74}$$

so that the mean displacement $\Delta x = T\bar{J}_N$, after P periods T, can be expressed in terms of the sum of the winding of the quasienergies of all the bands

$$\Delta x = -P \frac{2\pi}{T_k} \sum_{n=1}^{N} \int_0^{T_k} \frac{\mathrm{d}k}{2\pi} \frac{\partial \varepsilon_n}{\partial k} \tag{5.75}$$

Chapter 6

Conclusion and perspectives

This thesis has presented a theoretical exploration of topological properties of 2D periodically driven systems in the context of photonics. In the first part, topological regimes beyond that of band insulators are investigated. We have shown the existence of two new topological regimes: the first one is analogous to a semimetallic phase, while the other one exploits the winding of the spectrum thus having no static counterpart. Despite the existence of gapless edge states along with the gapless bulk states, in both the cases, their topological description strongly differs. In the winding regime, one can define a meaningful topological invariant by continuously deforming the bands to end up with a direct bandgap. In this regime, there exists an interplay of two topological properties: one is the winding of the quasienergy bands, and the other is the presence of chiral edge states in finite geometry. The former property manifests as Bloch oscillations of wavepackets, where stationary points in the oscillations are related to the winding number of the bands. This topological property can thus be probed directly in an experiment by the state-of-art technology. For instance, in waveguide arrays (Bellec, Michel, et al. 2017; Rechtsman et al. 2013), circular fibers (Regensburger, Bersch, Hinrichs, et al. 2011; Wimmer, Mohammed-Ali Miri, et al. 2015; Wimmer, Hannah M Price, et al. 2017; Wimmer, Regensburger, et al. 2013) or even quantum walks (L. Zhou et al. 2016). Moreover, the experiments are currently going in the group of Alberto Amo, PhLAM Lille.
In the second regime (semimetallic), we see how degeneracies can be specifically manipulated at the quasienergy 0 or π. Unlike the previous regime, as a consequence of the absence of any kind of gap (direct or indirect) the topology can be captured by enclosing the degeneracies in parameter space and calculating the Berry flux piercing through the enclosed surface.

In the second part of this thesis, we explored how topological properties can be engineered in 1D arrays of evanescently coupled optical waveguides. This is made possible by the interplay between crystalline symmetries of the network and the fundamental symmetries responsible for topology like chiral symmetry. However, due to the generalities of the argument, these concepts can easily be extended to higher dimensions, as well. In these same 1D waveguide networks, we identify the link between breaking bipartiteness of the structure and existence of a symmetry that has been overlooked before, namely the shifted-particle hole symmetry. We clearly point out in the same waveguide arrays its dissimilarity with respect to usual particle-hole symmetry. Similar to particle-hole symmetry, it is also responsible for giving rise to non-trivial topological properties..

Future directions of this study could include how non-Hermiticity can affect the Bloch oscillations and the definition of winding number. In other works, Bloch oscillations have been

observed in non-Hermitian systems that give rise to interesting phenomena, like unidirectional (or non-reciprocal) Bloch oscillations (Longhi 2009; Y.-l. Xu et al. 2016), super-Bloch oscillations (Turker et al. 2016), secondary emissions and resonant restoration of PT symmetry (Wimmer, Mohammed-Ali Miri, et al. 2015), there has been a proposal to probe the non-Hermitian skin effect (i.e. squeezing of bulk states to the edges)[1] by means of frequency Bloch oscillations (instead of usual lattice Bloch oscillations) (Qin et al. 2020).

Likewise, we can ask the non-Hermitian effects to quantized drift. In the recent works, it was seen that topological pumping in non-Hermitian systems can be realized without any dynamical control of (any) parameters of the Hamiltonian. This pumping can occur spontaneously, without having any analog in Hermitian systems (Yuce 2019). Quite recently, the spectral topology of non-Hermitian pumping has been classified using graph-theory, which is distinct from conventional topological classifications of the eigenstate (Lee, L. Li, et al. 2019).

[1] In a finite system, all the eigenmodes are localized at the boundaries. Thus, system is devoid of any extended states, even in the absence of any disorder. This has been connected to the non-Bloch behaviour of the eigenstates (Xiong 2018; Yao, Song, et al. 2018).

Bibliography

Agarwala, Adhip et al. (June 2017). "Topological Insulators in Amorphous Systems". In: *Phys. Rev. Lett.* 118 (23), p. 236402. DOI: 10.1103/PhysRevLett.118.236402. URL: https://link.aps.org/doi/10.1103/PhysRevLett.118.236402.

Albert, Victor V. et al. (Apr. 2015). "Topological Properties of Linear Circuit Lattices". In: *Phys. Rev. Lett.* 114 (17), p. 173902. DOI: 10.1103/PhysRevLett.114.173902. URL: https://link.aps.org/doi/10.1103/PhysRevLett.114.173902.

Altland, Alexander et al. (Jan. 1997). "Nonstandard symmetry classes in mesoscopic normal-superconducting hybrid structures". In: *Phys. Rev. B* 55 (2), pp. 1142–1161. DOI: 10.1103/PhysRevB.55.1142. URL: https://link.aps.org/doi/10.1103/PhysRevB.55.1142.

Anderson, P. W. (Mar. 1958). "Absence of Diffusion in Certain Random Lattices". In: *Phys. Rev.* 109 (5), pp. 1492–1505. DOI: 10.1103/PhysRev.109.1492. URL: https://link.aps.org/doi/10.1103/PhysRev.109.1492.

Armitage, N. P. et al. (Jan. 2018). "Weyl and Dirac semimetals in three-dimensional solids". In: *Rev. Mod. Phys.* 90 (1), p. 015001. DOI: 10.1103/RevModPhys.90.015001. URL: https://link.aps.org/doi/10.1103/RevModPhys.90.015001.

Asbóth, J. K. (Nov. 2012). "Symmetries, topological phases, and bound states in the one-dimensional quantum walk". In: *Phys. Rev. B* 86 (19), p. 195414. DOI: 10.1103/PhysRevB.86.195414. URL: https://link.aps.org/doi/10.1103/PhysRevB.86.195414.

Asbóth, J. K. et al. (Sept. 2014). "Chiral symmetry and bulk-boundary correspondence in periodically driven one-dimensional systems". In: *Phys. Rev. B* 90 (12), p. 125143. DOI: 10.1103/PhysRevB.90.125143. URL: https://link.aps.org/doi/10.1103/PhysRevB.90.125143.

Asbóth, János K et al. (2016). *A short course on topological insulators*. Vol. 919. Springer, p. 87. URL: https://www.springer.com/gp/book/9783319256054.

Bahari, Masoud et al. (Apr. 2019). "One-dimensional topological metal". In: *Phys. Rev. B* 99 (15), p. 155128. DOI: 10.1103/PhysRevB.99.155128. URL: https://link.aps.org/doi/10.1103/PhysRevB.99.155128.

Bandres, Miguel A. et al. (2018). "Topological insulator laser: Experiments". In: *Science* 359.6381. ISSN: 0036-8075. DOI: 10.1126/science.aar4005. URL: https://science.sciencemag.org/content/359/6381/eaar4005.

Banerjee, S. et al. (July 2009). "Tight-Binding Modeling and Low-Energy Behavior of the Semi-Dirac Point". In: *Phys. Rev. Lett.* 103 (1), p. 016402. DOI: 10.1103/PhysRevLett.103.016402. URL: https://link.aps.org/doi/10.1103/PhysRevLett.103.016402.

Banerjee, Swapnonil (2015). *Anderson localizaion for semi-Dirac semi-Weyl semi-metal*. arXiv: 1508.05145 [cond-mat.str-el]. URL: https://arxiv.org/abs/1508.05145.

Bellec, Matthieu, Ulrich Kuhl, et al. (Jan. 2013). "Topological Transition of Dirac Points in a Microwave Experiment". In: *Phys. Rev. Lett.* 110 (3), p. 033902. DOI: 10.1103/PhysRevLett.110.033902. URL: https://link.aps.org/doi/10.1103/PhysRevLett.110.033902.

Bellec, Matthieu, Claire Michel, et al. (2017). "Non-diffracting states in one-dimensional Floquet photonic topological insulators". In: *EPL (Europhysics Letters)* 119.1, p. 14003. URL: https://iopscience.iop.org/article/10.1209/0295-5075/119/14003.

Bernevig, B. Andrei, Taylor L. Hughes, et al. (2006). "Quantum Spin Hall Effect and Topological Phase Transition in HgTe Quantum Wells". In: *Science* 314.5806, pp. 1757–1761. ISSN: 0036-8075. DOI: 10.1126/science.1133734. URL: https://science.sciencemag.org/content/314/5806/1757.

Bernevig, B. Andrei and Shou-Cheng Zhang (Mar. 2006). "Quantum Spin Hall Effect". In: *Phys. Rev. Lett.* 96 (10), p. 106802. DOI: 10.1103/PhysRevLett.96.106802. URL: https://link.aps.org/doi/10.1103/PhysRevLett.96.106802.

Berry, M. V. (1984). "Quantal Phase Factors Accompanying Adiabatic Changes". In: *Proceedings of the Royal Society of London. Series A, Mathematical and Physical Sciences* 392.1802, pp. 45–57. ISSN: 00804630. URL: http://www.jstor.org/stable/2397741.

Bloch, Felix (July 1929). "Über die Quantenmechanik der Elektronen in Kristallgittern". In: *Zeitschrift für Physik* 52.7, pp. 555–600. DOI: 10.1007/BF01339455. URL: https://doi.org/10.1007/BF01339455.

Blömer, Dominik et al. (Mar. 2006). "Nonlinear refractive index of fs-laser-written waveguides in fused silica". In: *Opt. Express* 14.6, pp. 2151–2157. DOI: 10.1364/OE.14.002151. URL: http://www.opticsexpress.org/abstract.cfm?URI=oe-14-6-2151.

Born, M. et al. (1928). "Beweis des Adiabatensatzes". In: *Zeitschrift für Physik* 51.3, pp. 165–180. URL: https://doi.org/10.1007/BF01343193.

Bromberg, Yaron et al. (June 2009). "Quantum and Classical Correlations in Waveguide Lattices". In: *Phys. Rev. Lett.* 102 (25), p. 253904. DOI: 10.1103/PhysRevLett.102.253904. URL: https://link.aps.org/doi/10.1103/PhysRevLett.102.253904.

Broome, M. A. et al. (Apr. 2010). "Discrete Single-Photon Quantum Walks with Tunable Decoherence". In: *Phys. Rev. Lett.* 104 (15), p. 153602. DOI: 10.1103/PhysRevLett.104.153602. URL: https://link.aps.org/doi/10.1103/PhysRevLett.104.153602.

Budich, Jan Carl et al. (Mar. 2017). "Helical Floquet Channels in 1D Lattices". In: *Phys. Rev. Lett.* 118 (10), p. 105302. DOI: 10.1103/PhysRevLett.118.105302. URL: https://link.aps.org/doi/10.1103/PhysRevLett.118.105302.

Burkov, A. A. (Nov. 2016). "Topological semimetals". In: *Nature Materials* 15.11, pp. 1145–1148. DOI: 10.1038/nmat4788. URL: http://www.nature.com/articles/nmat4788%20http://arxiv.org/abs/1610.07866%20http://dx.doi.org/10.1038/nmat4788.

Burkov, A. A. et al. (Dec. 2011). "Topological nodal semimetals". In: *Phys. Rev. B* 84 (23), p. 235126. DOI: 10.1103/PhysRevB.84.235126. URL: https://link.aps.org/doi/10.1103/PhysRevB.84.235126.

Calvo, Hernán L. et al. (2011). "Tuning laser-induced band gaps in graphene". In: *Applied Physics Letters* 98.23, p. 232103. DOI: 10.1063/1.3597412. eprint: https://doi.org/10.1063/1.3597412. URL: https://doi.org/10.1063/1.3597412.

Cayssol, Jérôme et al. (2013). "Floquet topological insulators". In: *physica status solidi (RRL) – Rapid Research Letters* 7.1-2, pp. 101–108. DOI: 10.1002/pssr.201206451. URL: https://onlinelibrary.wiley.com/doi/abs/10.1002/pssr.201206451.

Chalker, JT et al. (1988). "Percolation, quantum tunnelling and the integer Hall effect". In: *Journal of Physics C: Solid State Physics* 21.14, p. 2665.

Chen, Chui-Zhen et al. (2019). arXiv: 1905.00638. URL: https://arxiv.org/abs/1905.00638.

Cheon, Taksu (1998). "Double spiral energy surface in one-dimensional quantum mechanics of generalized pointlike potentials". In: *Physics Letters A* 248.5, pp. 285–289. ISSN: 0375-9601. DOI: https://doi.org/10.1016/S0375-9601(98)00725-7. URL: http://www.sciencedirect.com/science/article/pii/S0375960198007257.

Chiodo, N. et al. (June 2006). "Imaging of Bloch oscillations in erbium-doped curved waveguide arrays". In: *Opt. Lett.* 31.11, pp. 1651–1653. DOI: 10.1364/OL.31.001651. URL: http://ol.osa.org/abstract.cfm?URI=ol-31-11-1651.

Chu, Shih-I et al. (2004). "Beyond the Floquet theorem: generalized Floquet formalisms and quasienergy methods for atomic and molecular multiphoton processes in intense laser fields". In: *Physics Reports* 390.1, pp. 1–131. ISSN: 0370-1573. DOI: 10.1016/j.physrep.2003.10.001. URL: http://www.sciencedirect.com/science/article/pii/S0370157303003946.

Cooper, N. R. et al. (Mar. 2019). "Topological bands for ultracold atoms". In: *Rev. Mod. Phys.* 91 (1), p. 015005. DOI: 10.1103/RevModPhys.91.015005. URL: https://link.aps.org/doi/10.1103/RevModPhys.91.015005.

Costa, Marcio et al. (Dec. 2019). "Toward Realistic Amorphous Topological Insulators". In: *Nano Letters* 19.12, pp. 8941–8946. DOI: 10.1021/acs.nanolett.9b03881. URL: https://doi.org/10.1021/acs.nanolett.9b03881.

Crespi, Andrea et al. (2013). "Anderson localization of entangled photons in an integrated quantum walk". In: *Nature Photonics* 7.4, pp. 322–328. DOI: 10.1038/nphoton.2013.26. URL: https://doi.org/10.1038/nphoton.2013.26.

Delplace, Pierre (2019). "Topological chiral modes in random scattering networks". In: arXiv: 1905.11194. URL: https://arxiv.org/abs/1905.11194.

Delplace, Pierre, Michel Fruchart, et al. (May 2017). "Phase rotation symmetry and the topology of oriented scattering networks". In: *Phys. Rev. B* 95 (20), p. 205413. DOI: 10.1103/PhysRevB.95.205413. URL: https://link.aps.org/doi/10.1103/PhysRevB.95.205413.

Delplace, Pierre, Álvaro Gómez-León, et al. (Dec. 2013). "Merging of Dirac points and Floquet topological transitions in ac-driven graphene". In: *Phys. Rev. B* 88 (24), p. 245422. DOI: 10.1103/PhysRevB.88.245422. URL: https://link.aps.org/doi/10.1103/PhysRevB.88.245422.

Delplace, Pierre, J. B. Marston, et al. (2017). "Topological origin of equatorial waves". In: *Science* 358.6366, pp. 1075–1077. ISSN: 0036-8075. DOI: 10.1126/science.aan8819. URL: https://science.sciencemag.org/content/358/6366/1075.

Dion, David R et al. (1976). "Time-Dependent Perturbation of a Two-State Quantum System by a Sinusoidal Field". In: *Advances in Chemical Physics* 35, pp. 265–350.

Eisenberg, H. S. et al. (Aug. 2000). "Diffraction Management". In: *Phys. Rev. Lett.* 85 (9), pp. 1863–1866. DOI: 10.1103/PhysRevLett.85.1863. URL: https://link.aps.org/doi/10.1103/PhysRevLett.85.1863.

Fang, Chen, Matthew J. Gilbert, et al. (June 2012). "Multi-Weyl Topological Semimetals Stabilized by Point Group Symmetry". In: *Phys. Rev. Lett.* 108 (26), p. 266802. DOI: 10.1103/PhysRevLett.108.266802. URL: https://link.aps.org/doi/10.1103/PhysRevLett.108.266802.

Fang, Chen, Hongming Weng, et al. (Nov. 2016). "Topological nodal line semimetals". In: *Chinese Physics B* 25.11, p. 117106. DOI: 10.1088/1674-1056/25/11/117106. URL: https://doi.org/10.1088%2F1674-1056%2F25%2F11%2F117106.

Faure, Frédéric (2019). "Manifestation of the topological index formula in quantum waves and geophysical waves". In: *arXiv preprint arXiv:1901.10592*. URL: https://arxiv.org/abs/1901.10592.

Feng, Liang et al. (2017). "Non-Hermitian photonics based on parity-time symmetry". In: *Nature Photonics* 11.12, pp. 752–762. DOI: 10.1038/s41566-017-0031-1.

Fleury, Romain et al. (2016). "Floquet topological insulators for sound". In: *Nature Communications* 7.1, p. 11744. DOI: 10.1038/ncomms11744. URL: https://doi.org/10.1038/ncomms11744.

Floquet, Gaston (1883). "Sur les équations différentielles linéaires à coefficients périodiques". In: *Annales scientifiques de l'École Normale Supérieure* 12, pp. 47–88. DOI: 10.24033/asens.220. URL: http://www.numdam.org/item/ASENS_1883_2_12__47_0/.

Fruchart, Michel (Mar. 2016). "Complex classes of periodically driven topological lattice systems". In: *Phys. Rev. B* 93 (11), p. 115429. DOI: 10.1103/PhysRevB.93.115429. URL: https://link.aps.org/doi/10.1103/PhysRevB.93.115429.

Fu, Liang et al. (July 2007). "Topological insulators with inversion symmetry". In: *Phys. Rev. B* 76 (4), p. 045302. DOI: 10.1103/PhysRevB.76.045302. URL: https://link.aps.org/doi/10.1103/PhysRevB.76.045302.

Fulga, I. C. et al. (Feb. 2016). "Scattering matrix invariants of Floquet topological insulators". In: *Phys. Rev. B* 93 (7), p. 075405. DOI: 10.1103/PhysRevB.93.075405. URL: https://link.aps.org/doi/10.1103/PhysRevB.93.075405.

El-Ganainy, Ramy et al. (Jan. 2018a). "Non-Hermitian physics and PT symmetry". In: *Nature Physics* 14.1, pp. 11–19. ISSN: 1745-2473. DOI: 10.1038/nphys4323. URL: http://dx.doi.org/10.1038/nphys4323%20http://www.nature.com/articles/nphys4323.

— (Jan. 2018b). "Non-Hermitian physics and PT symmetry". In: *Nature Physics* 14.1, pp. 11–19. ISSN: 1745-2473. DOI: 10.1038/nphys4323. URL: http://dx.doi.org/10.1038/nphys4323%20http://www.nature.com/articles/nphys4323.

Gao, Fei et al. (2016). "Probing topological protection using a designer surface plasmon structure". In: *Nat. Commun.* 7, p. 11619. URL: https://www.nature.com/articles/ncomms11619.

Glück, Markus et al. (2002). "Wannier–Stark resonances in optical and semiconductor superlattices". In: *Physics Reports* 366.3, pp. 103–182. ISSN: 0370-1573. DOI: https://doi.org/10.1016/S0370-1573(02)00142-4. URL: http://www.sciencedirect.com/science/article/pii/S0370157302001424.

Goerbig, M. O. et al. (July 2008). "Tilted anisotropic Dirac cones in quinoid-type graphene and $\alpha-(\mathrm{BEDT\text{-}TTF})_2\mathrm{I}_3$". In: *Phys. Rev. B* 78 (4), p. 045415. DOI: 10.1103/PhysRevB.78.045415. URL: https://link.aps.org/doi/10.1103/PhysRevB.78.045415.

Gómez-León, A. et al. (May 2013). "Floquet-Bloch Theory and Topology in Periodically Driven Lattices". In: *Phys. Rev. Lett.* 110 (20), p. 200403. DOI: 10.1103/PhysRevLett.110.200403. URL: https://link.aps.org/doi/10.1103/PhysRevLett.110.200403.

Gómez-León, Álvaro et al. (May 2014). "Engineering anomalous quantum Hall plateaus and antichiral states with ac fields". In: *Phys. Rev. B* 89 (20), p. 205408. DOI: 10.1103/PhysRevB.89.205408. URL: https://link.aps.org/doi/10.1103/PhysRevB.89.205408.

Graf, Gian Michele et al. (Mar. 2018). "Bulk–Edge Correspondence for Two-Dimensional Floquet Topological Insulators". In: *Annales Henri Poincaré* 19.3, pp. 709–741. ISSN: 1424-0661. DOI: 10.1007/s00023-018-0657-7. URL: https://doi.org/10.1007/s00023-018-0657-7.

Groth, C. W. et al. (Nov. 2009). "Theory of the Topological Anderson Insulator". In: *Phys. Rev. Lett.* 103 (19), p. 196805. DOI: 10.1103/PhysRevLett.103.196805. URL: https://link.aps.org/doi/10.1103/PhysRevLett.103.196805.

Guo, H.-M. et al. (Nov. 2010). "Topological Anderson Insulator in Three Dimensions". In: *Phys. Rev. Lett.* 105 (21), p. 216601. DOI: 10.1103/PhysRevLett.105.216601. URL: https://link.aps.org/doi/10.1103/PhysRevLett.105.216601.

Guzmán, Marcelo et al. (2020). "Geometry and Topology Tango in Chiral Materials". In: *arXiv preprint arXiv:2002.02850*. URL: https://arxiv.org/abs/2002.02850.

Hafezi, Mohammad et al. (2011). "Robust optical delay lines with topological protection". In: *Nature Physics* 7.11, pp. 907–912. DOI: 10.1038/nphys2063. URL: https://doi.org/10.1038/nphys2063.

Haldane, F. D. M. et al. (Jan. 2008). "Possible Realization of Directional Optical Waveguides in Photonic Crystals with Broken Time-Reversal Symmetry". In: *Phys. Rev. Lett.* 100 (1), p. 013904. DOI: 10.1103/PhysRevLett.100.013904. URL: https://link.aps.org/doi/10.1103/PhysRevLett.100.013904.

Hänggi, Peter (1998). "Driven quantum systems". In: URL: https://opus.bibliothek.uni-augsburg.de/opus4/frontdoor/deliver/index/docId/41737/file/chap5.pdf.

Hasan, M. Z. et al. (Nov. 2010). "Colloquium: Topological insulators". In: *Rev. Mod. Phys.* 82 (4), pp. 3045–3067. DOI: 10.1103/RevModPhys.82.3045. URL: https://link.aps.org/doi/10.1103/RevModPhys.82.3045.

Hasan, M. Zahid et al. (2011). "Three-Dimensional Topological Insulators". In: *Annual Review of Condensed Matter Physics* 2.1, pp. 55–78. DOI: 10.1146/annurev-conmatphys-062910-140432. URL: https://doi.org/10.1146/annurev-conmatphys-062910-140432.

Hasegawa, Yasumasa et al. (July 2006). "Zero modes of tight-binding electrons on the honeycomb lattice". In: *Phys. Rev. B* 74 (3), p. 033413. DOI: 10.1103/PhysRevB.74.033413. URL: https://link.aps.org/doi/10.1103/PhysRevB.74.033413.

Hatsugai, Yasuhiro (Nov. 1993a). "Chern number and edge states in the integer quantum Hall effect". In: *Phys. Rev. Lett.* 71 (22), pp. 3697–3700. DOI: 10.1103/PhysRevLett.71.3697. URL: https://link.aps.org/doi/10.1103/PhysRevLett.71.3697.

— (Oct. 1993b). "Edge states in the integer quantum Hall effect and the Riemann surface of the Bloch function". In: *Phys. Rev. B* 48 (16), pp. 11851–11862. DOI: 10.1103/PhysRevB.48.11851. URL: https://link.aps.org/doi/10.1103/PhysRevB.48.11851.

Hill, G. W. (1886). "On the part of the motion of the lunar perigee which is a function of the mean motions of the sun and moon". In: *Acta Mathematica* 8, pp. 1–36. DOI: 10.1007/BF02417081. URL: https://doi.org/10.1007/BF02417081.

Ho, C.-M. et al. (Sept. 1996). "Models for the integer quantum Hall effect: The network model, the Dirac equation, and a tight-binding Hamiltonian". In: *Phys. Rev. B* 54 (12), pp. 8708–8713. DOI: 10.1103/PhysRevB.54.8708. URL: https://link.aps.org/doi/10.1103/PhysRevB.54.8708.

Ho, Tak-San et al. (1983). "Semiclassical many-mode floquet theory". In: *Chemical Physics Letters* 96.4, pp. 464–471. ISSN: 0009-2614. DOI: 10.1016/0009-2614(83)80732-5. URL: http://www.sciencedirect.com/science/article/pii/0009261483807325.

Hsieh, D. et al. (2008). "A topological Dirac insulator in a quantum spin Hall phase". In: *Nature* 452.7190, pp. 970–974. DOI: 10.1038/nature06843. URL: https://doi.org/10.1038/nature06843.

Hu, Wenchao et al. (Feb. 2015a). "Measurement of a Topological Edge Invariant in a Microwave Network". In: *Phys. Rev. X* 5 (1), p. 011012. DOI: 10.1103/PhysRevX.5.011012. URL: https://link.aps.org/doi/10.1103/PhysRevX.5.011012.

— (Feb. 2015b). "Measurement of a Topological Edge Invariant in a Microwave Network". In: *Phys. Rev. X* 5 (1), p. 011012. DOI: 10.1103/PhysRevX.5.011012. URL: https://link.aps.org/doi/10.1103/PhysRevX.5.011012.

Huang, Huaqing et al. (Oct. 2015). "Emergence of a Chern-insulating state from a semi-Dirac dispersion". In: *Phys. Rev. B* 92 (16), p. 161115. DOI: 10.1103/PhysRevB.92.161115. URL: https://link.aps.org/doi/10.1103/PhysRevB.92.161115.

Inoue, Jun-ichi et al. (June 2010). "Photoinduced Transition between Conventional and Topological Insulators in Two-Dimensional Electronic Systems". In: *Phys. Rev. Lett.* 105 (1), p. 017401. DOI: 10.1103/PhysRevLett.105.017401. URL: https://link.aps.org/doi/10.1103/PhysRevLett.105.017401.

Jiang, Liang et al. (June 2011). "Majorana Fermions in Equilibrium and in Driven Cold-Atom Quantum Wires". In: *Phys. Rev. Lett.* 106 (22), p. 220402. DOI: 10.1103/PhysRevLett.106.220402. URL: https://link.aps.org/doi/10.1103/PhysRevLett.106.220402.

Joannopoulos J. D. Johnson Steven G., Winn Joshua N. et al. (2008). *Photonic Crystals: Molding the Flow of Light - Second Edition*. Princeton. ISBN: 9781400847129. URL: https://press.princeton.edu/books/ebook/9781400847129/photonic-crystals.

Jones, Alan L. (Mar. 1965). "Coupling of Optical Fibers and Scattering in Fibers*". In: *J. Opt. Soc. Am.* 55.3, pp. 261–271. DOI: 10.1364/JOSA.55.000261. URL: http://www.osapublishing.org/abstract.cfm?URI=josa-55-3-261.

Jotzu, Gregor et al. (Nov. 2014). "Experimental realization of the topological Haldane model with ultracold fermions". In: *Nature* 515, p. 237. URL: http://dx.doi.org/10.1038/nature13915.

Kane, C. L. et al. (Sept. 2005). "Z_2 Topological Order and the Quantum Spin Hall Effect". In: *Phys. Rev. Lett.* 95 (14), p. 146802. DOI: 10.1103/PhysRevLett.95.146802. URL: https://link.aps.org/doi/10.1103/PhysRevLett.95.146802.

Ke, Yongguan et al. (2016). "Topological phase transitions and Thouless pumping of light in photonic waveguide arrays". In: *Laser and Photonics Reviews* 10.6, pp. 995–1001. DOI: 10.1002/lpor.201600119.

Keldysh, LV et al. (1965). "Ionization in the field of a strong electromagnetic wave". In: *Sov. Phys. JETP* 20.5, pp. 1307–1314. URL: http://www.jetp.ac.ru/cgi-bin/e/index/e/20/5/p1307?a=list.

Khanikaev, Alexander B., Romain Fleury, et al. (2015). "Topologically robust sound propagation in an angular-momentum-biased graphene-like resonator lattice". In: *Nature Communications* 6.1, p. 8260. DOI: 10.1038/ncomms9260. URL: https://doi.org/10.1038/ncomms9260.

Khanikaev, Alexander B., S. Hossein Mousavi, et al. (2013). "Photonic topological insulators". In: *Nature Materials* 12.3, pp. 233–239. DOI: 10.1038/nmat3520. URL: http://dx.doi.org/10.1038/nmat3520.

Kitaev, Alexei (2009). "Periodic table for topological insulators and superconductors". In: *AIP Conference Proceedings* 1134.1, pp. 22–30. DOI: 10.1063/1.3149495. URL: https://aip.scitation.org/doi/abs/10.1063/1.3149495.

Kitagawa, Takuya, Erez Berg, et al. (Dec. 2010). "Topological characterization of periodically driven quantum systems". In: *Phys. Rev. B* 82 (23), p. 235114. DOI: 10.1103/PhysRevB.82.235114. URL: https://link.aps.org/doi/10.1103/PhysRevB.82.235114.

Kitagawa, Takuya, Matthew A Broome, et al. (2012). "Observation of topologically protected bound states in photonic quantum walks". In: *Nat. Commun.* 3, p. 882. DOI: 10.1038/ncomms1872. URL: https://doi.org/10.1038/ncomms1872.

Kitagawa, Takuya, Takashi Oka, et al. (Dec. 2011). "Transport properties of nonequilibrium systems under the application of light: Photoinduced quantum Hall insulators without Landau levels". In: *Phys. Rev. B* 84 (23), p. 235108. DOI: 10.1103/PhysRevB.84.235108. URL: https://link.aps.org/doi/10.1103/PhysRevB.84.235108.

Kitagawa, Takuya, Mark S. Rudner, et al. (Sept. 2010). "Exploring topological phases with quantum walks". In: *Phys. Rev. A* 82 (3), p. 033429. DOI: 10.1103/PhysRevA.82.033429. URL: https://link.aps.org/doi/10.1103/PhysRevA.82.033429.

Klitzing, K. v. et al. (Aug. 1980). "New Method for High-Accuracy Determination of the Fine-Structure Constant Based on Quantized Hall Resistance". In: *Phys. Rev. Lett.* 45 (6), pp. 494–497. DOI: 10.1103/PhysRevLett.45.494. URL: https://link.aps.org/doi/10.1103/PhysRevLett.45.494.

Knez, Ivan et al. (Sept. 2011). "Evidence for Helical Edge Modes in Inverted InAs/GaSb Quantum Wells". In: *Phys. Rev. Lett.* 107 (13), p. 136603. DOI: 10.1103/PhysRevLett.107.136603. URL: https://link.aps.org/doi/10.1103/PhysRevLett.107.136603.

Kohmoto, Mahito (1985). "Topological invariant and the quantization of the Hall conductance". In: *Annals of Physics* 160.2, pp. 343–354. ISSN: 0003-4916. DOI: https://doi.org/10.1016/0003-4916(85)90148-4. URL: http://www.sciencedirect.com/science/article/pii/0003491685901484.

König, Markus et al. (2007). "Quantum Spin Hall Insulator State in HgTe Quantum Wells". In: *Science* 318.5851, pp. 766–770. ISSN: 0036-8075. DOI: 10.1126/science.1148047. URL: https://science.sciencemag.org/content/318/5851/766.

Koshino, Mikito et al. (Jan. 2016). "Magnetic susceptibility in three-dimensional nodal semimetals". In: *Phys. Rev. B* 93 (4), p. 045201. DOI: 10.1103/PhysRevB.93.045201. URL: https://link.aps.org/doi/10.1103/PhysRevB.93.045201.

Kraus, Yaacov E., Yoav Lahini, et al. (Sept. 2012). "Topological States and Adiabatic Pumping in Quasicrystals". In: *Phys. Rev. Lett.* 109 (10), p. 106402. DOI: 10.1103/PhysRevLett.109.106402. URL: https://link.aps.org/doi/10.1103/PhysRevLett.109.106402.

Kraus, Yaacov E., Zohar Ringel, et al. (Nov. 2013). "Four-Dimensional Quantum Hall Effect in a Two-Dimensional Quasicrystal". In: *Phys. Rev. Lett.* 111 (22), p. 226401. DOI: 10.1103/PhysRevLett.111.226401. URL: https://link.aps.org/doi/10.1103/PhysRevLett.111.226401.

Kraus, Yaacov E. and Oded Zilberberg (Sept. 2012). "Topological Equivalence between the Fibonacci Quasicrystal and the Harper Model". In: *Phys. Rev. Lett.* 109 (11), p. 116404. DOI: 10.1103/PhysRevLett.109.116404. URL: https://link.aps.org/doi/10.1103/PhysRevLett.109.116404.

Krieger, J. B. et al. (Apr. 1986). "Time evolution of Bloch electrons in a homogeneous electric field". In: *Phys. Rev. B* 33 (8), pp. 5494–5500. DOI: 10.1103/PhysRevB.33.5494. URL: https://link.aps.org/doi/10.1103/PhysRevB.33.5494.

Krishnamoorthy, Harish N. S. et al. (2012). "Topological Transitions in Metamaterials". In: *Science* 336.6078, pp. 205–209. DOI: 10.1126/science.1219171. URL: https://science.sciencemag.org/content/336/6078/205.

Kuhl, U. et al. (Sept. 2010). "Dirac point and edge states in a microwave realization of tight-binding graphene-like structures". In: *Phys. Rev. B* 82 (9), p. 094308. DOI: 10.1103/PhysRevB.82.094308. URL: https://link.aps.org/doi/10.1103/PhysRevB.82.094308.

Kumar, Nitesh et al. (2019). "Extremely high conductivity observed in the triple point topological metal MoP". In: *Nature Communications* 10.1, p. 2475. DOI: 10.1038/s41467-019-10126-y. URL: https://doi.org/10.1038/s41467-019-10126-y.

Kundu, Arijit et al. (Dec. 2014). "Effective Theory of Floquet Topological Transitions". In: *Phys. Rev. Lett.* 113 (23), p. 236803. DOI: 10.1103/PhysRevLett.113.236803. URL: https://link.aps.org/doi/10.1103/PhysRevLett.113.236803.

Landau, L. D. (1937). "On the theory of phase transitions". In: *Zh. Eksp. Teor. Fiz.* 7. [Phys. Z. Sowjetunion 11, 26 (1937); Ukr. J. Phys.53,25(2008)], pp. 19–32. URL: https://web.archive.org/web/20151214124950/http://www.ujp.bitp.kiev.ua/files/journals/53/si/53SI08p.pdf.

Lee, Ching Hua, Stefan Imhof, et al. (2017). "Topolectrical circuits". In: *Communications Physics* 2018. ISSN: 2399-3650. DOI: 10.1038/s42005-018-0035-2. URL: http://www.nature.com/articles/s42005-018-0035-2.

Lee, Ching Hua, Linhu Li, et al. (Dec. 2019). "Unraveling non-Hermitian pumping: emergent spectral singularities and anomalous responses". In: pp. 1–28. arXiv: 1912.06974. URL: http://arxiv.org/abs/1912.06974.

Lenz, G. et al. (Aug. 1999). "Bloch Oscillations in an Array of Curved Optical Waveguides". In: *Phys. Rev. Lett.* 83 (5), pp. 963–966. DOI: 10.1103/PhysRevLett.83.963. URL: https://link.aps.org/doi/10.1103/PhysRevLett.83.963.

León, Álvaro Gómez (2014). "Dynamical and topological properties of periodically driven nanostructures". PhD thesis. URL: https://dialnet.unirioja.es/servlet/tesis?codigo=184939.

Li, Jian et al. (Apr. 2009). "Topological Anderson Insulator". In: *Phys. Rev. Lett.* 102 (13), p. 136806. DOI: 10.1103/PhysRevLett.102.136806. URL: https://link.aps.org/doi/10.1103/PhysRevLett.102.136806.

Li, Si et al. (Mar. 2020). "Type-II topological metals". In: pp. 1–10. URL: http://arxiv.org/abs/2003.03328.

Li, Xiao-Ping et al. (2019). "Type-III Weyl Semimetals and its Materialization". In: *arXiv preprint arXiv:1909.12178*.

Liang, G. Q. et al. (May 2013). "Optical Resonator Analog of a Two-Dimensional Topological Insulator". In: *Phys. Rev. Lett.* 110 (20), p. 203904. DOI: 10.1103/PhysRevLett.110.203904. URL: https://link.aps.org/doi/10.1103/PhysRevLett.110.203904.

Lignier, H. et al. (Nov. 2007). "Dynamical Control of Matter-Wave Tunneling in Periodic Potentials". In: *Phys. Rev. Lett.* 99 (22), p. 220403. DOI: 10.1103/PhysRevLett.99.220403. URL: https://link.aps.org/doi/10.1103/PhysRevLett.99.220403.

Lindner, Netanel H et al. (2011). "Floquet topological insulator in semiconductor quantum wells". In: *Nat. Phys.* 7.6, p. 490.

Liu, Changxu et al. (Nov. 2017). "Disorder-Induced Topological State Transition in Photonic Metamaterials". In: *Phys. Rev. Lett.* 119 (18), p. 183901. DOI: 10.1103/PhysRevLett.119.183901. URL: https://link.aps.org/doi/10.1103/PhysRevLett.119.183901.

Lohse, M. et al. (2016). "A Thouless quantum pump with ultracold bosonic atoms in an optical superlattice". In: *Nature Physics* 12.4, pp. 350–354. DOI: 10.1038/nphys3584. eprint: 1507.02225v1. URL: http://www.nature.com/articles/nphys3584.

Lohse, Michael et al. (2018). "Exploring 4D quantum Hall physics with a 2D topological charge pump". In: *Nature* 553.7686, pp. 55–58. DOI: 10.1038/nature25000. URL: https://doi.org/10.1038/nature25000.

Longhi, S. (2009). "Quantum-optical analogies using photonic structures". In: *Laser & Photonics Reviews* 3.3, pp. 243–261. DOI: 10.1002/lpor.200810055. URL: https://onlinelibrary.wiley.com/doi/abs/10.1002/lpor.200810055.

Lu, Ling et al. (Aug. 2015). "Experimental observation of Weyl points". In: *Science* 349.6248, pp. 622–624. DOI: 10.1126/science.aaa9273. URL: http://www.sciencemag.org/cgi/doi/10.1126/science.aaa9273.

Lustig, Eran et al. (Feb. 2019). "Photonic topological insulator in synthetic dimensions". In: *Nature*. ISSN: 0028-0836. DOI: 10.1038/s41586-019-0943-7. URL: http://www.nature.com/articles/s41586-019-0943-7.

Lyapunov, A. M. (1896). "Sur une série relative a la théorie des équations différentielles linéaires à coeficients périodiques". In: *Comptes Rendus Acad. Sci. Paris* 123.26, pp. 1248–1252. DOI: 12148/bpt6k30799. URL: http://gallica.bnf.fr/ark:/12148/bpt6k30799/f1248.item.

Maczewsky, Lukas J et al. (2018). "Fermionic time-reversal symmetry in a photonic topological insulator". In: *arXiv preprint arXiv:1812.07930*.

Mahmood, Fahad et al. (2016). "Selective scattering between Floquet-Bloch and Volkov states in a topological insulator". In: *Nature Physics* 12.4, pp. 306–310. ISSN: 17452481. DOI: 10.1038/nphys3609.

Marciani, Marco et al. (2019). "Chiral Maxwell waves in continuous media from Berry monopoles". In: *arXiv preprint arXiv:1906.09057*. URL: https://arxiv.org/abs/1906.09057.

Marcuse, D. (Apr. 1973). *Light transmission optics*. Van Nostrand Reinhold Company, Bell Laboratories. DOI: 10.1016/0030-3992(73)90045-5.

Martin, Ivar et al. (Oct. 2017). "Topological Frequency Conversion in Strongly Driven Quantum Systems". In: *Phys. Rev. X* 7 (4), p. 041008. DOI: 10.1103/PhysRevX.7.041008. URL: https://link.aps.org/doi/10.1103/PhysRevX.7.041008.

Matthews, Jonathan C. F. et al. (2013). "Observing fermionic statistics with photons in arbitrary processes". In: *Scientific Reports* 3.1, p. 1539. DOI: 10.1038/srep01539. URL: https://doi.org/10.1038/srep01539.

Mawrie, Alestin et al. (Aug. 2019). "Quantum thermoelectrics based on two-dimensional semi-Dirac materials". In: *Phys. Rev. B* 100 (8), p. 081403. DOI: 10.1103/PhysRevB.100.081403. URL: https://link.aps.org/doi/10.1103/PhysRevB.100.081403.

Mayers, Brian T. et al. (2005). "Arrays and Cascades of Fluorescent Liquid-Liquid Waveguides: Broadband Light Sources for Spectroscopy in Microchannels". In: *Analytical Chemistry* 77.5, pp. 1310–1316. DOI: 10.1021/ac048692n. URL: https://doi.org/10.1021/ac048692n.

McIver, J. W. et al. (2020). "Light-induced anomalous Hall effect in graphene". In: *Nature Physics* 16.1, pp. 38–41. ISSN: 17452481. DOI: 10.1038/s41567-019-0698-y. URL: http://dx.doi.org/10.1038/s41567-019-0698-y.

Miri, Mohammad-Ali et al. (Aug. 2012). "Optical mesh lattices with $\mathcal{PT}$ symmetry". In: *Phys. Rev. A* 86 (2), p. 023807. DOI: 10.1103/PhysRevA.86.023807. URL: https://link.aps.org/doi/10.1103/PhysRevA.86.023807.

Mittal, Sunil et al. (July 2019). "Photonic Anomalous Quantum Hall Effect". In: *Phys. Rev. Lett.* 123 (4), p. 043201. DOI: 10.1103/PhysRevLett.123.043201. URL: https://link.aps.org/doi/10.1103/PhysRevLett.123.043201.

Miyamoto, Manabu et al. (Oct. 2007). "Cheon's anholonomies in Floquet operators". In: *Phys. Rev. A* 76 (4), p. 042115. DOI: 10.1103/PhysRevA.76.042115. URL: https://link.aps.org/doi/10.1103/PhysRevA.76.042115.

Montambaux, G. et al. (Oct. 2009a). "Merging of Dirac points in a two-dimensional crystal". In: *Phys. Rev. B* 80 (15), p. 153412. DOI: 10.1103/PhysRevB.80.153412. URL: https://link.aps.org/doi/10.1103/PhysRevB.80.153412.

— (Oct. 2009b). "Merging of Dirac points in a two-dimensional crystal". In: *Phys. Rev. B* 80 (15), p. 153412. DOI: 10.1103/PhysRevB.80.153412. URL: https://link.aps.org/doi/10.1103/PhysRevB.80.153412.

Moore, J. E. et al. (Mar. 2007). "Topological invariants of time-reversal-invariant band structures". In: *Phys. Rev. B* 75 (12), p. 121306. DOI: 10.1103/PhysRevB.75.121306. URL: https://link.aps.org/doi/10.1103/PhysRevB.75.121306.

Moore, Joel E. (2013). "Chapter 2 - Theory of Three-Dimensional Topological Insulators". In: *Topological Insulators*. Ed. by Marcel Franz et al. Vol. 6. Contemporary Concepts of Condensed Matter Science. Elsevier, pp. 35–57. DOI: https://doi.org/10.1016/B978-0-444-63314-9.00002-0. URL: http://www.sciencedirect.com/science/article/pii/B9780444633149000020.

Morandotti, R. et al. (Dec. 1999). "Experimental Observation of Linear and Nonlinear Optical Bloch Oscillations". In: *Phys. Rev. Lett.* 83 (23), pp. 4756–4759. DOI: 10.1103/PhysRevLett.83.4756. URL: https://link.aps.org/doi/10.1103/PhysRevLett.83.4756.

Morimoto, Takahiro et al. (May 2017). "Floquet topological phases protected by time glide symmetry". In: *Phys. Rev. B* 95 (19), p. 195155. DOI: 10.1103/PhysRevB.95.195155. URL: https://link.aps.org/doi/10.1103/PhysRevB.95.195155.

Murakami, Shuichi (Sept. 2007). "Phase transition between the quantum spin Hall and insulator phases in 3D: emergence of a topological gapless phase". In: *New Journal of Physics* 9.9, pp. 356–356. DOI: 10.1088/1367-2630/9/9/356. URL: https://doi.org/10.1088%2F1367-2630%2F9%2F9%2F356.

Murakami, Shuichi et al. (Nov. 2007). "Tuning phase transition between quantum spin Hall and ordinary insulating phases". In: *Phys. Rev. B* 76 (20), p. 205304. DOI: 10.1103/PhysRevB.76.205304. URL: https://link.aps.org/doi/10.1103/PhysRevB.76.205304.

Nakagawa, Masaya et al. (Feb. 2020). "Wannier representation of Floquet topological states". In: *Phys. Rev. B* 101 (7), p. 075108. DOI: 10.1103/PhysRevB.101.075108. URL: https://link.aps.org/doi/10.1103/PhysRevB.101.075108.

Nakahara, Mikio (2003). *Geometry, topology and physics*. CRC Press. URL: https://www.crcpress.com/Geometry-Topology-and-Physics-Second-Edition/Nakahara/p/book/9780750306065.

Nakajima, Shuta et al. (Apr. 2016). "Topological Thouless pumping of ultracold fermions". In: *Nature Physics* 12.4, pp. 296–300. DOI: 10.1038/nphys3622. URL: http://www.nature.com/articles/nphys3622.

Nathan, Frederik et al. (Dec. 2015). "Topological singularities and the general classification of Floquet–Bloch systems". In: *New Journal of Physics* 17.12, p. 125014. DOI: 10.1088/1367-2630/17/12/125014. URL: https://doi.org/10.1088%2F1367-2630%2F17%2F12%2F125014.

Noh, Jiho et al. (2017). "Experimental observation of optical Weyl points and Fermi arc-like surface states". In: *Nature Physics* 13.6, pp. 611–617. DOI: 10.1038/nphys4072. URL: http://www.nature.com/articles/nphys4072.

Nolte, S. et al. (June 2003). "Femtosecond waveguide writing: a new avenue to three-dimensional integrated optics". In: *Applied Physics A* 77.1, pp. 109–111. ISSN: 1432-0630. DOI: 10.1007/s00339-003-2088-6. URL: https://doi.org/10.1007/s00339-003-2088-6.

Oka, Takashi et al. (Feb. 2009). "Photovoltaic Hall effect in graphene". In: *Phys. Rev. B* 79 (8), p. 081406. DOI: 10.1103/PhysRevB.79.081406. URL: https://link.aps.org/doi/10.1103/PhysRevB.79.081406.

Okamoto, Katsunari (2006). *Fundamentals of Optical Waveguides*. Ed. by Katsunari Okamoto. Second Edition. Burlington: Academic Press. ISBN: 978-0-12-525096-2. DOI: https://doi.org/10.1016/B978-012525096-2/50001-5. URL: http://www.sciencedirect.com/science/article/pii/B9780125250962500015.

Oki, Yuji et al. (July 2002). "Multiwavelength distributed-feedback dye laser array and its application to spectroscopy". In: *Opt. Lett.* 27.14, pp. 1220–1222. DOI: 10.1364/OL.27.001220. URL: http://ol.osa.org/abstract.cfm?URI=ol-27-14-1220.

Orfanidis, Sophocles J (2016). *Electromagnetic Waves and Antennas*. URL: https://www.ece.rutgers.edu/~orfanidi/ewa/.

Ozawa, Tomoki, Hannah M. Price, Alberto Amo, et al. (Mar. 2019). "Topological photonics". In: *Rev. Mod. Phys.* 91 (1), p. 015006. DOI: 10.1103/RevModPhys.91.015006. URL: https://link.aps.org/doi/10.1103/RevModPhys.91.015006.

Ozawa, Tomoki, Hannah M. Price, Nathan Goldman, et al. (Apr. 2016). "Synthetic dimensions in integrated photonics: From optical isolation to four-dimensional quantum Hall physics". In: *Phys. Rev. A* 93 (4), p. 043827. DOI: 10.1103/PhysRevA.93.043827. URL: https://link.aps.org/doi/10.1103/PhysRevA.93.043827.

Palumbo, Giandomenico et al. (Dec. 2015). "Two-dimensional Chern semimetals on the Lieb lattice". In: *Phys. Rev. B* 92 (23), p. 235106. DOI: 10.1103/PhysRevB.92.235106. URL: https://link.aps.org/doi/10.1103/PhysRevB.92.235106.

Parker, Colin V. et al. (2013). "Direct observation of effective ferromagnetic domains of cold atoms in a shaken optical lattice". In: *Nature Physics* 9.12, pp. 769–774. DOI: 10.1038/nphys2789. URL: https://doi.org/10.1038/nphys2789.

Pasek, Michael et al. (Feb. 2014). "Network models of photonic Floquet topological insulators". In: *Phys. Rev. B* 89 (7), p. 075113. DOI: 10.1103/PhysRevB.89.075113. URL: https://link.aps.org/doi/10.1103/PhysRevB.89.075113.

Pereira, Vitor M. et al. (July 2009). "Tight-binding approach to uniaxial strain in graphene". In: *Phys. Rev. B* 80 (4), p. 045401. DOI: 10.1103/PhysRevB.80.045401. URL: https://link.aps.org/doi/10.1103/PhysRevB.80.045401.

Perets, Hagai B. et al. (May 2008). "Realization of Quantum Walks with Negligible Decoherence in Waveguide Lattices". In: *Phys. Rev. Lett.* 100 (17), p. 170506. DOI: 10.1103/PhysRevLett.100.170506. URL: https://link.aps.org/doi/10.1103/PhysRevLett.100.170506.

Perrot, Manolis et al. (2019). "Topological transition in stratified fluids". In: *Nature Physics* 15.8, pp. 781–784. ISSN: 1745-2481. DOI: 10.1038/s41567-019-0561-1. URL: https://doi.org/10.1038/s41567-019-0561-1.

Pertsch, T., P. Dannberg, et al. (Dec. 1999). "Optical Bloch Oscillations in Temperature Tuned Waveguide Arrays". In: *Phys. Rev. Lett.* 83.23, pp. 4752–4755. ISSN: 0031-9007. DOI: 10.1103/PhysRevLett.83.4752. URL: http://link.aps.org/doi/10.1103/PhysRevLett.83.4752.

Pertsch, T., T. Zentgraf, et al. (Feb. 2002). "Anomalous Refraction and Diffraction in Discrete Optical Systems". In: *Phys. Rev. Lett.* 88 (9), p. 093901. DOI: 10.1103/PhysRevLett.88.093901. URL: https://link.aps.org/doi/10.1103/PhysRevLett.88.093901.

Peruzzo, Alberto et al. (2010). "Quantum Walks of Correlated Photons". In: *Science* 329.5998, pp. 1500–1503. ISSN: 0036-8075. DOI: 10.1126/science.1193515. URL: https://science.sciencemag.org/content/329/5998/1500.

Program, The Univalent Foundations (2013). "Homotopy Type Theory: Univalent Foundations of Mathematics". In: *arXiv preprint arXiv:1308.0729*. URL: https://arxiv.org/abs/1308.0729.

Qin, Chengzhi et al. (Feb. 2020). "Discrete diffraction and Bloch oscillations in non-Hermitian frequency lattices induced by complex photonic gauge fields". In: *Physical Review B*

101.6, p. 064303. DOI: 10.1103/PhysRevB.101.064303. URL: https://link.aps.org/doi/10.1103/PhysRevB.101.064303.

Raghu, S. et al. (Sept. 2008). "Analogs of quantum-Hall-effect edge states in photonic crystals". In: *Phys. Rev. A* 78 (3), p. 033834. DOI: 10.1103/PhysRevA.78.033834. URL: https://link.aps.org/doi/10.1103/PhysRevA.78.033834.

Rechtsman, Mikael C et al. (2013). "Photonic Floquet topological insulators". In: *Nature* 496.7444, pp. 196–200. DOI: 10.1038/nature12066. URL: http://www.nature.com/nature/journal/v496/n7444/abs/nature12066.html.

Regensburger, Alois, Christoph Bersch, Benjamin Hinrichs, et al. (Dec. 2011). "Photon Propagation in a Discrete Fiber Network: An Interplay of Coherence and Losses". In: *Phys. Rev. Lett.* 107 (23), p. 233902. DOI: 10.1103/PhysRevLett.107.233902. URL: https://link.aps.org/doi/10.1103/PhysRevLett.107.233902.

Regensburger, Alois, Christoph Bersch, Mohammad-Ali Miri, et al. (2012). "Parity–time synthetic photonic lattices". In: *Nature* 488.7410, pp. 167–171. DOI: 10.1038/nature11298. URL: https://doi.org/10.1038/nature11298.

Rohde, Peter P et al. (Jan. 2011). "Multi-walker discrete time quantum walks on arbitrary graphs, their properties and their photonic implementation". In: *New Journal of Physics* 13.1, p. 013001. DOI: 10.1088/1367-2630/13/1/013001. URL: https://doi.org/10.1088%2F1367-2630%2F13%2F1%2F013001.

Roth, Andreas et al. (2009). "Nonlocal Transport in the Quantum Spin Hall State". In: *Science* 325.5938, pp. 294–297. ISSN: 0036-8075. DOI: 10.1126/science.1174736. URL: https://science.sciencemag.org/content/325/5938/294.

Roy, Rahul (May 2009). "Z_2 classification of quantum spin Hall systems: An approach using time-reversal invariance". In: *Phys. Rev. B* 79 (19), p. 195321. DOI: 10.1103/PhysRevB.79.195321. URL: https://link.aps.org/doi/10.1103/PhysRevB.79.195321.

Roy, Rahul and Fenner Harper (Oct. 2017). "Periodic table for Floquet topological insulators". In: *Phys. Rev. B* 96 (15), p. 155118. DOI: 10.1103/PhysRevB.96.155118. URL: https://link.aps.org/doi/10.1103/PhysRevB.96.155118.

Rudner (n.d.). *Periodically driven quantum systems*. URL: https://www.youtube.com/watch?v=ZW2LQ8iVet0.

Rudner, Mark S. et al. (July 2013). "Anomalous Edge States and the Bulk-Edge Correspondence for Periodically Driven Two-Dimensional Systems". In: *Phys. Rev. X* 3 (3), p. 031005. DOI: 10.1103/PhysRevX.3.031005. URL: https://link.aps.org/doi/10.1103/PhysRevX.3.031005.

Sambe, Hideo (June 1973). "Steady States and Quasienergies of a Quantum-Mechanical System in an Oscillating Field". In: *Phys. Rev. A* 7 (6), pp. 2203–2213. DOI: 10.1103/PhysRevA.7.2203. URL: https://link.aps.org/doi/10.1103/PhysRevA.7.2203.

Sansoni, Linda et al. (Jan. 2012). "Two-Particle Bosonic-Fermionic Quantum Walk via Integrated Photonics". In: *Phys. Rev. Lett.* 108 (1), p. 010502. DOI: 10.1103/PhysRevLett.108.010502. URL: https://link.aps.org/doi/10.1103/PhysRevLett.108.010502.

Schmitz, H. et al. (Aug. 2009). "Quantum Walk of a Trapped Ion in Phase Space". In: *Phys. Rev. Lett.* 103 (9), p. 090504. DOI: 10.1103/PhysRevLett.103.090504. URL: https://link.aps.org/doi/10.1103/PhysRevLett.103.090504.

Schreiber, A., K. N. Cassemiro, V. Poto ček, A. Gábris, I. Jex, et al. (May 2011). "Decoherence and Disorder in Quantum Walks: From Ballistic Spread to Localization". In:

Phys. Rev. Lett. 106 (18), p. 180403. DOI: 10.1103/PhysRevLett.106.180403. URL: https://link.aps.org/doi/10.1103/PhysRevLett.106.180403.

Schreiber, A., K. N. Cassemiro, V. Poto ček, A. Gábris, P. J. Mosley, et al. (Feb. 2010). "Photons Walking the Line: A Quantum Walk with Adjustable Coin Operations". In: *Phys. Rev. Lett.* 104 (5), p. 050502. DOI: 10.1103/PhysRevLett.104.050502. URL: https://link.aps.org/doi/10.1103/PhysRevLett.104.050502.

Shankar, Suraj et al. (Sept. 2017). "Topological Sound and Flocking on Curved Surfaces". In: *Phys. Rev. X* 7 (3), p. 031039. DOI: 10.1103/PhysRevX.7.031039. URL: https://link.aps.org/doi/10.1103/PhysRevX.7.031039.

Shao, Zeng-Kai et al. (2020). "A high-performance topological bulk laser based on band-inversion-induced reflection". In: *Nature Nanotechnology* 15.1, pp. 67–72. URL: https://www.nature.com/articles/s41565-019-0584-x.

Shirley, Jon H. (May 1965). "Solution of the Schrödinger Equation with a Hamiltonian Periodic in Time". In: *Phys. Rev.* 138 (4B), B979–B987. DOI: 10.1103/PhysRev.138.B979. URL: https://link.aps.org/doi/10.1103/PhysRev.138.B979.

Sie, Edbert J. et al. (2015). "Valley-selective optical Stark effect in monolayer WS2". In: *Nature Materials* 14.3, pp. 290–294. DOI: 10.1038/nmat4156. URL: https://doi.org/10.1038/nmat4156.

Silveirinha, Mário G. (Sept. 2015). "Chern invariants for continuous media". In: *Phys. Rev. B* 92 (12), p. 125153. DOI: 10.1103/PhysRevB.92.125153. URL: https://link.aps.org/doi/10.1103/PhysRevB.92.125153.

Soluyanov, Alexey A. et al. (2015). "Type-II Weyl semimetals". In: *Nature* 527.7579, pp. 495–498. DOI: 10.1038/nature15768. URL: https://doi.org/10.1038/nature15768.

Somekh, S. et al. (1973). "Channel optical waveguide directional couplers". In: *Applied Physics Letters* 22.1, pp. 46–47. DOI: 10.1063/1.1654468. eprint: https://doi.org/10.1063/1.1654468. URL: https://doi.org/10.1063/1.1654468.

Sørensen, Anders S. et al. (Mar. 2005). "Fractional Quantum Hall States of Atoms in Optical Lattices". In: *Phys. Rev. Lett.* 94 (8), p. 086803. DOI: 10.1103/PhysRevLett.94.086803. URL: https://link.aps.org/doi/10.1103/PhysRevLett.94.086803.

Souslov, Anton, Kinjal Dasbiswas, et al. (Mar. 2019). "Topological Waves in Fluids with Odd Viscosity". In: *Phys. Rev. Lett.* 122 (12), p. 128001. DOI: 10.1103/PhysRevLett.122.128001. URL: https://link.aps.org/doi/10.1103/PhysRevLett.122.128001.

Souslov, Anton, Benjamin C. van Zuiden, et al. (2017). "Topological sound in active-liquid metamaterials". In: *Nature Physics* 13.11, pp. 1091–1094. DOI: 10.1038/nphys4193. URL: https://doi.org/10.1038/nphys4193.

Struck, J., C. Ölschläger, et al. (May 2012). "Tunable Gauge Potential for Neutral and Spinless Particles in Driven Optical Lattices". In: *Phys. Rev. Lett.* 108 (22), p. 225304. DOI: 10.1103/PhysRevLett.108.225304. URL: https://link.aps.org/doi/10.1103/PhysRevLett.108.225304.

Struck, J., M. Weinberg, et al. (2013). "Engineering Ising-XY spin-models in a triangular lattice using tunable artificial gauge fields". In: *Nature Physics* 9.11, pp. 738–743. DOI: 10.1038/nphys2750. URL: https://doi.org/10.1038/nphys2750.

Stützer, Simon et al. (Aug. 2018). "Photonic topological Anderson insulators". In: *Nature* 560.7719, pp. 461–465. ISSN: 0028-0836. DOI: 10.1038/s41586-018-0418-2. URL: http://www.nature.com/articles/s41586-018-0418-2.

Su, W. P. et al. (Aug. 1980a). "Soliton excitations in polyacetylene". In: *Phys. Rev. B* 22 (4), pp. 2099–2111. DOI: 10.1103/PhysRevB.22.2099. URL: https://link.aps.org/doi/10.1103/PhysRevB.22.2099.

— (Aug. 1980b). "Soliton excitations in polyacetylene". In: *Phys. Rev. B* 22 (4), pp. 2099–2111. DOI: 10.1103/PhysRevB.22.2099. URL: https://link.aps.org/doi/10.1103/PhysRevB.22.2099.

Sun, Song et al. (Mar. 2020). "Topological metals induced by the Zeeman effect". In: *Phys. Rev. B* 101 (12), p. 125118. DOI: 10.1103/PhysRevB.101.125118. URL: https://link.aps.org/doi/10.1103/PhysRevB.101.125118.

Sun, Xiao-Qi et al. (Nov. 2018). "Three-Dimensional Chiral Lattice Fermion in Floquet Systems". In: *Phys. Rev. Lett.* 121 (19), p. 196401. DOI: 10.1103/PhysRevLett.121.196401. URL: https://link.aps.org/doi/10.1103/PhysRevLett.121.196401.

Szameit, Alexander, Felix Dreisow, and Stefan Nolte (2012). "Discrete Optics in Femtosecond Laser Written Waveguide Arrays". In: *Femtosecond Laser Micromachining: Photonic and Microfluidic Devices in Transparent Materials*. Berlin, Heidelberg: Springer Berlin Heidelberg, pp. 351–388. ISBN: 978-3-642-23366-1. DOI: 10.1007/978-3-642-23366-1_13. URL: https://doi.org/10.1007/978-3-642-23366-1_13.

Szameit, Alexander, Felix Dreisow, Thomas Pertsch, et al. (Feb. 2007). "Control of directional evanescent coupling in fs laser written waveguides". In: *Opt. Express* 15.4, pp. 1579–1587. DOI: 10.1364/OE.15.001579. URL: http://www.opticsexpress.org/abstract.cfm?URI=oe-15-4-1579.

Szameit, Alexander and Stefan Nolte (2010). "Discrete optics in femtosecond-laserwritten photonic structures". In: *Journal of Physics B: Atomic, Molecular and Optical Physics* 43.16. DOI: 10.1088/0953-4075/43/16/163001. URL: https://iopscience.iop.org/article/10.1088/0953-4075/43/16/163001.

Tanaka, Atushi et al. (Apr. 2007). "Quasienergy Anholonomy and its Application to Adiabatic Quantum State Manipulation". In: *Phys. Rev. Lett.* 98 (16), p. 160407. DOI: 10.1103/PhysRevLett.98.160407. URL: https://link.aps.org/doi/10.1103/PhysRevLett.98.160407.

Tangpanitanon, Jirawat et al. (Nov. 2016). "Topological Pumping of Photons in Nonlinear Resonator Arrays". In: *Phys. Rev. Lett.* 117 (21), p. 213603. DOI: 10.1103/PhysRevLett.117.213603. URL: https://link.aps.org/doi/10.1103/PhysRevLett.117.213603.

Tauber, C. et al. (2019). "A bulk-interface correspondence for equatorial waves". In: *Journal of Fluid Mechanics* 868, R2. DOI: 10.1017/jfm.2019.233. URL: https://www.https://www.cambridge.org/core/journals/journal-of-fluid-mechanics/article/bulkinterface-correspondence-for-equatorial-waves/F67D410731550C55E3B00F50C88DBF00.

— (Feb. 2020). "Anomalous bulk-edge correspondence in continuous media". In: *Phys. Rev. Research* 2 (1), p. 013147. DOI: 10.1103/PhysRevResearch.2.013147. URL: https://link.aps.org/doi/10.1103/PhysRevResearch.2.013147.

Tauber, Clément et al. (2015). "Topological edge states in two-gap unitary systems: a transfer matrix approach". In: *New J. Phys.* 17.11, p. 115008.

Thouless, D. J. (May 1983). "Quantization of particle transport". In: *Phys. Rev. B* 27 (10), pp. 6083–6087. DOI: 10.1103/PhysRevB.27.6083. URL: https://link.aps.org/doi/10.1103/PhysRevB.27.6083.

Thouless, D. J. et al. (Aug. 1982). "Quantized Hall Conductance in a Two-Dimensional Periodic Potential". In: *Phys. Rev. Lett.* 49 (6), pp. 405–408. DOI: 10.1103/PhysRevLett.49.405. URL: https://link.aps.org/doi/10.1103/PhysRevLett.49.405.

Titum, Paraj, Erez Berg, et al. (May 2016). "Anomalous Floquet-Anderson Insulator as a Nonadiabatic Quantized Charge Pump". In: *Phys. Rev. X* 6 (2), p. 021013. DOI: 10.1103/PhysRevX.6.021013. URL: https://link.aps.org/doi/10.1103/PhysRevX.6.021013.

Titum, Paraj, Netanel H. Lindner, et al. (Feb. 2015). "Disorder-Induced Floquet Topological Insulators". In: *Phys. Rev. Lett.* 114 (5), p. 056801. DOI: 10.1103/PhysRevLett.114.056801. URL: https://link.aps.org/doi/10.1103/PhysRevLett.114.056801.

Trompeter, Henrike et al. (Feb. 2006). "Bloch Oscillations and Zener Tunneling in Two-Dimensional Photonic Lattices". In: *Phys. Rev. Lett.* 96 (5), p. 053903. DOI: 10.1103/PhysRevLett.96.053903. URL: https://link.aps.org/doi/10.1103/PhysRevLett.96.053903.

Turker, Z. et al. (2016). "Super Bloch oscillation in a [Formula presented] symmetric system". In: *Physics Letters, Section A: General, Atomic and Solid State Physics* 380.29-30, pp. 2260–2264. ISSN: 03759601. DOI: 10.1016/j.physleta.2016.05.008. URL: http://dx.doi.org/10.1016/j.physleta.2016.05.008.

Verbin, Mor, Oded Zilberberg, Yaacov E. Kraus, et al. (Feb. 2013). "Observation of Topological Phase Transitions in Photonic Quasicrystals". In: *Phys. Rev. Lett.* 110 (7), p. 076403. DOI: 10.1103/PhysRevLett.110.076403. URL: https://link.aps.org/doi/10.1103/PhysRevLett.110.076403.

Verbin, Mor, Oded Zilberberg, Yoav Lahini, et al. (Feb. 2015). "Topological pumping over a photonic Fibonacci quasicrystal". In: *Phys. Rev. B* 91 (6), p. 064201. DOI: 10.1103/PhysRevB.91.064201. URL: https://link.aps.org/doi/10.1103/PhysRevB.91.064201.

Volovik, G.E. (Mar. 1988). "Analog kvantovogo ehffekta Holla v sverkhtekuchej plenke 3He". In: *Zhurnal Ehksperimental'noj i Teoreticheskoj Fiziki* 20 (13). URL: http://www.jetp.ac.ru/cgi-bin/e/index/e/67/9/p1804?a=list.

Volovik, Grigory E. (Feb. 2009). *The Universe in a Helium Droplet*. Oxford University Press. ISBN: 9780199564842. DOI: 10.1093/acprof:oso/9780199564842.001.0001. URL: http://www.oxfordscholarship.com/view/10.1093/acprof:oso/9780199564842.001.0001/acprof-9780199564842.

Wan, Xiangang et al. (May 2011). "Topological semimetal and Fermi-arc surface states in the electronic structure of pyrochlore iridates". In: *Phys. Rev. B* 83 (20), p. 205101. DOI: 10.1103/PhysRevB.83.205101. URL: https://link.aps.org/doi/10.1103/PhysRevB.83.205101.

Wang, Hailong et al. (Apr. 2016). "Floquet Weyl phases in a three-dimensional network model". In: *Phys. Rev. B* 93 (14), p. 144114. DOI: 10.1103/PhysRevB.93.144114. URL: https://link.aps.org/doi/10.1103/PhysRevB.93.144114.

Wang, Y H et al. (Oct. 2013). "Observation of Floquet-Bloch States on the Surface of a Topological Insulator". In: *Science* 342.6157, 453 LP –457. DOI: 10.1126/science.1239834. URL: http://science.sciencemag.org/content/342/6157/453.abstract.

Wang, Zheng et al. (2009). "Observation of unidirectional backscattering-immune topological electromagnetic states". In: *Nature* 461.7265, pp. 772–775. DOI: 10.1038/nature08293. URL: https://doi.org/10.1038/nature08293.

Wang, Zhijun, Yan Sun, et al. (May 2012). "Dirac semimetal and topological phase transitions in A_3Bi (A = Na, K, Rb)". In: *Phys. Rev. B* 85 (19), p. 195320. DOI: 10.1103/PhysRevB.85.195320. URL: https://link.aps.org/doi/10.1103/PhysRevB.85.195320.

Wang, Zhijun, Hongming Weng, et al. (Sept. 2013). "Three-dimensional Dirac semimetal and quantum transport in Cd_3As_2". In: *Phys. Rev. B* 88 (12), p. 125427. DOI: 10.1103/PhysRevB.88.125427. URL: https://link.aps.org/doi/10.1103/PhysRevB.88.125427.

Weeks, C. et al. (Aug. 2010a). "Topological insulators on the Lieb and perovskite lattices". In: *Phys. Rev. B* 82 (8), p. 085310. DOI: 10.1103/PhysRevB.82.085310. URL: https://link.aps.org/doi/10.1103/PhysRevB.82.085310.

— (Aug. 2010b). "Topological insulators on the Lieb and perovskite lattices". In: *Phys. Rev. B* 82 (8), p. 085310. DOI: 10.1103/PhysRevB.82.085310. URL: https://link.aps.org/doi/10.1103/PhysRevB.82.085310.

Wilczek, Frank et al. (June 1984). "Appearance of Gauge Structure in Simple Dynamical Systems". In: *Phys. Rev. Lett.* 52 (24), pp. 2111–2114. DOI: 10.1103/PhysRevLett.52.2111. URL: https://link.aps.org/doi/10.1103/PhysRevLett.52.2111.

Wimmer, Martin, Mohammed-Ali Miri, et al. (Dec. 2015). "Observation of Bloch oscillations in complex PT-symmetric photonic lattices". In: *Sci. Rep.* 5, p. 17760. URL: http://dx.doi.org/10.1038/srep17760.

Wimmer, Martin, Hannah M Price, et al. (2017). "Experimental measurement of the Berry curvature from anomalous transport". In: *Nat. Phys.* 13.6, p. 545. URL: https://www.nature.com/articles/nphys4050.

Wimmer, Martin, Alois Regensburger, et al. (Oct. 2013). "Optical diametric drive acceleration through action–reaction symmetry breaking". In: *Nat. Phys.* 9, p. 780. URL: http://dx.doi.org/10.1038/nphys2777.

Wu, Weikang, Ying Liu, et al. (Mar. 2018). "Nodal surface semimetals: Theory and material realization". In: *Phys. Rev. B* 97 (11), p. 115125. DOI: 10.1103/PhysRevB.97.115125. URL: https://link.aps.org/doi/10.1103/PhysRevB.97.115125.

Wu, Weikang, Zhi-Ming Yu, et al. (2019). "Higher-order Dirac fermions in three dimensions". In: *arXiv preprint arXiv:1912.09036*. URL: https://arxiv.org/abs/1912.09036.

Wunsch, B et al. (Oct. 2008). "Dirac-point engineering and topological phase transitions in honeycomb optical lattices". In: *New Journal of Physics* 10.10, p. 103027. DOI: 10.1088/1367-2630/10/10/103027. URL: https://doi.org/10.1088%2F1367-2630%2F10%2F10%2F103027.

Xiao, Di et al. (July 2010). "Berry phase effects on electronic properties". In: *Rev. Mod. Phys.* 82 (3), pp. 1959–2007. DOI: 10.1103/RevModPhys.82.1959. URL: https://link.aps.org/doi/10.1103/RevModPhys.82.1959.

Xiong, Ye (Mar. 2018). "Why does bulk boundary correspondence fail in some non-hermitian topological models". In: *Journal of Physics Communications* 2.3, p. 035043. DOI: 10.1088/2399-6528/aab64a. eprint: 1705.06039. URL: https://iopscience.iop.org/article/10.1088/2399-6528/aab64a.

Xu, Ye-long et al. (2016). "Experimental realization of Bloch oscillations in a parity-time synthetic silicon photonic lattice". In: *Nature Communications* May 2015. DOI: 10.1038/ncomms11319.

Yang, Bohm-Jung et al. (2014). "Classification of stable three-dimensional Dirac semimetals with nontrivial topology". In: *Nature Communications* 5.1, p. 4898. DOI: 10.1038/ncomms5898. URL: https://doi.org/10.1038/ncomms5898.

Yang, Yan Bin et al. (2019). "Topological Amorphous Metals". In: *Physical Review Letters* 123.7, p. 76401. DOI: 10.1103/PhysRevLett.123.076401. URL: https://doi.org/10.1103/PhysRevLett.123.076401.

Yao, Shunyu, Fei Song, et al. (Sept. 2018). "Non-Hermitian Chern Bands". In: *Phys. Rev. Lett.* 121 (13), p. 136802. DOI: 10.1103/PhysRevLett.121.136802. URL: https://link.aps.org/doi/10.1103/PhysRevLett.121.136802.

Yao, Shunyu, Zhongbo Yan, et al. (Nov. 2017). "Topological invariants of Floquet systems: General formulation, special properties, and Floquet topological defects". In: *Phys. Rev. B* 96 (19), p. 195303. DOI: 10.1103/PhysRevB.96.195303. URL: https://link.aps.org/doi/10.1103/PhysRevB.96.195303.

Yariv, A. (Sept. 1973). "Coupled-mode theory for guided-wave optics". In: *IEEE Journal of Quantum Electronics* 9.9, pp. 919–933. ISSN: 1558-1713. DOI: 10.1109/JQE.1973.1077767.

Yariv, Amnon (1991). *Optical electronics*. Saunders College Publ. ISBN: 9780030532399. URL: https://www.ece.rutgers.edu/~orfanidi/ewa/ewa-2up.pdf.

Ying, Xuzhe et al. (Aug. 2018). "Symmetry-Protected Topological Metals". In: *Phys. Rev. Lett.* 121 (8), p. 086810. DOI: 10.1103/PhysRevLett.121.086810. URL: https://link.aps.org/doi/10.1103/PhysRevLett.121.086810.

— (June 2019). "Topological transitions in metals". In: *Phys. Rev. B* 99 (24), p. 245411. DOI: 10.1103/PhysRevB.99.245411. URL: https://link.aps.org/doi/10.1103/PhysRevB.99.245411.

Young, S. M. et al. (Apr. 2012). "Dirac Semimetal in Three Dimensions". In: *Phys. Rev. Lett.* 108 (14), p. 140405. DOI: 10.1103/PhysRevLett.108.140405. URL: https://link.aps.org/doi/10.1103/PhysRevLett.108.140405.

Yu, Zhi-Ming et al. (Mar. 2019). "Quadratic and cubic nodal lines stabilized by crystalline symmetry". In: *Phys. Rev. B* 99 (12), p. 121106. DOI: 10.1103/PhysRevB.99.121106. URL: https://link.aps.org/doi/10.1103/PhysRevB.99.121106.

Yuce, C. (Mar. 2019). "Spontaneous topological pumping in non-Hermitian systems". In: *Phys. Rev. A* 99 (3), p. 032109. DOI: 10.1103/PhysRevA.99.032109. URL: https://link.aps.org/doi/10.1103/PhysRevA.99.032109.

Zak, J. (Sept. 1988). "Comment on "Time evolution of Bloch electrons in a homogeneous electric field"". In: *Phys. Rev. B* 38 (9), pp. 6322–6323. DOI: 10.1103/PhysRevB.38.6322. URL: https://link.aps.org/doi/10.1103/PhysRevB.38.6322.

Zel'Dovich, Ya. B. (May 1967). "The Quasienergy of a Quantum-mechanical System Subjected to a Periodic Action". In: *Soviet Journal of Experimental and Theoretical Physics* 24, p. 1006. URL: http://www.jetp.ac.ru/cgi-bin/e/index/e/24/5/p1006?a=list.

Zener, Clarence et al. (1934). "A theory of the electrical breakdown of solid dielectrics". In: *Proceedings of the Royal Society of London. Series A, Containing Papers of a Mathematical and Physical Character* 145.855, pp. 523–529. DOI: 10.1098/rspa.1934.0116. URL: https://royalsocietypublishing.org/doi/abs/10.1098/rspa.1934.0116.

Zeng, Yongquan et al. (2020). "Electrically pumped topological laser with valley edge modes". In: *Nature* 578.7794, pp. 246–250. URL: https://www.nature.com/articles/s41586-020-1981-x.

Zhao, Han et al. (2018). "Parity-time symmetric photonics". In: *National Science Review* 5.2, pp. 183–199. DOI: 10.1093/nsr/nwy011. URL: https://academic.oup.com/nsr/article/5/2/183/4816747.

Zhong, Chengyong et al. (2017). "Semi-Dirac semimetal in silicene oxide". In: *Phys. Chem. Chem. Phys.* 19 (5), pp. 3820–3825. DOI: 10.1039/C6CP08439G. URL: http://dx.doi.org/10.1039/C6CP08439G.

Zhou, Longwen et al. (Aug. 2016). "Floquet semimetal with Floquet-band holonomy". In: *Phys. Rev. B* 94 (7), p. 075443. DOI: 10.1103/PhysRevB.94.075443. URL: https://link.aps.org/doi/10.1103/PhysRevB.94.075443.

Zhou, Peiheng et al. (2020). "Amorphous photonic topological insulator". In: *arXiv preprint arXiv:2001.03819*. URL: https://arxiv.org/abs/2001.03819.

Zhu, Shi-Liang et al. (June 2007). "Simulation and Detection of Dirac Fermions with Cold Atoms in an Optical Lattice". In: *Phys. Rev. Lett.* 98 (26), p. 260402. DOI: 10.1103/PhysRevLett.98.260402. URL: https://link.aps.org/doi/10.1103/PhysRevLett.98.260402.

Zhu, Ziming, Ying Liu, et al. (Sept. 2018). "Quadratic contact point semimetal: Theory and material realization". In: *Phys. Rev. B* 98 (12), p. 125104. DOI: 10.1103/PhysRevB.98.125104. URL: https://link.aps.org/doi/10.1103/PhysRevB.98.125104.

Zhu, Ziming, Georg W. Winkler, et al. (July 2016). "Triple Point Topological Metals". In: *Phys. Rev. X* 6 (3), p. 031003. DOI: 10.1103/PhysRevX.6.031003. URL: https://link.aps.org/doi/10.1103/PhysRevX.6.031003.

Zilberberg, Oded et al. (2018). "Photonic topological boundary pumping as a probe of 4D quantum Hall physics". In: *Nature* 553.7686, pp. 59–62. DOI: 10.1038/nature25011. URL: http://dx.doi.org/10.1038/nature25011.

Zirnbauer, Martin R. (1996). "Riemannian symmetric superspaces and their origin in random-matrix theory". In: *Journal of Mathematical Physics* 37.10, pp. 4986–5018. DOI: 10.1063/1.531675. URL: https://doi.org/10.1063/1.531675.